Aix*Marseille université
Socialement engagée

NNT : 2023AIXM0001

THÈSE DE DOCTORAT

Soutenue à Aix-Marseille Université
le 20 décembre 2024 par

Ravel Carlos De Miranda Pimenta

Non-Diffractive Bessel Beams for Near-Field Wireless RF Links

Discipline
Physique et Sciences de la Matière

Spécialité
Optique, Photonique et Traitement d'Image

École doctorale
ED 352 - Physique et sciences de la matière

Laboratoire/Partenaires de recherche
Institut Fresnel
Institut d'Electronique et des Technologies du Numérique (IETR)
Thales Reseach & Technology (TRT)

Composition du jury

Alessandra COSTANZO Professeur, Université de Bologne	Rapporteure
Walter FUSCALDO Chercheur, CNR	Rapporteur
Pascal PAGANI Directeur de Recherche, CEA LETI	Président du jury
Matthieu BERTRAND Ingénieur, TRT Palaiseau	Examinateur
MAURO ETTORRE Professeur, Michigan State University	Examinateur
Gabriel SORIANO Maitre de Conférences, Aix-Marseille Université	Directeur de thèse
Myriam ZERRAD Ingénieur de Recherche, Aix-Marseille Université	Co-Directrice de thèse
Claude AMRA Directeur de Recherche, CNRS Institut Fresnel	Co-Encadrant de thèse

INSTITUT FRESNEL
IETR
THALES
Building a future we can all trust

Affidavit

I, undersigned, Ravel Carlos de Miranda Pimenta, hereby declare that the work presented in this manuscript is my own work, carried out under the scientific supervision of Gabriel SORIANO, Myriam ZERRAD and Claude AMRA, in accordance with the principles of honesty, integrity and responsibility inherent to the research mission. The research work and the writing of this manuscript have been carried out in compliance with both the french national charter for Research Integrity and the Aix-Marseille University charter on the fight against plagiarism.

This work has not been submitted previously either in this country or in another country in the same or in a similar version to any other examination body.

Marseille, October 21, 2024



This work is licensed under Creative Commons Attribution-NonCommercial-NoDerivatives 4.0 International Public License

List of publications and participation in conferences

List of publications and/or patents produced as part of the thesis project :

1. R. Pimenta, G. Soriano, K. Paschaloudis, M. Ettorre, M. Zerrad, and C. Amra, "Power transfer efficiency for obstructed wireless links using Bessel beams," Opt. Express **31**, 35493-35506 (2023).

Participation in conferences and summer schools during the thesis period :

1. ESOA Course : Emerging antenna technologies for novel satellite telecommunication schemes (REVOLVE)) à Rennes, France
2. R. C. M. Pimenta, G. Soriano, K. D. Paschaloudis, M. Ettorre, M. Zerrad and C. Amra, "Self-Healing Analysis of Distorted Weakly-Diffracting Vector Beams," 2023 17th European Conference on Antennas and Propagation (EuCAP), Florence, Italy, 2023, pp. 1-3.
3. R. C. M. Pimenta, G. Soriano, K. D. Paschaloudis, M. Ettorre, M. Zerrad and C. Amra, "Comparing Self-Healing Properties of Polarized Weakly-Diffracting Beams," 2023 IEEE Conference on Antenna Measurements and Applications (CAMA), Genoa, Italy, 2023, pp. 820-822.
4. K. D. Paschaloudis, R. C. M. Pimenta, G. Soriano and M. Ettorre, "Near-Field Links with Obstructed Line of Sight via Bessel Beams," 2023 17th European Conference on Antennas and Propagation (EuCAP), Florence, Italy, 2023, pp. 1-3.
5. R. C. M. Pimenta et al., "Generation of Non-Diffractive Bessel Beams for Near-Field Links Applications Using Meta-Axicons," 2024 18th European Conference on Antennas and Propagation (EuCAP), Glasgow, United Kingdom, 2024, pp. 1-3.
6. K. D. Paschaloudis, R. C. M. Pimenta, D. González-Oveiero, G. Soriano and M. Ettorre, "Metasurface-Based Bessel-Beam Launcher with 100λ Non-Diffractive Range," 2024 18th European Conference on Antennas and Propagation (EuCAP), Glasgow, United Kingdom, 2024, pp. 1-3

7. R C. M. Pimenta et al., "Analyse Comparative de l'Autoréparation entre les Faisceaux de Bessel et les Faisceaux Gaussiens," 23ème édition des Journées Nationales Microondes, Juan Les Pins, 2024

Résumé et mots clés

Cette thèse explore l'analyse des liaisons sans fil utilisant des faisceaux de Bessel non diffractants, opérant dans la région du champ proche. Avec la constante évolution des systèmes de communication sans fil pour supporter des débits de données de plus en plus élevés, la fréquence et la bande passante s'étendent dans le domaine des ondes millimétriques, ce qui conduit à des opérations en champ proche plus fréquentes. Cette expansion introduit de nouveaux challenges. Un des défis qui se présente est la réduction des pertes de trajet (*path loss* en anglais), inhérentes à ces fréquences plus élevées, principalement causées par la diffusion de l'énergie électromagnétique. Les approches traditionnelles s'appuient souvent sur des antennes à gain élevé pour réduire ces pertes. Cependant, ce travail examine une approche alternative qui utilise des faisceaux de Bessel non diffractants pour améliorer l'efficacité du transfert de puissance d'une liaison sans fil. Ces faisceaux présentent un intérêt particulier en raison de leur propagation non diffractant et de leurs propriétés d'auto-régénération, ce qui les rend robustes face aux obstructions. Les faisceaux de Bessel ne peuvent pas être générés dans les applications réelles. Cependant, une bonne approximation de ces faisceaux peut être réalisée en utilisant des ouvertures finies. Ces faisceaux sont appelés faisceaux de Bessel tronqués, et ils conservent leurs propriétés non diffractives dans une région située en champ proche. Cette recherche commence par établir un cadre théorique pour analyser l'efficacité du transfert de puissance sans fil dans les conditions de champ proche et de champ lointain, en dérivant une formulation pour traiter les liaisons partiellement obstruées. L'étude se concentre ensuite sur les caractéristiques des faisceaux de Bessel tronqués. Dans les chapitres suivants, la thèse explore une stratégie visant à améliorer l'efficacité de ces faisceaux en appliquant une modulation de phase linéaire, par rapport à la coordonnée radiale transverse, sur l'ouverture rayonnante. Enfin, ce travail présente la conception et la caractérisation d'un nouveau lanceur de faisceaux Quasi-Bessel, qui utilise une métasurface reproduisant les effets d'un axicon, combinée à une antenne cornet, pour produire un émetteur très efficace et à longue portée.

Mots clés : faisceaux non-diffractants, faisceaux de Bessel, transfert d'énergie sans fil, champ proche, propagation, auto-réparation, diffraction, métasurfaces

Abstract and keywords

This thesis explores the analysis of wireless links radiating non-diffractive Bessel beams, specifically operating in the near-field region of the electromagnetic spectrum. As wireless communication systems evolve to accommodate higher data rates, they expand their frequency and bandwidth into the millimeter-wave domain, leading to more frequent near-field operation. This expansion introduces new challenges. One significant challenge is mitigating the increased path losses inherent in these higher frequencies, primarily driven by the diffractive spreading of electromagnetic energy. Traditional approaches often rely on high-gain antennas to reduce these losses. However, this work investigates an alternative approach that uses non-diffractive Bessel beams to enhance the power transfer efficiency of a wireless link. These beams are of particular interest due to their non-diffractive propagation and self-healing properties, making them robust against obstructions. Bessel beams cannot be generated in real-life applications. However, a good approximation of them can be realized using finite apertures. These beams are called truncated Bessel beams, and they retain their non-diffractive properties within a region that lies in the near field. This research begins by establishing a theoretical framework for analyzing wireless power transfer efficiency in both near-field and far-field conditions, deriving a formulation to address partially obstructed links. The study then focuses on the characteristics of truncated Bessel beams. In subsequent chapters, the thesis explores a strategy to improve the efficiency of these beams by applying a linear phase modulation, with respect to the transverse radial coordinate, over the radiating aperture. Finally, this work presents the design and characterization of a novel Quasi-Bessel beam launcher, which employs a metasurface reproducing the effects of an axicon, combined with a horn antenna to produce a highly efficient, long-range transmitter.

Keywords: non-diffractive beams, Bessel beams, wireless power transfer, near-field, propagation, self-healing, diffraction, metasurfaces

Résumé étendu

Les dispositifs sans fil sont désormais une partie essentielle de notre vie quotidienne. Que ce soit au travail ou pendant les loisirs, ces dispositifs intelligents nous maintiennent connectés les uns aux autres et à une large gamme de contenus. Pour répondre à la demande croissante de débits de données plus élevés, les systèmes sans fil fonctionneront finalement dans les bandes de fréquence millimétriques et sub-millimétriques.

Cependant, à mesure que la fréquence augmente, les antennes tendent à fonctionner dans leur région de champ proche, ce qui pose des défis pour maintenir un fonctionnement efficace en raison de l'augmentation associée des pertes du système. Ces pertes sont principalement dues à la perte de parcours en espace libre, une quantité qui est proportionnelle au carré de la distance entre les dispositifs et à leur fréquence de fonctionnement. Pour relever ce défi, la recherche actuelle se concentre souvent sur le développement d'antennes à gain élevé. Toutefois, il existe des approches alternatives, dont l'une est au cœur du projet auquel cette étude appartient, intitulé LinkAll.

LinkAll est un projet collaboratif impliquant l'Institut Fresnel, Thales Research and Technology (TRT) et l'Institut d'Electronique et des Technologies du numéRique (IETR), dédié à l'étude des faisceaux de Bessel non diffractifs comme un nouveau paradigme pour les liaisons sans fil de champ proche de prochaine génération. L'objectif est de surmonter les pertes de parcours, en développant des liaisons radio sans fil plus écologiques avec des plages de fonctionnement plus larges. Le choix d'utiliser des faisceaux de Bessel provient de leur propagation sans diffraction et de leur nature auto-réparatrice, car la perte de parcours en espace libre résulte de la diffusion quadratique de la puissance électromagnétique avec la distance. En pratique, les faisceaux de Bessel sont généralement générés à l'aide d'ouvertures finies, ce qui limite leurs propriétés non diffractantes au champ proche.

L'objectif principal de cette thèse est l'étude de la transmission de puissance sans fil des systèmes émettant des faisceaux de Bessel. Elle commence par présenter le cadre théorique utilisé pour examiner les liaisons sans fil fonctionnant dans le champ proche. Ce cadre est utilisé pour analyser les faisceaux de Bessel émis par des ouvertures. Ensuite, nous proposons une approche qui conduit à une augmentation de l'efficacité des liaisons sans fil rayonnant des faisceaux de Bessel. La dernière partie de cette thèse est consacrée à la conception et à la caractérisation d'un émetteur. Nous le définissons comme un émetteur de faisceau quasi-Bessel en raison des différences entre le contenu spectral de son faisceau émis et celui d'un faisceau de Bessel.

Dans le premier chapitre, nous établissons les concepts théoriques utilisés dans cette thèse pour analyser les champs électromagnétiques émis par des ouvertures

planes rayonnant dans l'espace libre ou confrontées à un obstacle métallique, comme illustré sur les figures 1 et 2. Pour calculer les champs radiés, une approche basée sur la fonction de Green spectrale est adoptée. Grâce à l'utilisation de la transformation de Fourier, cette approche facilite le calcul efficace des champs électromagnétiques. Nous avons également adopté l'approximation paraxiale pour traiter les champs en champ proche, simplifiant ainsi les fonctions de Green spectrales. Cette approximation permet des calculs pratiques tout en maintenant l'exactitude. De plus, nous avons étendu l'analyse aux problèmes de diffusion impliquant des systèmes rayonnants et un obstacle.

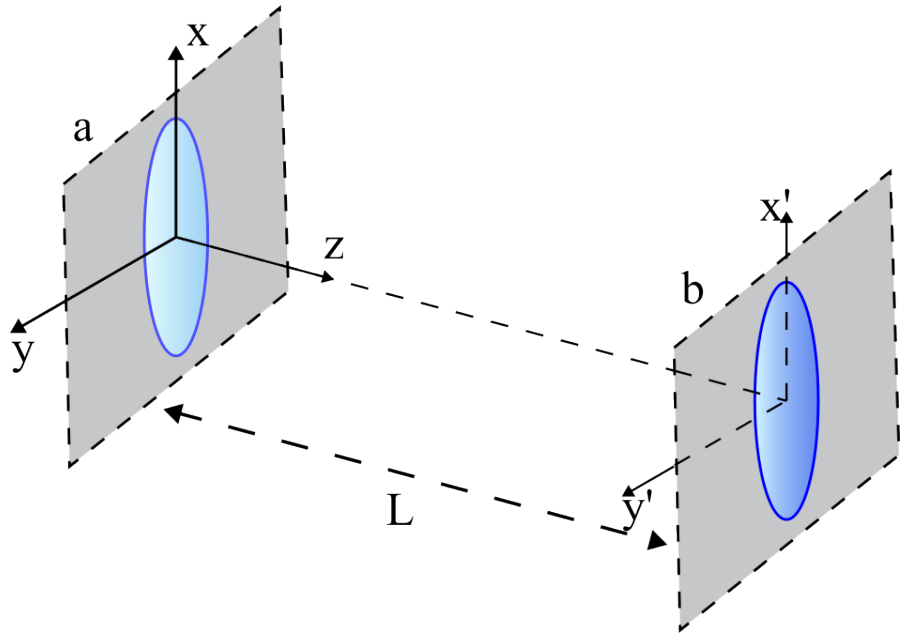

FIGURE 1 – Lien sans fil : deux ouvertures rayonnantes alignées axialement l'une en face de l'autre.

En dérivant le théorème de réciprocité, nous avons démontré comment l'interaction entre deux antennes ou éléments rayonnants peut être précisément quantifiée. Ce théorème établit un lien entre les grandeurs circuitales et les grandeurs des champs électromagnétiques, permettant ainsi l'analyse du transfert de puissance entre deux éléments rayonnants.

Une formule d'efficacité de transfert de puissance sans fil (WPTE) a été dérivée en considérant des antennes rayonnant dans l'espace libre. Nous supposons une condition de conjugaison simultanée d'adaptation d'impédance. En utilisant une formulation variationnelle, nous avons étendu cette formule pour prendre en compte les liaisons obstruées, en traitant le scénario pratique où un obstacle métallique entrave le chemin de propagation direct entre l'émetteur et le récepteur.

Enfin, nous avons comparé la formulation de la WPTE pour des liaisons non obstruées avec l'équation de transmission de Friis. Notre analyse a montré que, bien que les deux approches donnent des résultats identiques dans le champ lointain, la

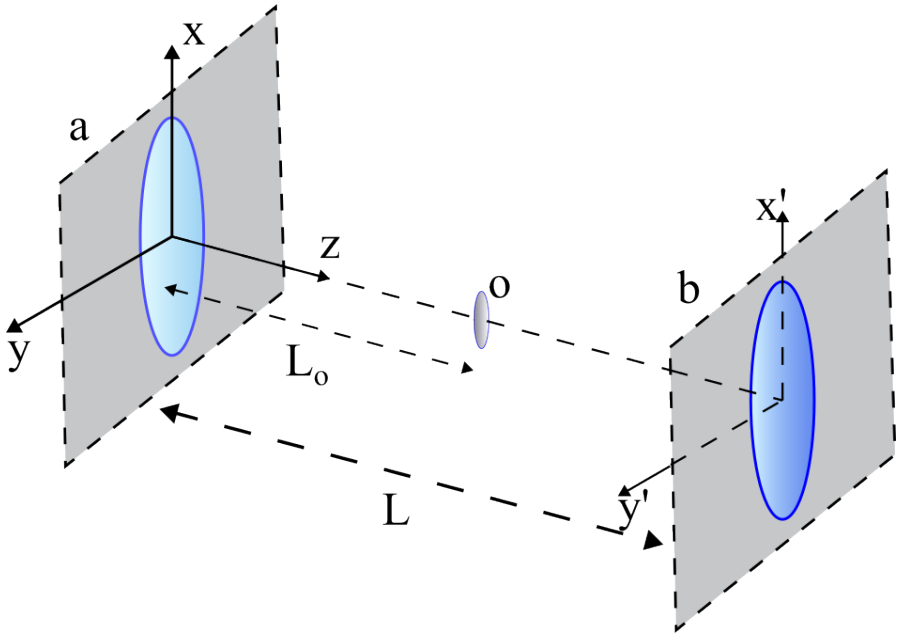

FIGURE 2 – Vue schématique d'un lien sans fil avec une obstruction métallique. L'obstruction a un rayon r_o, une épaisseur nulle, et est placée à $z = L_o$.

formulation WPTE est capable de quantifier les erreurs introduites par l'application de l'équation de Friis dans le champ proche. La comparaison est illustrée à la figure 3.

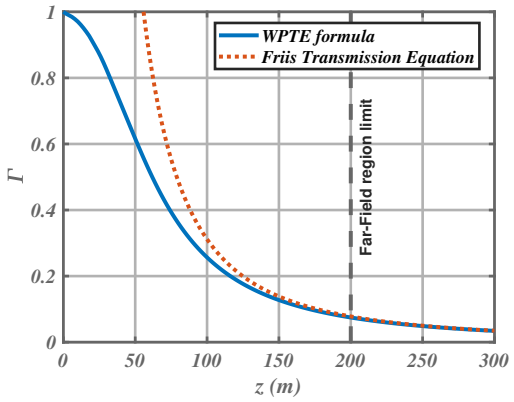

FIGURE 3 – Comparaison entre la formulation de Friis et la formulation de la WPTE. Rayon d'ouverture 0.5 m, fréquence de fonctionnement $f = 30\,\text{GHz}$.

Dans le chapitre suivant, nous avons exploré les propriétés des faisceaux de Bessel. Plus précisément, nous nous sommes concentrés sur leur nature non diffractive et leurs capacités d'auto-réparation. En examinant les fondements théoriques de ces faisceaux, nous avons mis en évidence leur capacité à maintenir un profil transversal stable sur de longues distances. Cette caractéristique distinctive, ainsi que leur capacité à se reconstruire après avoir rencontré des obstacles, renforce le potentiel des

faisceaux de Bessel dans divers domaines.

Nous avons étudié la WPTE entre deux ouvertures identiques rayonnant ces faisceaux, en montrant les différences qui résultent du choix de la troncature. Il a été observé que, pour des distances inférieures à la NDR (région de non diffraction), la WPTE des liaisons non obstruées semble diminuer avec la distance de manière presque linéaire. En revanche, lorsque la distance de séparation dépasse la NDR, l'efficacité de la liaison semble diminuer de façon quadratique, suggérant qu'elle suit le comportement prédit par l'équation de transmission de Friis. Pour la même ouverture et la même distance de séparation, un faisceau de Bessel avec de petites constantes de propagation transversales offre la plus grande efficacité. Ces résultats sont présentés dans les figures 4 et 5.

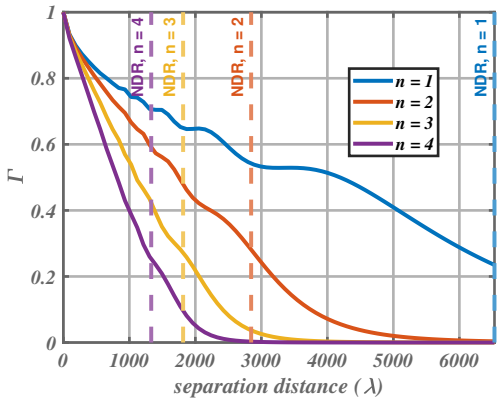

FIGURE 4 – WPTE considérant deux ouvertures axiales alignées émettant des faisceaux de Bessel tronqués, utilisant j_{0n}, qui représente la racine de la fonction de Bessel d'ordre zéro et de première espèce. Rayon d'ouverture $r_a = 50\lambda$ fonctionnant à 60 GHz.

L'impact de l'obstacle sur la WPTE a été étudié en fonction de sa position et de sa taille pour un faisceau de Bessel à polarisation radial. L'obstacle est un disque composé de PEC, axiellement aligné avec les ouvertures. Les résultats obtenus illustrent comment la taille de l'obstacle par rapport au rayon de l'ouverture rayonnante affecte la capacité du faisceau de Bessel à se reconstruire après une obstruction, et donc la possibilité d'établir un lien résilient. En particulier, pour des obstacles dont le rayon atteint jusqu'à 30% du rayon de l'ouverture, la WPTE est entièrement restaurée à son niveau sans obstruction. Il apparaît également que les faisceaux de Bessel avec une plus petite constante de propagation transversale peuvent surmonter des obstacles plus grands. Nous avons observé que la WPTE est plus affectée lorsque l'obstacle est situé à mi-chemin entre les ouvertures et que sa taille est comparable au rayon du faisceau généré. De plus, les résultats indiquent que la longueur de la région d'ombre n'est pas directement liée à la WPTE des liaisons obstruées pour les configurations étudiées. Ces résultats sont présentés dans les figures 6 et 7.

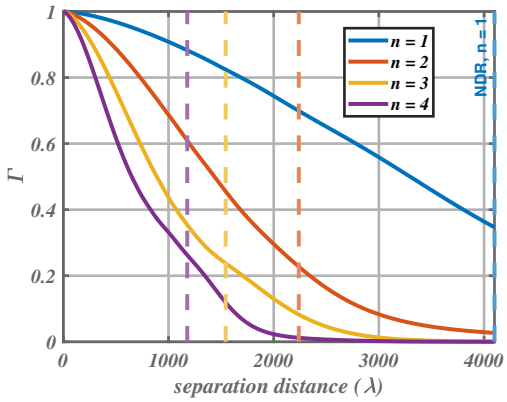

FIGURE 5 – WPTE considérant deux ouvertures axiales alignées émettant des faisceaux de Bessel tronqués, utilisant j_{1n}, , qui représente la racine de la fonction de Bessel du première ordre et de première espèce. Rayon d'ouverture $r_a = 50\lambda$ fonctionnant à 60 GHz.

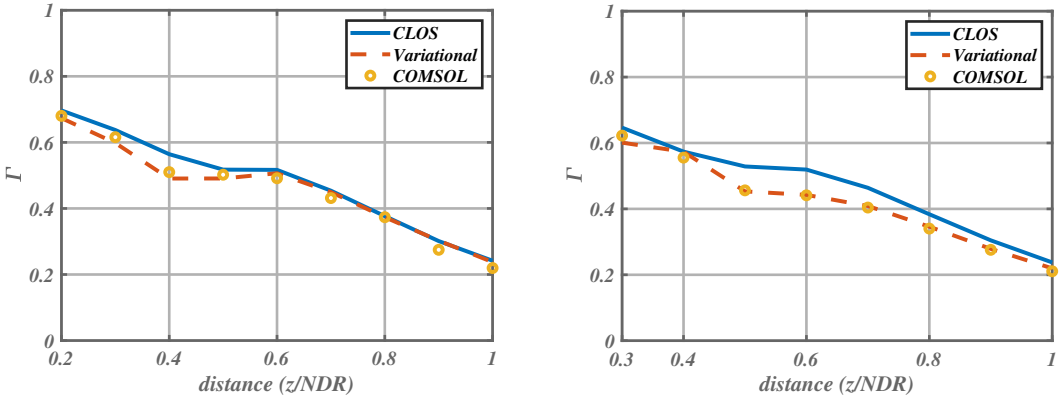

(a) (b)

FIGURE 6 – WPTE en fonction de la distance de séparation pour des liaisons obstruées. La ligne bleue représente la WPTE pour une liaison non obstruée, la ligne rouge en pointillés est le calcul numérique de la liaison obstruée, et les cercles représentent les résultats numériques obtenus par COMSOL. Les paramètres utilisés sont : $r_a = 4\lambda$, $r_o = 0.3r_a$, j_{11} et NDR $= 41\lambda$. Dans (a), l'obstacle est placé à $z = 0.1$ NDR, et dans (b), il est placé à $z = 0.2$ NDR.

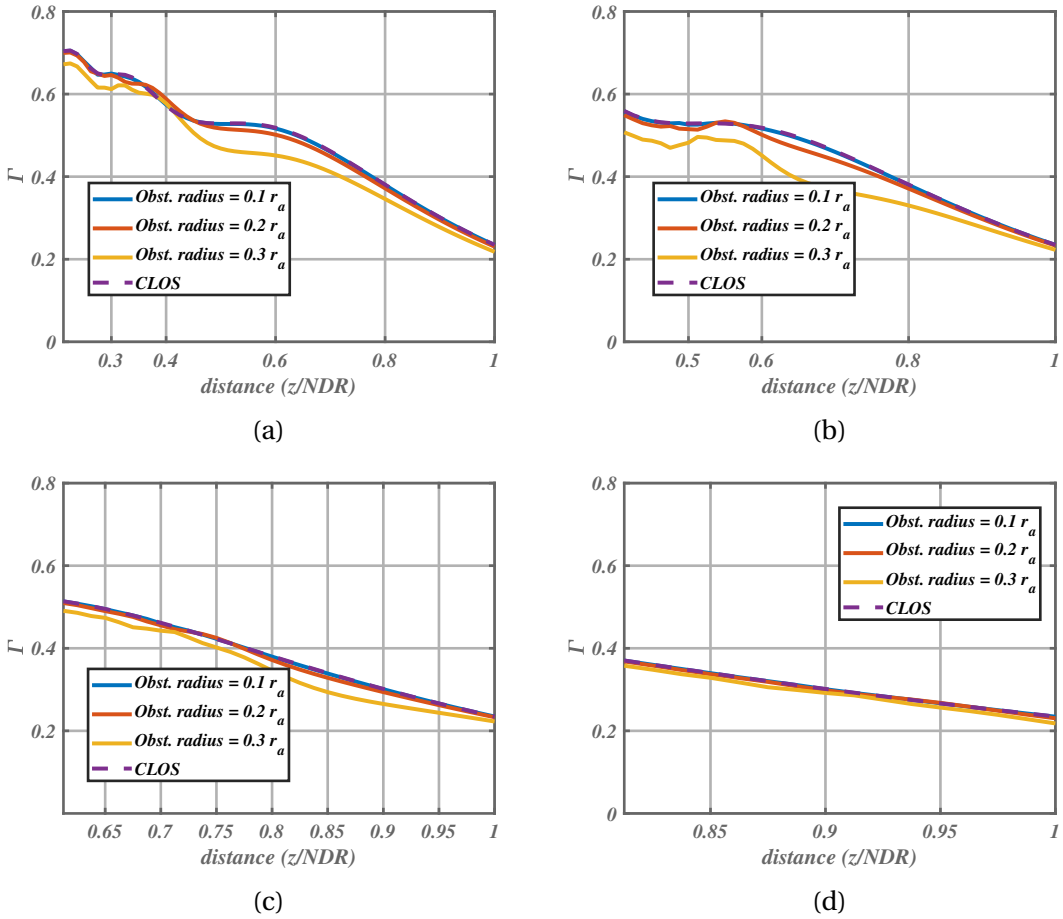

FIGURE 7 – WPTE pour des liaisons obstruées avec différents obstacles placés à différentes positions le long de z. La WPT est évaluée en fonction de la distance. La distance est normalisée par rapport à la NDR. La ligne en pointillés représente la WPTE pour la liaison non obstruée. Les paramètres utilisés sont : $r_a = 50\lambda$, $n = 1$, et NDR $= 6531\lambda$. L'obstacle est placé à $z = 0.2$ NDR (a), $z = 0.4$ NDR (b), $z = 0.6$ NDR (c), et $z = 0.8$ NDR (d).

Nous avons comparé la réponse aux obstacles de différents faisceaux, montrant un avantage pour le faisceau de Bessel par rapport aux faisceaux TEM et Bessel-Gauss. L'obstacle est un disque composé de PEC, axiellement aligné avec l'ouverture. Nous avons également présenté l'évaluation du degré d'auto-réparation des faisceaux de Bessel tronqués, à polarisation linéaire et radiale, en étudiant leur réponse en fonction du rayon de l'obstacle et de sa distance par rapport à l'axe z. Comme prévu, les obstacles plus grands réduisent l'auto-réparation, tandis qu'une augmentation du décalage par rapport au centre du faisceau l'améliore généralement. Enfin, il convient de mentionner que la polarisation radiale a démontré un degré d'auto-réparation plus élevé dans les situations que nous avons étudiées, en particulier lorsque l'obstacle est coaxial à l'ouverture, car il y a un point de champ nul au centre du faisceau.

Ensuite, dans un nouveau chapitre, nous avons étudié la relation complexe entre la

conception de l'ouverture, la modulation de phase spatiale et la WPTE dans le contexte de grandes ouvertures et de distances de fonctionnement encore plus grandes. Étant donné que la NDR est une quantité définie dans le régime de la GO, nous avons défini une plage de fonctionnement qui correspond à la distance de séparation à l'intérieur de laquelle la WPTE reste supérieure à 50%. Nous avons examiné des ouvertures rayonnantes avec des distributions de Bessel tronquées jusqu'à la troisième racine de la fonction de Bessel de première ordre et premier espèce.

Nous avons observé que nous pouvions augmenter la plage de fonctionnement des faisceaux de Bessel tronqués en appliquant une modulation de phase linéaire, par rapport à la composante radiale transversale, sur la distribution du champ tangentiel au niveau de l'ouverture rayonnante. La différence de phase entre les bords et le centre de l'ouverture a été utilisée comme paramètre de contrôle pour estimer la WPTE. De plus, notre analyse a révélé que le contenu spectral est légèrement affecté par la modulation de phase sur la plage d'angles examinés et que les propriétés d'auto-réparation sont maintenues. Nous désignons ces faisceaux comme des faisceaux de Bessel sous-focalisés.

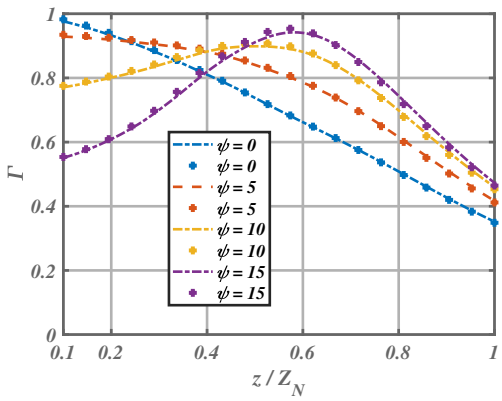

FIGURE 8 – WPTE en fonction de la distance de séparation normalisée, par la NDR (Z_N), en tenant compte de différentes modulations de phase pour la première racine de Bessel, j_{11}. Les lignes en pointillés représentent les données numériques et les signes plus les données de COMSOL.

Nous avons également observé qu'une profil de phase quadratique donnait des résultats comparables. Cependant, en raison de la nécessité de moins de paramètres de contrôle pour l'approche du profil de phase linéaire, nous avons opté pour celle-ci. L'augmentation de la plage de fonctionnement était de 15% de la NDR lorsque tronquée à la première racine de Bessel, de 20% pour la deuxième racine de Bessel, et de 16% pour la troisième racine de Bessel. Cette amélioration se traduit par une réduction de la taille d'ouverture requise pour atteindre la plage de fonctionnement souhaitée.

On a comparé les performances des faisceaux Bessel-Gauss et des faisceaux de Bessel sous-focalisés. Cette comparaison met en évidence un compromis clair entre la WPTE et la plage de fonctionnement. Alors que le faisceau Bessel-Gauss atteint une

WPTE maximale de 98%, sa plage de fonctionnement est relativement plus courte. En revanche, le faisceau de Bessel, avec une WPTE de pointe légèrement inférieure de 94%, étend sa plage de fonctionnement d'environ 20%, offrant des performances plus soutenues sur une plus grande distance.

Le dernier chapitre propose une exploration complète du méta-axicon, qui est une métasurface conçue pour reproduire les effets d'un axicon. Le méta-axicon a été modélisé à l'aide d'une approche théorique, et la comparaison de ce modèle avec des simulations en CST a confirmé la capacité du méta-axicon à imiter de près le comportement idéalisé d'un axicon linéaire. De plus, nous avons mis en évidence l'impact de la quantification de phase et de l'illumination de l'ouverture sur ses performances.

Ensuite, nous avons exploré en profondeur les caractéristiques opérationnelles du méta-axicon, en nous concentrant sur les implications de l'angle de l'axicon et du diamètre de l'ouverture sur la génération du faisceau. En introduisant une métrique numérique tenant compte du contenu spectral du faisceau généré, nous avons pu définir un angle critique qui distingue entre les régimes spectraux gaussien et Bessel. Nous avons défini quatre zones d'opération en relation avec l'angle de l'axicon et la taille de l'aperture. Cette analyse s'est avérée très précieuse, guidant l'optimisation de la conception du méta-axicon pour différentes applications.

Nous présentons la conception finale d'un émetteur à polarisation linéaire fonctionnant à 30 GHz, composé d'une antenne cornette rectangulaire couplée au méta-axicon, illustré dans la figure 9. L'émetteur est désigné sous le nom de lanceur quasi-Bessel, car le spectre de son champ électrique tangent radié diffère de celui d'un faisceau de Bessel tronqué.

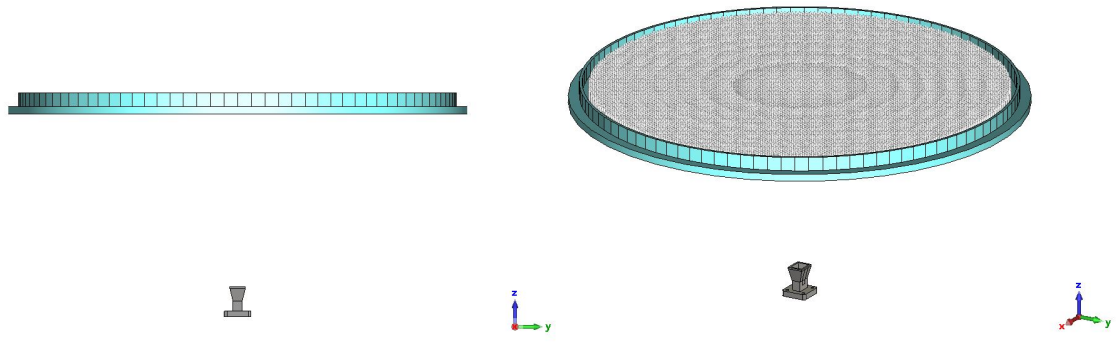

(a) (b)

FIGURE 9 – Structure simulée. En (a), nous pouvons voir une vue latérale, tandis que (b) offre une vue isométrique.

Ce système d'émetteur, optimisé pour un WPTE élevé sur de longues distances, illustre l'application pratique de la conception et des zones d'opération du méta-axicon. Les résultats théoriques et de simulation ont validé la performance du système, tandis qu'une analyse supplémentaire des bandes passantes, des effets de diffraction

et des considérations pratiques ont souligné la robustesse et la polyvalence du méta-axicon dans des scénarios réels.

Les résultats des simulations en CST sont présentés dans la figure 10, tandis que la figure 11 montre une comparaison entre les simulations en CST et le modèle théorique. Le tableau 1 compare deux lanceurs de pointe utilisant des axicons avec celui proposé. Nous observons que nous avons atteint un angle d'axicon plus faible, ce qui se traduit par une portée opérationnelle plus grande.

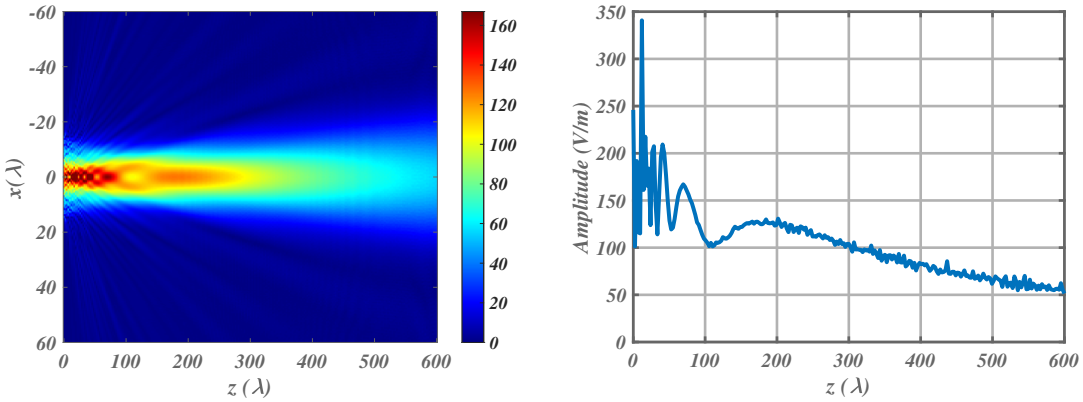

(a) (b)

FIGURE 10 – Résultats du meta-axicon obtenus avec CST. En (a), l'amplitude normalisée de $|E_y|$ dans le plan xz est présentée, tandis qu'en (b), l'amplitude normalisée de $|E_y|$ le long de l'axe z est représentée.

TABLE 1 – Comparaison avec d'autres émetteurs composés d'axicons

Technologie	θ_a	Portée	Rayon	f (GHz)
Meta-axicon (Proposé)	1°	505λ	15λ	30
Meta-axicon [1]	3°	80λ	6.25λ	15
Meta-axicon [2]	20°	15λ	7.5λ	300

Le transmetteur conçu et son analyse détaillée témoignent de l'application pratique des méthodologies et des outils développés dans cette thèse, montrant leur efficacité dans l'avancement de la conception des systèmes sans fil. Ces outils, spécialement créés pour la phase de conception du développement des systèmes sans fil, permettent aux concepteurs d'explorer diverses configurations avec des ressources informatiques minimales, facilitant ainsi les évaluations préliminaires avant de passer à des simulations plus exigeantes.

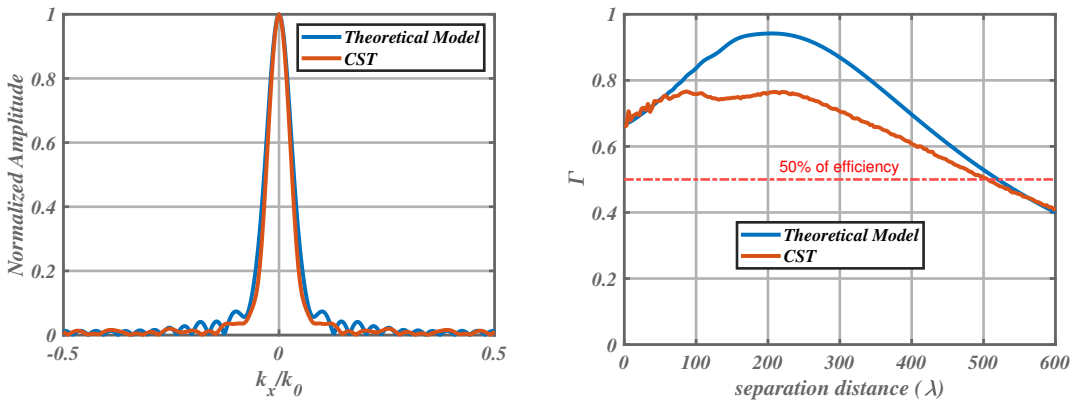

(a) (b)

FIGURE 11 – Comparaison entre le modèle théorique et la simulation CST. En (a), l'amplitude normalisée du contenu spectral de E_y pour $k_y = 0$ est présentée, tandis qu'en (b), la WPTE en fonction de la distance de séparation, en supposant des ouvertures identiques et axialement alignées, est comparée.

Acknowledgments

I would like to extend my heartfelt thanks to my family and friends, especially my wife. **This work is dedicated to you**. I can't wait to celebrate this achievement with all of you, especially over a Brazilian barbecue at my grandmother's house, accompanied by one of my mom's or my aunts' reenactments of the peculiar events that usually happen there, which often involve my godmother.

I would also like to express my sincere gratitude to Konstantinos Paschadoulis, Matthieu Bertrand, and Mauro Ettorre. It may sound "cliché" but it will truly be a pleasure to continue working with such talented colleagues.

Many thanks to the members of the Concept team and my supervisors. A heartfelt thanks to Claude, Myriam, and specially Gabriel.

Gabriel was always there for me providing guidance, motivation, and unwavering support throughout this three-year marathon. Your dedication and professionalism have been truly inspiring. It has been incredibly constructive and enriching to work with you.

This PhD thesis was funded by the National Research Agency (ANR) under the LinkAll (ANR-21-CE25-0014) project, a collaboration between the Institut d'Electronique et des Technologies du numéRique (IETR), Institut Fresnel, and Thales Research and Technology (TRT). The research, which spanned nearly three years, was primarily conducted at Institut Fresnel in Marseille. During this time, there was a constant exchange of data, results, and motivation among all project collaborators.

The computational routines used in this work were developed by me, with invaluable help and guidance from the LinkAll team. The full-wave simulations were carried out by Matthieu Bertrand, who also provided the metasurface used to build the axicon launcher.

While this thesis represents my individual efforts, it is the result of a collective endeavor. I hope this experience has been as rewarding and enjoyable for my colleagues as it has been for me. I wish you an engaging and insightful read.

Contents

Affidavit 2

List of publications and participation in conferences 3

Résumé et mots clés 5

Abstract and keywords 6

Résumé étendu 7

Acknowledgments 17

Contents 18

List of Figures 21

List of Tables 30

List of Acronyms 31

Glossary 33

Nomenclature 35

Introduction 36

1 Theoretical Derivations and Premises 41

1.1 Introduction . . . 41
1.2 Electromagnetic Propagation . . . 42
1.2.1 Radiating Apertures . . . 42
1.2.2 Spectral Domain Propagation . . . 45
1.2.3 Geometry Considerations . . . 46
1.2.4 Scattering Formulation . . . 47
1.3 Wireless Power Transfer Efficiency . . . 49
1.3.1 Electromagnetic Reaction and Reciprocity . . . 49
1.3.2 Simultaneous Conjugate Impedance Match . . . 54
1.3.3 Wireless Power transfer Efficiency Formula . . . 56
1.3.4 Geometry Considerations . . . 57
1.3.5 Obstructed Links . . . 59
1.4 Code Implementation in MATLAB . . . 64

1.5 Derivation of Friis Transmission Equation . . . 66
1.5.1 Exploring the Wireless Power Transfer Efficiency in the Far Field 66
1.5.2 Numerical Comparison . . . 71
1.6 Conclusion . . . 71

2 Weakly Diffractive Wireless Links 73
2.1 Introduction . . . 73
2.2 Bessel Beams . . . 74
2.2.1 Fundamentals and Properties of Bessel Beams . . . 74
2.2.2 Applications . . . 79
2.2.3 Generation Methods in RF domain . . . 80
2.3 Wireless Power Transfer Efficiency Analysis . . . 81
2.3.1 Clear Line of Sight . . . 82
2.3.2 Obstructed Links . . . 88
2.4 Analysis of Diffraction . . . 95
2.5 Metric for Self-healing . . . 98
2.6 Conclusion . . . 100

3 Under-Focused Bessel Beams with Large Operating Distances 102
3.1 Introduction . . . 102
3.2 Phased Modulation on Weakly Diffractive Beams . . . 103
3.3 Comparison with different truncated Bessel beams . . . 108
3.4 Partially obstructed wireless links . . . 110
3.5 Conclusion . . . 113

4 Design and Realization of a Quasi-Bessel Beam Transmitter 114
4.1 Introduction . . . 114
4.2 Axicon as a Phase Transformation . . . 115
4.2.1 Theoretical Model of an Axicon in RF for Linearly Polarized Fields 118
4.2.2 Numerical Results . . . 119
4.3 Meta-Axicon . . . 121
4.4 Comparison Between the Meta-Axicon and Theoretical Model . . . 125
4.4.1 Phase Quantization . . . 127
4.5 Characteristics of Operation . . . 129
4.5.1 Design Limitations and Operation Zones . . . 129
4.5.2 Analysis of Beam Waist Characteristics . . . 137
4.5.3 Exploring Smaller Axicon Angles . . . 139
4.5.4 Feeding considerations . . . 141
4.6 Transmitter Realization . . . 142
4.6.1 Theoretical Model Results . . . 144
4.6.2 CST simulations . . . 145
4.6.3 Comparison of Theoretical and CST results . . . 147
4.6.4 Bandwidth Analysis . . . 149
4.6.5 Diffraction Analysis . . . 150

4.7 Conclusion 154

Conclusion and Future Perspectives **155**

Bibliography **158**

List of Figures

1 Lien sans fil : deux ouvertures rayonnantes alignées axialement l'une en face de l'autre. 8
2 Vue schématique d'un lien sans fil avec une obstruction métallique. L'obstruction a un rayon r_o, une épaisseur nulle, et est placée à $z = L_o$. 9
3 Comparaison entre la formulation de Friis et la formulation de la WPTE. Rayon d'ouverture 0.5 m, fréquence de fonctionnement $f = 30\,\text{GHz}$. . . 9
4 WPTE considérant deux ouvertures axiales alignées émettant des faisceaux de Bessel tronqués, utilisant j_{0n}, qui représente la racine de la fonction de Bessel d'ordre zéro et de première espèce. Rayon d'ouverture $r_a = 50\lambda$ fonctionnant à 60 GHz. 10
5 WPTE considérant deux ouvertures axiales alignées émettant des faisceaux de Bessel tronqués, utilisant j_{1n}, , qui représente la racine de la fonction de Bessel du première ordre et de première espèce. Rayon d'ouverture $r_a = 50\lambda$ fonctionnant à 60 GHz. 11
6 WPTE en fonction de la distance de séparation pour des liaisons obstruées. La ligne bleue représente la WPTE pour une liaison non obstruée, la ligne rouge en pointillés est le calcul numérique de la liaison obstruée, et les cercles représentent les résultats numériques obtenus par COMSOL. Les paramètres utilisés sont : $r_a = 4\lambda$, $r_o = 0.3r_a$, j_{11} et NDR $= 41\lambda$. Dans (a), l'obstacle est placé à $z = 0.1\,\text{NDR}$, et dans (b), il est placé à $z = 0.2\,\text{NDR}$. 11
7 WPTE pour des liaisons obstruées avec différents obstacles placés à différentes positions le long de z. La WPT est évaluée en fonction de la distance. La distance est normalisée par rapport à la NDR. La ligne en pointillés représente la WPTE pour la liaison non obstruée. Les paramètres utilisés sont : $r_a = 50\lambda$, $n = 1$, et NDR $= 6531\lambda$. L'obstacle est placé à $z = 0.2\,\text{NDR}$ (a), $z = 0.4\,\text{NDR}$ (b), $z = 0.6\,\text{NDR}$ (c), et $z = 0.8\,\text{NDR}$ (d). 12
8 WPTE en fonction de la distance de séparation normalisée, par la NDR (Z_N), en tenant compte de différentes modulations de phase pour la première racine de Bessel, j_{11}. Les lignes en pointillés représentent les données numériques et les signes plus les données de COMSOL. . . . 13
9 Structure simulée. En (a), nous pouvons voir une vue latérale, tandis que (b) offre une vue isométrique. 14
10 Résultats du meta-axicon obtenus avec CST. En (a), l'amplitude normalisée de $|E_y|$ dans le plan xz est présentée, tandis qu'en (b), l'amplitude normalisée de $|E_y|$ le long de l'axe z est représentée. 15

11 Comparaison entre le modèle théorique et la simulation CST. En (a), l'amplitude normalisée du contenu spectral de E_y pour $k_y = 0$ est présentée, tandis qu'en (b), la WPTE en fonction de la distance de séparation, en supposant des ouvertures identiques et axialement alignées, est comparée. 16

1.1 System composed of a planar radiating aperture cut in a perfectly electric conductor placed at $z = 0$ [5] 43
1.2 Equivalent model. The aperture is replaced by an equivalent surface magnetic current distribution placed at $z = 0$ and limited by S_a [15] . . 44
1.3 Transmission line equivalent system of the medium [53]. Model considering a surface magnetic current distribution on the plane $x - y$ placed at $z = 0$. 46
1.4 Scattering model. In (a), the original problem is depicted, while in (b) the obstacle is removed an the incident fields are computed. In (c) the currents induced on the surface of the obstacle by the original sources radiate considering the obstacle removed. 48
1.5 Sources a and b radiating in the same medium 50
1.6 Antenna System 52
1.7 Current source and terminals of antenna a. The current $\vec{J}_a$ flows from 1^- to 1^+. 53
1.8 Current source and terminals of antenna b. The current $\vec{J}_b$ flows from 2^- to 2^+. 54
1.9 Four-terminal network representing the wireless system composed of two antennas. In (a), antenna a emitting and b receiving, while in (b), antenna b emitting and a receiving 54
1.10 Equivalent system representing the four-terminal network. In (a), antenna a is emitting and Y_1* is the input admittance, while in (b), antenna b is emitting and Y_2* is the input admittance. 54
1.11 Wireless link: two axially aligned radiating apertures facing each other and cut in parallel infinite ground planes 58
1.12 Schematic view of a wireless link with a metallic obstruction. The obstruction has a radius r_o, zero thickness, and is placed at $z = L_o$ 60
1.13 Scattering formulation. The original problem is shown in (a). In (b) and (c), the obstacle is removed, and we present equivalent scenarios to calculate the incident fields for configurations a and b, respectively. In (d) we have the equivalent problem to calculate the scattered fields radiating in free-space. 61
1.14 Illustration of the spatial grid structure, showing the planes along the z-axis and the corresponding x and y elements. The grid is discretized into Δx, Δy, and Δz steps, defining the spatial resolution across the domain. 65
1.15 Flowchart of the program structure, outlining the main steps in the calculation process. 66

1.16 Wireless link: two axially aligned radiating apertures facing each other and cut in parallel infinite ground planes 67
1.17 Comparison between Friis formulation and the WPTE formulation. Aperture radius 0.5 m, operating frequency $f = 30\lambda$ 71

2.1 Bessel functions of the first kind and different order n 74
2.2 Wave vectors lying on a cone with axicon angle θ_a 75
2.3 Normalized amplitude of the tangential component of a radially polarized truncated Bessel beam. The radius of the aperture is $r_a = 50\lambda$ and the axicon angle is $\theta = 3°$. In (a), the amplitude in the plane transverse to its direction of propagation is presented while in (b), we show the amplitude along coordinate z, in the plane xz. 77
2.4 Normalized amplitude of the spectral content of the tangential component of a radially polarized truncated Bessel beam of first kind and first order $J_1(\cdot)$. The amplitude in tha plane $k_x k_y$ is shown. The radius of the aperture is $r_a = 50\lambda$ and the axicon angle is $\theta = 3°$. 78
2.5 Schematic view of an aperture facing a metallic obstruction. The obstruction is a metallic disk with radius $r_o = 12\lambda$ is placed at $z = 100\lambda$ . . 78
2.6 79
2.7 Amplitude of the tangential component of a radially polarized truncated Bessel beam confronted by an obstruction. The radius of the aperture is $r_a = 50\lambda$ and the axicon angle is $\theta = 3°$. The obstruction is a metallic disk with radius $r_o = 12\lambda$ is placed at $z = 100\lambda$ 79
2.8 Normalized amplitude profile of the tangential electric distribution over the aperture. Aperture radius 50λ, and operation frequency 60 GHz. In (a), truncation using j_{04} and in (b), truncation using j_{14} 82
2.9 Schematic view of the wireless link without obstruction. The system is composed of two axially aligned radiating apertures. 83
2.10 Normalized Tangential field radiating in the plane xz considering $n = 2$ (a) and $n = 4$ (b) for truncation using j_{0n}. Aperture radius $r_a = 50\lambda$ and $f = 60$ GHz 83
2.11 Non-diffractive range as a function of the aperture radius for different j_{0n}. 84
2.12 Spectral content of the tangential component of the truncated Bessel beam using j_{0n}, for $n = 2$ (a) and $n = 4$ (b) 85
2.13 WPTE considering two axially aligned apertures radiating truncated Bessel beams, using j_{0n}. Aperture radius $r_a = 50\lambda$ operating at 60 GHz . 85
2.14 Normalized tangential field radiating in the plane xz considering $n = 2$ (a) and $n = 4$ (b) for truncation using j_{1n}. Aperture radius $r_a = 50\lambda$ and $f = 60$ GHz 86
2.15 Non-diffractive range as a function of the aperture radius for different j_{1n}. 87
2.16 Spectral content of the tangential component of the truncated Bessel beam using j_{1n}, for $n = 2$ (a) and $n = 4$ (b) 87
2.17 Spectral content of the tangential component of the truncated Bessel beam using j_{11} 88

2.18 WPTE considering two axially aligned apertures radiating truncated Bessel beams, using j_{1n}. Aperture radius $r_a = 50\lambda$ operating at 60 GHz . 88
2.19 Schematic view of a wireless link with a metallic obstruction. The system is composed of two apertures and one obstacle, all axially aligned. The obstruction has a radius r_o, zero thickness, and is placed at $z = L_o$ . . . 89
2.20 $\Delta\Gamma$ of VS and PPO solutions compared as function of the separation distance between the radiating apertures. The used parameters are: $r_o = 0.3r_a$, $n = 1$ and the obstacle is placed at $z = 0.2$ NDR. 90
2.21 WPTE as a function of the separation distance. The system operates with CLOS. The blue line shows the results of the numerical calculations and the yellow circles those obtained with COMSOL. The used parameters are: $r_a = 4\lambda$, $n = 1$, and NDR $= 41\lambda$. 91
2.22 WPTE as a function of the separation distance for obstructed links. The blue line is the WPTE for an unobstructed link, the dashed red line is the numerical calculation of the obstructed link and the circles are numerical results by COMSOL. The used parameters are: $r_a = 4\lambda$, $r_o = 0.3r_a$ $n = 1$, and NDR $= 41\lambda$. In (a), the obstacle placed at $z = 0.1$ NDR, and in (b), it is placed at $z = 0.2$ NDR 91
2.23 WPTE for obstructed links for different obstacles placed at different locations along z. The WPT is evaluated as a function of the distance. The distance is normalized with respect to the NDR. The dashed line represents the WPTE for the unobstructed link. The used parameters are: $r_a = 50\lambda$, $n = 1$, and NDR $= 6531\lambda$. The obstacle is placed at $z = 0.2$ NDR (a), $z = 0.4$ NDR (b), $z = 0.6$ NDR (c), and $z = 0.8$ NDR (d) 93
2.24 WPTE for obstructed links for different n: (a) $n = 2$, (b) $n = 3$ and (c) $n = 4$. The obstacle is placed at $z = 0.2$ NDR. Aperture radius $r_a = 50\lambda$. The dashed line represents the WPTE of an unobstructed link. 94
2.25 WPTE as a function of the obstacle radius. The obstacle is placed at $z = 0.2$ NDR and the WPTE is evaluated at $z = 0.8$ NDR. The dashed red line shows the value of the WPTE of an unobstructed link with a separation distance of $L = 0.8$ NDR. The used parameters are: $r_a = 50\lambda$, $n = 1$, and NDR $= 6531\lambda$. 95
2.26 Schematic view of an aperture facing a metallic obstruction. The obstruction is a metallic disk with radius $r_o = 12\lambda$ is placed at $z = 100\lambda$ . . 95
2.27 Amplitude of $E_\rho^{tot}(\rho, z)$ for the BB distribution, considering $r_a = 8\lambda$ and $r_o = 4\lambda$. The shadow distance extends until $z = 0.306$ m. 97
2.28 In (a), (b) and (c) $|E_\rho^{tot}|$ normalized by $|E_\rho^{in}|$ in the plane $z = 0.5$ m is shown. The curves A, B and C are referenced to obstacles of radius 1.6λ, 2.4λ and 4λ, respectively. The dashed purple line represents the normalized $|E_\rho^{in}|$, plotted here for comparison. In (d) it is presented the comparison of the results from our approach and those from COMSOL, considering $|E_\rho^{tot}|$ radiated by the BB distribution in the plane $z = 0.5$ m. 97

2.29 Amplitude of the normalized total tangential electric field propagating along z. The fields are normalized by the maximum amplitude of the incident field. The obstruction is placed at $(x = 10\lambda, y = 0, z = 57\lambda)$, $r_a = 25\lambda$. In (a) case A is shown and the NDR = 453λ, while in (b) case B is shown and the NDR = 385λ. 99
2.30 Self-healing degree relation to the obstacle radius (r_o) and the distance of the obstacle's center to the z-axis is depicted in (a) and (b) respectively. In both cases, the obstacle is placed at $z = 113\lambda$ and the self-healing degree is evaluated at $z = 226.5\lambda$ (dashed line) and at $z = 453\lambda$ (solid line), and $r_a = 25\lambda$. 99

3.1 WPTE considering identical apertures of arbitrary radius as a function of normalized separation distance 103
3.2 WPTE as a function of the normalized separation distance considering different phase modulations for the first Bessel root, j_{11}. The dashed lines represent the numerical data and the plus signs the data from COMSOL. 104
3.3 WPTE as a function of the separation distance for the second Bessel root, j_{12}, for the focused and unfocused cases. The blue and red dashed lines respectively denote the operating ranges for focused ($\psi = 1$) and unfocused ($\psi = 0$) beams, while TP1 and TP2 denote turning points 1 and 2. 105
3.4 WPTE as a function of the distance normalized by Z_N for arbitrary aperture sizes, j_{11} and $\theta_M = 75.6°$, $f = 60\,\text{GHz}$. 106
3.5 Normalized amplitude profile of the spectral content of the tangential field for different θ_M at $z = 0$ and $k_y = 0$ for j_{11} (a), j_{12} (b) and j_{13} (c). . 106
3.6 Z_O as a function of the radius of the apertures. The first, second and third Bessel roots are represented by j_{11}, j_{12} and j_{13} respectively. The dashed curves represent the under-focused Bessel beams operating at θ_C, while the continuous lines represent the truncated Bessel beam. . . 107
3.7 WPTE as a function of the normalized separation distance considering a linear and quadratic phase approaches. 108
3.8 Comparison between linear and quadratic phase profiles considering the second Bessel root, j_{21}, and $\theta_M = 91°$. In (a), the normalized amplitude of the spectral content of the tangential component of the electric field is shown, and in (b), the normalized amplitude of the tangential component of the electric field is presented. 108
3.9 WPTE as a function of the normalized separation distance considering a phase modulation for the first Bessel root, j_{11} and the truncated under-focused Bessel-Gauss beam. The aperture radius is $r = 5\lambda$, apodization width $\omega_0 = 4.25\lambda$ and $f = 60\,\text{GHz}$. 109
3.10 Apertures radiating in the presence of an obstruction. In (a), we have an aperture facing an obstruction, while in (b), a link composed of two apertures and an axially aligned obstruction is shown. 110

3.11 Amplitude of the tangential component of the radially polarized electric field of the truncated Bessel beams (unfocused) for obstructed and unobstructed beams. The obstacle is placed at $z = 358\lambda$. In (a) the amplitude of the field as a function of z/Z_N for j_{12} and $x = 0$ is presented, while in (b), the amplitude profile of the tangential field at $z = Z_m$ for j_{12} and $x = 0$ is shown 111
3.12 Amplitude of the tangential component of the radially polarized electric field of the under-focused beams for obstructed and unobstructed beams. The used parameters are $r_a = 50\lambda$, $r_o = 12.5\lambda$, and $f = 60\,\text{GHz}$. The obstacle is placed at $z = 358\lambda$. In (a), the amplitude as a function of z for j_{12} (third root), $y = 0$ is shown, while in (b), the amplitude of the spectral content for j_{12} (third root) at $z = 0$ is presented 112
3.13 WPTE as a function of the separation distance after the obstruction for the truncated and under-focused Bessel beams. The used parameters are $r_a = 50\lambda$, $r_o = 12.5\lambda$, and $f = 60\,\text{GHz}$. The obstacle is placed at $z = 358\lambda$. 112
3.14 WPTE evaluated at $z = Z_N$ for the under-focused and truncated Bessel beams as a function of the obstruction radius. The used parameters are $r_a = 50\lambda$ and $f = 60\,\text{GHz}$. The obstacle is placed at $z = 358\lambda$. 113

4.1 Axicon composed of a cone made of glass with apex in the point A. A light beam, represented by a single ray, travels from left to right and is refracted by the axicon, crossing the optical axis at point B. Adapted from [106]. 116
4.2 Diffractive Axicon HOLO/OR sold by Edmund Optics company. 116
4.3 Circular phase screen representing the axicon. An incident field, represented by a single ray, travels from left to right and is refracted by the axicon. 117
4.4 Axicon. Ray diagram showing its operation. Rays come from the left, hitting the axicon at $z = 0$, that generates the interference region (in blue) limited by the NDR highlighted in red. Adapted from [102]. 118
4.5 Normalized $|E_x|$ radiated by the axicon. In (a), we show the radiated field in the plane xz, while in (b), the radiated field along z-axis is presented. 119
4.6 Amplitude of normalized $|E_x|$ radiated by the axicon in different z planes. In (a), $z = 10\,\text{cm}$, while in (b), $z = 20\,\text{cm}$. The dotted black circle delimits the null-to-null transverse spot size S_p. 120
4.7 Normalized amplitude profile of the tangential electric radiated field at different plan z and $y = 0$. The orange curve represents the Bessel function $J_0(k_1 x)$. 121
4.8 Normalized amplitude profile of the spectral content of tangential electric radiated field for $k_y = 0$. 121
4.9 Metasurface showing wavefront transformation [119]. 122
4.10 Top view of the meta-axicon, plan xy. 122
4.11 Lateral view of the meta-axicon, plan ZX. 123

4.12 Meta-axicon's unit cell 123
4.13 Amplitude (a) and phase (b) of the unit cell's transmission coefficient as a function of the frequency for fixed height $h = 15.5$ and variable r_p (pillar radius). 124
4.14 Comparison of the tangential electric field from CST and from the theoretical model. In (a) the normalized amplitude along the z-axis is presented, and in (b) the normalized spectral content over the radiating aperture is compared. 126
4.15 Comparison of the WPTE as a function of the separation distance, from CST and theoretical model 126
4.16 Flowchart illustrating the process used to calculate the WPTE from the CST simulation. 127
4.17 Comparison between the continuous and the staircased phase variations for 5 levels. 127
4.18 Normalized tangential electric field amplitude along z-axis for different quantization level n: (a) $n = 5$, (a) $n = 10$, (a) $n = 15$, and (d) $n = 20$. . . 128
4.19 Phase distribution over the radiating aperture for different quantization level n: (a) $n = 5$, (a) $n = 10$, (a) $n = 15$, and (d) $n = 20$. 129
4.20 Normalized spectral content profile of Gaussian distribution, $k_y = 0$. . 130
4.21 Normalized spectral content of the tangential electric field over the axicon aperture with $k_y = 0$, for different axicon angles θ_a. 130
4.22 Critical θ_a as a function of the diameter of the aperture and axicon angle. 131
4.23 Distance where the WPTE drops to 50% after its maximum value as a function of the axicon angle and aperture diameter. Four zones are depicted relating the technological limit and θ_c. 132
4.24 WPTE as a function of the axicon angle and aperture diameter for different z planes. The θ_c line presented separating the two regimes of operation. 133
4.25 Meta-axicon operating in zone 1, $D = 25\lambda, \theta_a = 10°$. In (a), normalized $|E_x|$ along z-axis, in (b) normalized $|E_x|$ in the plane xz, in (c), the WPTE as a function of the separation distance, and in (d), the normalized amplitude of the spectrum of $|E_x|$ with $k_y = 0$. 134
4.26 Meta-axicon operating in zone 2, $D = 50\lambda, \theta_a = 10°$. In (a), normalized $|E_x|$ along z-axis, in (b) normalized $|E_x|$ in the plane xz, in (c), the WPTE as a function of the separation distance, and in (d), the normalized amplitude of the spectrum of $|E_x|$ with $k_y = 0$. 135
4.27 Meta-axicon operating in zone 3, $D = 25\lambda, \theta_a = 3°$. In (a), normalized $|E_x|$ along z-axis, in (b) normalized $|E_x|$ in the plane xz, in (c), the WPTE as a function of the separation distance, and in (d), the normalized amplitude of the spectrum of $|E_x|$ with $k_y = 0$. 136
4.28 Meta-axicon operating in zone 4, $D = 44\lambda, \theta_a = 2°$. In (a), normalized $|E_x|$ along z-axis, in (b) normalized $|E_x|$ in the plane xz, in (c), the WPTE as a function of the separation distance, and in (d), the normalized amplitude of the spectrum of $|E_x|$ with $k_y = 0$. 137

4.29 Comparison of the WPTE, as a function of the separation distance, of a truncated Gaussian beam and the radiated Bessel beam. 138
4.30 Axicon angle effect on the WPTE and radiated field intensity. In (a) the tangential electric field radiated by an aperture along z-axis is presented. In (b) the WPTE as a function of the separation distance is shown. . . . 139
4.31 Comparison of a truncated Gaussian beam and the radiated phased beam. In (a), normalized amplitude of $|E_x|$ in the plane xz for the phased beam ($\theta_a = 0.7°$) is shown. In (b), the normalized amplitude spectrum of the tangential component of the truncated Gaussian beam is compared with that of the radiated beam with $\theta_a = 0.7°$. 140
4.32 Comparison of the truncated Gaussian beam and the radiated phased beam ($\theta_a = 0.7°$). In (a) the amplitude of $|E_x|$ along z-axis is depicted, while in (b), the WPTE as a function of the separation distance is shown. 140
4.33 WR-28 Waveguide Antenna used in the project 141
4.34 Comparison between horn's tangential electric field and ideal Gaussian distribution at optimal distance, $z = 124\,\text{mm}$. 142
4.35 Designed Transmitter System 142
4.36 Amplitude (a) and phase (b) of the unit cell's transmission coefficient as a function of the pillar radius for fixed height $h = 15.5$ and frequency $f = 30\,\text{GHz}$. The variable α represents incidence angle. 143
4.37 Meta-axicon results from the theoretical model. In (a), the normalized amplitude of $|E_y|$ in the plane xz for is shown, while in (b), the normalized amplitude of $|E_y|$ along z-axis is depicted. 144
4.38 Meta-axicon results from the theoretical model. In (a), the normalized amplitude of the spectrum of E_y over the aperture considering $k_y = 0$ is shown, while in (b), the WPTE as a function of the separation distance is shown. 145
4.39 Simulated structure. In (a), we can see a lateral view, while (b) provides an isometric view. 145
4.40 Meta-axicon results from CST. In (a), the normalized amplitude of $|E_y|$ in the plane xz for is shown, while in (b), the normalized amplitude of $|E_y|$ along z-axis is depicted. 146
4.41 Meta-axicon results from CST. In (a), the normalized amplitude of the spectrum of $|E_y|$ over the aperture considering $k_y = 0$ is shown, while in (b), the WPTE as a function of the separation distance, assuming identical and axially aligned apertures, is shown. 147
4.42 Comparison theoretical model and CST simulation. In (a), the phase profile of the tangential electric field, considering $x = 0$, is shown, while in (b), the phase profile is presented for $y = 0$. 148
4.43 Comparison theoretical model and CST simulation. In (a), the amplitude profile of the tangential electric field, considering $x = 0$, is shown, while in (b), the amplitude profile is presented for $y = 0$. 148

4.44 Comparison theoretical model and CST simulation. In (a), the normalized amplitude of the spectral content of E_y for $k_y = 0$ is shown, while in (b), the WPTE as a function of the separation distance, assuming identical and axially aligned apertures, is compared. 149
4.45 WPTE as a function of the separation distance considering different operating frequencies. 150
4.46 Radiated obstructed tangential electric component in the plane xz. The obstacle is axially aligned and placed at $z = 120\lambda$. 150
4.47 Comparison of unobstructed and obstructed amplitude profile of $|E_y|$ with $y = 0$ at different z. The obstacle is placed at $z = 120\lambda$. In (a), $z = 180\lambda$ and in (b) at $z = 505\lambda$ 151
4.48 Self-healing degree as a function of the radius of the obstacle, normalized by the radius of the aperture, calculated at $z = 536\lambda$. 152
4.49 WPTE, as a function of the separation distance, of obstructed link for obstacles with different radii. In blue, the WPTE assuming no obstructions.152
4.50 Radiated obstructed tangential electric component in the plane yz. The obstacle off-centered, placed at $x = 3\lambda, y = 3\lambda, z = 120\lambda$ in (a), and at $x = 5\lambda, y = 5\lambda, z = 120\lambda$ in (b). 153
4.51 WPTE, as a function of the separation distance, of the obstructed link for the off-centered obstacle with radius $r_o = 0.2r_a$ placed at $z = 120\lambda$. The distance from the obstacle's center to the coordinate system's center is denoted by Δx and Δy. In blue, the WPTE assuming no obstructions. 153

List of Tables

1 Comparaison avec d'autres émetteurs composés d'axicons 15

2.1 NDR and ratio k_1/k_0 for an aperture of $r_a = 50\lambda$ Bessel roots of $J_0(\cdot)$ . . 84
2.2 NDR and ratio k_1/k_0 for an aperture of $r_a = 50\lambda$, Bessel roots of $J_1(\cdot)$ . . 86

3.1 WPTE as a function of Z_N for truncated Bessel beams of arbitrary radii 103
3.2 WPTE as a function of Z_N for under-focused truncated Bessel beams operating at θ_C 107

4.1 Design Parameters 144
4.2 Comparison with other launchers composed of axicons 154

List of Acronyms

TRT
Thales Research and Technology. 25, 103

IETR
Institut d'Electronique et des Technologies du numéRique. 25

WPTE
wireless power transfer efficiency. 26, 31, 45, 90, 91, 143

PEC
perfectly electrically conducting. 26, 32, 138

PPW
parallel-plate waveguide. 26

RF
radio frequency. 27

NDR
non-diffractive range. 27, 91

PO
Physical Optics. 29, 37, 52, 143

TM
transverse magnetic. 34

TE
transverse electric. 34

GO
Geometrical Optics. 37

MTs
Modal Techniques. 37

IEs
Integral Equations. 37

MOM
Method of Moments. 46

FDTD
Finite-difference Time-domain method. 46

FEM
Finite Element Method. 46

CLOS
clear line of sight. 48

WPTE PPO
wireless power transfer efficiency pure Physical Optics solution. 52

WPTE VS
wireless power transfer efficiency Variational solution. 52

FFT
Fast Fourier Transform. 53

OCT
optical coherence tomography. 68

BG
Bessel-Gauss. 82

TEM
transverse electromagnetic. 82, 143

Z_O
operating range. 90, 91

CST
CST Studio Suite. 102

FIT
Finite Integration Technique. 113

Glossary

near field

The near-field region surrounding an antenna extends up to a distance $d = 2D^2/\lambda$, where λ is the operating wavelength and D is the largest dimension of the antenna. In this region, the angular field distribution varies significantly with distance from the antenna, and the relationship between the electric and magnetic fields is complex. Obstacles placed within the near field can interfere with the source and alter its radiation characteristics. For distances less than $0.62\sqrt{D^3/\lambda}$ from the antenna, reactive fields dominate. In this reactive near-field region, energy oscillates between the antenna and the surrounding space, behaving like reactance that stores energy without dissipating it [3]. Systems operating in this region can be found in [4]. Beyond the reactive near-field, but still within the near-field, lies the radiative near-field (Fresnel zone). In this region, fields transition from reactive to propagating, and approximations based on the distance between the antenna and observation points can simplify calculations. In this work, the fields are evaluated within the radiative near-field. 25, 31, 143

free-space path loss

The attenuation of a wireless signal as it travels through free space. It is a quantity usually associated with the far field and the Friss transmission equation [5]. It is caused by the geometric spreading of waves and it is mathematically written as:

$$\text{FSPL} = \left(\frac{4\pi f d}{c}\right)^2$$

where f is the operating frequency, d is the distance and c is the speed of light in vacuum. 25

far field

The region where the distance from a radiating source is sufficiently large such that the angular distribution of the field becomes independent of the distance from the source, and the field components are essentially transverse to propagation[5]. Within the far-field region, the wavefronts appear very closely as spherical waves, so that only the power radiated in a particular direction is of importance, rather than the particular shape of the antenna [3]. Also, in this region, the relationship between electric ($\vec{E}$) and magnetic field is ($\vec{H}$) is written

as:

$$\vec{H}(r,\theta,\phi) \approx \frac{1}{\eta_0}\hat{r} \times \vec{E}(r,\theta,\phi)$$

where r,θ,ϕ represent the coordinates the spherical system, $\hat{r}$ is the unitary vector in the r direction, and η_0 denotes the impedance of free space. The far-field condition is typically satisfied when the distance r from the source obeys $r \gg \frac{2D^2}{\lambda}$, where D is the largest dimension of the antenna and λ is the operating wavelength. In most applications, antennas operate in the far-field region, where the Friis transmission equation [5] is usually applied to account for the power transmission. 26, 55, 143

truncated Bessel beam

An approximation of a Bessel beam generated using a finite aperture. 27

operating range

Indicates the maximum separation distance at which two antennas can maintain at least 50% of wireless power transfer efficiency. 27

electromagnetic beams

The term electromagnetic beam lacks a precise, universally accepted definition. However, it generally refers to the flow of electromagnetic waves with a well-defined propagation direction. The field distribution of a beam over any plane normal to the direction of propagation is typically described by a complex function, reflecting its structured nature. Unlike random or scattered emissions, as seen in diffuse reflection, a beam implies a more organized distribution of energy. 62, 63

transverse profile

The cross-sectional distribution of field intensity or power of a beam or wavefront, typically perpendicular to the direction of propagation. 62

beam integrity

A measure of how well an electromagnetic beam maintains its characteristics, such as shape, direction and power distribution, as it propagates through a medium. 62

Nomenclature

ω
: Denotes angular frequency. 31

ϵ
: Denotes the permittivity of a medium. 31

μ
: Denotes the permeability of a medium. 31

k_0
: Denotes the wavenumber in vacuum. 31

σ
: Denotes conductivity. 31

η_0
: Denotes the intrinsic impedance of free space, approximately equal to 377 ohms. 35

$\langle \cdot, \cdot \rangle$
: Denotes the electromagnetic reaction. 40

Y
: Denotes admittance. 44

λ
: Denotes wavelength. 46

Introduction

Electromagnetic waves can be considered as couriers of the universe. They are an efficient way by which the cosmos conveys its messages and deepest secrets. Perhaps, at this very moment, an extraterrestrial species living in a galaxy billions of light-years away is scanning the universe with electromagnetic waves, searching for signs of life beyond their own planet. Since Maxwell's seminal work "A Dynamical Theory of the Electromagnetic Field" [6], humanity has remarkably mastered the use of electromagnetic waves for transmitting both energy and information. The development of modern computation, combined with the blood, sweat, and tears of countless researchers around the globe, has made possible the creation of devices that enable incredible achievements, such as sending a man to the moon or calling family members on the other side of the Atlantic Ocean.

Wireless devices are now an essential part of our daily lives. Whether at work or during leisure, these smart devices keep us connected to each other and to a wide array of content. To meet the growing demand for higher data rates, wireless systems will eventually operate at millimeter and sub-millimeter frequency bands. Yet, as the frequency increases, antennas tend to operate within their near field region, leading to challenges in maintaining efficient operation, due to the associated rise in system losses. These losses are mainly composed by the free-space path loss, a quantity that is quadratically proportional to the distance between the devices and their frequency of operation. To address this challenge, current research often focuses on developing high-gain antennas [7]. However, there are alternative approaches, one of which is the focus of the project to which this study belongs, entitled LinkAll.

LinkAll is a collaborative project involving the Institut Fresnel, Thales Research and Technology (TRT), and the Institut d'Electronique et des Technologies du numéRique (IETR), dedicated to investigating nondiffracting Bessel beams as a new paradigm for next-generation near-field wireless links. The goal is to overcome path loss, developing greener wireless radio links with larger operating ranges. The choice for using Bessel beams comes from their diffraction-free propagation and self-healing nature, as the free-space path loss results from the quadratic spreading of the electromagnetic power with the distance [5]. In practice, Bessel beams are typically generated using finite apertures, which restricts their nondiffracting properties to the near field.

The primary objective of this thesis is the study of the wireless power transmission of systems radiating Bessel beams. It starts by presenting the theoretical framework used to investigate wireless links operating in the near-field. This framework is used to examine Bessel beams radiated by aperture. Then, we propose an approach that leads to an increase in the efficiency of wireless links radiating Bessel beams. The last part of this thesis is dedicated to the design and characterization of a transmitter.

We define it as a quasi-Bessel beam transmitter due to the differences between the spectral content of its radiated beam and that of a Bessel beam.

The main themes of this thesis are outlined in the following paragraphs.

Main Themes

Wireless Power Transfer in the Near-field

The general theory for wireless power transfer efficiency (WPTE) between two antennas, based on electromagnetic reciprocity [8] and thus valid for both near field and far field, was derived in [9, 10]. In [9], the author takes an approach which explores the connections between circuital and field quantities. The derived formula of the WPTE delivers exact results provided that the radiated fields are computed with both antennas in place, which is not a trivial task. In contrast, [10] takes a wave-theory approach and the WPTE formula is derived assuming the antennas to be far apart so the radiation of one device does not affect the other, which is similar to neglecting the reflections between them [11].

The analysis of the power transfer efficiency of two planar aperture antennas, cut in perfectly electrically conducting (PEC) planes and directed toward each other, based on [9, 10], is discussed in [12, 13]. While in [12] reflection is neglected, [13] computes the radiated fields assuming that the two PEC planes emulate a parallel-plate waveguide (PPW) environment, where resonances arise with multiple reflections. These resonances, characteristic of the reactive near field, lead us to adopt the reflectionless approach developed in [12], which is more suitable for the radiative near field. In particular, it is demonstrated in [12] that maximum efficiency is obtained when the amplitude and phase of the illumination of the receiving antenna are matched to the field of the emitter antenna at the plane of the receiving antennas.

The first major step of this publication is deriving the WPTE formula following the reflectionless approach. Our goal is to present a clear and efficient derivation that can serve as a reliable reference. This is presented in **chapter 1**, after the introduction of the theoretical framework used in this thesis. Next, employing a variational approach [14], we extend the WPTE formulation to account for partially obstructed wireless. Furthermore, in **chapter 1**, we present a comparison between the Friis transmission equation [5] and the formulation used in this thesis, showing that they deliver identical results in the far-field region.

Bessel Beams

In **chapter 2**, we present the nondiffracting Bessel beams. We start investigating their formulation derived from the wave function [15]. We then examine the properties of Bessel beams generated by finite apertures, acknowledging that ideal Bessel beams are not physically realizable in practical settings. In [16, 17], it was first demonstrated that a Bessel beam could be generated using a finite aperture in the optical domain,

even though earlier works had suggested the existence of nondiffracting solutions to the wave equation [18].

It was only a matter of time before researchers working in radio frequency (RF) and terahertz domains began presenting results related to Bessel beams in their respective fields [1, 2, 13, 19–37]. When a Bessel beam is generated using finite apertures, it is typically referred to as truncated Bessel beam. The effect of truncation due to the aperture, limits the nondiffracting properties of Bessel beams up to a distance called non-diffractive range (NDR). The NDR is located within the near field of the radiating element. However, this quantity was derived resorting to a ray-optics approach and it is obviously more suited for devices operating in the optical domain. In RF applications, inward Hankel and Bessel distributions are usually employed across apertures to generate Bessel beams. Furthermore, some RF applications make use of axicons illuminated by Gaussian beams [38] to generate Bessel beams.

Additionally, in **chapter 2**, the analysis of the robustness of truncated Bessel beams is presented. A metric known as the self-healing degree [39] is used to evaluate the difference between the propagated fields with and without an obstruction. Beyond investigating the self-healing capabilities in terms of radiation and propagation, our focus is on evaluating the impact of an obstruction on the power transmission between two identical antennas radiating truncated Bessel beams, separated by arbitrary distances.

Enhancing the Operating Range of Truncated Bessel Beams

The reflectionless condition [12] is also considered in the investigation of the power transfer efficiency of circular apertures radiating truncated Gaussian beams [40] and truncated Bessel beams [41]. In [40], it is shown that a truncated linearly polarized Gaussian beam is close to optimal performance, provided that the emitter-receiver distance is exactly two times the Rayleigh length, with the beam waist located in the middle. However, performances for a given set of antennas when the distance is varied are not studied. In [41], it is revealed that radially polarized beams with Bessel amplitude outperform radially polarized beams with Gaussian amplitude in terms of WPTE within the Fresnel region (radiative near field). Additionally, in [41] the authors use a linear combination of Bessel functions as the aperture field distribution to achieve optimal efficiency for a determined separation distance.

Unlike the approaches taken in [40] and [41], which, along with [12], focus on maximizing the WPTE between two apertures separated by a fixed distance, in **chapter 3** we investigate the potential of sustaining high efficiency over a larger distance range by utilizing under-focused Bessel beams. To achieve this objective, we first define the operating range of a wireless link, which indicates the maximum separation distance at which two antennas can maintain at least 50% of WPTE. Then, to enhance the coupling between the apertures, we adopt a focusing strategy: over the radiating apertures we assume a Bessel distribution with a linear phase profile with respect to the transverse radial coordinate. This approach extends the operating range, though it comes with the trade-off of reduced WPTE at shorter distances and a slight decrease

in the maximum WPTE achievable. A study of the self-healing properties of this under-focused beam is also presented, comparing it with a truncated Bessel beam.

Quasi-Bessel Beam Launcher Design

In **chapter 4** we present the design of a linearly polarized transmitter operating at 30 GHz. The device consists of a horn antenna coupled with a metasurface. This metasurface replicates the properties of an axicon [42], a type of optical component. Therefore, it is called meta-axicon. This transmitter is designed to deliver high WPTE over extended distances, making it suitable for long-range applications. This metasurface, which was provided by TRT, was already used in previous projects [43, 44]. As the transmitter radiates a beam whose spectral content deviates from the one of a traditional truncated Bessel beam, we refer to this device as a quasi-Bessel beam transmitter.

We initially focus into the theoretical model underlining the design and operation of axicon-based systems, which describes the generation of a linearly polarized Bessel beam. This model is basically composed of a tangential field distribution over a circular aperture, characterized by a Gaussian amplitude profile with a linear phase distribution with respect to the transverse radial coordinate. Then, the meta-axicon is simulated using full-wave software, and the results are compared with those of the theoretical model to assess its applicability. The performance of the system in terms of WPTE, bandwidth and robustness is presented. Furthermore, by studying the limitations imposed by the design, we recognized the opportunity to explore its full potential.

Main Contributions

The main contributions of this work can be summarized as:

Derivation of the WPTE for wireless links radiating in free-space, valid for near and far-field regions

Following the path of [9, 10], we present a complete and self-consistent derivation of the WPTE formula for unobstructed wireless links. We consider this a valuable contribution because this derivation, along with the relationship between circuital and field quantities in terms of electromagnetic reaction, is rarely covered in recent publications [45] and is primarily found in older literature that is often difficult to access.

Extension of the WPTE formula to address partial obstructions in wireless links

We present a formulation that extends the existing WPTE model to account for obstructions in wireless links. This formulation explores the properties of the reaction concept, leading to a variational approach that is more robust against errors caused by the Physical Optics (PO) approximation. The results of this formulation were presented in a journal publication [46].

Operating range enhancement

We demonstrate that it is possible to increase the operating range of truncated Bessel beams by applying a phase sub-modulation on the tangential field distribution over the radiating apertures of both transmitter and receiver. While a specific launcher design is not presented, its feasibility is supported by existing implementations [47] that couple a Bessel beam launcher with a metasurface lens in the RF domain.

Quasi-Bessel beam launcher design

We present the design of a launcher composed of a metasurface coupled with a horn antenna, conceived to operate at large distances. It operates at 30 GHz, achieving 50% of WPTE at distances greater than 5 meters, using antennas with a diameter of 30 cm. Notably, the radiated beam exhibits a distinct Fourier spectrum compared to a traditional truncated Bessel beam. Therefore, we name it Quasi-Bessel beam launcher.

Spectral domain analysis of truncated Bessel beams

We investigate the spectral content of truncated Bessel beams, revealing the inherent limitations of utilizing axicons for their generation. We introduce a numerical criterion capable of providing the aperture size at which the spectral characteristics of the beam radiated by an axicon deviate from those of a truncated Bessel beam.

1 Theoretical Derivations and Premises

Table of contents

1.1 Introduction . . . 41
1.2 Electromagnetic Propagation . . . 42
1.2.1 Radiating Apertures . . . 42
1.2.2 Spectral Domain Propagation . . . 45
1.2.3 Geometry Considerations . . . 46
1.2.4 Scattering Formulation . . . 47
1.3 Wireless Power Transfer Efficiency . . . 49
1.3.1 Electromagnetic Reaction and Reciprocity . . . 49
1.3.2 Simultaneous Conjugate Impedance Match . . . 54
1.3.3 Wireless Power transfer Efficiency Formula . . . 56
1.3.4 Geometry Considerations . . . 57
1.3.5 Obstructed Links . . . 59
1.3.5.1 Pure Physical Optics Solution . . . 62
1.3.5.2 Variational formulation . . . 63
1.4 Code Implementation in MATLAB . . . 64
1.5 Derivation of Friis Transmission Equation . . . 66
1.5.1 Exploring the Wireless Power Transfer Efficiency in the Far Field 66
1.5.2 Numerical Comparison . . . 71
1.6 Conclusion . . . 71

1.1 Introduction

Antennas are widely used devices that play a crucial role in the radiation and reception of radio waves [5]. While they can be configured in various complex arrangements to optimize performance, the most fundamental wireless system comprises one antenna functioning as a transmitter and another as a receiver. In this research, our focus is on aperture antennas, a category that includes horns, reflectors, lenses, and open-ended waveguides [45]. Aperture antennas can be modeled by an equivalent radiating surface, characterized by a defined field distribution across a specific area, with negligible fields outside this region [48]. Notably, this equivalent surface may not coincide with the physical structure of the antenna but can be represented on a

nearby fictitious surface that effectively captures the antenna's radiating properties [45].

One of the objectives of this study is to characterize electromagnetic fields radiated by planar apertures in both free-space and obstructed scenarios. By applying the field equivalence principle [15] in conjunction with the Plane Wave Spectrum and Fourier transform techniques [49], we can accurately compute the radiated fields from these apertures in a computationally efficient manner. For scenarios involving metallic obstructions, we incorporate a scattered field formulation combined with Physical Optics (PO) [50].

Another key objective of our work is to evaluate the wireless power transfer efficiency (WPTE) between antennas operating in the near field. To derive a WPTE formulation suitable for our system, we build on the work of [9], extending its results to account for partially obstructed links. This is achieved by exploiting the properties of electromagnetic reaction [8].

This chapter reviews the theoretical concepts employed throughout this thesis to compute the radiated fields from apertures, and to estimate the WPTE. The first part is dedicated to the electromagnetic propagation, examining the methods and tools for computing the radiation and scattering [15] of electromagnetic fields radiated by apertures. In the second part, we derive the WPTE formula between two radiating elements, considering both clear and obstructed lines of sight. Then, we present a comparison between the WPTE formula with the Friis transmission equation [5]. The final section presents the chapter's conclusions.

1.2 Electromagnetic Propagation

1.2.1 Radiating Apertures

This Ph.D. thesis investigates the electromagnetic fields emitted by planar radiating apertures [45]. We assume a time-harmonic regime [15] at an angular frequency ω, $\omega > 0$, characterized by a dependence of $e^{j\omega t}$. A time-harmonic field can be expressed as [51]

$$\vec{A}(\vec{r}, t) = \mathrm{Re}\left\{\vec{A}(\vec{r})e^{j\omega t}\right\} \tag{1.1}$$

where $\vec{r}$ represents the position vector and $\vec{A}(\vec{r})$ is a complex vector (phasor). For simplicity, we suppress the time dependence term $e^{j\omega t}$ throughout the text. The permittivity and the permeability of the media studied at ω are defined as ϵ and μ respectively. The wavenumber, k_0, at the operating frequency is defined as $k_0 = \omega\sqrt{\mu\epsilon}$ and the conductivity of the medium is denoted as σ. In a linear and isotropic medium, where the electric source $\vec{J}$ and the magnetic source $\vec{M}$ are present, Maxwell's equa-

tions in differential form write [51]

$$\nabla \times \vec{E} = -j\omega\mu\vec{H} - \vec{M} \tag{1.2}$$

$$\nabla \times \vec{H} = (j\omega\epsilon + \sigma)\vec{E} + \vec{J} \tag{1.3}$$

where $\vec{E}$ and $\vec{H}$ represent the time-harmonic electric and magnetic fields respectively.

Consider a system composed of a planar aperture cut in a perfectly electrically conducting (PEC) infinite plane, as shown in figure 1.1. The aperture is placed at the center of the three-dimensional Cartesian coordinate system (x, y, z), with its dimensions denoted by L and H. The $z = 0$ plane separates the problem into two regions. All the sources are located within the first region, $z < 0$. This region can be represented by a waveguide, for example. In the second region $z > 0$, which consists of free space, the electric and magnetic fields radiated by the aperture are defined as $\vec{E}_a$ and $\vec{H}_a$ respectively. Due to the PEC boundary conditions, the tangential components of $\vec{E}_a$ on the plane $z = 0$ are zero everywhere except within the surface S_a. While the same conclusion can not be drawn for $\vec{H}_a$, the knowledge of the tangential components of the electric field is sufficient to obtain the electromagnetic fields radiated by the aperture as concluded by the uniqueness concept [50]. The equivalence principle [15] and the image theory [51] can be applied to the studied system to obtain an equivalent problem that delivers the same fields $(\vec{E}_a, \vec{H}_a)$ in $z > 0$.

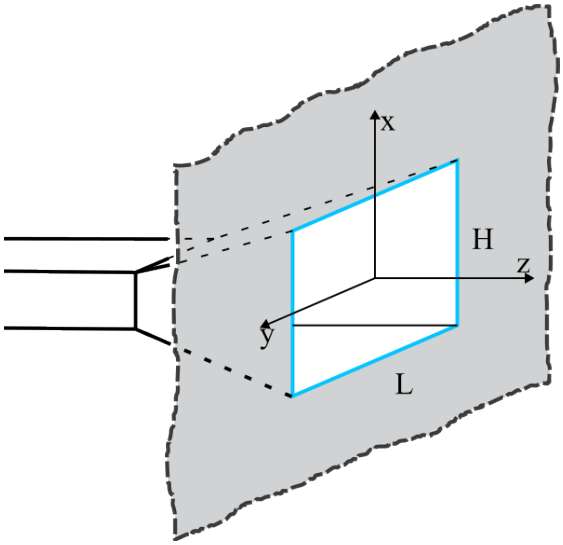

Figure 1.1 – System composed of a planar radiating aperture cut in a perfectly electric conductor placed at $z = 0$ [5]

In the equivalent problem, rather than an aperture cut in an infinite ground plane, the system consists of equivalent currents radiating in free-space. More specifically, the problem will be replaced by an equivalent magnetic current density $\vec{M}_a$, limited

by S_a, radiating in free-space, that writes [52]

$$\vec{M}_a = -2\hat{n}_a \times \vec{E}_a \tag{1.4}$$

where $\hat{n}_a$ represents the unitary vector normal to the aperture in the original problem directed towards positive z. The equivalent system is shown in figure 1.2. The electric field can then be computed as [51]

$$\vec{E}_a = \frac{1}{\epsilon}\nabla \times \vec{F}_a \tag{1.5}$$

$$\vec{F}_a = \frac{\epsilon}{4\pi}\iint_{S_a} \vec{M}_a \frac{e^{-jk_0 d}}{d}\, ds \tag{1.6}$$

where $\vec{F}_a$ represents the electric vector potential due to a magnetic current and the integral is computed over the surface S_a. The term d represents the distance from a point on $\vec{M}_a$, indicated by (x', y', z'), to an observation point, indicated by (x, y, z), that is written as

$$d = \sqrt{(x-x')^2 + (y-y')^2 + (z-z')^2}.$$

To obtain a complete characterization of the electromagnetic field, the magnetic field is subsequently computed based on the electric field as

$$\vec{H}_a = -\frac{1}{j\omega\mu}\nabla \times \vec{E}_a \tag{1.7}$$

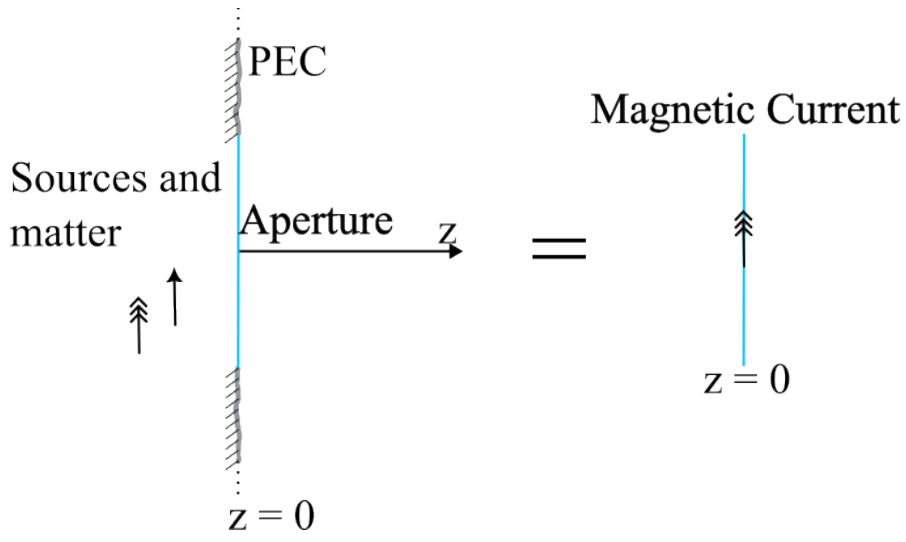

Figure 1.2 – Equivalent model. The aperture is replaced by an equivalent surface magnetic current distribution placed at $z = 0$ and limited by S_a [15]

1.2.2 Spectral Domain Propagation

The integral presented in equation 1.6 usually does not have an analytical closed form. Consequently, it is numerically solved. However, computing it can be a very time-consuming task, as the computation of the integral over all points of the source is required for each observation point. One alternative to address this problem is to resort to a spectral free-space Green's function approach [53], which allows us to calculate the radiated fields in the spectral domain. This is the approach employed in this project.

To go back and forth from the space domain to the spectral domain, the Fourier transform [54] along x and y is used. The Fourier direct transform $\mathscr{F}\{A\}$ and the Fourier inverse transform $\mathscr{F}^{-1}\{\mathscr{A}\}$ of functions A and $\mathscr{A}$ are written as [54]

$$\mathscr{F}\{A(x,y)\} = \mathscr{A}(k_x,k_y) = \iint_{-\infty}^{\infty} A(x,y)e^{jk_x x + jk_y y}\,dx\,dy \tag{1.8}$$

$$\mathscr{F}^{-1}\{\mathscr{A}(k_x,k_y)\} = A(x,y) = \frac{1}{4\pi^2}\iint_{-\infty}^{\infty} \mathscr{A}(k_x,k_y)e^{-jk_x x - jk_y y}\,dk_x\,dk_y \tag{1.9}$$

where k_x and k_y represent the spectral variables, and the spectral domain variables (k_x,k_y), and the direct space variables (x,y), are explicitly shown. In the spectral domain, $\vec{E}_a$, $\vec{H}_a$ and $\vec{M}_a$ are defined as $\vec{\mathscr{E}}_a$, $\vec{\mathscr{H}}_a$, and $\vec{\mathscr{M}}_a$ respectively. We also define the propagation vector $\vec{k}$, for which $\vec{k}\cdot\vec{k} = k_0^2$, as

$$\vec{k} = k_x\hat{x} + k_y\hat{y} + k_z\hat{z} \tag{1.10}$$

where $\hat{m}$ indicates the unitary vector in the m direction, and complex spectral variable k_z is defined as

$$k_z = \begin{cases} \sqrt{k_0^2 - \left(k_x^2 + k_y^2\right)}, \text{ when } \left(k_x^2 + k_y^2\right) \leq k_0^2 \\ -j\sqrt{\left(k_x^2 + k_y^2\right) - k_0^2}, \text{ when } \left(k_x^2 + k_y^2\right) > k_0^2 \end{cases} \tag{1.11}$$

To obtain the radiated fields along z due to the source $\vec{\mathscr{M}}_a$, the dyadic Green's function corresponding to the magnetic current is utilized in an equivalent transmission line model of the medium [53, 55]. This model is illustrated in figure 1.3, where we have equivalent models associated with transverse magnetic (TM) and transverse electric (TE) modes [56]. The voltages and currents along the transmission line are calculated as

$$v_{\text{tm}} = v_{\text{te}} = -\frac{1}{2}e^{-jk_z z} \tag{1.12}$$

$$i_{\text{tm}} = \frac{1}{2Z_{\text{tm}}}e^{-jk_z z} \tag{1.13}$$

$$i_{\text{te}} = \frac{1}{2Z_{\text{te}}}e^{-jk_z z} \tag{1.14}$$

and the wave impedances Z_{tm} and Z_{te} are defined as

$$Z_{\text{tm}} = \eta_0 \frac{k_z}{k_0} \tag{1.15}$$

$$Z_{\text{te}} = \eta_0 \frac{k_0}{k_z} \tag{1.16}$$

where η_0 represents the characteristic impedance of free-space, and the subscripts tm and te indicate the TM and TE modes respectively. In this thesis,

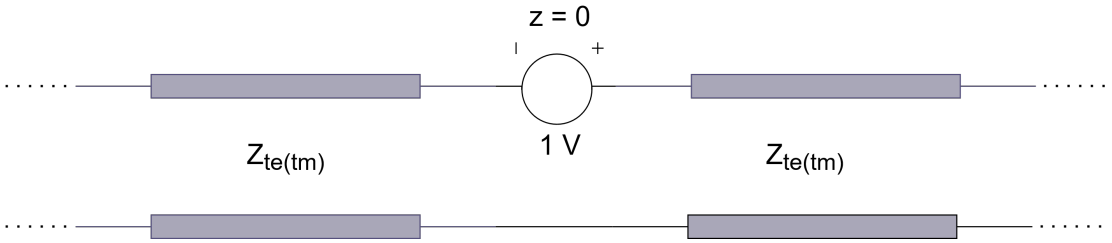

Figure 1.3 – Transmission line equivalent system of the medium [53]. Model considering a surface magnetic current distribution on the plane $x-y$ placed at $z=0$.

In Cartesian coordinates, and considering a magnetic current source placed at $z=0$ and polarized along the tangential coordinates x, y, the spectral dyadic Green's functions write [53]

$$\mathcal{G}_m^e = \begin{pmatrix} \mathcal{G}_m^e xx & \mathcal{G}_m^e xy & \mathcal{G}_m^e xz \\ \mathcal{G}_m^e yx & \mathcal{G}_m^e yy & \mathcal{G}_m^e yz \\ \mathcal{G}_m^e zx & \mathcal{G}_m^e zy & \mathcal{G}_m^e zz \end{pmatrix} = \begin{pmatrix} \frac{(v_{\text{tm}}-v')k_x k_y}{k_x^2+k_y^2} & -\frac{v_{\text{tm}}k_x^2+v_{\text{te}}k_y^2}{k_x^2+k_y^2} & 0 \\ \frac{v_{\text{te}}k_x^2+v_{\text{tm}}k_y^2}{k_x^2+k_y^2} & \frac{(v_{\text{te}}-v_{\text{tm}})k_x k_y}{k_x^2+k_y^2} & 0 \\ -i_{\text{tm}}\frac{\eta_0 k_y}{k_0} & i_{\text{tm}}\frac{\eta_0 k_x}{k_0} & 0 \end{pmatrix} \tag{1.17}$$

$$\mathcal{G}_m^h = \begin{pmatrix} \mathcal{G}_m^h xx & \mathcal{G}_m^h xy & \mathcal{G}_m^h xz \\ \mathcal{G}_m^h yx & \mathcal{G}_m^h yy & \mathcal{G}_m^h yz \\ \mathcal{G}_m^h zx & \mathcal{G}_m^h zy & \mathcal{G}_m^h zz \end{pmatrix} = \begin{pmatrix} -\frac{i_{\text{te}}k_x^2+i_{\text{tm}}k_y^2}{k_x^2+k_y^2} & \frac{(i_{\text{tm}}-i_{\text{te}})k_x k_y}{k_x^2+k_y^2} & 0 \\ \frac{(i_{\text{tm}}-i_{\text{te}})k_x k_y}{k_x^2+k_y^2} & -\frac{i_{\text{tm}}k_x^2+i_{\text{te}}k_y^2}{k_x^2+k_y^2} & 0 \\ v_{\text{te}}\frac{k_x}{\eta_0 k_0} & v_{\text{te}}\frac{k_y}{\eta_0 k_0} & 0 \end{pmatrix} \tag{1.18}$$

and the fields in space domain for all positions in space are computed as

$$\vec{E}_a(x,y,z) = \mathcal{F}^{-1}\left\{\vec{\mathcal{M}}_a(x,y)\mathcal{G}_m^e(x,y,z)\right\} \tag{1.19}$$

$$\vec{H}_a(x,y,z) = \mathcal{F}^{-1}\left\{\vec{\mathcal{M}}_a(x,y)\mathcal{G}_m^h(x,y,z)\right\} \tag{1.20}$$

1.2.3 Geometry Considerations

As outlined in subsection 1.2.1, this project primarily focuses on planar radiating apertures. We operate in the near-field region, specifically within the Fresnel zone

(radiating near-field) [51]. Our objective is to operate at distances significantly larger than the radius of the radiating aperture, which is also large relative to the operating wavelength. Therefore, we assume that we are operating in a small angles (paraxial) condition [54]. In the spectral domain, this means that the width of the angular spectrum of the field is much smaller than k_0. The paraxial approximation is applied to the spectral variable k_z, which in terms of the binomial approximation [54] is written as

$$k_z = k_0\left(1 - \frac{k_x^2 + k_y^2}{2k_0^2} + \frac{(k_x^2 + k_y^2)^2}{8k_0^2} + ...\right) \tag{1.21}$$

Analyzing equations 1.17, 1.18, 1.19 and 1.20, it is noticed that k_z appears both in the argument of the exponential and in the denominator. In the denominator, we only retain the first term of the expression, as the errors introduced by neglecting the other terms is generally considered acceptably small [54]. For the exponential, however, where the errors are more critical, we use the two first terms. This approach is justified by the fact that even slight phase variations, on the order of a fraction of a radian, can significantly affect the value of the exponential [54]. Therefore, we write

$$k_z \approx \begin{cases} k_0\left(1 - \frac{k_x^2+k_y^2}{2k_0^2}\right) & \text{in the exponential} \\ k_0 & \text{in the denominator} \end{cases} \tag{1.22}$$

For illustrative purposes, the $\hat{x}$ component of the magnetic field (H_x) generated by a magnetic current with only a component in the $\hat{x}$ (M_x) direction writes

$$H_x(x,y,z) \approx \frac{-1}{8\pi^2\eta_0}\iint_{-\infty}^{\infty} \mathscr{M}_x e^{-jk_0\left(1-\frac{k_x^2+k_y^2}{2k_0^2}\right)z} e^{-j(k_x x + jk_y y)}\, dk_x dk_y \tag{1.23}$$

where $\mathscr{M}_x$ is $\mathscr{F}\{M_x\}$ and the paraxial approximation is assumed.

1.2.4 Scattering Formulation

The definitions previously presented referred to a system radiating in free space without any obstructions. However, in many situations, radiating systems encounter structures of different materials and sizes. The scattering problem then consists of a background medium with known electromagnetic properties that occupies the entire space studied, fields radiated by finite sources, and a scatterer (object) whose electromagnetic properties differ from those of the background medium. It is important to note that the sources occupy a subdomain outside of the scatterer [57].

To determine the radiated fields in the presence of an obstruction, we define three different types of fields [51]. First, the incident fields are calculated, representing the fields that would be radiated by the existing sources in the absence of the obstacle, i.e., as if the sources radiated in an unbounded medium. Next, the scattered fields are determined, representing the fields radiated by the sources (scattered sources) induced

on the obstacle by the incident fields. We assume that the scattered sources radiate in an unbounded medium. Finally, the total fields are calculated as a superposition of the incident and scattered fields, considering the entire system [15]. The procedure is presented in figure 1.4 and we write

$$\vec{A}^t = \vec{A}^i + \vec{A}^s \tag{1.24}$$

where the superscripts i, s and t represent, respectively, the incident, the scattered and the total fields, and A represents the electric or the magnetic field. In our approach, multiple scattering is neglected assuming that the obstacle is small relative to the sources, and the distance between the source and the scatterer is several wavelengths long.

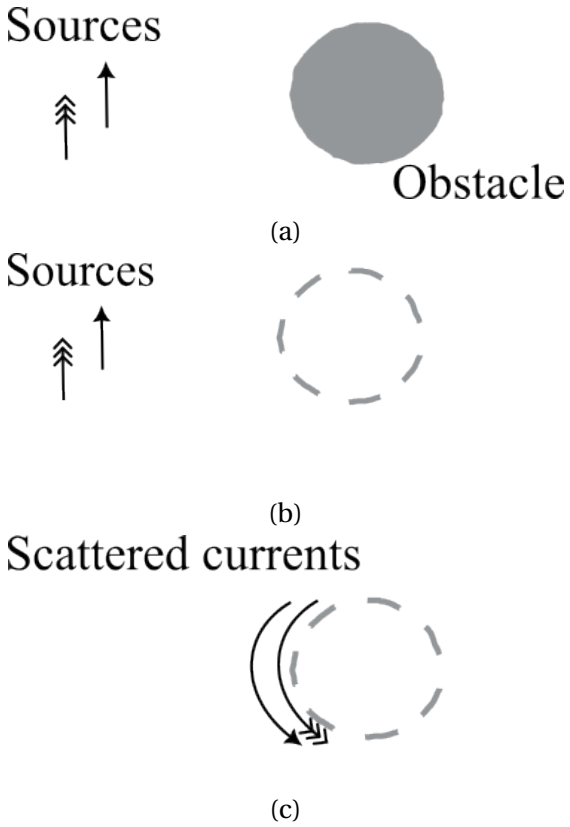

Figure 1.4 – Scattering model. In (a), the original problem is depicted, while in (b) the obstacle is removed an the incident fields are computed. In (c) the currents induced on the surface of the obstacle by the original sources radiate considering the obstacle removed.

Many techniques can be employed to compute the scattered fields, such as Geometrical Optics (GO) , Modal Techniques (MTs), Physical Optics (PO), and Integral Equations (IEs) [51]. Each of these techniques offers distinct advantages depending on the nature of the scattering problem. GO is very accurate for studying scattering

problems where all variations in the amplitude and phase of the field occur over spatial scales that are significantly larger than the wavelength [54]. The MTs are best suited for solving scattering problems involving resonant structures, where the fields can be expanded into a set of orthogonal modes [58]. PO excels in solving scattering from electrically large and smooth conducting bodies, where edge diffraction can be neglected [50]. Finally, IEs offer a more rigorous approach, suitable for complex geometries and inhomogeneous media, but often requiring more computational resources [15, 59].

1.3 Wireless Power Transfer Efficiency

1.3.1 Electromagnetic Reaction and Reciprocity

The electromagnetic reaction [8] and the reciprocity theorem [5] are powerful tools employed in the analysis of electromagnetic systems. While the reaction can be understood as a quantity that measures the interaction between primary electromagnetic sources, the reciprocity theorem brings up the notion that the interchange between the receiver and emitter in a wireless system will not change its response. Following the derivations present in [60] and [15], these concepts can be related to circuital and electromagnetic field quantities, opening a door to very interesting formulations, such as the one derived in [9] for the WPTE between two radiating elements.

The reciprocity theorem is derived considering two sets of electromagnetic sources, a and b, that produce respectively two sets of time-harmonic fields ($e^{j\omega t}$ dependence) $\vec{E}_a$, $\vec{H}_a$ and $\vec{E}_b$, $\vec{H}_b$, as shown in figure 1.5. These sources are operating at the same frequency, and in the same linear isotropic (but not necessarily homogeneous or lossless) medium [15, 51, 61]. This theorem still holds considering anisotropic media provided that the permittivity and permeability matrices are symmetric [62]. Resorting to Maxwell's equations [51], these currents and fields are related by

$$\nabla \times \vec{E}_m = -j\omega\mu\vec{H}_m - \vec{M}_m \tag{1.25}$$

$$\nabla \times \vec{H}_m = (j\omega\epsilon + \sigma)\vec{E}_m + \vec{J}_m \tag{1.26}$$

where the subscript m is a or b depending on the set of elements, $\vec{J}_m$ is an electric source, $\vec{M}_m$ a magnetic source, ω is the angular frequency, σ is the conductivity of the medium, and ϵ and μ are the electric permittivity and magnetic permeability respectively.

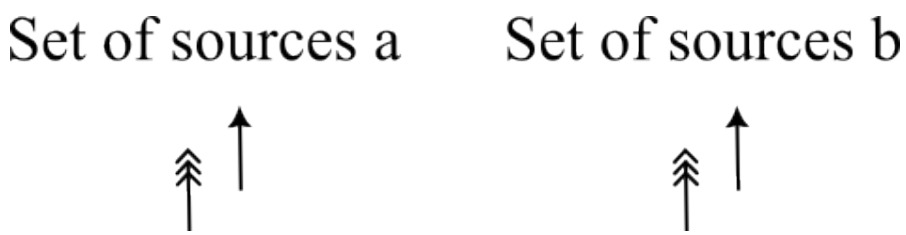

Figure 1.5 – Sources a and b radiating in the same medium

The reciprocity theorem in differential form can be expressed as [15]

$$\nabla \cdot (\vec{E}_a \times \vec{H}_b - \vec{E}_b \times \vec{H}_a) = \vec{J}_a \cdot \vec{E}_b - \vec{M}_a \cdot \vec{H}_b - \vec{J}_b \cdot \vec{E}_a + \vec{M}_b \cdot \vec{H}_a \tag{1.27}$$

where the vector identity $\nabla \cdot (\vec{A} \times \vec{B}) = \vec{B} \cdot (\nabla \times \vec{A}) - \vec{A} \cdot (\nabla \times \vec{B})$ is applied. Furthermore, by performing a volume integral on equation 1.27, and applying the divergence theorem [51], we have

$$\oint_S (\vec{E}_a \times \vec{H}_b - \vec{E}_b \times \vec{H}_a) \cdot \hat{n}\, ds = \iiint_U \vec{J}_a \cdot \vec{E}_b - \vec{M}_a \cdot \vec{H}_b - \vec{J}_b \cdot \vec{E}_a + \vec{M}_b \cdot \vec{H}_a \, du \tag{1.28}$$

where U is a volume comprising the two sources, S is a surface that encloses this volume and the unit normal vector $\hat{n}$ is directed outward from surface S.

We assume that sources a and b are of finite extent, each restricted to its own individual region of existence. As a consequence, we can extend S to infinity, thereby encompassing the entirety of the three-dimensional vector space $\mathbb{R}^3$ within volume U. At infinity, there are only waves propagating outward from the sources, and the electromagnetic fields are related as [51]

$$\vec{E} \times \hat{r} = -\eta_0 \vec{H} \tag{1.29}$$

where η_0 represents the intrinsic impedance of vacuum and $\hat{r}$ is a unitary vector that has the same direction as $\hat{n}$. Furthermore, the fields are required to satisfy the radiation condition [9], also known as Silver–Müller condition, that writes [63]

$$\lim_{L\to\infty} L\vec{E} \text{ is finite,} \tag{1.30}$$

$$\lim_{L\to\infty} L\left[(\hat{n} \times \vec{H}) + \frac{1}{\eta_0}\vec{E}\right] = 0 \tag{1.31}$$

$$\lim_{L\to\infty} L\vec{H} \text{ is finite,} \tag{1.32}$$

$$\lim_{L\to\infty} L\left[\left(\frac{1}{\eta_0}\hat{n} \times \vec{E}\right) - \vec{H}\right] = 0 \tag{1.33}$$

where L is the distance from the source to S. Equations 1.30-1.33 imply that the

electromagnetic fields approach zero at infinity. As a result,

$$\oint_S (\vec{E}_a \times \vec{H}_b - \vec{E}_b \times \vec{H}_a) \cdot \hat{n}\, ds = 0 \tag{1.34}$$

allowing us to rewrite equation 1.28, yielding:

$$\iiint_{\mathbb{R}^3} \vec{J}_a \cdot \vec{E}_b - \vec{M}_a \cdot \vec{H}_b \, du = \iiint_{\mathbb{R}^3} \vec{J}_b \cdot \vec{E}_a - \vec{M}_b \cdot \vec{H}_a \, du \tag{1.35}$$

which represents one of the most useful forms of the reciprocity theorem [51] and brings up the concept of reaction between the two electromagnetic sources. By definition, electromagnetic reaction is expressed as [8]

$$\langle b, a \rangle = \iiint_{U_a} \vec{J}_a \cdot \vec{E}_b - \vec{M}_a \cdot \vec{H}_b \, du \tag{1.36}$$

$$\langle a, b \rangle = \iiint_{U_b} \vec{J}_b \cdot \vec{E}_a - \vec{M}_b \cdot \vec{H}_a \, du \tag{1.37}$$

where sources a and b are limited to volumes U_a and U_b respectively. The reaction can be seen as a coupling between a set of fields and a set of sources, which produce another set of fields [5], and is represented using the symbols $\langle \cdot , \cdot \rangle$. For example, the reaction of field a on source b is written as $\langle a, b \rangle$, while the reaction of field b on source a is written as $\langle b, a \rangle$.

The reciprocity theorem and electromagnetic reaction can also be expressed in terms of closed surfaces contained within S_0. We define two surfaces S_a and S_b, ensuring that these surfaces completely separate sources a and b. In other words, a is entirely contained within S_a, while all parts of b lie outside S_a, and b is entirely contained within S_b, while all parts of a lie outside S_b [8]. Thus, we have

$$\oint_{S_a} (\vec{E}_a \times \vec{H}_b - \vec{E}_b \times \vec{H}_a) \cdot \hat{n}_a \, ds = \oint_{S_b} (\vec{E}_a \times \vec{H}_b - \vec{E}_b \times \vec{H}_a) \cdot \hat{n}_b \, ds \tag{1.38}$$

where unit normal vector $\hat{n}_a$ is directed outward from surface S_a while unit normal vector $\hat{n}_b$ is directed inward from surface S_b. Then, we can write

$$\langle b, a \rangle = \oint_{S_a} (\vec{E}_a \times \vec{H}_b - \vec{E}_b \times \vec{H}_a) \cdot \hat{n}_a \, ds \tag{1.39}$$

$$\langle a, b \rangle = \oint_{S_b} (\vec{E}_a \times \vec{H}_b - \vec{E}_b \times \vec{H}_a) \cdot \hat{n}_b \, ds \tag{1.40}$$

To clarify the connection between circuital elements, field quantities and the reciprocity theorem, we examine a system comprising two antennas, denoted as a and b, illustrated in figure 1.6. Antenna a is connected to a power supply via its input terminals, while the input terminals of antenna b are connected to a load Z_b. Referring to figure 1.6, antennas a and b are within volume U_0 which is enclosed by surface S_0. We assume that the primary independent electromagnetic sources $\vec{J}_a$ and $\vec{M}_a$ exist

only within volume U_a, generating fields $\vec{E}_a$ and $\vec{H}_a$. Within volume U_b, we have $\vec{J}_b$ and $\vec{M}_b$, resulting in $\vec{E}_b$ and $\vec{H}_b$.

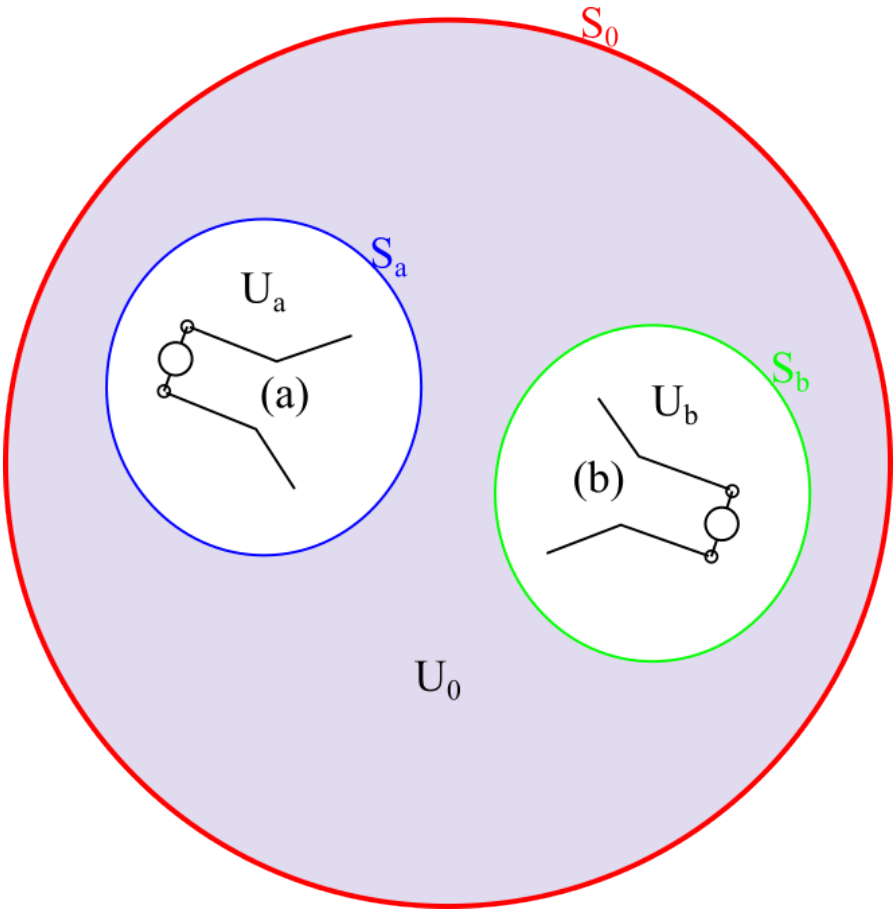

Figure 1.6 – Antenna System

The power supply connected to the input terminals $1^- - 1^+$ of antenna a is an ideal current source limited to this terminals, as depicted in figure 1.7, which can be seen as an impressed electric source [15] oriented in the direction of the unitary vector $\hat{t}_1$. Therefore, $\vec{J}_a = I_{1a}\hat{t}_1\delta_{1^- - 1^+}$, $\vec{M}_a = 0$, and equation 1.36 reduces to

$$\langle b,a\rangle = \iiint_{U_a} \vec{J}_a \cdot \vec{E}_b \, du = I_{1a} \int_{1^-}^{1^+} \vec{E}_b \cdot \hat{t}_1 \, dl_1$$

where l_1 is the path between terminals $1^- - 1^+$ and the integral on the right term gives

$$-V_{1b} = \int_{1^-}^{1^+} \vec{E}_b \cdot \hat{t}_1 \, dl$$

yielding

$$\langle b,a\rangle = -I_{1a}V_{1b} \tag{1.41}$$

where V_{1b} is the voltage induced at the terminals of antenna a due to antenna b. Comparing equation 1.36 and 1.41 a direct relation between field and circuital quantities is observed.

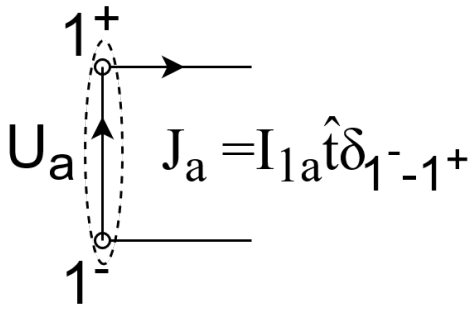

Figure 1.7 – Current source and terminals of antenna a. The current $\vec{J}_a$ flows from 1^- to 1^+.

The same procedure can be applied, with the distinction that, this time, the input terminals of antenna a are connected to a load while the feed, impressed electric current source $\vec{J}_b = I_{2b}\hat{t}_2\delta_{2^- - 2^+}$ is connected to the input terminals of antenna b, and $\hat{t}_2$ is an unitary vector pointing from 2^- to 2^+, as shown in figure 1.8. Under such conditions

$$\langle a,b\rangle = \iiint_{U_b} \vec{J}_b \cdot \vec{E}_a \, du = I_{2b} \int_{2^-}^{2^+} \vec{E}_a \cdot \hat{t}_2 \, dl_2$$

where l_2 is the path between the terminals of b. The voltage between them due to antenna a, V_{2a}, is calculated as

$$-V_{2a} = \int_{2^-}^{2^+} \vec{E}_a \cdot \hat{t}_2 \, dl_2$$

resulting in

$$\langle a,b\rangle = -I_{2b}V_{2a} \tag{1.42}$$

where applying again the reciprocity between the elements of the system yields [64]

$$\langle a,b\rangle = \langle b,a\rangle \tag{1.43}$$

$$V_{1a}I_{1b} = V_{2a}I_{2b} \tag{1.44}$$

where V_{1a} represents the voltage across the terminals of antenna a due to the feeder connected at them, while I_{1b} is the current induced on these terminals due to antenna b. These two quantities are defined for a transmitting and b receiving.

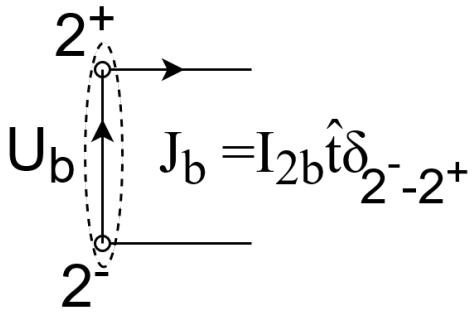

Figure 1.8 – Current source and terminals of antenna b. The current $\vec{J}_b$ flows from 2^- to 2^+.

1.3.2 Simultaneous Conjugate Impedance Match

The system depicted in figure 1.6 can be represented as a two-port network [61], illustrated in figure 1.9. In figure 1.9a, antenna a serves as the emitter and antenna b as the receiver, whereas in figure 1.9b, we have the opposite configuration. Additionally, an equivalent network of the system shown in figure 1.9 is depicted in figure 1.10 for both configurations.

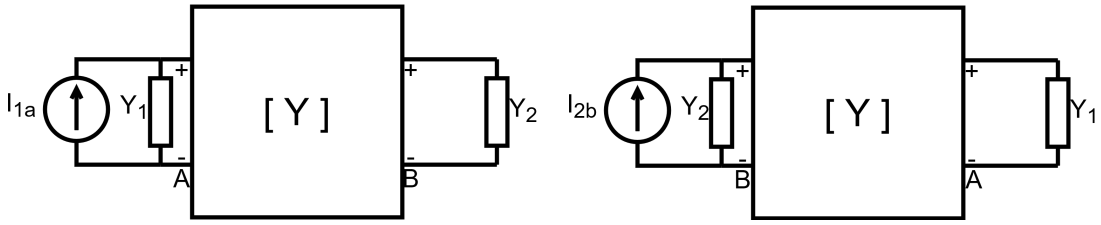

(a) (b)

Figure 1.9 – Four-terminal network representing the wireless system composed of two antennas. In (a), antenna a emitting and b receiving, while in (b), antenna b emitting and a receiving



(a) (b)

Figure 1.10 – Equivalent system representing the four-terminal network. In (a), antenna a is emitting and Y_1* is the input admittance, while in (b), antenna b is emitting and Y_2* is the input admittance.

To obtain maximum power transfer from source to load, the admittance (impedance) of the generator connected to the emitter must be equal to the complex conjugate of the input admittance (impedance) of the system [61].The admittance is represented by the symbol Y. Referring to figure 1.10, we have $Y_i = Y_1^*$ and $Y_o = Y_2^*$, and this condition is known as the simultaneous conjugate impedance match [13, 65]. Therefore, we can write

$$I_{1a} = 2G_1 V_{1a} \tag{1.45}$$
$$I_{2b} = 2G_2 V_{1b} \tag{1.46}$$

considering that $Y_1 = G_1 + jB_1$ and $Y_2 = G_2 + jB_2$, where $G_{1(2)}$ and $B_{1(2)}$ represent the conductance and susceptance of $a(b)$ respectively.

When antenna a is transmitting, the power delivered to the input admittance of antenna a, P_{1a}, which can be understood as the power delivered by I_{1a} to antenna a is written as [5]

$$P_{1a} = \frac{1}{2} G_1 |V_{1a}|^2$$

while the power delivered to the load, P_{2a}, is denoted as

$$P_{2a} = \frac{1}{2} G_2 |V_{2a}|^2$$

and the ration between them is expressed as

$$\frac{P_{2a}}{P_{1a}} = \frac{\frac{1}{2} G_2 |V_{2a}|^2}{\frac{1}{2} G_1 |V_{1a}|^2} \tag{1.47}$$

Considering now the opposite situation, b emitting and a receiving, the power delivered by V_{2g} to antenna b, P_{2b}, and the power dissipated on the load, P_{1b}, can be written as

$$P_{2b} = \frac{1}{2} G_2 |V_{2b}|^2$$
$$P_{1b} = \frac{1}{2} G_1 |V_{1b}|^2$$

and the ration between them expressed as

$$\frac{P_{1b}}{P_{2b}} = \frac{\frac{1}{2} G_1 |V_{1b}|^2}{\frac{1}{2} V_2 |V_{2b}|^2} \tag{1.48}$$

We can employ the reciprocity theorem to establish the connection between equations 1.47 and 1.48. Initially, we rewrite equation 1.44 in terms of the admittance of

our 2-port network system, yielding

$$V_{1a} G_1 V_{1b} = V_{2b} G_2 V_{2a} \tag{1.49}$$

and we take the complex conjugate of it, which is expressed as

$$V_{1a}^* G_1 V_{1b}^* = V_{2b}^* G_2 V_{2a}^* \tag{1.50}$$

Then, multiplying equation 1.49 and 1.50 we obtain

$$\begin{aligned} G_1^2 |V_{1a}|^2 |V_{1b}|^2 &= R_2^2 |V_{2b}|^2 |V_{2a}|^2 \\ \frac{\frac{1}{2} G_1 |V_{1b}|^2}{\frac{1}{2} G_2 |V_{2a}|^2} &= \frac{\frac{1}{2} G_2 |V_{2b}|^2}{\frac{1}{2} G_1 |V_{1a}|^2} = \frac{P_{1b}}{P_{2a}} = \frac{P_{2b}}{P_{1a}} \\ \frac{P_{2a}}{P_{1a}} &= \frac{P_{1b}}{P_{2b}} \end{aligned} \tag{1.51}$$

Equation 1.51 embodies the reciprocity theorem regarding the power transfer between antennas [9]. Essentially, from equation 1.51, it is evident that under a simultaneous conjugate impedance matched condition, interchanging the roles of two antennas in a wireless system (emitter, receiver) does not influence the ratio of antenna input power to power dissipated by the load [9].

1.3.3 Wireless Power transfer Efficiency Formula

The formula for the wireless power transfer efficiency (WPTE) is presented herein following the derivations provided in [9], where the connection between the circuital quantities and electromagnetic quantities is explored through the application of the reciprocity theorem. Combining equations 1.39, 1.41 and 1.45, we write

$$-2 V_{1a} G_1 V_{1b} = \oint_{S_a} (\vec{E}_a \times \vec{H}_b - \vec{E}_b \times \vec{H}_a) \cdot \hat{n}_a \, ds \tag{1.52}$$

while combining equations 1.40, 1.42 and 1.46, we obtain

$$-2 V_{2b} G_2 V_{2a} = \oint_{S_b} (\vec{E}_a \times \vec{H}_b - \vec{E}_b \times \vec{H}_a) \cdot \hat{n}_b \, ds \tag{1.53}$$

By invoking the reciprocity theorem, we can establish a relationship between the circuital and field quantities, yielding

$$-2 V_{1a} G_1 V_{1b} = -2 V_{2b} G_2 V_{2a} = \oint_{S_a} (\vec{E}_a \times \vec{H}_b - \vec{E}_b \times \vec{H}_a) \cdot \hat{n}_a \, ds \tag{1.54}$$

Taking the complex conjugate of equation 1.54

$$-2V_{1a}^{*}G_1V_{1b}^{*} = -2V_{2b}^{*}G_2V_{2a}^{*} = \left(\oint_{S_a}(\vec{E}_a \times \vec{H}_b - \vec{E}_b \times \vec{H}_a)\cdot \hat{n}_a\, ds\right)^{*} \tag{1.55}$$

and multiplying 1.54 and 1.55, we find

$$\begin{aligned} 4|V_{1a}|^2G_1^2|V_{1b}|^2 = 4|V_{2b}|^2G_2^2|V_{2a}|^2 &= \left|\oint_{S_a}\left(\vec{E}_a \times \vec{H}_b - \vec{E}_b \times \vec{H}_a\right)\cdot \hat{n}_a\, ds\right|^2 \\ \frac{\frac{1}{2}G_1|V_{1b}|^2}{\frac{1}{2}G_2|V_{2a}|^2} = \frac{\frac{1}{2}G_2|V_{2b}|^2}{\frac{1}{2}G_1|I_{Va}|^2} &= \frac{\left|\oint_{S_a}\left(\vec{E}_a \times \vec{H}_b - \vec{E}_b \times \vec{H}_a\right)\cdot \hat{n}_a\, ds\right|^2}{16\left(\frac{1}{2}G_2|V_{2a}|^2\frac{1}{2}|V_{1a}|^2G_1\right)} \\ \Gamma = \frac{\left|\oint_{S_a}\left(\vec{E}_a \times \vec{H}_b - \vec{E}_b \times \vec{H}_a\right)\cdot \hat{n}_a\, ds\right|^2}{16\left(\frac{1}{2}G_2|I_{2a}|^2\frac{1}{2}|V_{1a}|^2G_1\right)} & \end{aligned} \tag{1.56}$$

where Γ is the WPTE of our link. The calculation presented by equation 1.56 provides a versatile and rigorous method for computing the efficiency between two antennas, regardless of their dimensions, relative spatial orientation, or the polarization characteristics of the radiated fields [9]. A more compact form of this formula, in terms of the electromagnetic reaction between the sources, is written as [12]

$$\Gamma = \frac{|\langle b, a\rangle|^2}{16P_{1a}P_{2b}} \tag{1.57}$$

where P_{1a} and P_{2b} are the power radiated by antennas a and b respectively. Additionally, as $\langle a, b\rangle = \langle b, a\rangle$, the numerator of equation 1.57 can be changed to $\langle a, b\rangle$ without changing the result.

1.3.4 Geometry Considerations

In our work, we consider two planar circular axially aligned radiating apertures facing each other, cut in PEC planes parallel to each other. The system is depicted in figure 1.11, where the Cartesian coordinate system (x, y, z) is adopted to describe the geometry of the problem. The transmitter, denoted as a, and the receiver, denoted as b, are located respectively at z = 0 and z = L. Aperture a generates the fields $\vec{E}_a$, $\vec{H}_a$ and aperture b, $\vec{E}_b$, $\vec{H}_b$.

If the fields radiated by a and b are calculated considering both antennas in place, Γ emerges as an exact solution. However, obtaining the fields in this configuration is a challenging task that requires the use of computational electromagnetic methods, such as the Method of Moments (MOM) [59, 66], the Finite-difference Time-domain method (FDTD) [67, 68] or the Finite Element Method (FEM) [69, 70]. Therefore, and due to the objectives of this thesis, some approximations will be made.

We focus on the use of electrically large apertures, with radii exceeding 10λ, where λ denotes the operating wavelength. The goal is to establish an efficient wireless link,

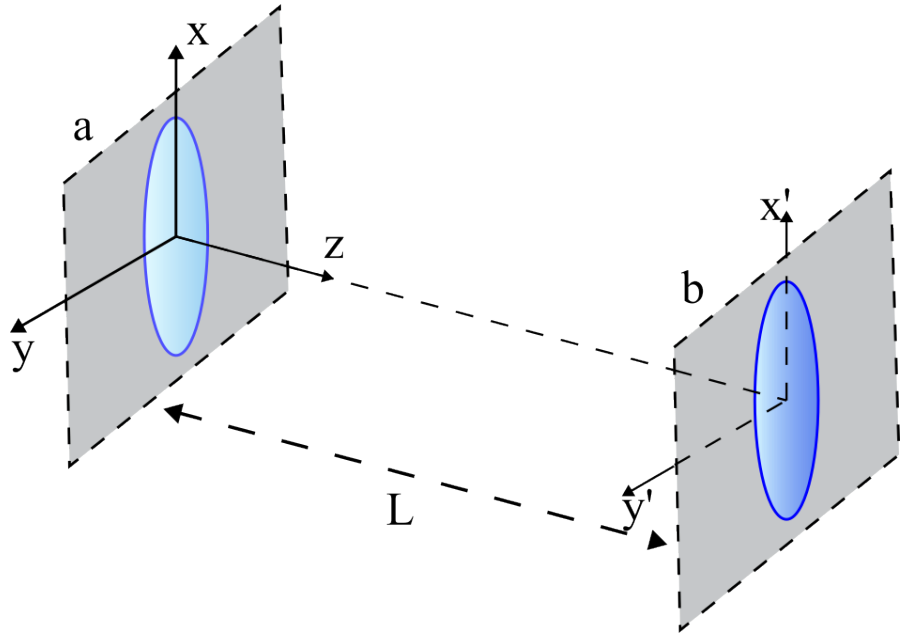

Figure 1.11 – Wireless link: two axially aligned radiating apertures facing each other and cut in parallel infinite ground planes

where $\Gamma \geq 50\%$, operating at distances much larger than the apertures' size. Therefore, considering a PPW environment, such as in [13], appears irrelevant, and the approach by [12, 41] is preferred. Thus, $\vec{E}_a$ and $\vec{H}_a$ are computed assuming that the physical structure of b is removed, while $\vec{E}_b$ and $\vec{H}_b$ are calculated assuming that a is removed [64]. As stated in [9], this is equivalent to neglecting the reflections between the antennas. In other words, we consider that the antennas are coupled and that the most significant interaction between them is described by their reaction.

The surface equivalence principle is used to represent the two radiating apertures cut in ground planes as equivalent magnetic current distributions radiating in the free-space. For antenna a, the feeding terminals and the feeding source I_{1a} are located in the region $z < 0$, while for antenna b the feeding terminals and the feeding source I_{2b} are located in the region $z < L$. Therefore, the feeding elements are located in the regions which are not of interest for our present analysis, and the reaction will be computed using the equivalent magnetic currents obtained from the tangential field distributions over the radiating apertures. The equivalent magnetic currents of apertures a and b, denoted as $\vec{M}_a$ and $\vec{M}_b$, are defined as

$$\vec{M}_a = -2\hat{n}_a \times \vec{E}_a \tag{1.58}$$

$$\vec{M}_b = -2\hat{n}_b \times \vec{E}_b \tag{1.59}$$

where $\vec{n}_a$ and $\vec{n}_b$ are $\hat{z}$ and $-\hat{z}$ respectively. The reaction between a and b can then be

written as

$$\langle a, b \rangle = -\iint_{S_b} \vec{M}_b \cdot \vec{H}_a \, ds \tag{1.60}$$

$$\langle b, a \rangle = -\iint_{S_a} \vec{M}_a \cdot \vec{H}_b \, ds \tag{1.61}$$

where $\vec{J}_b = \vec{J}_a = 0$, and $S_{a(b)}$ represents the surface that encloses source $a(b)$ completely, while all parts of $b(a)$ are outside of it. The power radiated by surfaces a and b are denoted P_{1a} and P_{2b} respectively. Then, we write

$$P_{1a} = \frac{1}{2}\mathrm{Re}\left[\iint_{S_a} (\vec{E}_a \times \vec{H}_a^*) \cdot \hat{n}_a \, ds\right] \tag{1.62}$$

$$P_{2b} = \frac{1}{2}\mathrm{Re}\left[\iint_{S_b} (\vec{E}_b \times \vec{H}_b^*) \cdot \hat{n}_b \, ds\right] \tag{1.63}$$

where $\mathrm{Re}\left[f(x)\right]$ indicates the real part of $f(x)$.

1.3.5 Obstructed Links

The formulation presented in section 1.3.3 was derived for systems operating in clear line of sight (CLOS). However, in a real case scenario, obstacles may obstruct the link, prompting the need to extend this formulation to obstructed links, as shown in figure 1.12. In our approach, the system is modeled as a scattering problem [15] with a metallic obstacle between emitter and receiver. Therefore, the fields are divided in incident, scattered and total fields.

The incident fields are defined as the fields of a radiating source with the obstacle absent, while the scattered fields are the fields due to the electric current on the surface of the obstacle radiating in free space. Finally, the total fields are the ones considering both the obstacle and the radiating aperture, written as

$$\vec{E}^t = \vec{E}^i + \vec{E}^s \tag{1.64}$$

$$\vec{H}^t = \vec{H}^i + \vec{H}^s \tag{1.65}$$

where $\vec{E}^i$ and $\vec{H}^i$ represent the incident fields, while $\vec{E}^s$ and $\vec{H}^s$ define the scattered fields and $\vec{E}^t$ and $\vec{H}^t$ the total ones.

To proceed extending the formulation previously derived for unobstructed links, we recall that the reaction is a linear operation [8]. It can be seen as an inner product between two field quantities which are elements of a linear vector space [71]. Therefore, considering three sources (a, b and c) radiating in the same region, at the same

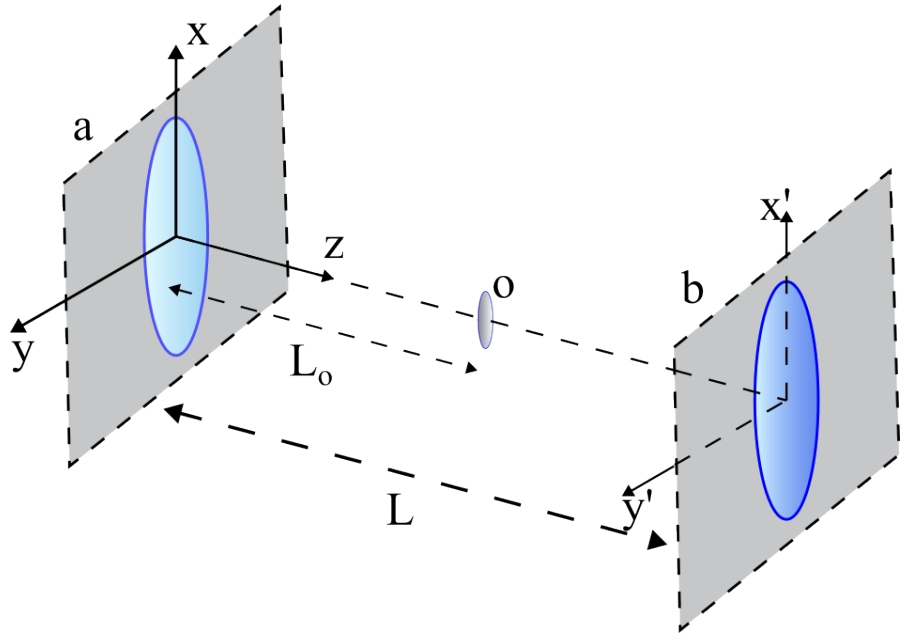

Figure 1.12 – Schematic view of a wireless link with a metallic obstruction. The obstruction has a radius r_o, zero thickness, and is placed at $z = L_o$

frequency, we write

$$\langle (a+c), b\rangle = \iiint_{U_b} \vec{J}_b \cdot \left(\vec{E}_a + \vec{E}_c\right) - \vec{M}_b \cdot \left(\vec{H}_a + \vec{H}_c\right) du \tag{1.66}$$

$$\langle (a+c), b\rangle = \iiint_{U_b} \vec{J}_b \cdot \vec{E}_a - \vec{M}_b \cdot \vec{H}_a \, du + \iiint_{U_b} \vec{J}_b \cdot \vec{E}_c - \vec{M}_b \cdot \vec{H}_c \, du \tag{1.67}$$

which can be expressed in a more condensed notation as

$$\langle (a+c), b\rangle = \langle a, b\rangle + \langle c, b\rangle = \langle a, b\rangle + \langle b, c\rangle \tag{1.68}$$

where the reciprocity property was also used in the last term. Another identity which comes from linearity is expressed as [50]

$$\langle \beta a, b\rangle = \beta \langle a, b\rangle = \langle a, \beta b\rangle \tag{1.69}$$

provided that β is a scalar and a and b two electromagnetic sources.

In our formulation, a, b and c represent the emitter, the receiver and the obstacle, respectively. In this case, the source c is created due to the fields radiated by a, generating currents over c radiating the scattered fields $\vec{E}_a^s$ and $\vec{H}_a^s$. If b is acting as the emitter, c is dependent on b and it radiates the scattered fields $\vec{E}_b^s$ and $\vec{H}_b^s$. We also define the incident fields as the ones radiating from the apertures without the obstacle. Thus, if a is the emitter, the incident fields are $\vec{E}_a^i$ and $\vec{H}_a^i$, while if b is emitting, the incident fields are $\vec{E}_b^i$ and $\vec{H}_b^i$. Moreover, we denote $\vec{M}_b^i$ and $\vec{J}_b^i$ as the magnetic and

electric current of source b, respectively, while $\vec{M}_a^i$ and $\vec{J}_a^i$ are the analogous quantities of source a, when these sources are emitting in the absence of the obstacle. This is depicted in figure 1.13.

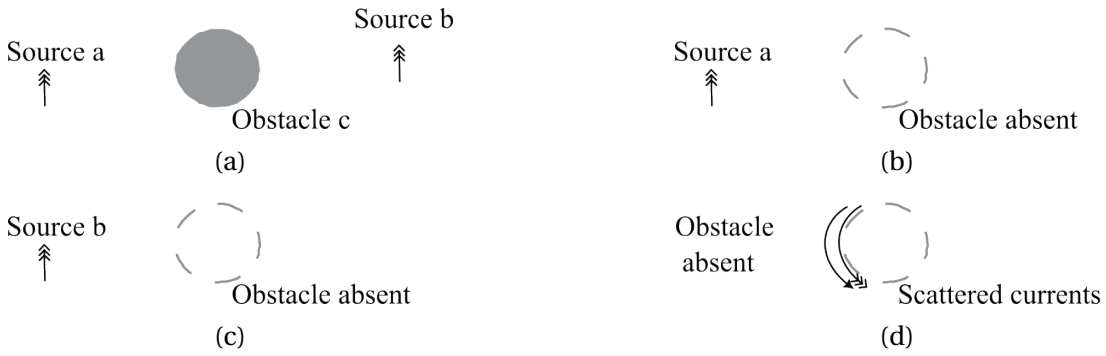

Figure 1.13 – Scattering formulation. The original problem is shown in (a). In (b) and (c), the obstacle is removed, and we present equivalent scenarios to calculate the incident fields for configurations a and b, respectively. In (d) we have the equivalent problem to calculate the scattered fields radiating in free-space.

We define the total reaction, $\langle a,b\rangle_T$, as the reaction of a and b with the scattered source c present. The total reaction is composed by two terms, the incident reaction and the scattered reaction [15], and it writes

$$\langle a,b\rangle_T = \langle (a+c),b\rangle = \iiint_{U_b} \vec{J}_b^i \cdot \left(\vec{E}_a^i + \vec{E}_a^s\right) - \vec{M}_b^i \cdot \left(\vec{H}_a^i + \vec{H}_a^s\right) du \tag{1.70}$$

$$\langle a,b\rangle_T = \iiint_{U_b} \vec{J}_b^i \cdot \vec{E}_a^i - \vec{M}_b^i \cdot \vec{H}_a^i \, du + \iiint_{U_b} \vec{J}_b^i \cdot \vec{E}_a^s - \vec{M}_b^i \cdot \vec{H}_a^s \, du \tag{1.71}$$

for which we define $\langle a,b\rangle^i$ and $\langle a,b\rangle^s$ as

$$\iiint_{U_b} \vec{J}_b^i \cdot \vec{E}_a^i - \vec{M}_b^i \cdot \vec{H}_a^i \, du = \langle a,b\rangle^i \tag{1.72}$$

$$\iiint_{U_b} \vec{E}_a^s \cdot \vec{J}_b^i - \vec{H}_a^s \cdot \vec{M}_b^i \, du = \langle a,b\rangle^s \tag{1.73}$$

where $\langle a,b\rangle^i$ represents the reaction of the incident components, $\langle a,b\rangle^s$ the reaction of the scattered component generated by source a with source b. The total reaction can then be expressed as

$$\langle a,b\rangle_T = \langle a,b\rangle^i + \langle a,b\rangle^s \tag{1.74}$$

Equation 1.73 can be recast as an integral over the scattered electric and magnetic currents denoted by $\vec{J}_c$ and $\vec{M}_c$, respectively. These currents are the ones existing on the surface of the obstacle due to the emitter as surface current densities. Thus, we

have

$$\langle a,b\rangle^s = \langle b,c\rangle = \iint_{S_c} \vec{E}_b^i \cdot \vec{J}_c - \vec{H}_b^i \cdot \vec{M}_c \, ds \tag{1.75}$$

where S_c represents the surface that supports the scattered currents. Finally, equation 1.57 can be extended to the obstructed condition using equations 1.72, 1.74 and 1.75. Therefore, the wireless power transfer efficiency formula for obstructed links writes

$$\Gamma = \frac{|\langle a,b\rangle^i + \langle a,b\rangle^s|^2}{16 P_{1a} P_{2b}} \tag{1.76}$$

where the incident reaction can be calculated as discussed in subsection 1.3.3, and the scattered reaction can be estimated using an approximation technique. Two solutions for obtaining the scattered reaction are presented in this work. The calculations are performed considering that the obstacle is composed of PEC material, yielding

$$\langle a,b\rangle^s = \iint_{S_c} \vec{E}_b^i \cdot \vec{J}_c \, ds \tag{1.77}$$

and the following boundary conditions [15] on the surface of the obstacle, $z = L_o$

$$-\hat{n}_c \times \vec{E}_a^i = \hat{n}_c \times \vec{E}_a^s \tag{1.78}$$

$$-\hat{n}_c \times \vec{E}_b^i = \hat{n}_c \times \vec{E}_b^s \tag{1.79}$$

where unit normal $\hat{n}_c$ is directed outward from surface S_c. Equation 1.77 is then rewritten as

$$\langle a,b\rangle^s = -\iint_{S_c} \vec{E}_b^s \cdot \vec{J}_c \, ds \tag{1.80}$$

1.3.5.1 Pure Physical Optics Solution

The first solution, defined as the wireless power transfer efficiency pure Physical Optics solution (WPTE PPO), entails computing the scattered reaction using equation 1.77, employing the PO approximation to evaluate $\vec{J}_c$. In the PO approximation, the surface of the obstacle illuminated by the source is considered to be electrically large. Put differently, this illuminated surface is large with respect to the wavelength [51]. The region of the surface not illuminated, known as the shadow region, is assumed to have zero tangential electric current. Conversely, within the illuminated region, the tangential electric current is computed as

$$\vec{J}_c = \hat{n}_c \times (\vec{H}_a^i + \vec{H}_a^s) \tag{1.81}$$

Moreover, assuming that the obstacle can be locally approximated by an infinite plane surface, allowing the use of image theory [15], we have $\hat{n}_c \times \vec{H}_a^i = \hat{n}_c \times \vec{H}_a^s$, thus yielding

$$\vec{J}_c = 2\hat{n}_c \times \vec{H}_a^i \tag{1.82}$$

For the case of the system presented in subsection 1.3.4, where two circular radiating surfaces a and b are considered, and the link is partially obstructed by obstacle c, the WPTE PPO solution writes

$$\Gamma_P = \frac{\left| \iint_{S_b} -\vec{M}_b^i \cdot \vec{H}_a^i \, ds + \iint_{S_c} \vec{E}_b^i \cdot (2\hat{n}_c \times \vec{H}_a^i) \, ds \right|^2}{16 P_a P_b} \tag{1.83}$$

1.3.5.2 Variational formulation

To reduce the difference between the correct and the approximated value of $\langle a, b \rangle^s$ due to the estimated current, we propose using a variational approach [14]. The variational procedure is used here to obtain a formula that is almost insensitive to relatively small variations around the correct value [15]. This stationary formula, or variational solution, is derived treating the problem as a differential scattering problem [8, 50]. Thus, the second proposed solution is defined as the wireless power transfer efficiency Variational solution (WPTE VS).

When a is the emitter, the exact current on the obstacle is defined by c_a and its approximation is g. Similarly, when b is emitting, the exact current on the obstacle is defined by c_b and its approximation by h. These approximated currents must have the same self-reaction term as on their respective correct currents [15]. To ensure this condition, we impose

$$\langle g, h \rangle \approx \langle a, b \rangle_s \tag{1.84}$$

$$\langle g, h \rangle = \langle c_b, g \rangle = \langle h, c_a \rangle \tag{1.85}$$

which can be interpreted as imposing that the reaction calculated using the two approximated currents g and h, must be the same obtained using the approximated and the exact ones. Additionally, equation 1.85 can be related to the sources a and b if we use equation 1.78 and 1.79

$$\langle g, h \rangle = -\langle b, g \rangle = -\langle a, h \rangle \tag{1.86}$$

This relation can be further explored giving

$$\langle g, h \rangle \langle g, h \rangle = \langle b, g \rangle \langle a, h \rangle \tag{1.87}$$

that, along with the imposed condition on equation 1.84, yields

$$\langle a, b \rangle_s \approx \frac{\langle b, g \rangle \langle a, h \rangle}{\langle g, h \rangle} \tag{1.88}$$

The relation expressed in 1.88 can be combined with equation 1.80 to obtain the stationary formula for $\langle a,b\rangle^s$ [8, 15]:

$$\langle a,b\rangle_s \approx \frac{\left(\iint_{S_c} \vec{E}_b^i \cdot \vec{J}_g \, ds\right)\left(\iint_{S_c} \vec{E}_a^i \cdot \vec{J}_h \, ds\right)}{\iint_{S_c} \vec{E}_h \cdot \vec{J}_g \, ds} \tag{1.89}$$

where $\vec{J}_g$ represents the approximated electric current on the surface of the obstacle induced by the a, when a is the emitter, and $\vec{J}_h$ the one induced by the b, when b is the emitter. The field $\vec{E}_h$ represents the free-space electric field radiated by $\vec{J}_h$.

The sources $\vec{J}_g$ and $\vec{J}_h$, in equation 1.89, are calculated using the PO approximation. Thus, for the case of the system presented in subsection 1.3.4, where two circular radiating surfaces a and b are considered, and the link is partially obstructed by obstacle c, the WPTE VS solution writes

$$\Gamma_V = \frac{\left| \iiint_{S_b} -\vec{M}_b^i \cdot \vec{H}_a^i \, ds + \frac{\left(\iint_{S_c} \vec{E}_b^i \cdot (2\hat{n}_c \times \vec{H}_a^i) \, ds\right)\left(\iint_{S_c} \vec{E}_a^i \cdot \left(-2\hat{n}_c \times \vec{H}_b^i\right) ds\right)}{\iint_{S_c} \vec{E}_h \cdot (2\hat{n}_c \times \vec{H}_a^i) \, ds} \right|^2}{16 P_{1a} P_{2b}} \tag{1.90}$$

1.4 Code Implementation in MATLAB

All the code used in this research was developed in MATLAB. The most relevant MATLAB functions used in this implementation were matrix multiplication and the 2D Fast Fourier Transform (FFT) [72], which are computationally efficient and central to the analysis. Therefore, the code can be easily ported to Python for further development or integration with other tools. The code was specifically designed to calculate the radiated fields from a tangential electric field distribution over an aperture.

The field data is organized in 3D matrices representing the points in (x, y, z), with the emitter positioned at $z = 0$, as shown in figure 1.14. The grid dimensions are N along the x-axis, M along the y-axis, and L along the z-axis, while Δx, Δy, and Δz represent the discretization steps in each respective direction, determining the subdivision of the spatial domain. The grid has a regular spacing of Δx and Δy in the transverse directions, while the spacing in the longitudinal direction Δz may vary and does not need to be uniform across different values of z.

Additionally, the code computes the WPTE between two identical and axially aligned apertures placed at varying distances. The calculations account for both CLOS and obstructed scenarios, with the assumption that no reflections occur between the apertures. The obstacle is a metallic disk. The flow of the program is illustrated in Figure 1.15, providing a visual representation of the sequence of operations. The code follows the steps below:

— The fields radiated by the emitter are calculated at each plane z using the 2D FFT.

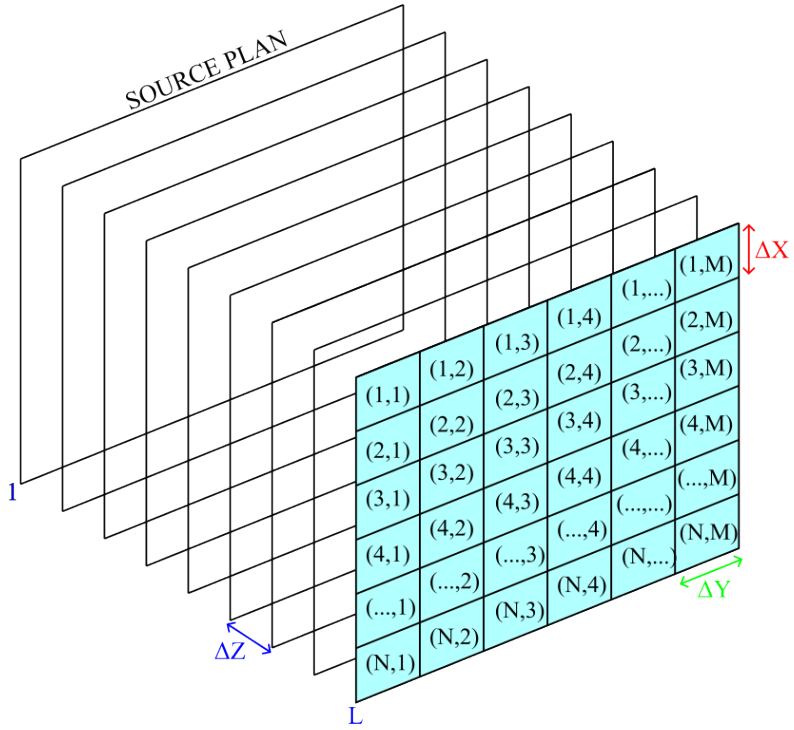

Figure 1.14 – Illustration of the spatial grid structure, showing the planes along the z-axis and the corresponding x and y elements. The grid is discretized into Δx, Δy, and Δz steps, defining the spatial resolution across the domain.

— The reaction between the emitter and the receiver is computed as a function of the distance between them. To compute this interaction, the fields radiated by the receiver are derived from those radiated by the emitter (assuming identical apertures).
— If an obstruction is present, the scattered and total fields, considering only the emitter and the obstruction, are calculated using the PO approximation. If not, end program.
— Next, the scattered and total fields considering only the receiver and the obstruction are computed using PO approximation.
— Finally, reaction between the scattered components is calculated and the WPTE for the obstructed scenario is computed.

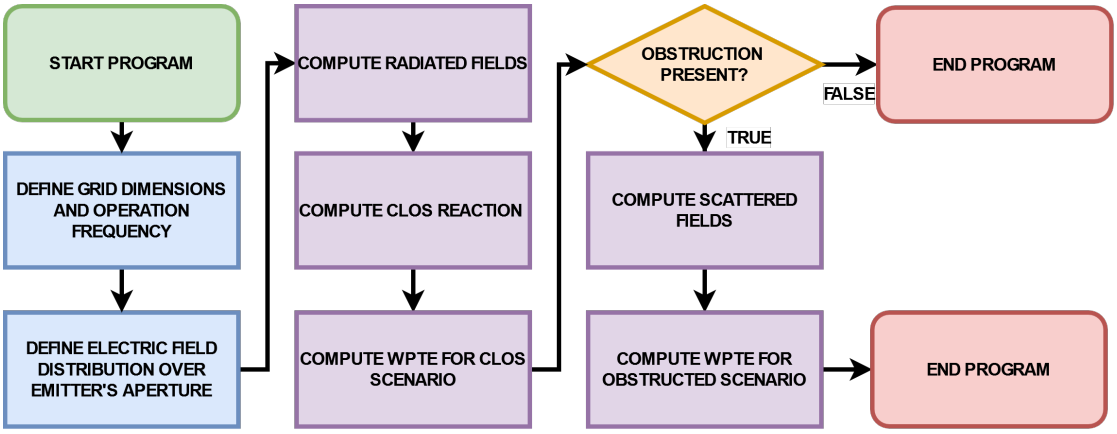

Figure 1.15 – Flowchart of the program structure, outlining the main steps in the calculation process.

1.5 Derivation of Friis Transmission Equation

1.5.1 Exploring the Wireless Power Transfer Efficiency in the Far Field

The WPTE formulas derived in the previous sections are valid in both the near field and far field. However, in far-field links, the relationship between the power received and the power transmitted is usually described by the Friis transmission equation [5]. Our aim here is to demonstrate that the Friis equation can be derived from the WPTE formula for unobstructed links, defined in equation 1.57.

To do so, we consider two radiating apertures, denoted as a and b, which serve as transmitter and receiver, respectively. The system is presented in figure 1.16, and we assume the Cartesian coordinate system (x, y, z). These apertures are assumed to operate in a simultaneous conjugate match and are aligned for maximum radiation. Aperture a is positioned at $z = L$, with its radiating aperture lying in the xy plane, while b is located at $z = 0$,with its radiating aperture also lying in the xy plane. Let us also consider that they are operating in the far field. Equation 1.57, which shows the WPTE between a and b, is repeated here for convenience

$$\Gamma = \frac{|\langle b, a \rangle|^2}{16 P_a P_b} \tag{1.91}$$

with P_a and P_b representing the power radiated by antennas a and b respectively, and $\langle b, a \rangle$ being the electromagnetic reaction between them.

The electric and magnetic fields radiated by antenna a are denoted as $\vec{E}_a$ and $\vec{H}_a$, respectively, while those radiated by antenna b are denoted as $\vec{E}_b$ and $\vec{H}_b$. Let us consider that a radiates as b was removed, while b radiates as if a was not present because the distance between them is very large with respect to their size. The equivalent magnetic currents over a and b can be obtained using the equivalence principle,

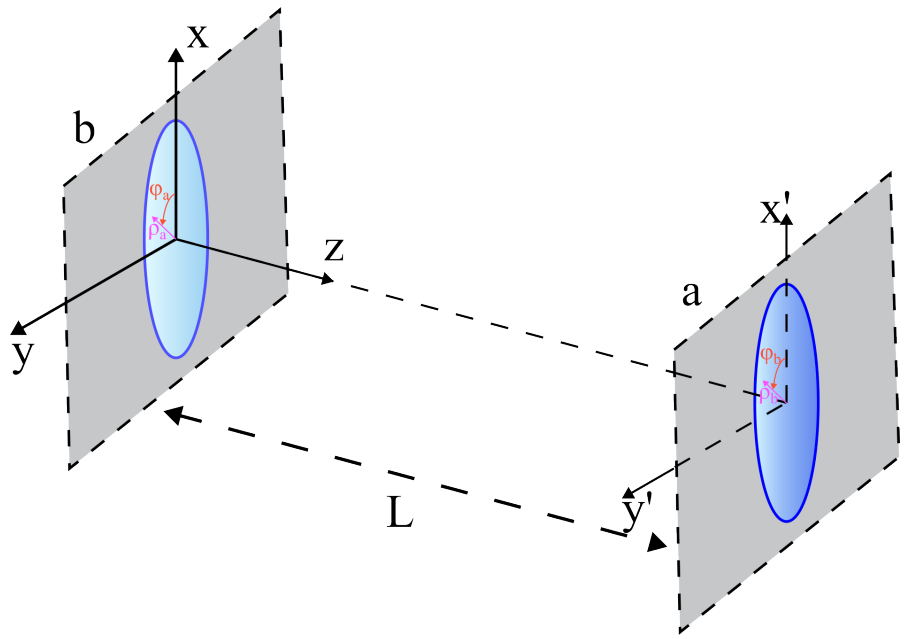

Figure 1.16 – Wireless link: two axially aligned radiating apertures facing each other and cut in parallel infinite ground planes

$\vec{M} = -2\hat{n} \times \vec{E}$, yielding

$$\vec{M}_a = 2f(x,y)\hat{p}_a \tag{1.92}$$

$$\vec{M}_b = 2g(x',y')\hat{p}_b \tag{1.93}$$

where $f(x,y)$ and $g(x,y)$ are scalar functions defined on a and b respectively, and the polarization vector $\hat{p}_{a(b)}$ is referred to $a(b)$. Furthermore, equation 1.91 can be rewritten as:

$$\Gamma = \frac{\left| -\iint_{S_a} \vec{M}_a \cdot \vec{H}_b \, ds \right|^2}{16 P_a P_b} \tag{1.94}$$

where S_a is the radiating surface of aperture a. $P_{a(b)}$ is the power radiated by $a(b)$, which can be obtained using equations 1.62 and 1.63, yielding

$$P_a = \frac{1}{2\eta_0} \iint_{S_a} \left| f(x,y) \right|^2 ds \tag{1.95}$$

$$P_b = \frac{1}{2\eta_0} \iint_{S_b} \left| g(x',y') \right|^2 ds' \tag{1.96}$$

where η_0 is the characteristic impedance of free space. Furthermore, equation 1.94 indicates that we need to compute $\vec{H}_b$ at the plane of a ($z = L$).

The potential vector magnetic can be written as:

$$\vec{F}_b = \frac{\epsilon}{4\pi}\iint_{S_b} \vec{M}_b \frac{e^{-jk_0 d}}{d}\, ds' \tag{1.97}$$

where $d = |\vec{r} - \vec{r}'|$, and S_b represents the surface enclosing the radiating aperture b. The position vector $\vec{r}$ corresponds to the observation points, specifically over the surface S_a, while the position vector $\vec{r}'$ corresponds to points over the radiating aperture S_b. Therefore, we write

$$\vec{r}' = \rho_b \hat{\rho}_b + \phi_b \hat{\phi}_b \tag{1.98}$$

$$\vec{r} = \rho_a \hat{\rho}_a + \phi_a \hat{\phi}_a + L\hat{z} \tag{1.99}$$

where the unit vectors $\hat{\rho}_b$ and $\hat{\phi}_b$ are defined relative to the center of b, while the unity vectors $\hat{\rho}_a$ and $\hat{\phi}_a$ are defined relative to the center of a. The two polar auxiliary systems (ρ_a, ϕ_a) and (ρ_b, ϕ_b) are respectively defined over apertures a and b.

The electromagnetic fields can be calculated from $\vec{F}_b$, yielding

$$\vec{E}_b = \frac{1}{\epsilon}\nabla \times \vec{F}_b \tag{1.100}$$

$$\vec{H}_b = \frac{1}{j\omega\mu}\nabla \times \frac{1}{\epsilon}\nabla \times \vec{F}_b \tag{1.101}$$

where ϵ and μ denote the permittivity and permeability of the medium respectively, and ω represents the angular frequency of operation. When the distance between a and b is sufficiently large we can formulate certain assumptions regarding d and $\vec{r}$, which simplify the computation of the fields. The following approximations are made under the assumption that a and b operate in the far-field region, where $k_0 d \gg 1$ (k_0 is the operating wavenumber).

In the first assumption, d can be approximated by [15]:

$$d = |\vec{r} - \vec{r}'| \rightarrow |r| - |r'|\cos\gamma \tag{1.102}$$

where γ represents the angle between vectors $\vec{r}$ and $\vec{r}'$. This approximation is obtained using the binomial expansion and taking the first two terms. Similar to the approximations done in subsection 1.2.3, d in the denominator of the integral of $\vec{F}_b$ will only take the first term of the expression, as the errors introduced by removing the other term is generally acceptably small. For the exponential, which is more sensible to variations, d will be written using the two terms. Therefore, d is expressed as as

$$d \approx \begin{cases} |r| - |r'|\cos\gamma & \text{in the exponential} \\ |r| & \text{in the denominator.} \end{cases} \tag{1.103}$$

Using the approximations of d in the calculation of $\vec{F}_b$ yields

$$\vec{F}_b \approx \frac{\epsilon}{4\pi} \iint_{S_b} \frac{1}{|r|} \vec{M}_b e^{-jk_0|r|} e^{jk_0|r'|\cos\gamma} \, ds' \tag{1.104}$$

$$\vec{F}_b \approx \frac{\epsilon e^{-jk_0|r|}}{4\pi|r|} \iint_{S_b} \vec{M}_b e^{jk_0|r'|\cos\gamma} \, ds' \tag{1.105}$$

where we have removed from the integral the terms that do not depend on $|r'|$.

In the second assumption, $\vec{r} \approx L\hat{z}$ and $\gamma \approx \pi/2$, implying that the distance between the antennas is sufficiently large for the field radiated by b to be considered uniform over the surface S_a. Consequently, the exponential term in the integral of equation 1.105 is approximated as $e^{jk_0|r'|\cos\gamma} \approx 1$, and $\vec{F}_b$ writes

$$\vec{F}_b \approx \frac{\epsilon e^{-jk_0 L}}{4\pi L} \iint_{S_b} \vec{M}_b \, ds'. \tag{1.106}$$

The electric field can be then expressed as [45]

$$\vec{E}_b \approx \frac{jk_0 e^{-jk_0 L}}{4\pi L} \hat{r} \times \iint_{S_b} \vec{M}_b \, ds'. \tag{1.107}$$

where $\hat{r}$ represents the unit vector in the direction of $\vec{r}$. In the far field, the magnetic field is expressed as

$$\vec{H}_b \approx \frac{1}{\eta_0} \hat{r} \times \vec{E}_b \tag{1.108}$$

In our case, $\hat{r} = \hat{z}$, and $\vec{H}_b$ is given by

$$\vec{H}_b = \frac{1}{\eta_0} \hat{z} \times \frac{jk_0 e^{-jk_0 L}}{4\pi L} \hat{z} \times \iint_{S_b} \vec{M}_b \, ds' \tag{1.109}$$

$$\vec{H}_b = -\frac{jk_0 e^{-jk_0 L}}{4\pi L \eta_0} \iint_{S_b} \vec{M}_b \, ds' \tag{1.110}$$

where equation 1.110 shows us that, under the assumptions taken, $\vec{H}_b$ over S_a can be computed only considering the the elements of b.

The numerator of equation 1.94 then writes

$$|\langle a,b\rangle|^2 = \left| \iint_{S_a} \vec{M}_a \cdot \frac{jk_0 e^{-jk_0 L}}{4\pi L \eta_0} \iint_{S_b} \vec{M}_b \, ds' ds \right|^2 \tag{1.111}$$

$$|\langle a,b\rangle|^2 = \frac{k_0^2}{(4\pi)^2 L^2 \eta_0^2} \left| \iint_{S_a} \vec{M}_a \, ds \cdot \iint_{S_b} \vec{M}_b \, ds' \right|^2 \tag{1.112}$$

$$|\langle a,b\rangle|^2 = \frac{k_0^2}{(4\pi)^2 L^2 \eta_0^2} \left| \iint_{S_a} 2f(x,y)\, ds \iint_{S_b} 2g(x',y')\, ds' \hat{p}_a \cdot \hat{p}_b \right|^2 \tag{1.113}$$

$$|\langle a,b\rangle|^2 = \frac{16k_0^2}{(4\pi)^2 L^2 \eta_0^2} \left| \iint_{S_a} f(x,y)\, ds \iint_{S_b} g(x',y')\, ds' \right|^2 \left| \hat{p}_a \cdot \hat{p}_b \right|^2 \tag{1.114}$$

where $\left|\hat{p}_a \cdot \hat{p}_b\right|^2$ accounts for polarization mismatches. We can then express the WPTE as:

$$\Gamma = \frac{\frac{16k_0^2}{(4\pi)^2 L^2 \eta_0^2} \left| \iint_{S_a} f(x,y)\, ds \iint_{S_b} g(x',y')\, ds' \right|^2 \left| \hat{p}_a \cdot \hat{p}_b \right|^2}{\frac{16}{(2\eta_0)^2} \iint_{S_a} \left| f(x,y) \right|^2 ds \iint_{S_b} \left| g(x',y') \right|^2 ds'} \tag{1.115}$$

that can be simplified, resulting in:

$$\Gamma = \frac{\left| \iint_{S_a} f(x,y)\, ds \iint_{S_b} g(x',y')\, ds' \right|^2 \left| \hat{p}_a \cdot \hat{p}_b \right|^2}{\lambda^2 L^2 \iint_{S_a} \left| f(x,y) \right|^2 ds \iint_{S_b} \left| g(x',y') \right|^2 ds'} \tag{1.116}$$

where λ is the operating wavelength.

Let us now verify the similarities between equation 1.116 and Friis transmission equation, which is given by [73]:

$$\eta = \frac{G_a G_b \lambda^2}{16\pi^2 L^2} e_p \tag{1.117}$$

where G_a and G_b are the gains of apertures a and b respectively, and e_p is the polarization mismatch. Defining G_a and G_b as

$$G_a = \frac{4\pi \left| \iint_{S_a} 2f(x,y)\, ds \right|^2}{\lambda^2 \iint_{S_a} |f(x,y)|^2 \, ds} \tag{1.118}$$

$$G_b = \frac{4\pi \left| \iint_{S_b} 2g(x,y)\, ds' \right|^2}{\lambda^2 \iint_{S_b} |g(x,y)|^2 \, ds'}, \tag{1.119}$$

we can see that equation 1.117 is identical to 1.116.

1.5.2 Numerical Comparison

To compare the two formulations, we assume that a and b have the same aperture illumination given by

$$f(x,y) = g(x,y) = e^{-((x^2+y^2)/w_0^2)} \tag{1.120}$$

where the Gaussian waist w_0 is given by

$$w_0 = \frac{r}{\sqrt{\ln 10}} \tag{1.121}$$

where r is the radius of the apertures. In our comparison, $r = 50\lambda$ and the frequency of operation 30 GHz ($\lambda = 1$cm). The results are presented in figure 1.17.

In figure 1.17, we observe that as the distance between the apertures increases, the results of the two approaches begin to converge. For example, at $z = 100$, the difference in efficiencies is 6%, and at $z = 150$, it reduces to 1%. Beyond the far-field distance, both formulations yield identical results.

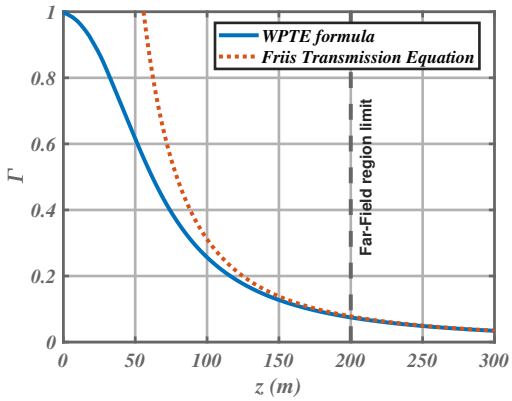

Figure 1.17 – Comparison between Friis formulation and the WPTE formulation. Aperture radius 0.5 m, operating frequency $f = 30\lambda$

1.6 Conclusion

This chapter establishes the theoretical concepts used in this thesis for analyzing electromagnetic fields emitted by planar apertures radiating in free space or confronted by a metallic obstacle. To compute the radiated fields, a spectral Green's function approach is adopted. By the use of the Fourier transform, this approach facilitates the efficient computation of electromagnetic fields by transforming the problem into the spectral domain, where the fields are expressed in terms of spectral variables. We also adopted the paraxial approximation to handle the fields in the near field, simplifying the spectral Green's functions. This approximation allows for

practical calculations while maintaining accuracy. Furthermore, we extended the analysis to scattering problems involving radiating systems and an obstacle.

Through the derivation of the reciprocity theorem, we demonstrated how the interaction between two antennas or radiating elements can be precisely quantified. This theorem provides a bridge between circuital quantities and electromagnetic field quantities, enabling the analysis of power transfer between two radiating elements. Furthermore, we discussed the importance of simultaneous conjugate impedance matching in maximizing power transfer. This matching condition ensures that the impedance of the emitting antenna matches the complex conjugate of the receiving antenna's impedance, leading to optimal power transfer. A wireless power transfer efficiency formula was derived considering antennas radiating in free-space. Using a variational formulation, we have extended this formula to account for obstructed links, addressing the practical scenario where a metallic obstacle impedes the direct propagation path between the transmitter and receiver.

Finally, we compared the WPTE formulation for unobstructed links with the Friis transmission equation. Our analysis demonstrated that, although both approaches yield identical results in the far-field, the WPTE formulation is capable of quantifying the errors introduced by applying the Friis transmission equation in the near field.

2 Weakly Diffractive Wireless Links

Table of contents

2.1 Introduction . . . 73
2.2 Bessel Beams . . . 74
2.2.1 Fundamentals and Properties of Bessel Beams . . . 74
2.2.2 Applications . . . 79
2.2.3 Generation Methods in RF domain . . . 80
2.3 Wireless Power Transfer Efficiency Analysis . . . 81
2.3.1 Clear Line of Sight . . . 82
2.3.1.1 k_1 obtained using the roots of $J_0(\cdot)$, j_{0n} . . . 82
2.3.1.2 k_1 obtained using the roots of $J_1(\cdot)$, j_{1n} . . . 86
2.3.2 Obstructed Links . . . 88
2.3.2.1 Validation of the approach . . . 89
2.3.2.2 Numerical results . . . 92
2.4 Analysis of Diffraction . . . 95
2.5 Metric for Self-healing . . . 98
2.6 Conclusion . . . 100

2.1 Introduction

Bessel beams [16] are part of a class of electromagnetic beams known for their non-diffractive nature and remarkable propagation properties. Bessel beams can maintain a consistent transverse profile over long distances, making them interesting in applications where beam integrity is crucial. Bessel beams can be considered as a superposition of plane waves, with their wavevectors lying on the surface of a cone relative to the beam's axis. This geometric configuration supports their non-diffractive nature and contributes to their self-healing ability. However, ideal Bessel beams, which possess infinite energy, are not realizable in practical applications. Instead, truncated Bessel beams, which approximate the ideal ones, are typically used.

This chapter explores the fundamental principles and properties of truncated Bessel beams, focusing first on their theoretical framework. We investigate how these beams exhibit nondiffracting behavior even when partially obstructed. These characteristics are particularly relevant in applications requiring robust beam propagation, such as wireless power transfer and optical communications. We also analyze the diffraction effects and self-reconstruction abilities of truncated Bessel beams. By comparing these beams with other kinds of beams, we highlight the differences between them.

The chapter is structured as follow. We begin with an overview of the theoretical framework for Bessel beams, including examples of launchers and considerations regarding their behavior in the RF domain. Next, we examine the wireless power transfer efficiency (WPTE) of axially aligned apertures radiating truncated Bessel beams, considering both clear and obstructed lines of sight. This is followed by an analysis of the self-healing capabilities of Bessel beams. Finally, the chapter concludes with a summary of the key findings.

2.2 Bessel Beams

2.2.1 Fundamentals and Properties of Bessel Beams

Electromagnetic beams [74] typically experience diffractive spreading during propagation due to their wave nature. For example, the cross-sectional area of a Gaussian beam [38] doubles after propagating a distance known as the Rayleigh range [75]. However, a notable exception exists in the form of Bessel beams [16], which do not undergo diffraction and maintain their transverse profile while propagating in free space. Furthermore, these beams exhibit a distinctive property known as self-healing, which is the capability of a beam to reconstruct itself after encountering an obstacle placed along its propagation path. The term "Bessel beam" originates from the fact that their transverse profile is mathematically described by Bessel functions of the first kind. Figure 2.1 depicts Bessel functions of the first kind and different orders. Early descriptions of this kind of beam can be found in [76, 77].

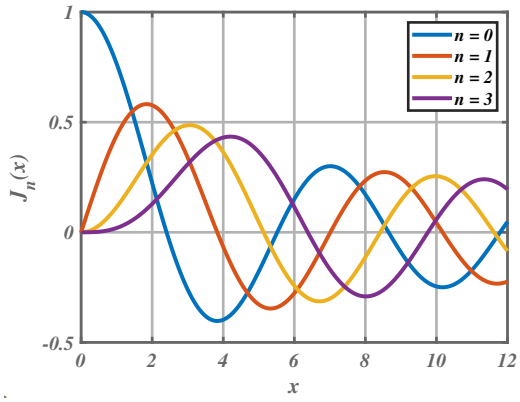

Figure 2.1 – Bessel functions of the first kind and different order n

In [16, 17], Bessel beams are obtained from the Helmholtz equation, or homogeneous complex scalar wave equation, which is written as [15]

$$\left(\nabla^2 - \frac{1}{c^2}\frac{\partial^2}{\partial t^2}\right) U(\vec{r}, t) = 0 \tag{2.1}$$

where c is the speed of light, ∇ represents the vector differential operator, and $U(\vec{r},t)$ is the solution, expressed as a function of the position $\vec{r}$ and time, t. An exact axially symmetric solution of equation 2.1, assuming a cylindrical coordinate system, (ρ,ϕ,z), and considering a scalar field propagating into the source-free region $z \geq 0$, is given by

$$U(\rho, z \geq 0) = J_0(k_1\rho)e^{-jk_z z}e^{j\omega t} \tag{2.2}$$

where $J_0(x)$ is the Bessel function of first kind and zeroth order, ω represents the angular frequency, and the dispersion relation is written as $k_1^2 + k_z^2 = k_0^2$. The operating wavenumber is denoted k_0, while k_1 and k_z are the tangential and the longitudinal wavenumbers respectively.

Equation 2.2 represents a Bessel beam of first kind and zeroth order traveling along direction z. As it can be observed, if $k_1 = 0$, equation 2.2 represents a plane wave. In fact, a Bessel beam can be seen as a superposition of plane waves with wavevectors $\vec{k}$ lying on the surface of a cone with semi-angle $\theta_a = \tan^{-1} k_1/k_z$ relative to the propagation direction [18], as shown in figure 2.2. The angle θ_a is called axicon angle, and for the wavenumbers we also write $k_1 = k_0 \sin\theta_a$ and $k_z = k_0 \cos\theta_a$. From equation 2.2, we notice that the Bessel beam time-averaged intensity profile at $z = 0$ is exactly reproduced for all $z > 0$ in every plane normal to the z axis [16]. In other words, $|U(\rho,0)| = |U(\rho,z)|$. Bessel beams presenting azimuthal phase variation due to the ϕ dependency are given by

$$U(\rho,\phi,z) = CJ_n(k_1\rho)e^{-jn\phi}e^{-jk_z z}e^{j\omega t} \tag{2.3}$$

where n is the order of the Bessel function, and C is an arbitrary constant. However, this family of beams are not the focus of our study.

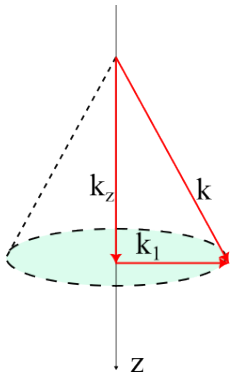

Figure 2.2 – Wave vectors lying on a cone with axicon angle θ_a

The scalar formulation can be extended to the vector case [78, 79]. For example, a radially polarized and transverse magnetic (TM) with respect to the z coordinate (TM_z [15]) mode of a Bessel beam in cylindrical coordinates can be derived considering the

z component of the electric field as $J_0(k_1\rho)e^{-jk_z z}$, obtaining [19, 80]

$$\vec{E} = j\frac{k_z}{k_1}J_1(k_1\rho)e^{-jk_z z}\hat{\rho} + J_0(k_1\rho)e^{-jk_z z}\hat{z} \tag{2.4}$$

$$\vec{H} = j\frac{k_0}{\eta_0 k_1}J_1(k_1\rho)e^{-jk_z z}\hat{\phi} \tag{2.5}$$

where $\vec{E}$ and $\vec{H}$ represent the electric and magnetic fields respectively, η_0 is the impedance of vacuum and $J_1(x)$ is the Bessel function of the first kind and first order. The time dependency term $e^{j\omega t}$ was omitted.

As previously stated, the Bessel beams also posses a property known as self-healing [39, 81–86]. Quantitative descriptions of the self-healing property can be found in [39, 85], while a study of non-diffractive beams encountering non-opaque obstacles is presented in [86]. In [82], the authors employ a wave-optics framework to explain this ability, ultimately concluding that this property can be explained in terms of the propagation of plane waves with radial wave vectors situated on a ring. In [87], the authors state that the self-healing property is related to the dynamics of conical wave fields rather than to their non-diffractive nature. According to them, since the incident non-diffracting beam is created by the superposition of conical waves, the unobstructed parts of the beam will generate outgoing conical waves after passing through the axis, thereby reconstructing the original transverse intensity pattern. In this sense, after encountering an obstacle, the Bessel beam will reform itself after a distance [83]:

$$z_s = \frac{D_o}{2}\cot\theta_a \tag{2.6}$$

where z_s is known as shadow distance and D_o is the diameter of the obstruction.

Ideal Bessel beams have infinite transverse extent and energy, making them impossible to be generated experimentally [88]. However, it is possible to create finite-size approximations of Bessel beams that propagate in a diffraction-free manner over a finite distance called non-diffractive range (NDR) [16]. The NDR is calculated using geometrical optics, yielding

$$\text{NDR} = r_a\sqrt{\left(\frac{k_0}{k_1}\right)^2 - 1} = \frac{r_a}{\tan\theta_a} \tag{2.7}$$

where r_a represents the radius of the finite circular aperture supporting the Bessel beam. Also, the NDR is always located within the near field of the structure radiating the beam. Moreover, the self-healing property is also only valid within the NDR. Analyzing equation 2.7 together with the dispersion relation and the axicon angle relations, we observe that $\text{NDR} \propto k_1^{-1}$ [18] for fixed r_a. Therefore, as k_1 increases, the NDR reduces and the beam presents more rings, if we compare apertures with the same radius.

In this work, Bessel beams generated by finite apertures are defined as truncated

Bessel beams. Figure 2.3 presents the normalized amplitude of the tangential component of a radially polarized truncated Bessel beam. We can see its amplitude as a function of z, in the plane xz, and its amplitude in the plane transverse to its direction of propagation, where the lobes and the null at the center of the beam are clearly visible.

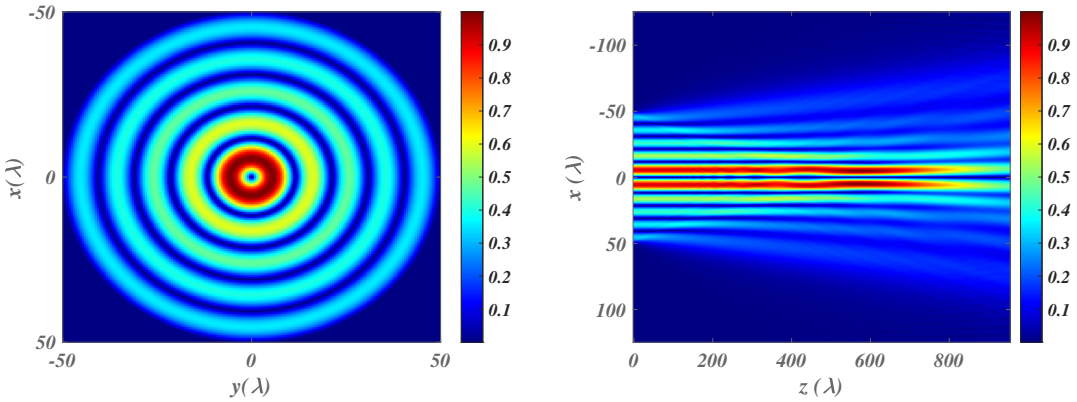

(a) (b)

Figure 2.3 – Normalized amplitude of the tangential component of a radially polarized truncated Bessel beam. The radius of the aperture is $r_a = 50\lambda$ and the axicon angle is $\theta = 3°$. In (a), the amplitude in the plane transverse to its direction of propagation is presented while in (b), we show the amplitude along coordinate z, in the plane xz.

Figure 2.4 presents the normalized amplitude of the spectral content of the tangential component of the radially polarized beam. In the Fourier domain, the spatial spectrum of ideal Bessel beams consists of a single, narrow and well-defined ring (annulus) [19], corresponding to their perfect non-diffracting behavior. Truncated Bessel beams also exhibit a ring in the spectral domain, but this ring has a finite thickness due to the limited dimensions of the radiating aperture.

As the aperture size increases relative to the wavelength, the spectrum increasingly resembles that of an ideal Bessel beam. In the radio frequency (RF) regime and in the optical regime, Bessel beams exhibit different characteristics due to the relative sizes of the apertures used. In the optical regime, apertures are typically thousands of wavelengths in size, allowing for the generation of Bessel beams that closely approximate the ideal form. In contrast, in the RF regime, such as at 30 GHz, apertures are usually tens of wavelengths in size. This difference in aperture size affects the fidelity of the generated Bessel beam, with RF beams having broader and more complex spectral characteristics compared to their optical counterparts. Furthermore, in the RF regime, the NDR is not an accurate measure of non-diffractive behaviour. Even before reaching the theoretical limit of the NDR, the beam slightly diffracts, indicating that the practical behavior of the beam deviates from the ideal non-diffracting scenario predicted by geometrical optics.

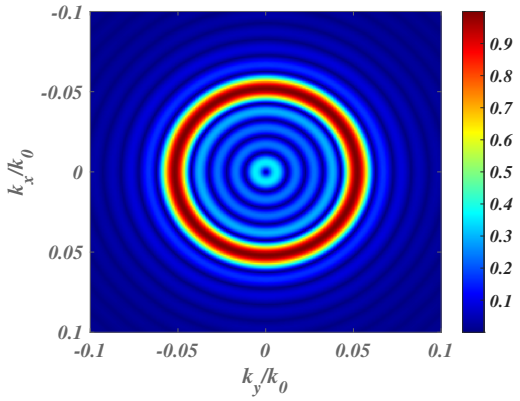

Figure 2.4 – Normalized amplitude of the spectral content of the tangential component of a radially polarized truncated Bessel beam of first kind and first order $J_1(\cdot)$. The amplitude in tha plane $k_x k_y$ is shown. The radius of the aperture is $r_a = 50\lambda$ and the axicon angle is $\theta = 3°$.

To present the behavior of the truncated Bessel beam in the presence of an obstruction, we analyze the system depicted in figure 2.5. The obstacle is a metallic disk with radius $r_o = 12.5\lambda$ placed at $z = L_o = 100\lambda$. The aperture and the obstacle are axially aligned. The results are presented in figure 2.7, where the radiated fields are shown, starting from $z = L_o$. We can see the shadow that is cast after the obstruction followed by the gradual reconstruction of the beam. An analysis of the self-healing is presented in a late section of this chapter.

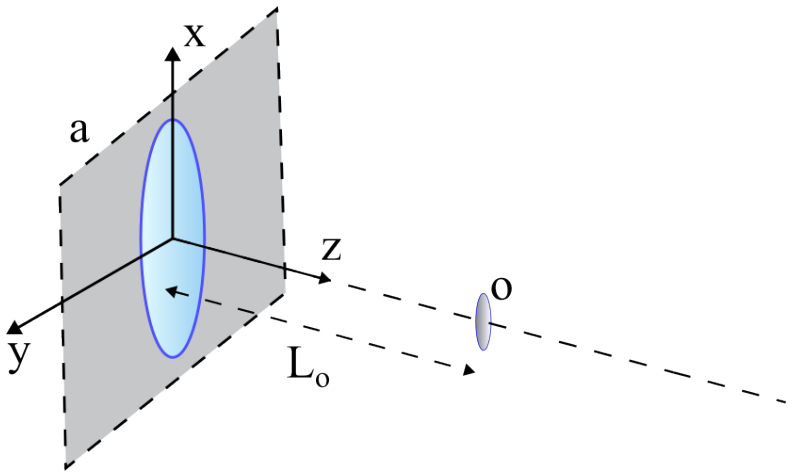

Figure 2.5 – Schematic view of an aperture facing a metallic obstruction. The obstruction is a metallic disk with radius $r_o = 12\lambda$ is placed at $z = 100\lambda$

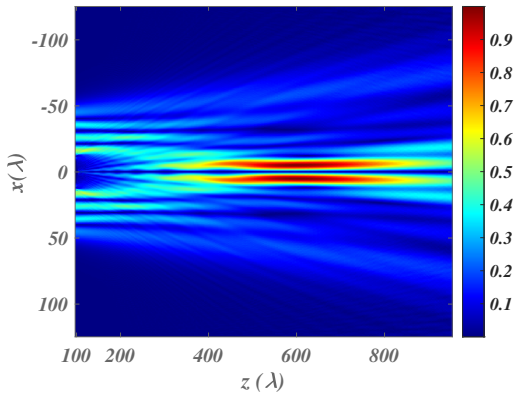

Figure 2.6

Figure 2.7 – Amplitude of the tangential component of a radially polarized truncated Bessel beam confronted by an obstruction. The radius of the aperture is $r_a = 50\lambda$ and the axicon angle is $\theta = 3°$. The obstruction is a metallic disk with radius $r_o = 12\lambda$ is placed at $z = 100\lambda$

2.2.2 Applications

Most research on Bessel beams is conducted in the optics domain, leveraging the larger equivalent apertures available. Consequently, Bessel beams are primarily used in optical applications, where their unique characteristics are exploited. Some of the applications in which they are used are optical trapping, material processing and coherence tomography [46].

In optical trapping and optical tweezing, Bessel beams are used to enhance the manipulation capabilities of these systems. The narrow central spot of Bessel beams, which remains preserved along its NDR, provides high accuracy and precision in manipulation. This allows for significantly improved control over manipulated objects, facilitating the development of practical and flexible micromanipulation systems [89].

In material processing, the narrow central spot of Bessel beams allows for high precision in targeting specific areas, minimizing collateral damage to surrounding material. This precision is crucial in micro- and nano-technologies, where detailed and manageable manufacturing tools are required to structure materials with full precision and minimal loss. Additionally, the non-diffractive nature of Bessel beams enables deep penetration and consistent energy distribution over an extended focal area, which is advantageous for applications such as Bragg grating inscription, microchannel formation, and photopolymerization. These properties make Bessel beams ideal for advanced laser material processing techniques that demand sub-diffraction-limit precision and high-quality microstructuring [89].

In optical coherence tomography (OCT), the ability to maintain a high resolution over an extended depth of focus is crucial, and Bessel beams excel in this area. Unlike Gaussian beams, Bessel beams allow for a longer focusing range without losing resolution, which is particularly beneficial for imaging biological tissues in situ and

non-invasively. This capability enhances the performance of endoscopic OCT systems, which require precise and deep penetration to examine internal organs. The use of Bessel beams in OCT also helps to overcome the limitations of traditional probes, such as the need for fine focus adjustments and limited depth of field. Furthermore, the non-diffractive nature of Bessel beams improves the illumination and collection efficiency, making them ideal for high-resolution imaging applications in medical diagnostics [89].

Bessel beams potential in wireless communications is particularly promising. With the increasing demand for faster and more reliable networks [90], wireless communication systems are transitioning to millimeter wave frequencies. However, this transition comes at the cost of increased propagation losses [5], primarily due to electromagnetic diffraction [19]. The most relevant part of the propagation losses is dominated by free-space path loss which results from the quadratic spreading (diffraction) of the electromagnetic power with the distance. In the light of this, Bessel beams offer are an attractive solution for enhancing wireless communication systems.

2.2.3 Generation Methods in RF domain

In the optical regime, axicons [42] are the most commonly used method for generating Bessel beams [91]. Additionally, diffracting rings placed in the focal plane of a convergent lens [17] and computer-generated holograms [92] can also be employed to produce Bessel beams.

Despite efforts to generate Bessel beams at optical frequencies not being matched by equivalent attempts in the RF range [19], there has been a gradual increase in the development and presentation of Bessel beam launcher designs in this frequency domain. These launchers are conceived exploring diverse theoretical frameworks, such as leaky-wave theory, holography, array theory and principles of optics [35], and they can be divided in resonant and wideband launchers.

Resonant launchers are characterized by a compact structure and a narrow operating band [93]. Examples of this kind of launchers can be found in [20, 27, 94], where the authors employ a leaky-waves framework to design the launchers. In this type of structures, cylindrical leaky waves are excited along a planar surface by a centrally located probe. These outward-propagating cylindrical leaky waves reflect off the metal rim at the antenna boundary, generating inward-propagating cylindrical leaky waves. The superposition of the incident and reflected waves produces a truncated Bessel beam within a finite triangular-shaped region of space, defined by the loci of constructive interference of the rays emitted by the radiating aperture [35].

Wideband launchers, as the name suggests, offer a broader operating bandwidth compared to resonant ones. However, this advantage comes at the cost of increased bulkiness, larger electrical size, and complexity in their structures [93]. Examples of such wideband launchers can be found in [1, 2, 21, 22, 24, 25, 28–33, 37]. In [30], the authors achieve a wideband launcher using a leaky-wave approach, whereas in [21], the launcher design employs an antenna array with a sub-sampled distribution to minimize the number of required antennas. Additionally, in [22, 24, 25, 28], radial-

line slot array (RLSA) technology is utilized for wideband launcher designs. RLSA antennas are planar structures comprising radial waveguides with slots fabricated on the top surface. These slots radiate a specific field pattern determined by their size, position, and type [35]. While RLSA launchers depend on the full-wave solution of the fields generated by the slot configuration, leaky-wave antennas require numerical determination of the dispersive behavior of the complex wavenumber associated with the inward aperture field [35].

In [29, 32, 37], the authors design launchers that radiate X-waves, which are localized pulses formed by the superposition of Bessel beams with a common axicon angle. In [29, 32], the launcher employs a metamaterial to bend the rays of an electric monopole, achieving the desired field distribution. In contrast, [37] utilizes a mode-matching framework to radiate X-waves using a full-metallic horn antenna.

The designs presented in [1, 2, 31, 33] are performed using a dielectric lens approach. Basically, this kind of launcher is compose of a horn which radiates a Gaussian beam that intercepts one or more lenses. The system is calculated so that the "equivalent" lens can provide the required phase profile to transform the Gaussian beam from the feeding horn into a truncated Bessel beam.

2.3 Wireless Power Transfer Efficiency Analysis

In this section, we analyze the WPTE, also denoted as Γ, of apertures radiating truncated Bessel beams. We consider unobstructed and obstructed links. We study TM_z radially polarized beams. The radiating aperture a is placed at the center of the cylindrical coordinate system (ρ, ϕ, z), its radius is defined as r_a and its surface is S_a. We assume over the radiating aperture the following tangential electric field distribution

$$\vec{E}_t = AJ_1(k_1\rho)\hat{\rho} \quad (0 \leq \rho \leq r_a) \tag{2.8}$$

where $k_1 = k_0 \sin\theta_a$ and A is an arbitrary complex function. Figure 2.8 shows the profile of the amplitude field distribution over the aperture. The transverse wavenumber k_1 is obtained in terms of the zeros of the Bessel function of first kind and order m. Then, k_1 is given by

$$k_1 = \frac{j_{mn}}{r_a} \tag{2.9}$$

where j_{mn} represents the nth zero of the Bessel function of first kind and mth order, $J_m(\cdot)$.

The radiated fields will be derived using a spectral Green's function approach, considering equivalent magnetic current distributions over the radiating apertures. The equivalent magnetic current $\vec{M}_a$ writes

$$\vec{M}_a = -2\hat{n}_a \times \vec{E}_t = -2AJ_1(k_1\rho)\hat{\phi} \tag{2.10}$$

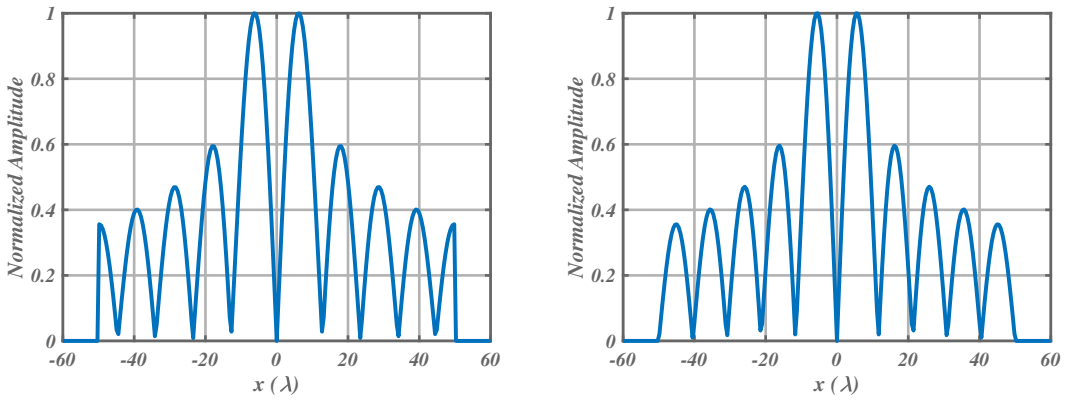

(a) (b)

Figure 2.8 – Normalized amplitude profile of the tangential electric distribution over the aperture. Aperture radius 50λ, and operation frequency 60 GHz. In (a), truncation using j_{04} and in (b), truncation using j_{14}

where $\hat{n}_a$ is the normal directed outward of surface S_a. An analogous equation can be derived for the receiver, antenna b, giving

$$\vec{M}_b = -2\hat{n}_b \times \vec{E}_t = 2BJ_1(k_1\rho')\hat{\phi}' \tag{2.11}$$

where B represents an arbitrary complex function, $\hat{n}_b$ represents the normal directed outward of surface S_b (support of b), and the cylindrical coordinate system of antenna b is given by (ρ', ϕ', z').

2.3.1 Clear Line of Sight

The system for which we are calculating the power transfer efficiency is depicted in Figure 2.9. We assume two identical circular apertures facing each other. The frequency of operation is 60 GHz, and the radius of the apertures is $r_a = r_b = 50\lambda$. Initially, we will analyze the situation where k_1 is calculated using the roots of $J_0(\cdot)$, through equation 2.9. Following this, we will present the results obtained when k_1 is calculated considering the roots of $J_1(\cdot)$. By comparing these two sets of results, we aim to highlight the differences and potential advantages of each method.

2.3.1.1 k_1 obtained using the roots of $J_0(\cdot)$, j_{0n}

Figure 2.10 shows the normalized amplitude of the tangential component of the electric field of apertures in free-space radiating truncated Bessel beams with different k_1 obtained using the roots of $J_0(\cdot)$. We observe that the Bessel beam has two lobes for $n = 2$ and four for $n = 4$. For all cases, we have zero field amplitude along the axis z. The impact of beam truncation becomes apparent when we observe diffraction occurring around the edges of the aperture. This effect is apparent because the beam

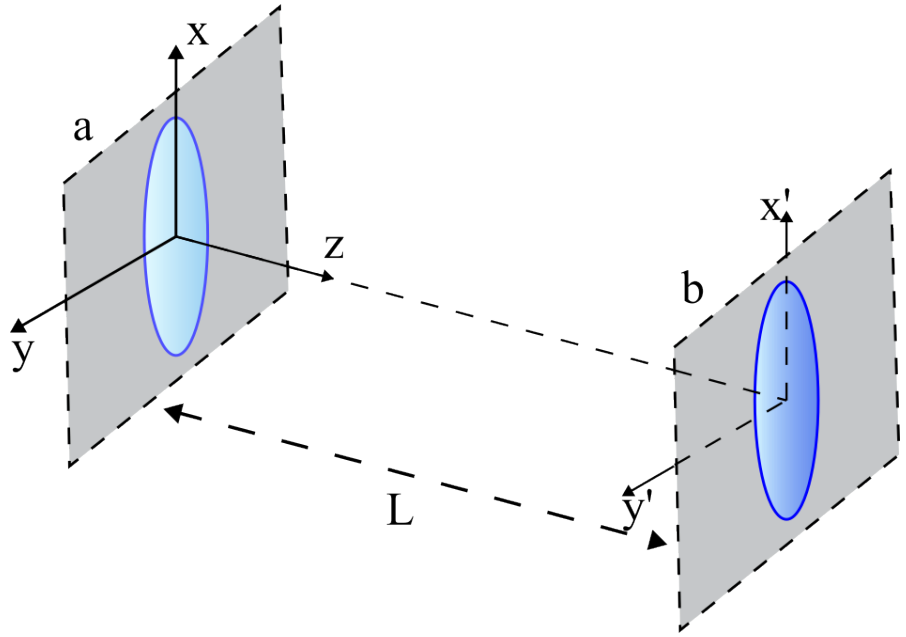

Figure 2.9 – Schematic view of the wireless link without obstruction. The system is composed of two axially aligned radiating apertures.

is truncated using the roots of $J_0(\cdot)$, and the tangential component of the beam has a $J_1(\cdot)$ profile, thus presenting a considerable amplitude of field at the edge of the aperture.

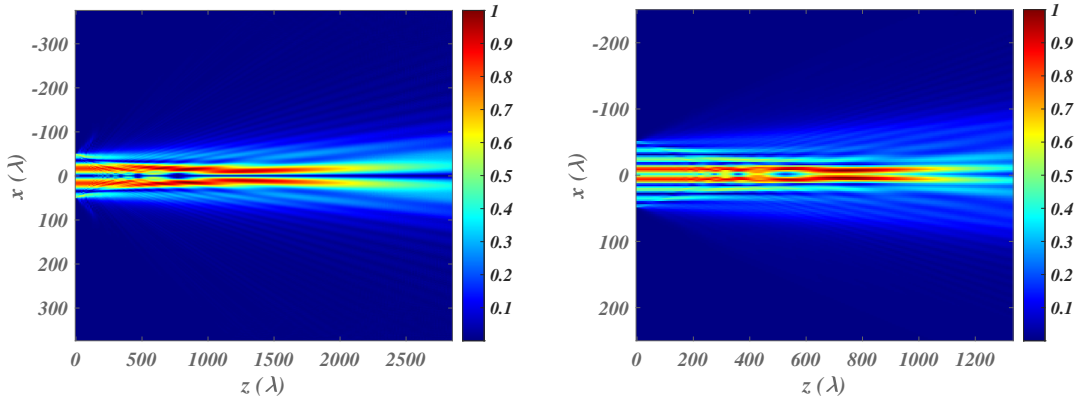

(a) (b)

Figure 2.10 – Normalized Tangential field radiating in the plane xz considering $n = 2$ (a) and $n = 4$ (b) for truncation using j_{0n}. Aperture radius $r_a = 50\lambda$ and $f = 60\,\text{GHz}$

The calculated NDR and the ratio k_1/k_0 are presented in Table 2.1. We observe that the NDR decreases as the root number n of the Bessel function increases, while the ratio k_1/k_0 increases. Additionally, the difference between the NDR of $n = 1$ and $n = 2$

is almost three times greater than the difference between the NDR of $n = 2$ and $n = 3$. This indicates that as n increases, the difference between the NDR of n and $n+1$ becomes smaller. Figure 2.11 illustrates the evolution of the NDR as a function of the aperture radius for different n. Notably, as n increases, the slope of the curve gradually decreases. The NDR is obtained using the radius of the aperture r_a, k_0 and k_1, as shown in equation 2.7. As $j_{0n} < j_{0(n+1)}$, it is clear that for the same aperture radius the largest NDR is achieved when $n = 1$. As we can conclude, in terms of optimizing the distance of coverage in a communication system, $n = 1$ is the most interesting choice.

Table 2.1 – NDR and ratio k_1/k_0 for an aperture of $r_a = 50\lambda$ Bessel roots of $J_0(\cdot)$

$J_0(\cdot)$	$k_1 = j_{0n}/r_a$	k_1/k_0	NDR	$\theta_a = \arcsin k_1/k_0$
$n = 1$	$4.81\,\mathrm{m}^{-1}$	0.0077	6532λ	0.44°
$n = 2$	$11.04\,\mathrm{m}^{-1}$	0.0176	2845λ	1.01°
$n = 3$	$17.31\,\mathrm{m}^{-1}$	0.0275	1815λ	1.58°
$n = 4$	$23.58\,\mathrm{m}^{-1}$	0.0375	1331λ	2.15°

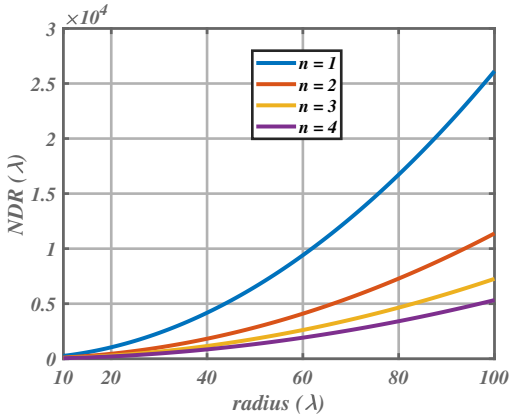

Figure 2.11 – Non-diffractive range as a function of the aperture radius for different j_{0n}.

Furthermore, the parameter k_1/k_0 is particularly interesting in our analysis. For small angles, the approximation $\arcsin x \approx x$ holds true when x is in radians. The axicon angle is calculated as $\theta_a = \arcsin k_1/k_0$, so this implies that θ_a, when expressed in radians, can be directly used as the parameter k_1/k_0 in our calculations, as we usually consider small angles. This simplification is advantageous as it allows us to work with the axicon angle in radians without the need for further conversion, streamlining our analysis and computations.

The spectral content for different n is shown in Figure 2.12. The normalized amplitude profile of the tangential component of the electric field is presented as a function of the spectral variable k_x at $(k_y = 0, z = 0)$. We observe that as n increases, k_1 also increases, shifting the peak in the spectral domain to the new $k_x = k_1$. Due to the limited aperture, the peaks in the spectral domain are not Dirac delta functions; they

exhibit a certain width and side lobes. However, the amplitude of these side lobes does not exceed 20% of the maximum amplitude observed in the main lobe.

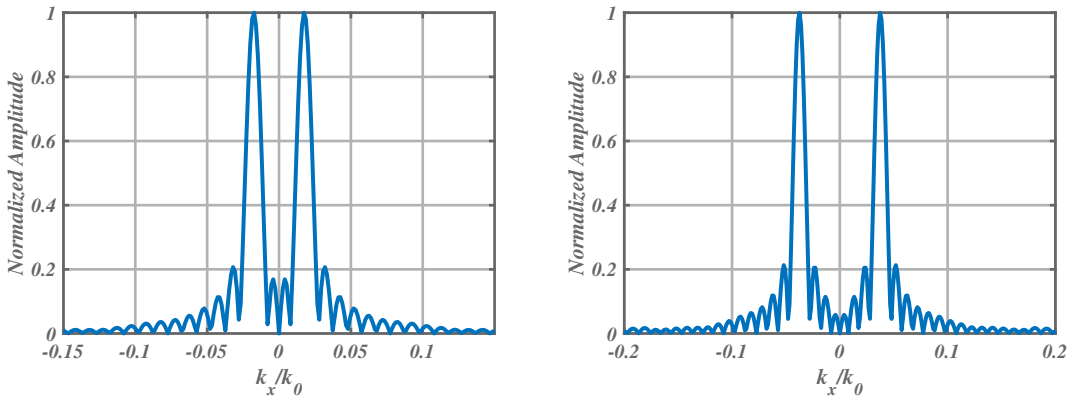

(a) (b)

Figure 2.12 – Spectral content of the tangential component of the truncated Bessel beam using j_{0n}, for $n = 2$ (a) and $n = 4$ (b)

In figure 2.13, the WPTE is shown. We observe the impact of different Bessel root n on the efficiency of the unobstructed link for a constant aperture radius. As indicated by the larger NDR, we obtain the highest efficiency using $n = 1$. Once again, this tells us that the most interesting choice for long wireless links is the first root. We can notice that the NDR marks the limit between two different regimes for the WPTE. For $z <$ NDR, the efficiency decreases almost linearly with the distance, mostly due to the weakly diffractive nature of the beam. For $z >$ NDR, the Bessel beam is more impacted by diffraction and so the link efficiency decreases more rapidly and in a quadratic fashion.

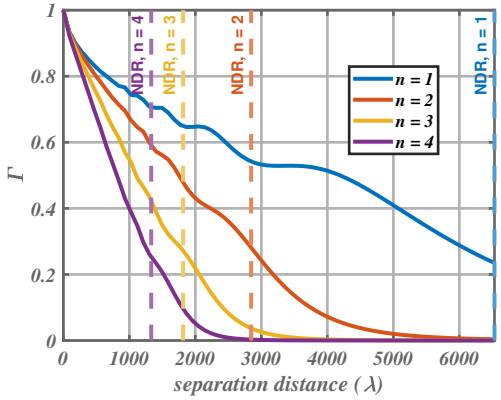

Figure 2.13 – WPTE considering two axially aligned apertures radiating truncated Bessel beams, using j_{0n}. Aperture radius $r_a = 50\lambda$ operating at 60 GHz

2.3.1.2 k_1 obtained using the roots of $J_1(\cdot)$, j_{1n}

Now, in figure 2.14, we present the results of the normalized amplitude of the tangential component of the electric field of apertures in free-space radiating truncated Bessel beams with different k_1, obtained using the roots of $J_1(\cdot)$.

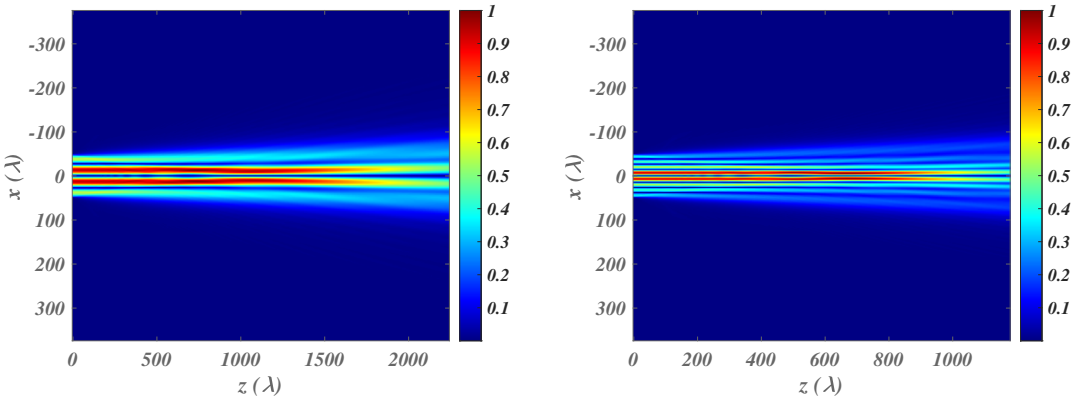

(a) $n = 2$ (b) $n = 4$

Figure 2.14 – Normalized tangential field radiating in the plane xz considering $n = 2$ (a) and $n = 4$ (b) for truncation using j_{1n}. Aperture radius $r_a = 50\lambda$ and $f = 60\,\text{GHz}$

This time, as the tangential field is truncated at the point of zero field at the edge of the aperture, there is no diffraction at the edges and the beam is less disturbed. As in the previous case, the Bessel beam has two lobes for $n = 2$ and four for $n = 4$, and we have zero field amplitude along the axis z.

Table 2.2 summarizes the calculated NDR and the ratio k_1/k_0 for different j_{1n}. The same conclusions can be can be drawn from table 2.1 with respect to the NDR. One interesting aspect to be observed is that as $j_{0n} < j_{1n}$ for the same n, the largest possible NDR is obtained using the first root of $J_0(\cdot)$. The NDR obtained using j_{01} for $r_a = 50$ is 2433λ greater than the one obtained using j_{11}.

Table 2.2 – NDR and ratio k_1/k_0 for an aperture of $r_a = 50\lambda$, Bessel roots of $J_1(\cdot)$

$J_1(\cdot)$	$k_1 = j_{1n}/r_a$	k_1/k_0	NDR	$\theta_a = \arcsin k_1/k_0$
$n = 1$	$7.66\,\text{m}^{-1}$	0.0122	4099λ	0.70°
$n = 2$	$14.03\,\text{m}^{-1}$	0.0223	2238λ	1.28°
$n = 3$	$20.35\,\text{m}^{-1}$	0.0324	1543λ	1.86°
$n = 4$	$26.65\,\text{m}^{-1}$	0.0424	1178λ	2.43°

Comparing figures 2.11 and 2.15, where the NDR is shown as a function of the radius of the aperture for j_{0n} and j_{1n} respectively, we notice that the difference in the NDR for $r_a = 100\lambda$ achieves 9730λ, which at 60 GHz represents 48.65 m. Therefore, in terms

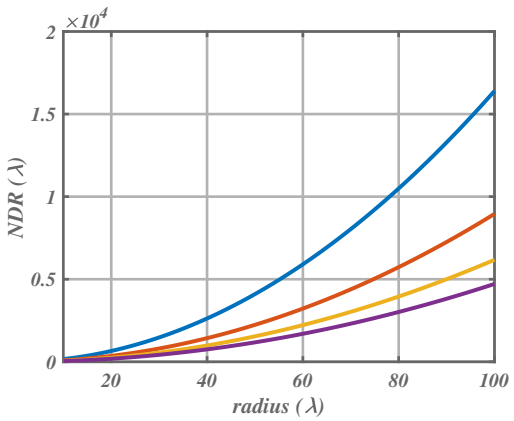

Figure 2.15 – Non-diffractive range as a function of the aperture radius for different j_{1n}.

of distance of coverage, truncating the aperture using the j_{01} appears as the most interesting solution.

The spectral content for different n is shown in Figure 2.16. The normalized amplitude profile of the tangential component of the electric field is presented as a function of the spectral variable k_x at $(k_y = 0, z = 0)$. The same comments can be drawn from the analysis of figure 2.12, but this time, the spectral content presents greater side lobes than when using the roots of $J_0(\cdot)$. For instance, the amplitude of the side lobes achieve more than 50% of the maximum amplitude of the peak when $n = 2$. The only exception is when $n = 1$, where the intensity of the side lobes is lower than 10% of the maximum intensity of the spectrum, as shown in figure 2.17.

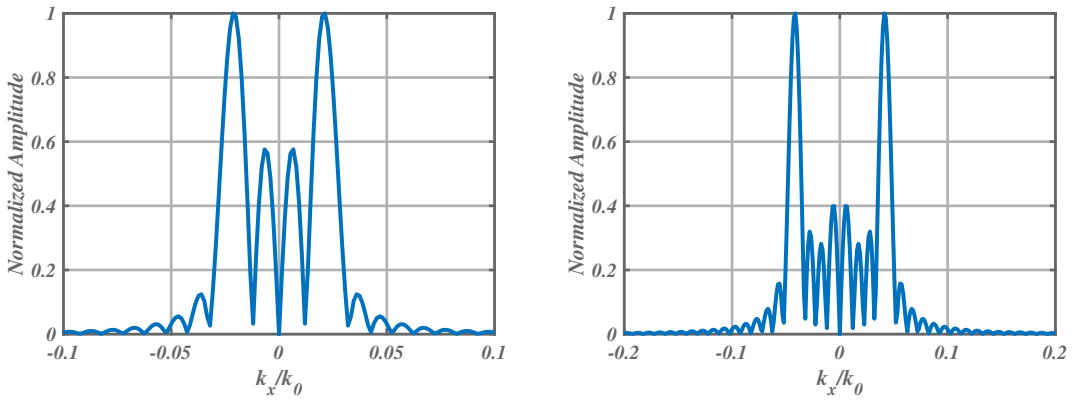

(a) (b)

Figure 2.16 – Spectral content of the tangential component of the truncated Bessel beam using j_{1n}, for $n = 2$ (a) and $n = 4$ (b)

Figure 2.18 illustrates the WPTE between two identical apertures as a function of the separation distance for the roots j_{1n}. The impact of different n is evident. The

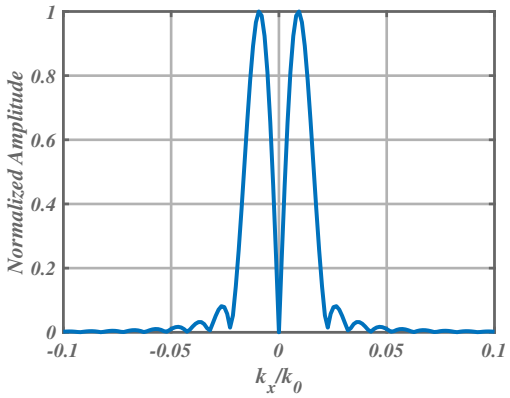

Figure 2.17 – Spectral content of the tangential component of the truncated Bessel beam using j_{11}

efficiency curve exhibits fewer oscillations, attributed to the absence of diffraction at the aperture edges.However, as previously mentioned, the maximum NDR is smaller compared to the case of j_{0n}. For a given aperture size and frequency, the smallest k_1 yields the largest NDR, regardless of whether there is diffraction or not at the aperture edges.

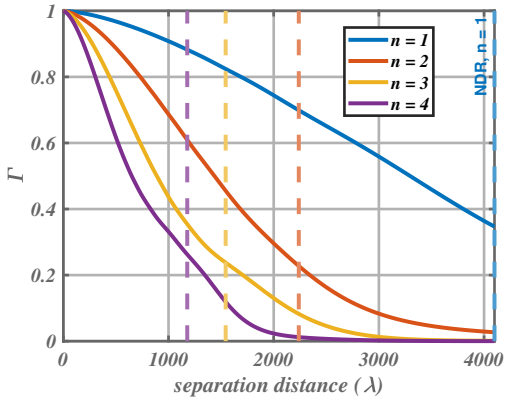

Figure 2.18 – WPTE considering two axially aligned apertures radiating truncated Bessel beams, using j_{1n}. Aperture radius $r_a = 50\lambda$ operating at 60 GHz

2.3.2 Obstructed Links

The system under consideration for computing the WPTE using equation 1.76 is illustrated in figure 2.19. The system is composed of two identical circular apertures facing each other with a metallic disk obstructing their line of sight. The system is axially aligned. The frequency of operation is 60 GHz. We proceed first to a validation of the theory proposed in subsection 1.3.5. Then, this formulation is used to perform a thorough study of an obstructed wireless link from a power transfer efficiency

point of view. The transverse wavenumber k_1 is calculated using the roots of $J_0(\cdot)$, so $k_1 = j_{0n}/r_a$. Analogous conclusions are drawn if we use j_{1n} instead of j_{0n}.

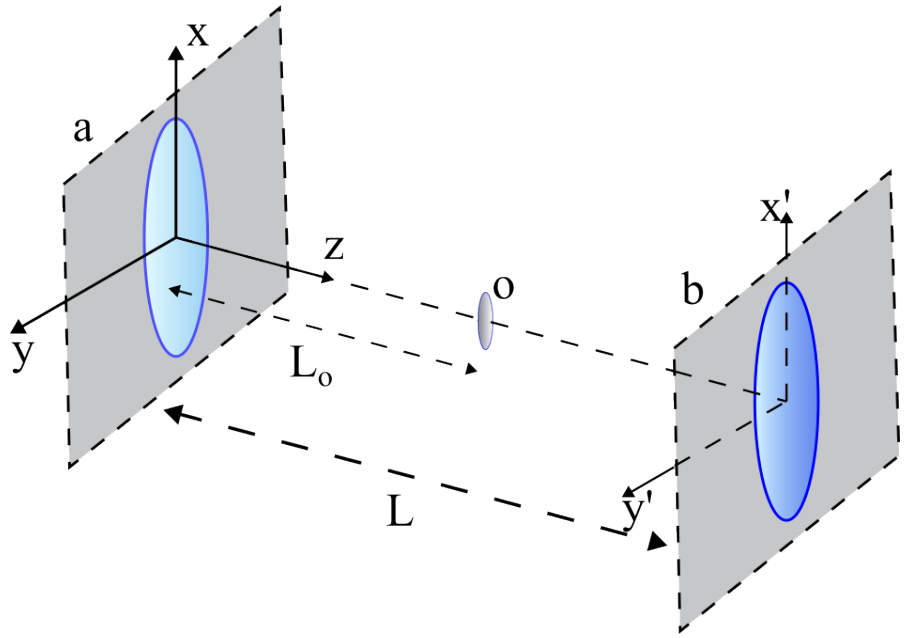

Figure 2.19 – Schematic view of a wireless link with a metallic obstruction. The system is composed of two apertures and one obstacle, all axially aligned. The obstruction has a radius r_o, zero thickness, and is placed at $z = L_o$

2.3.2.1 Validation of the approach

Initially, the PPO and VS solutions are compared, considering equal apertures facing each other. On this comparison, the obstacle is a perfectly electric PEC disk axially aligned to the apertures. The obstacle is placed at $z = 0.2$NDR, its radius, r_o, is 30% of the aperture radius, r_a, and $2\lambda \leq r_a \leq 50\lambda$. For this analysis, we define $\Delta\Gamma$ as the impact of the scattered reaction, $\langle a,b\rangle^s$, on the WPTE. $\Delta\Gamma$ is calculated using equation 2.12. Figure 2.20 shows $\Delta\Gamma$ as a function of the separation distance between the apertures.

$$\Delta\Gamma = \frac{|\langle a,b\rangle^i + \langle a,b\rangle^s|^2 - |\langle a,b\rangle^i|^2}{16P_aP_b} \tag{2.12}$$

On Figure 2.20, we can see that when $r_a = 2\lambda$, the PPO and VS results do not agree. The maximum relative difference between the two solutions observed is around 70%. As we increase the dimensions of the problem (aperture radius and separation distance) this difference rapidly decreases. For the larger apertures, the maximum relative difference observed do not exceed 3 %. Furthermore, this confirm that single scattering is the dominant mechanism here.

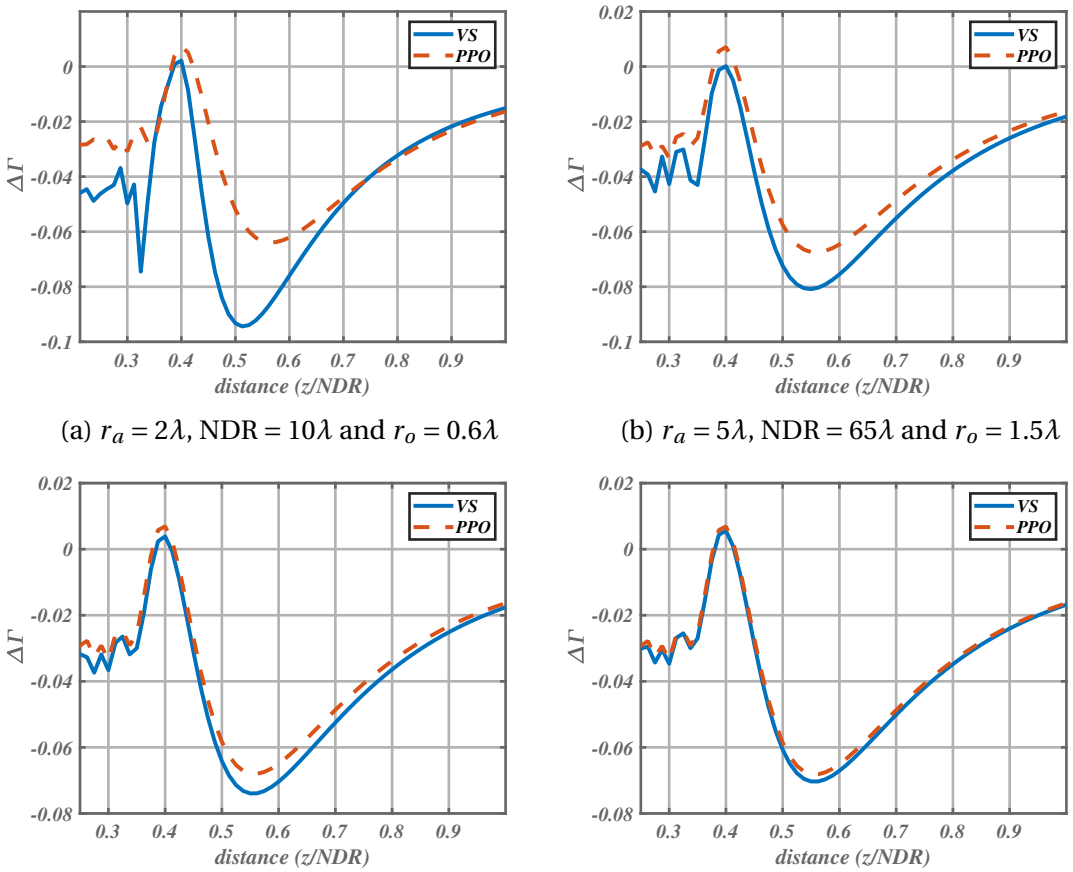

(a) $r_a = 2\lambda$, NDR $= 10\lambda$ and $r_o = 0.6\lambda$

(b) $r_a = 5\lambda$, NDR $= 65\lambda$ and $r_o = 1.5\lambda$

(c) $r_a = 10\lambda$, NDR $= 261\lambda$ and $r_o = 3\lambda$

(d) $r_a = 50\lambda$, NDR $= 6531\lambda$ and $r_o = 15\lambda$

Figure 2.20 – $\Delta\Gamma$ of VS and PPO solutions compared as function of the separation distance between the radiating apertures. The used parameters are: $r_o = 0.3r_a$, $n = 1$ and the obstacle is placed at $z = 0.2$ NDR.

The VS and the full-wave commercial software COMSOL Multiphysics [95] are compared in order to validate the proposed approach. We evaluate the WPTE as a function of the separation distance between the apertures. Furthermore, the distance is normalized by the NDR. For this validation, the radius of aperture a and b are defined as r_a and r_b, respectively, and $r_a = r_b = 4\lambda$. The obstacle is a PEC disk axially aligned to the apertures, its radius is $r_o = 0.3r_a$, $k_1 = 20.04$, and the NDR $= 41\lambda$. These parameters were chosen to reduce the computational time without affecting the overall conclusions. The results are presented in figures 2.21 and 2.22.

On figure 2.21, the WPTE of an unobstructed link is verified to establish a reference. The numerical results are compared with those of COMSOL. Overall, we observe, in average, small differences of about 0.01. Close to $z =$ NDR, the difference is not greater than 0.02 for an efficiency of 0.25. Figures 2.22a and 2.22b show the results of the VS formulation and COMSOL for an obstructed link. On figure 2.22a, the obstacle is placed at $z = 0.1$ NDR, while on figure 2.22b the obstacle is placed at $z = 0.2$ NDR. We

can see a close agreement between the results. The differences are smaller than 0.02.

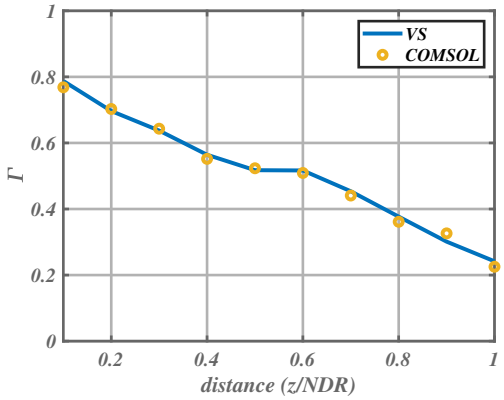

Figure 2.21 – WPTE as a function of the separation distance. The system operates with CLOS. The blue line shows the results of the numerical calculations and the yellow circles those obtained with COMSOL. The used parameters are: $r_a = 4\lambda$, $n = 1$, and NDR $= 41\lambda$.

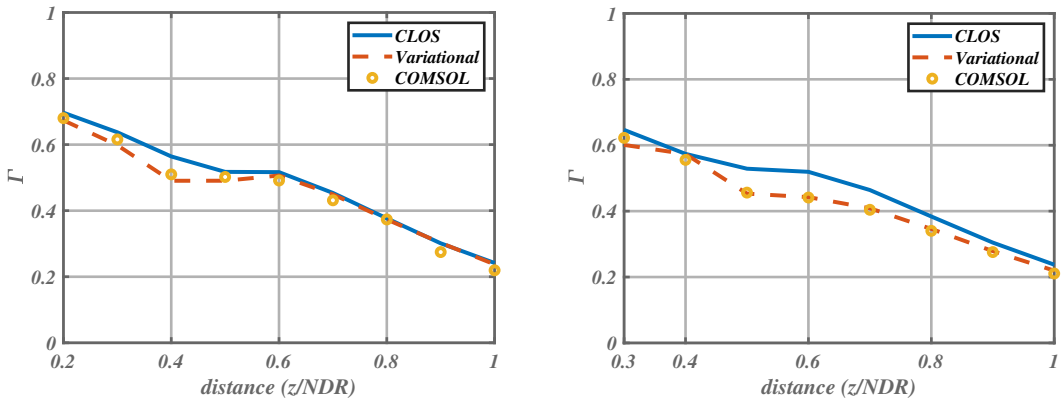

(a) (b)

Figure 2.22 – WPTE as a function of the separation distance for obstructed links. The blue line is the WPTE for an unobstructed link, the dashed red line is the numerical calculation of the obstructed link and the circles are numerical results by COMSOL. The used parameters are: $r_a = 4\lambda$, $r_o = 0.3 r_a$ $n = 1$, and NDR $= 41\lambda$. In (a), the obstacle placed at $z = 0.1$ NDR, and in (b), it is placed at $z = 0.2$ NDR

The dimensions of the problem studied are not ideal for the VS formulation developed because, as stated earlier, it assumes that the radii of the apertures is much smaller than the separation distance between the apertures. Therefore we can expect our model to be much more accurate than 0.02 on the efficiency. As a conclusion,

this comparison shows that our model is sufficiently accurate in order to quantify the influence of obstructions on the link efficiency.

2.3.2.2 Numerical results

In the numerical analysis, r_o assumes three values: $0.1r_a$, $0.2r_a$ and $0.3r_a$. The aperture radius is $r_a = 50\lambda$. Again, the WPTE is evaluated as a function of the distance. All calculations are performed using the VS solution derived in subsection 1.3.5. The results of this configuration are shown in figures 2.23, 2.25 and 2.24.

Figure 2.23 shows the WPTE as a function of the separation distance for a partially obstructed link. The obstacle is placed at four different positions along the z axis. The separation distance goes from the obstacle until the NDR (NDR= 6531λ). We can notice that the obstacle of $0.1r_a$ does not disturb the WPTE, regardless of its position. When the obstacle radius is $0.2r_a$, we can see a drop in efficiency and its gradual recovery to the level of the unobstructed link. For an obstacle with a radius equal to $0.3r_a$, we can also see a drop in efficiency and its consequent recovery. However, the efficiency is not fully restored to the level of the unobstructed link. In figure 2.23, the complete (or almost complete) recovery of the efficiency to the level of the unobstructed link constitutes an impressive illustration of the self-healing properties of Bessel Beams. Contra-intuitively, we see that the link efficiency is more disturbed when the obstacle is placed halfway between the two apertures, and not close to the apertures. Therefore, for focused systems [41], we can expect even greater disturbances on the efficiency for obstacles located near the focal point. According to the Geometrical Optics theory, the shadow due to an obstacle, which is the region where the electromagnetic fields are yet not reconstructed, is $s \approx r_o k_0/k_n$ [81]. However, the results of our wave model do not show a direct relationship between the shadow region and the WPTE.

Furthermore, in figure 2.24, we can see that for $n = 4$ the efficiency is disturbed even for obstacles with $r_o = 0.1r_a$. For $n = 2$ and $n = 3$ the smallest obstruction affects the efficiency but it is regenerated to its original value. For the obstacles with $r_o = 0.2r_a$ and $r_o = 0.3r_a$, the efficiency is disturbed and not completely healed when n is different than $n = 1$.

Finally, figure 2.25 illustrates the relation between the WPTE the obstacle radius for a given configuration. For this study, we considered $r_a = 50\lambda, n = 1, 0 < r_o \leq r_a$, and the obstruction was placed at $z = 0.2\,\mathrm{NDR}$. The WPTE was evaluated at $z = 0.8\,\mathrm{NDR}$ in order to evaluate the influence of the obstacle radius on the efficiency for distances within the NDR. We observe that when $r_o \leq 0.2r_a$ the impact of the efficiency is almost negligible. As the obstacle radius increases to the range of $0.2r_a \leq r_o \leq 0.4r_a$, the impact of the obstacle becomes more visible although the efficiency drop is not greater than 0.07 in this region. For obstacles greater than $0.4r_a$, we observe a notable change in the curve's trend, indicating that the link becomes more sensitive to the radius of obstacle. This can be clearly seen as the efficiency drops 0.15 when the radius increases from $0.4r_a$ to $0.6r_a$.

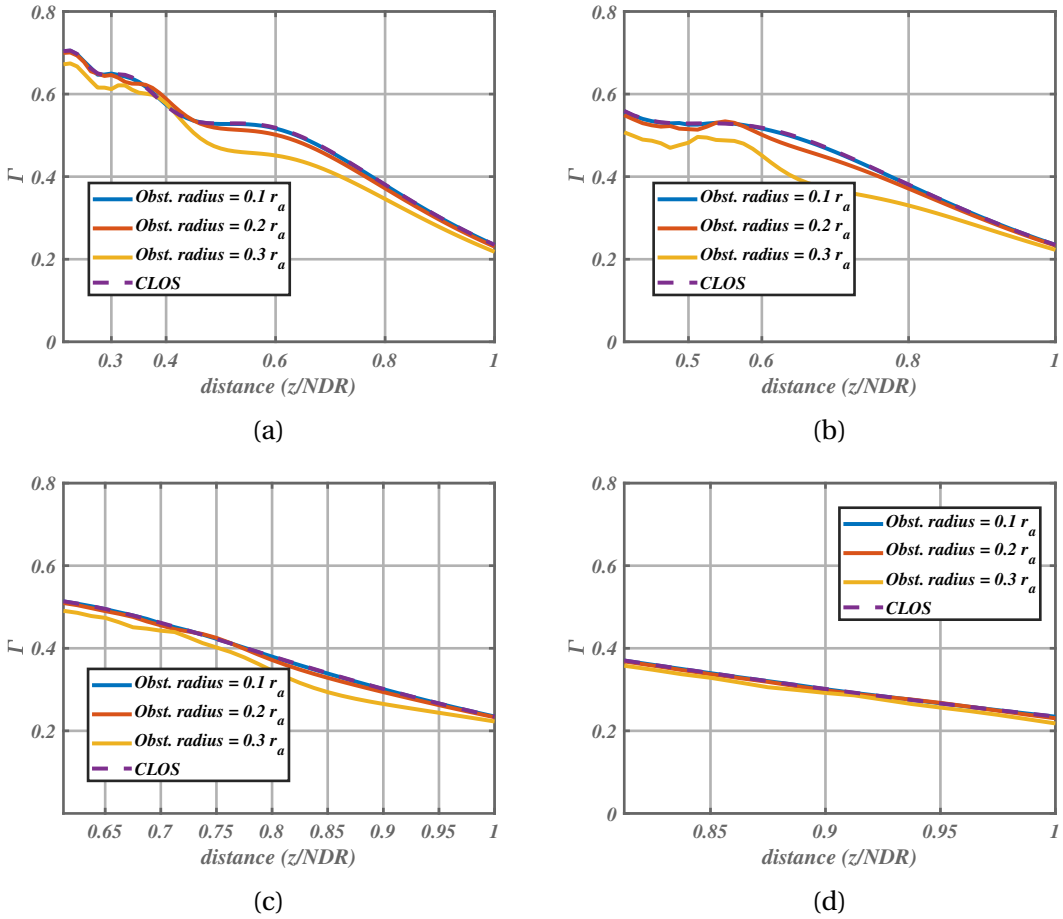

Figure 2.23 – WPTE for obstructed links for different obstacles placed at different locations along z. The WPT is evaluated as a function of the distance. The distance is normalized with respect to the NDR. The dashed line represents the WPTE for the unobstructed link. The used parameters are: $r_a = 50\lambda$, $n = 1$, and NDR $= 6531\lambda$. The obstacle is placed at $z = 0.2$ NDR (a), $z = 0.4$ NDR (b), $z = 0.6$ NDR (c), and $z = 0.8$ NDR (d)

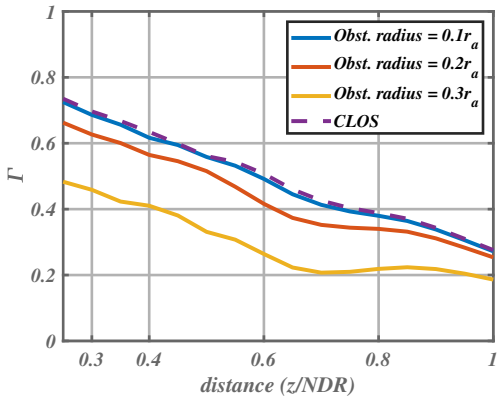

(a)

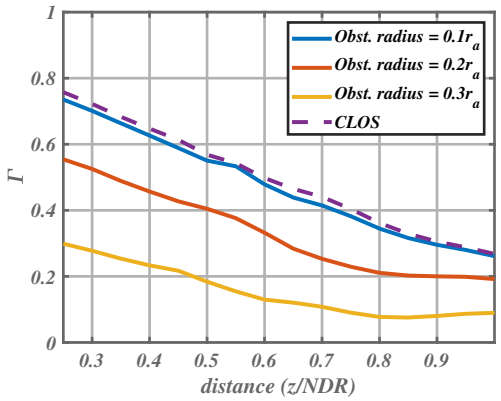

(b)

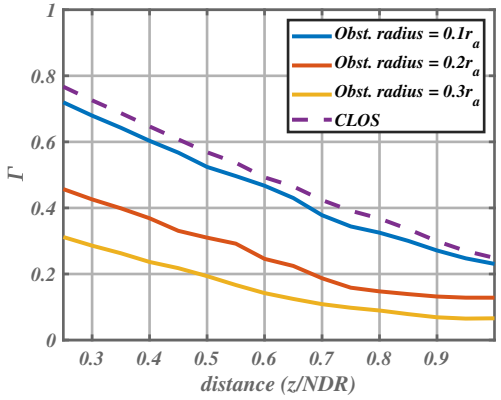

(c)

Figure 2.24 – WPTE for obstructed links for different n: (a) $n = 2$, (b) $n = 3$ and (c) $n = 4$. The obstacle is placed at $z = 0.2$ NDR. Aperture radius $r_a = 50\lambda$. The dashed line represents the WPTE of an unobstructed link.

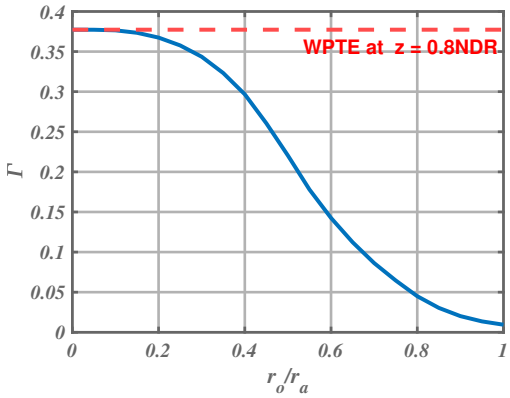

Figure 2.25 – WPTE as a function of the obstacle radius. The obstacle is placed at $z = 0.2\,\text{NDR}$ and the WPTE is evaluated at $z = 0.8\,\text{NDR}$. The dashed red line shows the value of the WPTE of an unobstructed link with a separation distance of $L = 0.8\,\text{NDR}$. The used parameters are: $r_a = 50\lambda$, $n = 1$, and $\text{NDR} = 6531\lambda$.

2.4 Analysis of Diffraction

In this section we analyze the the self-reconstruction of truncated Bessel Beams. For this purpose, we study the electromagnetic scattering by a PEC circular disk. The system is depicted in figure 2.26. Considering the cylindrical coordinate system (ρ, ϕ, z), the TM_z tangential component of the electric field of the truncated Bessel beam (BB) have the form of equation 2.8. We compare this field distribution with other two field field distributions over radiating apertures: the truncated Bessel-Gauss (BG) distribution, which is also non-diffractive, and the transverse electromagnetic (TEM) of a coaxial cable [13].

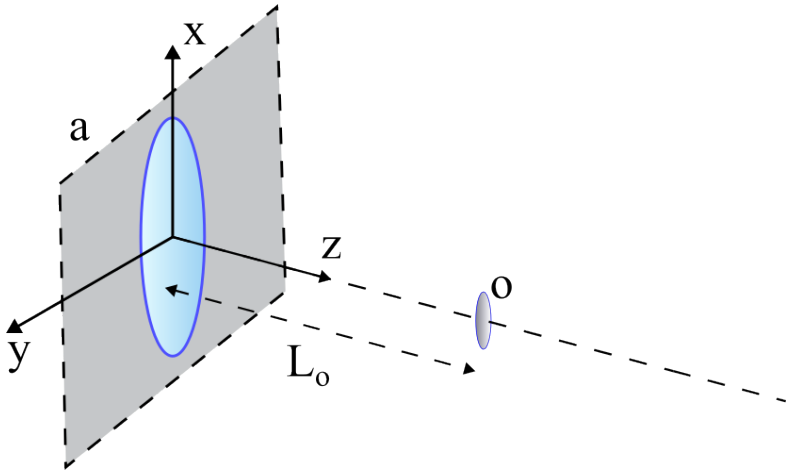

Figure 2.26 – Schematic view of an aperture facing a metallic obstruction. The obstruction is a metallic disk with radius $r_o = 12\lambda$ is placed at $z = 100\lambda$

The BG tangential field distribution is given by

$$E_t = e^{-(\rho^2)/w_g^2} J_1(k_1\rho)\hat{\rho} \quad (0 \le \rho \le r_a) \tag{2.13}$$

where w_g is the apodization width. The TEM mode tangential field distribution is given by

$$E_t = \frac{-V_0}{\rho \ln r_b/r_a} \quad (0 \le \rho \le r_a) \tag{2.14}$$

where V_0 is an arbitrary amplitude, r_b is the inner conductor radius and r_a is the outer radius of the coaxial cable.

The radiating aperture is placed on the plane $z = 0$, and it is centered at the origin of the cylindrical coordinate system. The obstacle is placed perpendicular to the axis z, at a distance L_0 from the aperture. We have chosen an aperture with a radius of 8λ which operates at 10 GHz, having $\lambda = 0.03$ m. Only TM_z polarized fields are considered.

The NDR of both the Bessel and Bessel-Gauss beams equals 0.99 m (33.15λ), and $k_1 \approx 0.23k_0$. The obstacle and the aperture are axially aligned, and the distance between them is $L_0 = 0.05$ m. For the TEM distribution, the inner radius is 0.8λ, or 10% of the outer radius. To study the impact of the obstacle's radius (r_o) on the electromagnetic fields, we have varied its radius. Thus, we have three different cases, namely A ($r_o = 1.6\lambda$), B ($r_o = 2.4\lambda$), and C ($r_o = 4\lambda$). The calculated minimum shadow distance is 0.102 m, 0.154 m, and 0.256 m for cases A, B, and C, respectively.

Figure 2.27 exhibits the case for obstacle C. The system aperture-obstacle is modeled as a scattering problem discussed in **chapter 1**. Therefore, the fields are divided in incident ($\vec{E}(\vec{H})^{in}$), scattered ($\vec{E}(\vec{H})^{s}$) and total fields ($\vec{E}(\vec{H})^{tot}$), giving $\vec{E}(\vec{H})^{tot} = \vec{E}(\vec{H})^{in} + \vec{E}(\vec{H})^{s}$. The scattered fields are calculated using PO. The amplitude of the tangential component of the total electric field, $|E_\rho^{tot}|$, disturbed by the obstacle, is shown propagating along z. We can observe a high resonant region between the obstacle and the source. Furthermore, there is a region of null field just behind the obstacle, until $z = 0.12$ m. Then, the field starts to self-recover, gradually regaining its intensity.

In figure 2.28, the total tangential electric field is shown for the three different field distributions at $z = 0.5$ m. The total field at this z plan is compared to the incident tangential field at the same plan. Furthermore, figure 2.28 shows the comparison between the BB results with the commercial full-wave software COMSOL and the approach developed in this work. The results from our diffraction formulation using the PO approximation for the induced currents show good agreement with COMSOL. We can observe the impact of the size of the obstacle in the amplitude of the tangential electric field. For the worst case, obstacle C, $|E_\rho^{tot}|$ is approximately $0.66|E_\rho^{in}|$, $0.40|E_\rho^{in}|$ and $0.30|E_\rho^{in}|$ for BB, BG and TEM distributions respectively. We can verify the the self-healing effect in the BB and BG beams. However, while the field profile is restored, the amplitude is not fully recovered.

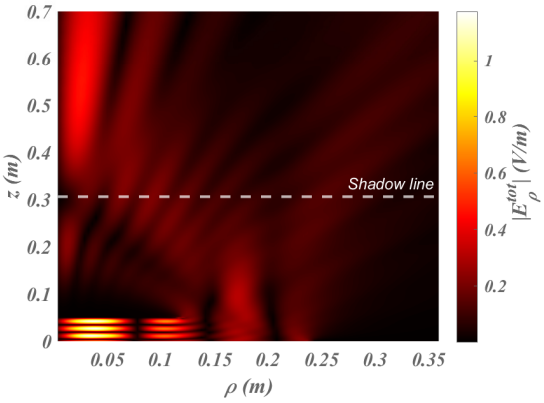

Figure 2.27 – Amplitude of $E_\rho^{tot}(\rho, z)$ for the BB distribution, considering $r_a = 8\lambda$ and $r_o = 4\lambda$. The shadow distance extends until $z = 0.306\,\text{m}$.

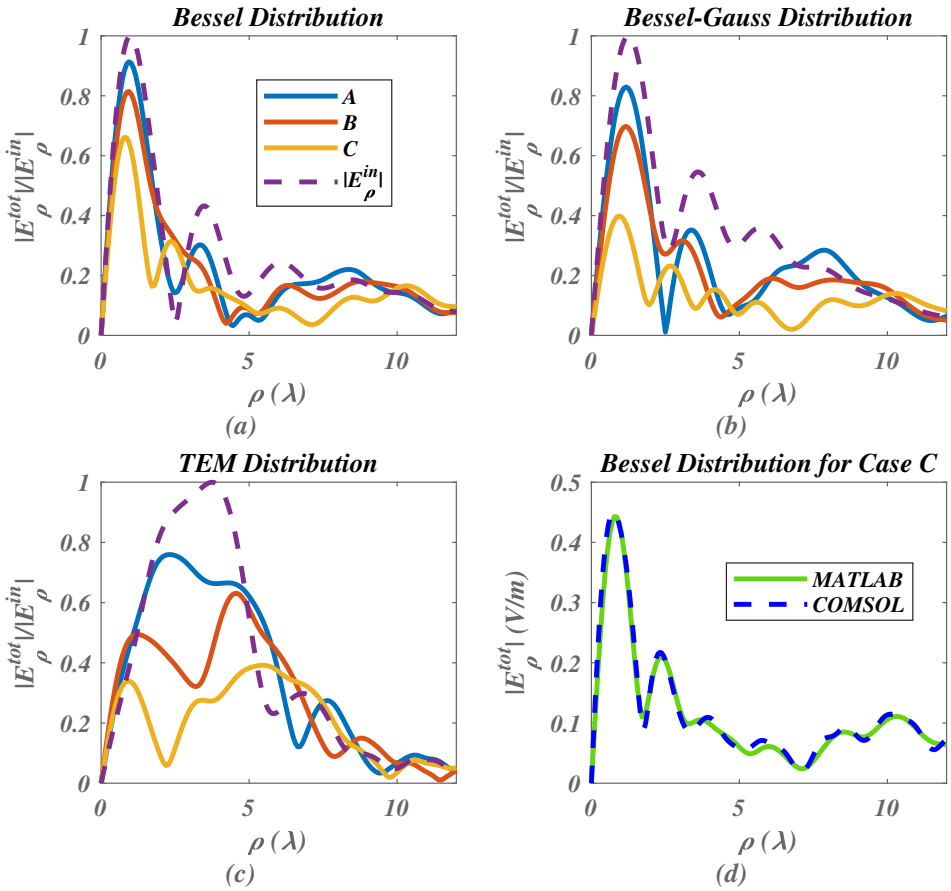

Figure 2.28 – In (a), (b) and (c) $|E_\rho^{tot}|$ normalized by $|E_\rho^{in}|$ in the plane $z = 0.5\,\text{m}$ is shown. The curves A, B and C are referenced to obstacles of radius 1.6λ, 2.4λ and 4λ, respectively. The dashed purple line represents the normalized $|E_\rho^{in}|$, plotted here for comparison. In (d) it is presented the comparison of the results from our approach and those from COMSOL, considering $|E_\rho^{tot}|$ radiated by the BB distribution in the plane $z = 0.5\,\text{m}$.

2.5 Metric for Self-healing

To evaluate the self-reconstruction properties, we employ the self-healing degree as a metric. Aiello et al. [39] were the first to propose a degree of self-healing as a means to quantify the self-reconstruction ability of general beams. In their publication, this metric was used to evaluate the self-reconstruction properties of a Gaussian beam. This approach involves comparing the field distribution of the original beam with that of the obstructed one, rather than comparing their intensities. This degree, denoted as D_{sh}, can be understood as a relative distance between the incident and total fields in a defined region, S. This region is limited by the obstacle dimensions and lies on the plane transverse to the direction of propagation. The self-healing degree is written as:

$$D_{sh} = 1 - \frac{||E_t^{in} - E_t^{tot}||}{||E_t^{in}|| + ||E_t^{tot}||} \tag{2.15}$$

$$||f|| = \left(\int_S f^*(x,y,z) f(x,y,z)\, dS \right)^{1/2} \tag{2.16}$$

where the subscript t indicates the tangential component. In this section we compare Bessel beams with different polarization: linear and radial. Considering the coordinate system (x, y, z) and $\rho = \sqrt{x^2 + y^2}$, the linearly polarized Bessel field distributions over a radiating aperture can written as [78]

$$\vec{E}(\rho, z = 0) = -iBk_1 J_0(k_1\rho)\hat{x} - B\frac{k_1^2}{k_z} J_1(k_1\rho)\hat{z} \tag{2.17}$$

where B is an arbitrary amplitude coefficient. It is assumed that the beams are transverse magnetic with respect to the z coordinate (TM_z).

The source center is positioned on the origin of the coordinate system and the obstruction is placed parallel to the source. The formulation used is frequency independent. The dimensions of the problem are expressed in terms of the wavelength (λ) and the aperture radius is set to 25λ. We define case A as the one in which the aperture radiates a linearly polarized beam while case B is the one related to the radially polarized one (see equation 2.4). For each case, the obstacle is placed at different positions, whether axially aligned with the radiating apertures or not. Note that the transverse propagation constant is selected to minimize diffraction. As a result, k_1 in case A is different from k_1 in case B.

The total electric tangential fields along z in both cases is shown in figure 2.29, where we notice a shadow region immediately after the obstruction. The self-healing degree as a function of the obstacle radius and the distance of its center from the z-axis is depicted on figure 2.30, where r_o is the obstruction radius and r_a is the aperture radius. The self-healing degree is evaluated at $z = 226.5\lambda$ and $z = 453\lambda$ for both cases.

In figure 2.30a, the obstacle is axially aligned to the aperture and placed $z = 113\lambda$. We observe that the self-healing degree decreases as the obstruction size increases. Case B exhibits a higher self-healing degree when compared to A considering the same

evaluation distance. This is not valid only for $0.6r_a \leq r_o \leq 0.85r_a$ at $z = 226.5\lambda$, and $0.6r_a \leq r_o \leq 0.7r_a$ at $z = 453\lambda$.

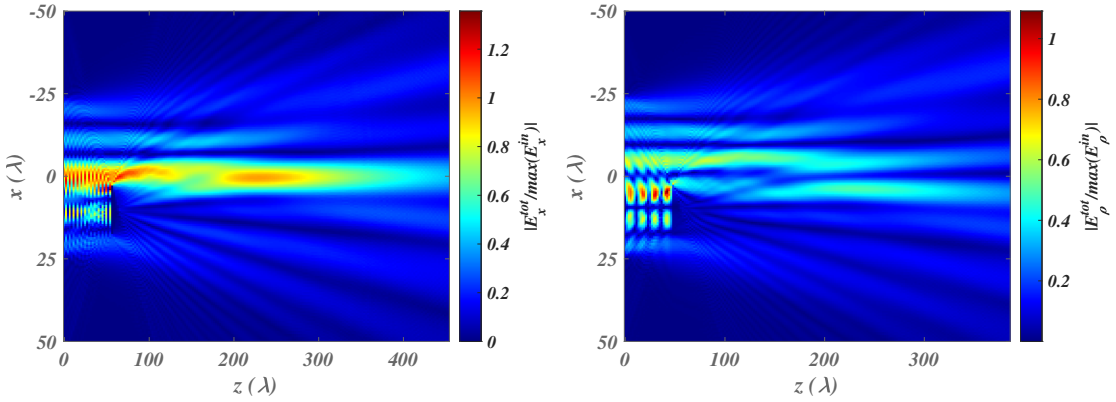

(a) (b)

Figure 2.29 – Amplitude of the normalized total tangential electric field propagating along z. The fields are normalized by the maximum amplitude of the incident field. The obstruction is placed at $(x = 10\lambda, y = 0, z = 57\lambda)$, $r_a = 25\lambda$. In (a) case A is shown and the NDR = 453λ, while in (b) case B is shown and the NDR = 385λ.

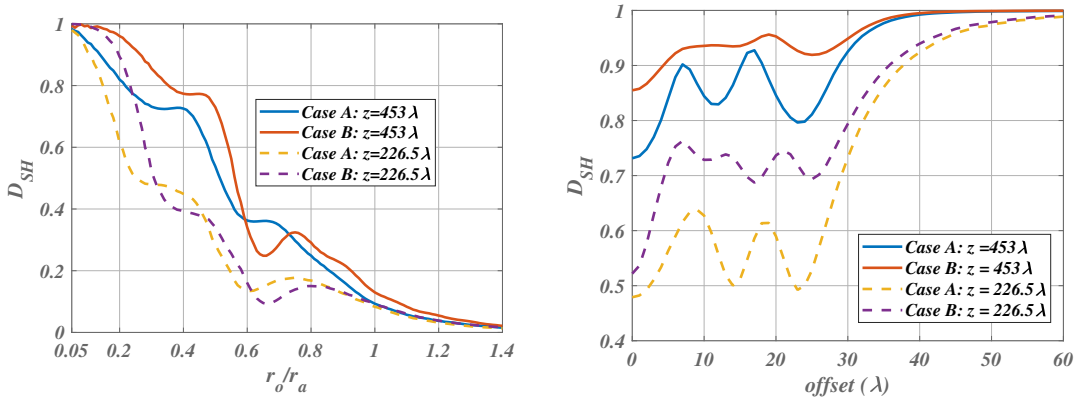

(a) (b)

Figure 2.30 – Self-healing degree relation to the obstacle radius (r_o) and the distance of the obstacle's center to the z-axis is depicted in (a) and (b) respectively. In both cases, the obstacle is placed at $z = 113\lambda$ and the self-healing degree is evaluated at $z = 226.5\lambda$ (dashed line) and at $z = 453\lambda$ (solid line), and $r_a = 25\lambda$.

In figure 2.30b, the obstacle is placed $z = 113\lambda$ and we evaluate its impact on self-healing degree as a function of its distance from the z-axis (offset), with $r_o = 0.3r_a$. We

observer that, again, Case B exhibits a superior self-healing degree when compared to case A when evaluated at the same distance. Furthermore, there is a common region for both cases, ranging from $5\lambda \leq \text{offset} \leq 25\lambda$, where the self-healing degree shows an oscillatory behavior.

2.6 Conclusion

In this chapter, we have explored the properties of Bessel beams. Specifically, we focused on their non-diffractive nature and self-healing capabilities. Through an examination of the theoretical foundation of these beams, we have highlighted their ability to maintain a stable transverse profile over long distances. This distinctive feature, together with their capacity of self-reconstruction after encountering obstacles, reinforce the potential of Bessel beams in various domains.

Our analysis extended to the practical realization of truncated Bessel beams, examining their performance in scenarios with and without obstructions. We studied the WPTE between apertures radiating these beams, showing the differences that come due the choice of truncation. It was observed that for distances smaller than the NDR, the WPTE of unobstructed links appears to decrease with distance in an almost linear fashion. In contrast, when the separation distance exceeds the NDR, the link efficiency appears to decrease in a quadratic trend, suggesting it follows the behavior predicted by Friis transmission equation. For the same aperture and separation distance, Bessel beam with small transverse propagation constants provides the highest efficiency.

The impact of the obstacle on the WPTE was studied considering its position and size. The obtained results illustrate how the size of the obstacle with respect to the radiating aperture radius affect the capability of the Bessel beam to self-heal after an obstruction and thus on the possibility to establish a resilient link. Particularly, for obstacles with radius up to 30% of the aperture radius, the WPTE is fully restored to its unobstructed level. It also appears that Bessel beams with smaller transverse propagation constant can overcome larger obstacles. We saw that WPTE is most affected when the obstacle is located halfway between the apertures and its size is comparable to the radius of the generated beam. Furthermore, the results indicate that the length of the shadow region is not directly related to the WPTE of obstructed links for the studied configurations.

Finally, we compared the response to obstacles of different beams, showing an advantage for the Bessel beam over TEM and Bessel-Gauss beams. Also, we have reported the evaluation of the self-healing degree of TM_z linear and radially polarized weakly-diffracting vector beams, studying their response to obstacle radius and distance from the z-axis. As expected, larger obstacles reduced self-healing, while increasing the offset generally improved it, though with oscillations for offsets between 15λ and 25λ. Finally, its worth mentioning that radial polarization demonstrated a higher self-healing degree in the situations we considered, specially when the obstacle is coaxial to the aperture, as there is a point of zero field in the center of the beam. As part of the LinkAll project, we developed Bessel beam launchers with two polar-

ization schemes: one radially polarized and the other linearly polarized. The linearly polarized launcher is detailed in **Chapter 4**, while the radially polarized launcher is presented in [96, 97].

3 Under-Focused Bessel Beams with Large Operating Distances

Table of contents

3.1 Introduction 102
3.2 Phased Modulation on Weakly Diffractive Beams 103
3.3 Comparison with different truncated Bessel beams 108
3.4 Partially obstructed wireless links 110
3.5 Conclusion 113

3.1 Introduction

As previously stated, Bessel beams operating in the radio frequency (RF) domain are more sensitive to truncation, because, differently from the optical domain, the electrical size of the apertures seldom exceeds few tens of wavelengths. Consequently, the non-diffractive range (NDR), denoted as Z_N in this chapter, winds up lacking precision for designing systems in terms of wireless power transfer efficiency (WPTE), as this parameter is calculated assuming geometrical optics.

In this chapter, our focus is on enhancing the WPTE between two planar apertures radiating truncated Bessel beams. Instead of optimizing efficiency for a fixed distance between antennas, our study aims to maintain high efficiency across an extensive range of distances. We propose a new design parameter, the operating range, denoted as Z_O, defined as the separation distance over which the WPTE remains greater than 50%. Our approach to enhance the WPTE between two apertures is based on applying a modulated linear phase profile, with respect to the transverse radial coordinate, across these apertures. While a quadratic phase profile could theoretically achieve similar results, as demonstrated in our analysis, the linear phase approach presents a key advantage: it requires fewer control parameters, simplifying the design and implementation process. Both unobstructed and partially obstructed links are examined, and a comparative analysis with a focus on assessing the obstruction's influence on the WPTE is presented.

This chapter is structured as follows. In section 3.2 we present the technique used to enhance the WPTE between two radiating apertures. Then, section 3.3 provides a comparison between the WPTE results of our proposed method and other Bessel beam implementations. In Section 3.4 the WPTE is evaluated for partially obstructed links.

We chose an axially aligned perfectly electrically conducting (PEC) disk as obstruction. Finally, the conclusions with the most relevant results are presented in the last section.

3.2 Phased Modulation on Weakly Diffractive Beams

Returning to the WPTE computation for an unobstructed link radiating radially polarized truncated Bessel beams, figure 3.1 illustrates the results for different transverse wavenumber, k_1. We are using the Bessel roots of $J_1(\cdot)$ to calculate k_1 in order to reduce diffraction around the edges. Therefore, $k_1 = j_{1n}/r_a$, where r_a is the radius of the aperture. Also, we define Z_N as the position corresponding to the NDR. It is then observed that the relationship between the normalized separation distance (z/Z_N) and WPTE, as presented in figure 3.1, remains consistent regardless of the aperture size. We observe that at $z = Z_N$, the efficiency of the wireless link is 35%, 23% and 24% for $n = 1$, $n = 2$ and $n = 3$ respectively.

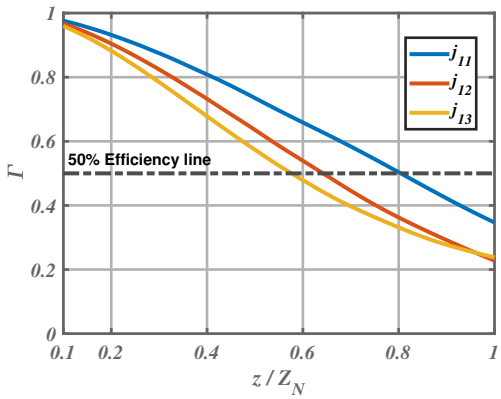

Figure 3.1 – WPTE considering identical apertures of arbitrary radius as a function of normalized separation distance

We define the operating range (Z_O) as the distance at which the efficiency decreases to 50%. We aimed to utilize a parameter that would provide more insightful data in the context of WPTE. Consequently, from figure 3.1, we observe that Z_O is $0.8\,Z_N$, $0.64\,Z_N$ and $0.57\,Z_N$ for j_{11}, j_{12} and j_{13} respectively. These observations are summarized in table 3.1.

Table 3.1 – WPTE as a function of Z_N for truncated Bessel beams of arbitrary radii

Bessel root (j_{1n})	Γ at $z = Z_N$	Z_O
First zero (j_{11})	35%	$0.8\,Z_N$
Second zero (j_{12})	23%	$0.64\,Z_N$
Third zero (j_{13})	24%	$0.57\,Z_N$

In [98], the researchers reduce the radius of the Bessel beam angular spectrum ring, thus increasing its non-diffractive range, by implementing phase modulation in the spatial domain. Their geometry considers much larger apertures than the ones we intend to use in this study and they work in the optics domain. However, we decided to investigate if this approach is suitable for our case, with the aim of extending the operating range of our system.

We consider that the complex scalar A in equation 2.8 will be responsible to provide a linear phase, with respect to the cylindrical coordinate $\rho = \sqrt{x^2 + y^2}$, to the Bessel distribution over the aperture. In terms of physical realization, an axicon [42] placed over a truncated Bessel beam launcher [19, 20] could be used to provide the required phase profile. Over aperture a the tangential electric field writes

$$\vec{E}_a^t = e^{i2\pi\psi\rho} J_1(k_\rho \rho)\hat{\rho} \quad (0 \leq \rho \leq r_a) \tag{3.1}$$

where ψ is the unite-less phase modulating factor. Our goal is to provide a slight linear phase to the field distribution over the apertures, justifying the name under-focused Bessel beams. Initially, we analyze its impact on the WPTE of our system.

To validate the WPTE results for this case, we compare our results with a full-wave software. The chosen parameters for the validation are j_{11} and $r_a = 5\lambda$, due to computational resources. The results are presented in figure 3.2, where we can observe that the phase modulation has a notable impact on the WPTE. Notably, when $\psi = 15$, the efficiency is 55% at $z = 0.1\,Z_N$ and 46% at $z = Z_N$, compared to 98% at $z = 0.1\,Z_N$ and 35% at $z = Z_N$ in the absence of phase modulation ($\psi = 0$). We observe that, at $z = Z_N$, the WPTE increases by 6%, 10%, and 11% for $\psi = 5$, $\psi = 10$, and $\psi = 15$, respectively, compared to $\psi = 0$.

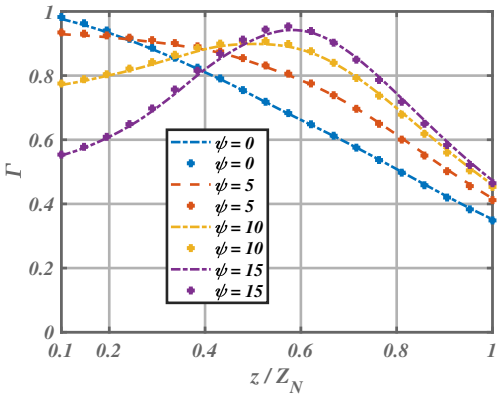

Figure 3.2 – WPTE as a function of the normalized separation distance considering different phase modulations for the first Bessel root, j_{11}. The dashed lines represent the numerical data and the plus signs the data from COMSOL.

After validation, we can employ our model to simulate and compare larger apertures for both the focused and unfocused cases. The efficiency as a function of the separation distance, z, is depicted in figure 3.3, with the parameters set to Bessel

root j_{12}, $r_a = 50\lambda$, $f = 60$ GHz, and ψ assumes two values, 0 and 1. It is observed that the operating range, Z_O, for $\psi = 0$ is 1433λ, whereas for $\psi = 1$, it extends to 1880λ, indicating a relative increase of 447λ in the operating range.

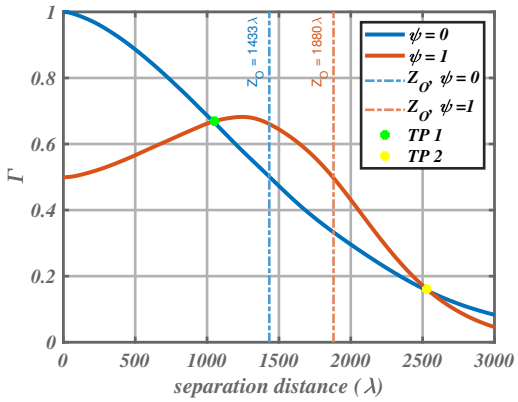

Figure 3.3 – WPTE as a function of the separation distance for the second Bessel root, j_{12}, for the focused and unfocused cases. The blue and red dashed lines respectively denote the operating ranges for focused ($\psi = 1$) and unfocused ($\psi = 0$) beams, while TP1 and TP2 denote turning points 1 and 2.

Furthermore, in figure 3.3, we observe three distinct regions separated by two turning points, TP1 and TP2. In the first region, $0 \leq z \leq 1052\lambda$, the efficiency is higher for the unfocused case, while in the second region, $1052 \leq z \leq 2529\lambda$, the focused case presents higher efficiency. Finally, in the third region $z \geq 2529\lambda$ the unfocused beam, once more, shows better performance.

By examining the term $e^{i2\pi\psi\rho}$, we verify that the maximum phase occurs at the edges of the radiating surface, precisely at $\rho = r_a$. Consequently, we denote the phase at the aperture's edge as $\theta_M = 2\pi\psi r_a$. It's worth noting that θ_M serves as a key parameter for characterizing the WPTE behavior across apertures of varying sizes but consistent j_{1n}, as shown in figure 3.4. Moreover, we introduce a critical angle θ_C, defined as the θ_M value that yields 50% efficiency at $z = 0$, which is determined numerically, and results in 140.4°, 91° and 85.32° for j_{11}, j_{12} and j_{13} respectively.

In figure 3.5, we observe that for the angles analyzed, the spectral content of the tangential electric field is not considerably altered. We verified that to shift the location of the maximum, as done in [98], consequently enlarging the range of ring in the spectral domain, we need to increase drastically the phase modulating factor, resulting in $\theta_M > \theta_C$, which goes further than the scope of this research.

We can clearly see that the phase modulation increases the operating range of the radiated beams. These results are summarized in table 3.2. Figure 3.6 shows the operational range as a function of the aperture radius. It acts as a guide for designing apertures radiating truncated Bessel beams up to three zeros (j_{13}) for operational distances up to 4000λ. We observe that in terms of Z_O, $j_{1n} = j_{11}$ is the best choice.

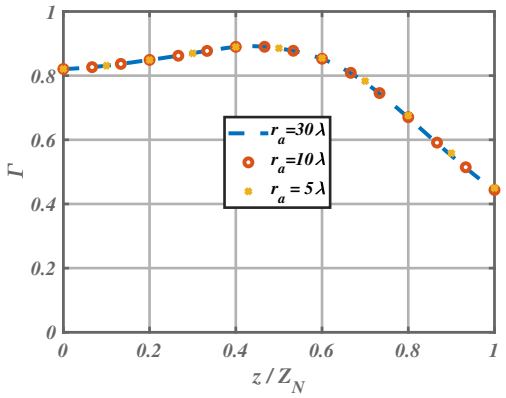

Figure 3.4 – WPTE as a function of the distance normalized by Z_N for arbitrary aperture sizes, j_{11} and $\theta_M = 75.6°$, $f = 60\,\text{GHz}$.

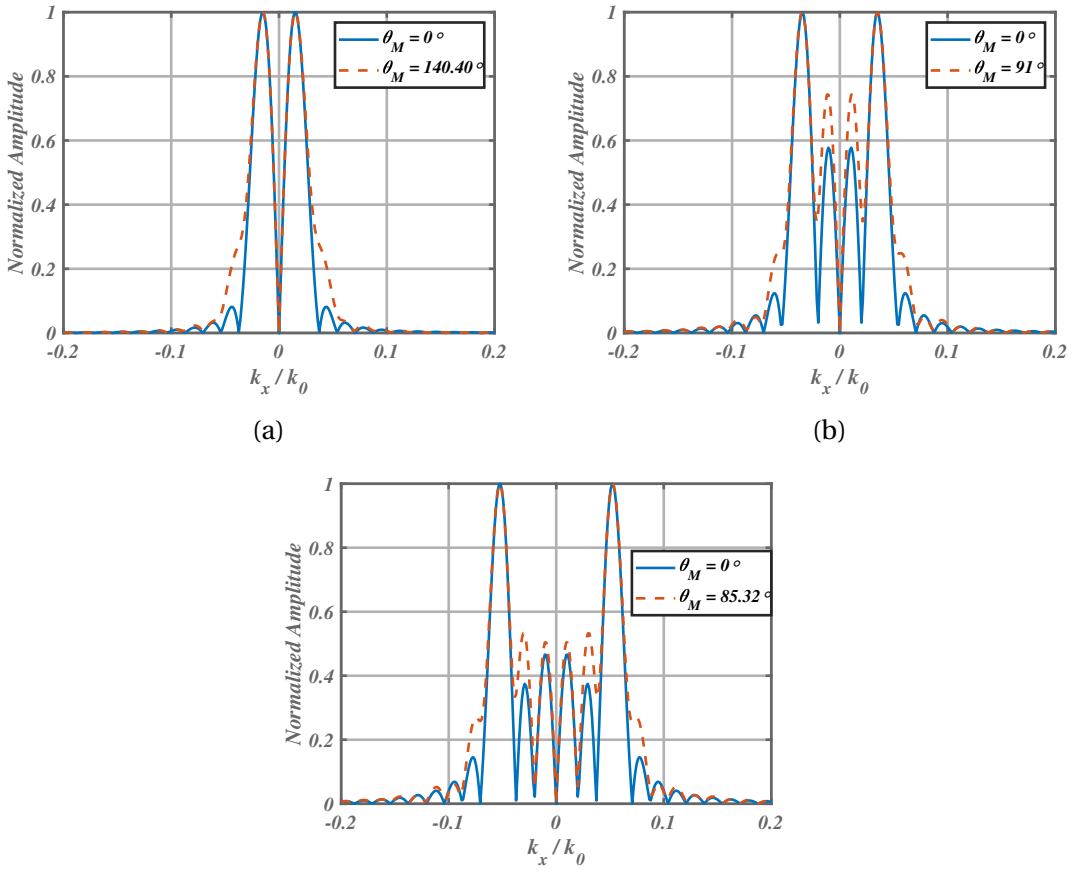

(a) (b)

(c)

Figure 3.5 – Normalized amplitude profile of the spectral content of the tangential field for different θ_M at $z = 0$ and $k_y = 0$ for j_{11} (a), j_{12} (b) and j_{13} (c).

Generally, in focused near-field applications, quadratic phase profiles are used [40,

41]. This kind of phase profile can be expressed as:

$$f(\rho) = e^{i\psi k_0 \frac{\rho^2}{2L_0}} \tag{3.2}$$

where L_0 represents the focal length. We have observed that, due to the size of the apertures and maximum phase applied, we are working in a condition for which the results for quadratic phase are very similar to the ones obtained using the linear phase profile we propose. As an example, we compare our proposed approach and the quadratic phase considering the same critical angle at the edge of the aperture. Therefore, the control parameter ψ will present different values for the two approaches. Figure 3.7 depicts the WPTE results of both approaches.

Table 3.2 – WPTE as a function of Z_N for under-focused truncated Bessel beams operating at θ_C

Bessel root (j_{1n})	Γ at $z = Z_N$	Z_O
First zero (j_{11})	46%	$0.97\,Z_N$
Second zero (j_{12})	30%	$0.84\,Z_N$
Third zero (j_{13})	24%	$0.73\,Z_N$

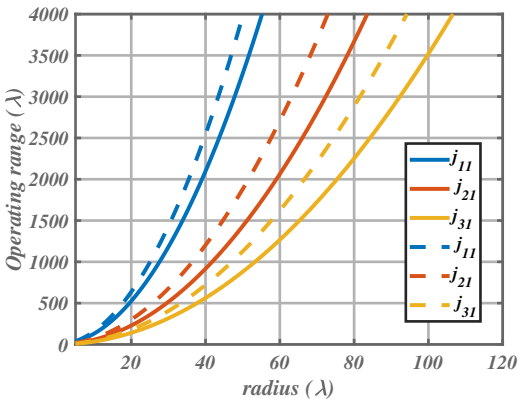

Figure 3.6 – Z_O as a function of the radius of the apertures. The first, second and third Bessel roots are represented by j_{11}, j_{12} and j_{13} respectively. The dashed curves represent the under-focused Bessel beams operating at θ_C, while the continuous lines represent the truncated Bessel beam.

We can see that they have the same operating range. Furthermore, the two curves present a similar behavior, despite the small differences observed related to the maximum efficiency and when the separation distance approaches to zero. This similar behavior is also observed when we analyze the spectrum and the amplitude profile, presented in figures 3.8b and 3.8a respectively. Therefore, we conclude that using the linear or quadratic phase profile delivers the same results for the cases studied.

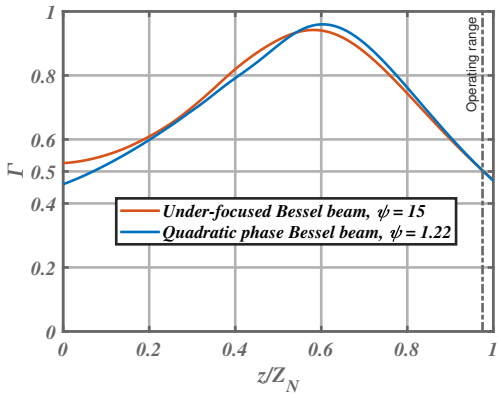

Figure 3.7 – WPTE as a function of the normalized separation distance considering a linear and quadratic phase approaches.

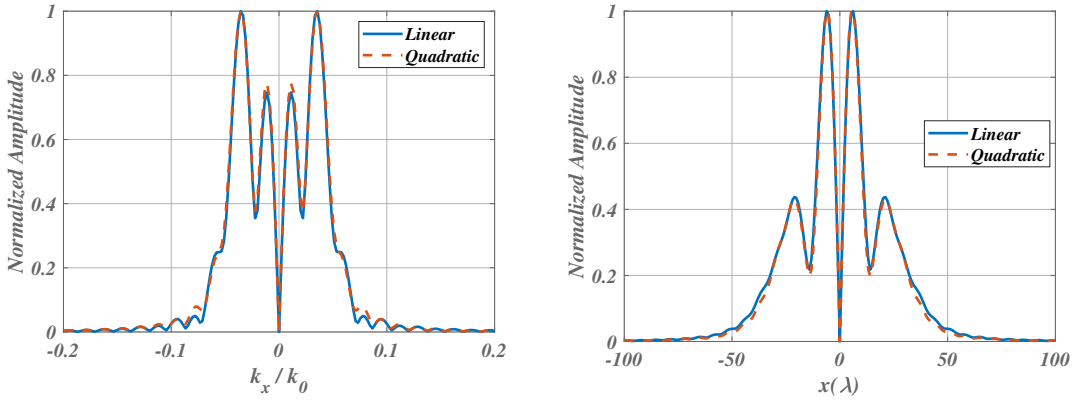

(a) (b)

Figure 3.8 – Comparison between linear and quadratic phase profiles considering the second Bessel root, j_{21}, and $\theta_M = 91°$. In (a), the normalized amplitude of the spectral content of the tangential component of the electric field is shown, and in (b), the normalized amplitude of the tangential component of the electric field is presented.

3.3 Comparison with different truncated Bessel beams

Several launchers radiating electromagnetic beams derived of Bessel beams are present in literature, such as [13, 41]. In [41], a tangential field distribution based on the superposition of Bessel beams with different transverse wavenumbers is proposed. The coefficients of this combination are optimized to increase the WPTE for a specific separation distance between emitter and receiver. Thus, a comparison with our approach does not seem to be relevant, as our goal is to achieve a certain level of

efficiency across a broad operational area, rather than at a fixed separation distance.

In [13], a Bessel-Gauss launcher is designed to overcome the eventual problems related to diffraction at the edges of the radiating aperture. This launcher demonstrated superior performance compared to the truncated Bessel beam over the studied distances, prompting us to compare our method to this Bessel-Gauss launcher. Adding the modulation factor ψ and linear phase to the Bessel-Gauss launcher results in a tangential field distribution written as

$$\vec{E}_a^t = e^{-\frac{\rho^2}{\omega_0^2}} J_1(k_\rho \rho) e^{i2\pi\psi\rho} \hat{\rho} \quad (\rho \leq 0 \leq r_a) \tag{3.3}$$

where the apodization width, ω_0, is the minimum value for which the NDR of the Bessel-Gauss beam is equal to the NDR of the corresponding Bessel beam. The apodization width is calculated as [34]:

$$\omega_0 = \frac{r}{\sqrt{\ln 4}} \tag{3.4}$$

This choice of ω_0 is done to ensure that the beams are compared in equal conditions. We compare the under-focused Bessel-Gauss beam (equation 3.3) and our proposed beam in terms of WPTE checking their behavior for the same angle at the aperture edge $\theta_M = 135°$.

In figure 3.9, we notice that the under-focused Bessel beam outperforms the under-focused Bessel-Gauss beam in terms of operating range. While the under-focused Bessel-Gauss beam achieves a higher efficiency within the range $0 \leq z/Z_N \leq 0.52$, reaching a peak of 98%, its overall operating range is limited to $0.8\,Z_N$. In contrast, the under-focused Bessel beam extends its operating range to $0.97\,Z_N$ and exhibits a peak efficiency lower than that of the Bessel-Gauss beam (94%).

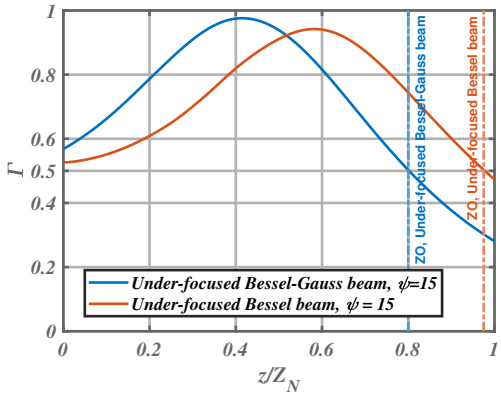

Figure 3.9 – WPTE as a function of the normalized separation distance considering a phase modulation for the first Bessel root, j_{11} and the truncated under-focused Bessel-Gauss beam. The aperture radius is $r = 5\lambda$, apodization width $\omega_0 = 4.25\lambda$ and $f = 60\,\text{GHz}$.

3.4 Partially obstructed wireless links

To evaluate and compare the self-healing properties of focused and unfocused beams, we analyze the impact of an object placed between the two apertures on the radiated fields and WPTE. The considered systems are depicted in figure 3.10. The obstacle is a disk axially aligned to the apertures composed of PEC material. The simulations parameters are $r_a = 50\lambda$, $f = 60\,\text{GHz}$ and $j_{1n} = j_{12}$.

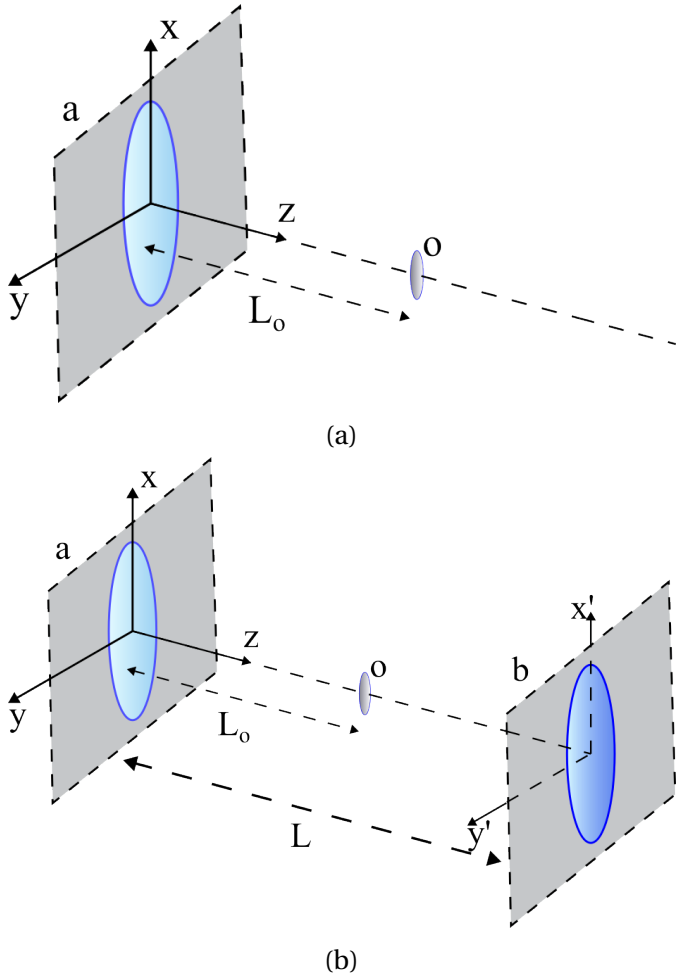

Figure 3.10 – Apertures radiating in the presence of an obstruction. In (a), we have an aperture facing an obstruction, while in (b), a link composed of two apertures and an axially aligned obstruction is shown.

Initially, we investigate the tangential electric fields radiated by the aperture in the presence of the obstruction, and the results are presented in figures 3.11 and 3.12. The problem is analyzed as a scattering problem [50], and the obstacle is placed at $z = 358\lambda$. The shadow limit is calculated using equation 2.6.

In figure 3.11, the results for the truncated Bessel beams are shown. Figure 3.11a depicts the tangential electric field radiated by an aperture relative to z/Z_N, whereas fig-

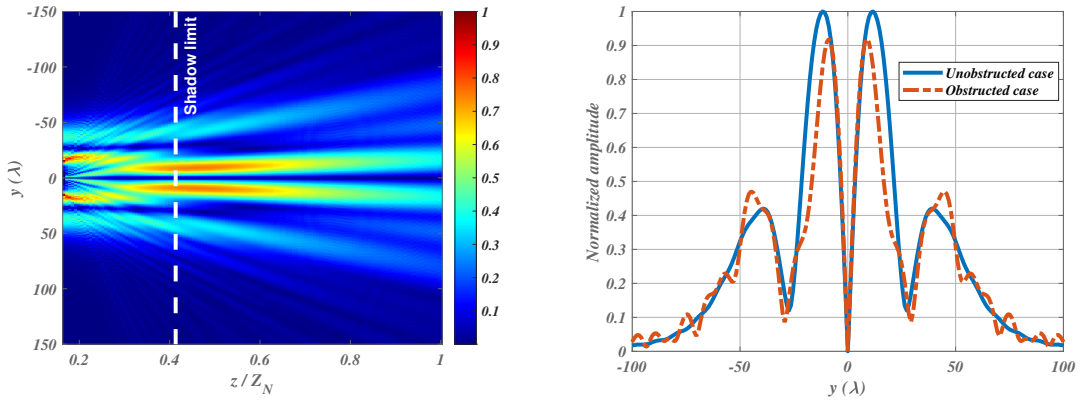

(a) (b)

Figure 3.11 – Amplitude of the tangential component of the radially polarized electric field of the truncated Bessel beams (unfocused) for obstructed and unobstructed beams. The obstacle is placed at $z = 358\lambda$. In (a) the amplitude of the field as a function of z/Z_N for j_{12} and $x = 0$ is presented, while in (b), the amplitude profile of the tangential field at $z = Z_m$ for j_{12} and $x = 0$ is shown

ure 3.11b compares the tangential electric field profiles immediately after the shadow limit for both obstructed and unobstructed cases. In figure 3.11a, we clearly see the disturbances created by the presence of the obstacle and its consequent reconstruction after the shadow limit, that is more explicit on the two central lobes. In figure 3.11b, we notice that the maximum amplitude of the reconstructed beam is 8% smaller than the amplitude of the unperturbed beam.

In figure 3.12, we present the results concerning under-focused beams. Figure 3.12a illustrates the tangential field radiation from an aperture in relation to z/Z_N, while figure 3.12b contrasts the tangential field profiles right after reaching the shadow limit for both obstructed and unobstructed scenarios. Again, we observe the disturbances created due to the presence of the obstruction and the consequent reconstruction of the tangential field. The reconstructed field's maximum amplitude in this case is 13% smaller than the maximum of the unobstructed field.

Figure 3.13 shows the results of WPTE for the truncated and under-focused beams as a function of the separation distance for a fixed obstacle position. The obstacle is placed at $z = 358\lambda$, and its radius is $r_o = 12.5\lambda$. We notice that the efficiency of both the truncated and under-focused beams are highly impacted by presence of the obstacle. Immediately after the obstruction, the WPTE drops 28.5% and 15.12%, respectively, for the truncated and under-focused beams when compared to the unobstructed case. Two distinct behaviors are observed as we go increase the separation distance between emitter and receiver in the obstructed case. While the efficiency of the truncated Bessel beam drops from 64% to 15%, the under-focused beam's efficiency drops from 39.19% to 20%. Furthermore, between 400λ and 1268λ, the truncated Bessel beam presents

higher efficiency, while between 1268λ and 2238λ the best choice is the under-focused beam.

In figure 3.14, the relationship between WPTE and obstacle radius for a given configuration is shown. The obstacle is placed at $z = 358\lambda$, aperture radius $r_a = 50\lambda$, frequency $f = 60\,\text{GHz}$, and the WPTE is computed at $z = Z_N$ for $0.1 \leq r_o/r_a \leq 1$. Notably, we observe a higher efficiency on the under-focused beam for the whole range analyzed. Additionally, both beams are more affected by the radius of the obstacle in the region $0.15 \leq r_o/r_a \leq 0.45$.

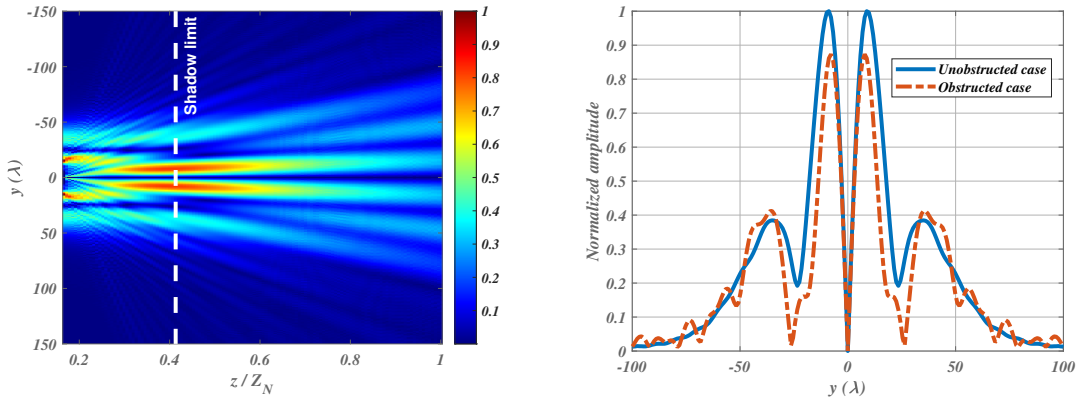

(a) (b)

Figure 3.12 – Amplitude of the tangential component of the radially polarized electric field of the under-focused beams for obstructed and unobstructed beams. The used parameters are $r_a = 50\lambda$, $r_o = 12.5\lambda$, and $f = 60\,\text{GHz}$. The obstacle is placed at $z = 358\lambda$. In (a), the amplitude as a function of z for j_{12} (third root), $y = 0$ is shown, while in (b), the amplitude of the spectral content for j_{12} (third root) at $z = 0$ is presented

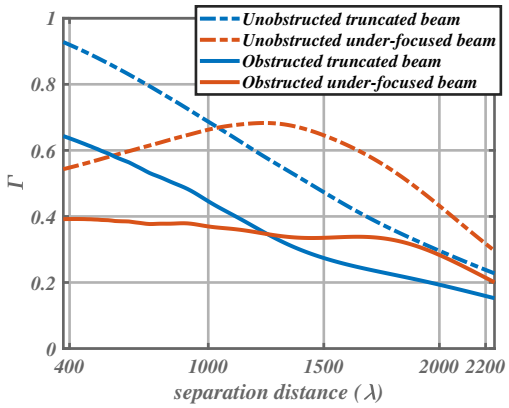

Figure 3.13 – WPTE as a function of the separation distance after the obstruction for the truncated and under-focused Bessel beams. The used parameters are $r_a = 50\lambda$, $r_o = 12.5\lambda$, and $f = 60\,\text{GHz}$. The obstacle is placed at $z = 358\lambda$.

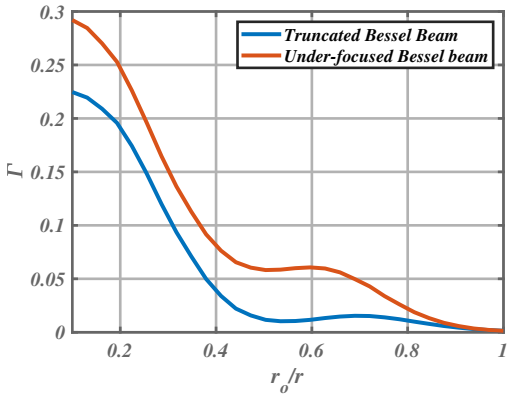

Figure 3.14 – WPTE evaluated at $z = Z_N$ for the under-focused and truncated Bessel beams as a function of the obstruction radius. The used parameters are $r_a = 50\lambda$ and $f = 60\,\text{GHz}$. The obstacle is placed at $z = 358\lambda$.

3.5 Conclusion

In this chapter, we have investigated the complex relationship between the aperture design, space phase modulation, and WPTE within the context of large apertures and even larger operation distances. As the NDR is a quantity defined in GO regime, we defined a the operating range that is the separation distance over which the WPTE remains greater than 50%. We investigated radiating apertures with Bessel distributions truncated up to the third Bessel root of $J_1(\cdot)$.

We have observed that we can increase the operating range of truncated Bessel beams by applying a linear phase modulation, with respect to the transverse radial component, on the tangential field distribution over the radiating aperture. The phase difference between the edges and the center of the aperture was used as control parameter to estimate estimate the WPTE. Furthermore, our analysis revealed that the spectral content is slightly affected by the phase modulation across the range of angles examined and the self-healing properties are maintained.

We also observed that employing a quadratic phase profile yielded comparable results. However, due to the linear phase profile approach requiring fewer control parameters, we opted for it. The increase in the operating range was 15% of the NDR when truncated at the first Bessel root, 20% for the second Bessel root, and 16% for the third Bessel root. This enhancement translates to a reduction in the required aperture size to achieve the desired operation range.

The comparison between the under-focused Bessel and Bessel-Gauss beams highlights a clear trade-off between WPTE efficiency and operating range. While the Bessel-Gauss beam achieves a higher peak WPTE of 98%, its operating range is comparatively shorter. In contrast, the Bessel beam, with a slightly lower peak efficiency of 94%, extends its operating range by approximately 20%, offering a more sustained performance over a larger distance.

4 Design and Realization of a Quasi-Bessel Beam Transmitter

Table of contents

4.1 Introduction . . . 114
4.2 Axicon as a Phase Transformation . . . 115
4.2.1 Theoretical Model of an Axicon in RF for Linearly Polarized Fields 118
4.2.2 Numerical Results . . . 119
4.3 Meta-Axicon . . . 121
4.3.0.1 Unit-Cell Characteristics . . . 123
4.3.0.2 Unit-Cell Characterization . . . 124
4.4 Comparison Between the Meta-Axicon and Theoretical Model . . . 125
4.4.1 Phase Quantization . . . 127
4.5 Characteristics of Operation . . . 129
4.5.1 Design Limitations and Operation Zones . . . 129
4.5.2 Analysis of Beam Waist Characteristics . . . 137
4.5.3 Exploring Smaller Axicon Angles . . . 139
4.5.4 Feeding considerations . . . 141
4.6 Transmitter Realization . . . 142
4.6.1 Theoretical Model Results . . . 144
4.6.2 CST simulations . . . 145
4.6.3 Comparison of Theoretical and CST results . . . 147
4.6.4 Bandwidth Analysis . . . 149
4.6.5 Diffraction Analysis . . . 150
4.7 Conclusion . . . 154

4.1 Introduction

In this final chapter, our goal is to design a wireless transmitter based on an optical component known as axicon [42], which is widely used in optics to generate truncated Bessel beams. To replicate its properties, we have chosen an all-dielectric metasurface, referred to as "meta-axicon". We employ an analytical model to characterize the behavior of the meta-axicon and compare its results with those obtained using the commercial full-wave software CST Studio Suite (CST) [99], specifically analyzing the radiated fields. We also investigate the impact of the meta-axicon's illumination on the system's overall response.

In addition to designing and characterizing the meta-axicon using both analytical models and full-wave simulations, we investigate the limitations of generating truncated Bessel beams using axicons, highlighting different operational zones determined by the combination of axicon angle and aperture size. Finally, we evaluate the wireless power transfer efficiency (WPTE) of a system consisting of two identical, axially aligned launchers, under both unobstructed and obstructed conditions, and provide a comparison with existing launcher designs.

The development of the launcher was made possible through a highly successful collaboration with Thales Research and Technology (TRT). Not only did TRT propose the original concept and provide the metasurface, but they were also closely involved in every step of the design process, offering invaluable support in the analysis and interpretation of results. Furthermore, TRT conducted the full-wave simulations that provided key information to bridge theoretical analysis with practical implementation.

In its first section, the chapter begins by modeling the generation of a truncated Bessel beam utilizing an axicon modeled as a phase mask, and then it transitions to exploring metasurfaces, leading to the design of the meta-axicon using an all-dielectric metasurface. The next section further investigates the operational characteristics of meta-axicons. Then, we present the final design of a wireless transmitter operating at 30 GHz, featuring a rectangular horn antenna coupled with the meta-axicon, discussing the impact of non-ideal feeding conditions, the system's self-healing capability, and the influence of obstructions on WPTE. The conclusions are presented in the last section.

4.2 Axicon as a Phase Transformation

An axicon [42] is an optical component that, unlike conventional lenses, does not focus light to a single point. Several types of axicons exist, including linear axicons, logarithmic axicons, lenses with spherical aberration, toric lenses, narrow annular apertures, and Arago spots (Poisson spot) [100]. These components find numerous applications such as in alignment and triangulation, beam transformation, optical pumping of plasma, scanning optical systems, generation of truncated Bessel beams, and atom guiding [101].

In this chapter, we concentrate our analysis on the most widely studied variant, the linear axicon, which will hereafter be referred to simply as the 'axicon'. We examine its role in the generation of Bessel beams. The simplest axicon is a cone made of glass [102], depicted in figure 4.1. Modern applications, however, make use of diffractive axicons [103], which are gratings composed of circular fringes [104]. Figure 4.2 shows a diffractive axicon commercialized by Edmund Optics. Axicons also find applications in other frequency ranges, not only the optical regime. We can find examples in millimeter-wave [105] and Terahertz [23] frequencies.

In figure 4.1, an axicon composed of a dielectric cone is illuminated by a collimated [38] beam of light. Point A denotes the the apex of the axicon and α defines its wedge angle. A single ray, traveling from left to right, is shown to illustrate the behavior of the

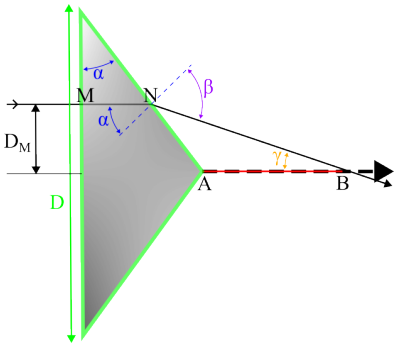

Figure 4.1 – Axicon composed of a cone made of glass with apex in the point A. A light beam, represented by a single ray, travels from left to right and is refracted by the axicon, crossing the optical axis at point B. Adapted from [106].



Figure 4.2 – Diffractive Axicon HOLO/OR sold by Edmund Optics company.

entire beam. The ray enters the axicon and exits at point N, where it is refracted by the axicon at an angle γ relative to its initial direction. The ray then crosses the optical axis at point B. The line segment $\overline{AB}$ can be calculated as

$$\overline{AB} = D_M\left(\tan\gamma - \tan\alpha\right) \tag{4.1}$$

where D_M is the distance between point M and the axis of the axicon. The angles γ and α are related to each other and to β according to

$$\sin\beta = n\sin\alpha \tag{4.2}$$

$$\gamma + \beta = \frac{\pi}{2} + \alpha \tag{4.3}$$

where n represents the refractive index of the material composing the axicon. Equation 4.1 can be simplified provided that $\alpha < 10°$, yielding [106]

$$\overline{AB} \approx \frac{D_M}{\alpha(n-1)}. \tag{4.4}$$

The maximum $\overline{AB}$, denoted by L, achieved by the rays of the light beam diffracted

by the axicon can be calculated with the aid of equation 4.4 as

$$L \approx \frac{D}{2\alpha(n-1)} \tag{4.5}$$

where D is the diameter of the axicon and L is called by some authors as focal line [101, 102] or length of the focal range [100]. In the context of this project, L will be defined as the non-diffractive range (NDR) of the axicon, because it represents the distance along the optical axis over which a Bessel beam generated by an axicon maintains its shape and does not diffract significantly.

Let's further investigate the axicon by approximating the dielectric cone as a phase transformation [54] within a wave-optics framework. In this context, the axicon is treated as an plane screen [38] that introduces a phase delay to the incident wave as it passes through. Consequently, the axicon will be represented by a multiplicative phase transformation [54], t_a. This approximation is crucial to our analysis, as one of our objectives is to design a metasurface that mimics the behavior of an axicon. Figure 4.3 depicts the axicon as a phase screen. Again, a single ray, traveling from left to right, is used to illustrate the whole field.

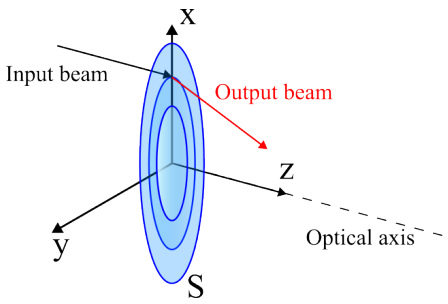

Figure 4.3 – Circular phase screen representing the axicon. An incident field, represented by a single ray, travels from left to right and is refracted by the axicon.

Figure 4.4 represents the operation of the axicon, within our context. The relationship between the incident field, $\vec{A}_i$, on the plane of the axicon and the field, $\vec{A}_o$, transmitted by the axicon is written as [54]

$$\vec{A}_o = t_a \vec{A}_i \tag{4.6}$$

where t_a represents a linear phase profile, with respect to the coordinate $\rho = \sqrt{x^2 + y^2}$, written as

$$t_a = e^{-jk_0\rho\sin\theta_a}, \qquad \rho \leq r_a. \tag{4.7}$$

Here, k_0 is the operating wavenumber and θ_a is the axicon angle. In figure 4.4, the interference zone is put in evidence. This is the region where the Bessel beam is

observed [100–102, 107]. Finally, the NDR, highlighted in red, can be obtained by

$$\text{NDR} = \frac{R_a}{\tan\theta_a} \tag{4.8}$$

where R_a is the axicon radius.

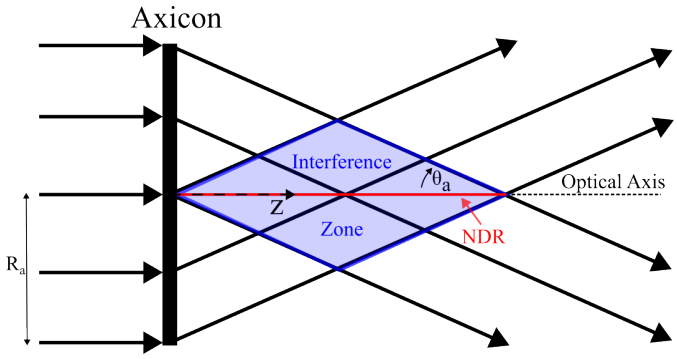

Figure 4.4 – Axicon. Ray diagram showing its operation. Rays come from the left, hitting the axicon at $z = 0$, that generates the interference region (in blue) limited by the NDR highlighted in red. Adapted from [102].

4.2.1 Theoretical Model of an Axicon in RF for Linearly Polarized Fields

The axicon approximation presented before is employed to develop a model for generating Bessel beams in the RF domain. In this model, a linearly polarized Bessel beam is generated by imposing a tangential electric-field distribution over a circular aperture. This field distribution is characterized by a Gaussian amplitude profile multiplied by the axicon phase function. Therefore, the tangential electric field writes

$$\vec{E}_t(x, y, z = 0) = Ae^{-((x^2+y^2)/w_0^2)}e^{-j\phi}\hat{x}, \qquad \rho \leq r_a \tag{4.9}$$

where A represents the amplitude factor, w_0 is the Gaussian waist, r_a is the radius of the aperture, $\hat{x}$ is the unitary vector in the x direction, $\rho = \sqrt{x^2 + y^2}$, and the linear phase profile is represented by ϕ. In our model, the Gaussian waist is defined in such a way to provide a 10 dB field intensity drop at the edges of the aperture thus reducing the effect of diffraction. Therefore, w_0 is defined as

$$w_0 = \frac{r_a}{\sqrt{\ln 10}} \tag{4.10}$$

where 'ln' represents the natural logarithm. The variable ϕ is written as function of ρ, yielding

$$\phi(\rho) = \rho k_0 \sin\theta_a \tag{4.11}$$

To calculate the NDR in this case, we need to take into account that the surface of the radiating aperture (axicon) is not uniformly illuminated. Therefore, equation 2.7 needs to be adapted considering the waist of the amplitude of the Gaussian distribution over the aperture. The NDR then is written as [108]

$$\text{NDR} = w_0\sqrt{\left(\frac{k_0}{k_0\sin\theta_a}\right)^2 - 1} = \frac{w_0}{\tan\theta_a} \tag{4.12}$$

The radiated beam is expected to have a null-to-null transverse spot size, denoted as S_p, which is given by [109]

$$S_p = \frac{\lambda j_{01}}{\pi\sin\theta_a} \tag{4.13}$$

where $j_{01} = 2.405$ is the first zero of the Bessel function $J_0(\cdot)$. The region limited by S_p defines a central core that is assumed to be propagation-invariant [108] within the NDR, for a system operating in the optical domain.

4.2.2 Numerical Results

Figure 4.5 shows the radiated fields calculated by theoretical model. The radiating aperture is positioned at the origin of the coordinate system, in the plane $z = 0$. The aperture radius is $r_a = 7.5\,\text{cm}$, $\theta_a = 13°$, and the system operates at 30 GHz. In figures 4.5a and 4.5b, we depict the normalized amplitude of the tangential electric field radiated by the axicon in the plane xz and along the axis z respectively. The computed NDR equals 21 cm. It is evident that the field exhibits greater intensity in the range from $z = 5\,\text{cm}$ to $z = 21\,\text{cm}$, corresponding to our focal line, where we observe a Bessel-like field pattern.

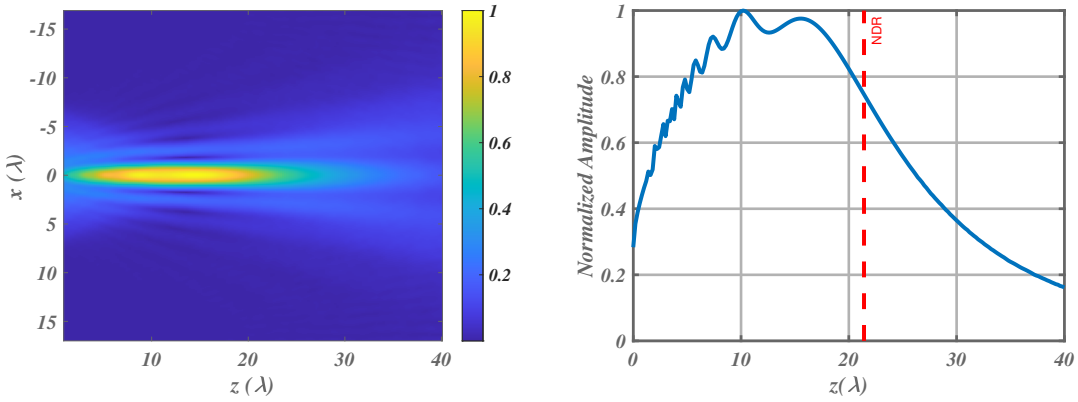

(a) (b)

Figure 4.5 – Normalized $|E_x|$ radiated by the axicon. In (a), we show the radiated field in the plane xz, while in (b), the radiated field along z-axis is presented.

Figure 4.6, shows the normalized amplitude of the tangential electric field in different z planes. In figure 4.6a, $z = 10\,\text{cm}$, while in figure 4.6b, $z = 20\,\text{cm}$. We notice the bright spot characteristic of the Bessel beam, as well as its secondary lobes. The beam is normalized by its maximum on the axis z. Furthermore, we notice that the central lobe has the same spot size in both z planes, defined by the dashed black circle. At $z = 20\,\text{cm}$, the peak intensity of the beam is approximately 80% of the maximum observed along the z-axis, whereas at $z = 10\,\text{cm}$, the peak intensity reaches nearly 100% of the maximum along the same axis.

This observation leads us to conclude that the amplitude of the radiated beam decreases even within NDR. The primary reason for this, as discussed earlier in this thesis, is that the NDR is calculated under the assumption that the system operates in the optical domain, where apertures are very electrically large. In radio frequency (RF) applications, however, the apertures are smaller relative to the wavelength, and the effects of truncation are more pronounced, resulting in deviations from the ideal behavior predicted by optical models.

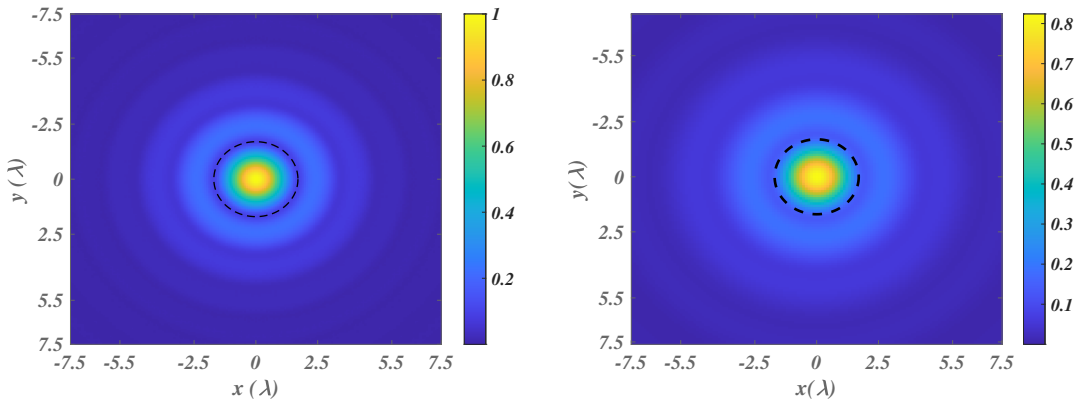

(a) (b)

Figure 4.6 – Amplitude of normalized $|E_x|$ radiated by the axicon in different z planes. In (a), $z = 10\,\text{cm}$, while in (b), $z = 20\,\text{cm}$. The dotted black circle delimits the null-to-null transverse spot size S_p.

Figure 4.7 shows the amplitude profile of the tangential electric radiated field ($y = 0$), at different plans z, normalized by its maximum amplitude on the z-axis. The amplitude of a Bessel function $J_0(\cdot)$ with similar k_1 is also presented for comparison purposes. Again, we can observe the amplitude peak difference between $z = 10\,\text{cm}$ and $z = 20\,\text{cm}$. We also observe that the null-to-null spot size of the radiated beam aligns with that of the Bessel function. However, the side lobes of the beam differ from those of the ideal Bessel function, exhibiting lower intensity and a shift in the position of the points that should correspond to zero intensity.

Finally, figure 4.8 presents the profile of the normalized spectral content of the tangential electric radiated field ($k_y = 0$), where we can see the two peaks characteristic of the Bessel beam, centered around the transverse wave number, k_1. Notably, the

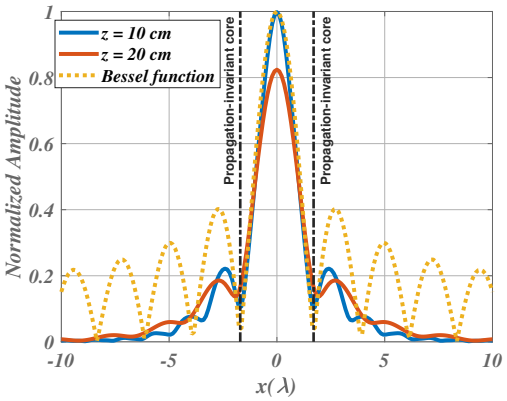

Figure 4.7 – Normalized amplitude profile of the tangential electric radiated field at different plan z and $y = 0$. The orange curve represents the Bessel function $J_0(k_1 x)$.

spectral content is mostly concentrated in the region $|k_x/k_0| < 0.5$. Furthermore, we observe that differently from the radiated $J_1(\cdot)$ in the previous chapter, the spectral content of the radiated $J_0(\cdot)$ does not present a zero at $k_x = 0$, but rather a peak that reaches up to 43% of the maximum amplitude.

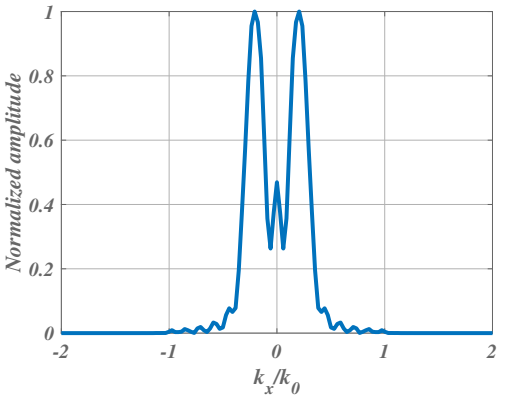

Figure 4.8 – Normalized amplitude profile of the spectral content of tangential electric radiated field for $k_y = 0$.

4.3 Meta-Axicon

Metasurfaces are artificial structures composed of sub-wavelength elements, designed to induce abrupt changes in the electromagnetic properties of incident waves, enabling control over their phase, amplitude, and polarization [110]. They are considered planar components, as their thickness is generally very small compared to their effective surface area [111]. In this work we use a metasurface to replicate the effects

of the axicon, justifying the term meta-axicon. Due to their low profile and low-loss properties [112], meta-surfaces have been used in many applications such as antenna design [113–115] and wavefront manipulation [116].

A metasurface is composed of a collection of subwavelength cells, that can be arranged in periodic or nonperiodic arrays. According to Huygens' principle[54], each cell generates a wave packet at the metasurface-air interface when exposed to incident electromagnetic waves. The collective wave packets produced by all the metasurface elements combine to form the transmitted electromagnetic wavefront [117, 118]. The simplified diagram of a generic metasurface is depicted in figure 4.9, where the brown circles are the metasurface's cells.

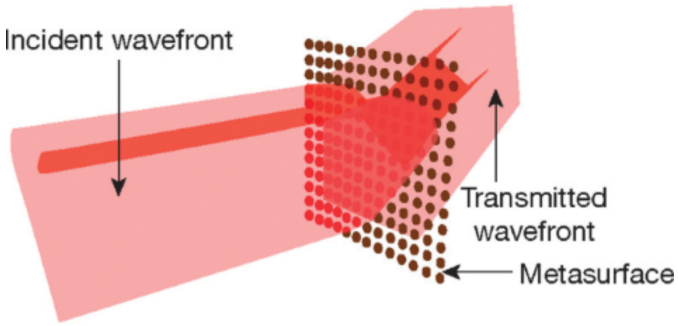

Figure 4.9 – Metasurface showing wavefront transformation [119].

The metasurface selected to replicate the properties of the axicon is a quasi-periodic all-dielectric circular metasurface comprising pillar structures [44], provided by Thales Research & Technology. Schematics of the metasurface are presented in figures 4.10 and 4.11, where we show its top and lateral views respectively. The required phase profile of the transmitted fields is achieved by structuring the material at a sub-wavelength scale (radius of the pillar).

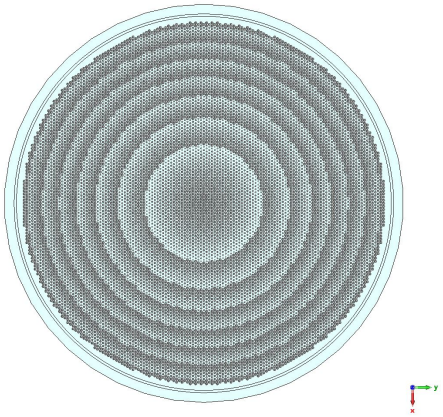

Figure 4.10 – Top view of the meta-axicon, plan xy.

This metasurface is fully 3D-printed by FDM (Fused Deposition Modelling) technique [120] with a high-permittivity dielectric material. Furthermore, it is designed to

operate in the Ka band. The Ka band (26.5 GHz–40 GHz) is part of the K-band and is primarily used for satellite communications.

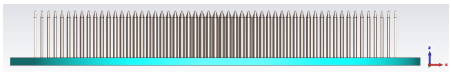

Figure 4.11 – Lateral view of the meta-axicon, plan ZX.

4.3.0.1 Unit-Cell Characteristics

The unit-cell of the meta-axicon is a pillar arranged in a hexagonal grid of 2.6 mm pitch. The pillar elements are made with a high permittivity material (up to $\epsilon_r = 8.8$, and $\tan\delta = 0.001$), whose reflection level is reduced by the conical tip with a height of 2.5 mm. The pillars are mechanically supported by a 5 mm thick plate made with a low permittivity material ($\epsilon_r = 2.3$, $\tan\delta = 0.001$). This plate thickness is adjusted to minimize reflection level at the operation frequency.

Typically, in a single metasurface, the unit cells have several common properties, with only one or two differing characteristics to introduce varying phase shifts [121]. In our design, the unit-cells have the same value for size, substrate thickness and pillar height. In figure 4.12, the unit cell is depicted. We can notice the substrate in light blue and the pillar with its conical tip in gray. Each pillar is characterized by the ratio of its diameter (d_c) to the unit cell size (l_c), referred to as the fill factor $\tau = d_c/l_c$.

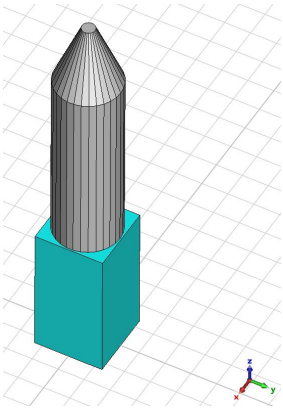

Figure 4.12 – Meta-axicon's unit cell

The pillar material is based on COC-TiO_2 composite, which is a cyclic olefin copolymer (COC) matrix loaded with titanium oxide (TiO_2). This material was developed by [122] and is currently commercialized by a company called NANOE. It possess a low loss tangent, $\tan\delta = 1.10^{-3}$ at 30 GHz, high permittivity (up to $\epsilon_r = 8.8$) and a high glass-transition temperature, $T_g = 130°$. Additionally, this material is also recyclable, which makes it also interesting in an environmental perspective. A special particular 3D-printing process is used, detailed in [44], which allows for a resolution of 0.7 mm, quasi-zero porosity, reduced printing time and also the possibility of locally repairing damaged areas.

4.3.0.2 Unit-Cell Characterization

The characterization of a unit cell is now presented to illustrate its response. The unit cell was simulated in CST using periodic boundary conditions [123] to truncate the simulation space in the x and y directions. These conditions approximate the behavior of the structure by assuming the cells are identical. The simulation results correspond to pillars with three different radii (r_p), all of the same height of $h = 15.5\,\text{mm}$ (including the conical tip) and the same permittivity ($e_\text{r} = 7.5$), under normal incidence. In figure 4.13 the amplitude and phase of the unit cell's transmission coefficient is shown.

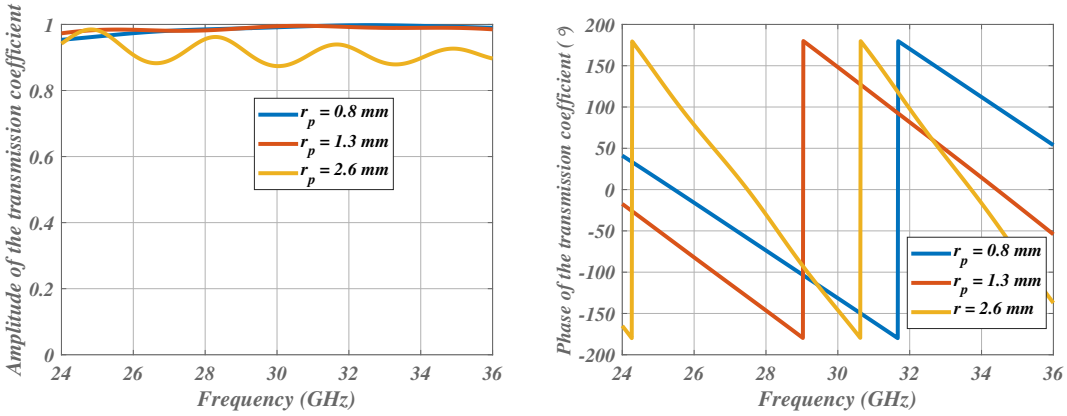

(a) (b)

Figure 4.13 – Amplitude (a) and phase (b) of the unit cell's transmission coefficient as a function of the frequency for fixed height $h = 15.5$ and variable r_p (pillar radius).

The amplitude of the unit cell's transmission coefficient is presented in figure 4.13a, while its phase is shown in figure 4.13b. For $r_p = 0.8\,\text{mm}$ and $r_p = 1.3\,\text{mm}$, the amplitude is almost stable for the range studied, with a small drop of around 3% for frequencies smaller than 27 GHz. When $r_p = 2.6\,\text{cm}$, we notice some oscillations due to resonance. However, the amplitude is not reduced more than 15%, highlighting the low-loss nature of the unit cell. Furthermore, we observe that the phase is highly sensitive to changes in frequency, with unit cells featuring larger pillars being more affected by frequency variations. This indicates that our system is optimized for narrowband performance.

While in practice the cells have pillars with varying diameters (though the height remains constant), the use of periodic boundary conditions is justified due to its ability to significantly reduce simulation complexity and computational resource requirements. Moreover, this approach provides an accurate characterization of the cell, as long as the variations in diameter between adjacent cells are kept minimal during the fabrication of the metasurface. In our design, the maximum phase range $\Delta\phi$ achievable with a pillar of fixed length L can be estimated by

$$\Delta\phi = k_0 L\left(\tau_\text{max}\sqrt{\epsilon_r} - 1\right) \tag{4.14}$$

where L is the height of the pillar, $\tau_{\max}$ is the maximum fill factor, and ϵ_r is the permittivity of the material of the pillar.

According to equation 4.11, the maximum phase variation required for circular axicon of radius r_a is $\Delta\phi_{max} = r_a k_0 \sin\theta_a$. Therefore, if $\Delta\phi_{max} \leq \Delta\phi$, phase wrapping will be avoided. Phase wrapping occurs when the required phase shift exceeds 2π, causing the phase to "wrap around" back to zero. This effect is undesirable because it indicates that there are significant discrepancies in the diameter of some adjacent cells throughout the metasurface. Consequently, the periodic boundary conditions used in simulations may become inaccurate, undermining the precision of the results.

4.4 Comparison Between the Meta-Axicon and Theoretical Model

In this section, we compare the results of our theoretical model with those obtained using the commercial full-wave software CST, specifically analyzing the radiated fields. The goal is to verify the accuracy and applicability of our model, which consumes way less computational resources than the full-wave simulation.

The simulations were performed for a system operating at 30 GHz, $\lambda = 1$ cm, with an aperture radius of 7.5λ, and an axicon angle $\theta_a = 13°$. In CST, the meta-axicon is also illuminated by a Gaussian beam amplitude whose waist is located on its lower interface, providing a tapered amplitude profile with 10 dB field intensity drop on the edge. Furthermore, the results were obtained assuming an hexagonal mesh and the unit cell characteristics are: pitch 2.6 mm, pillar height $h = 15.5$ mm and permittivity $\epsilon_r = 8.5$. In CST, we conducted the simulations using the Transient Solver, which operates based on the Finite Integration Technique (FIT), a core method of the Time Domain Solver. The results are presented in figures 4.14 and 4.15.

The amplitude of the radiated tangential electric fields along the z axis, ($x = y = 0$), is shown in figure 4.14a. Each field is normalized by its own maximum. We observe a good agreement between the field generated by the ideal aperture and the one obtained with the meta-axicon. The observed differences are due to the slight imperfections of the meta-axicon aperture field, resulting mainly from its discretized character, and the paraxial approximation used to calcualted the fields in the theoretical model. Also, we can notice that the field amplitude is maximum at $z = 15$ cm and it reaches 50% of this value at $z = 25$ cm.

The normalized spectrum of the tangential electric field over the radiating aperture is presented in figure 4.14b. Both the theoretical and simulated results exhibit peaks around $k_x/k_0 = 0.20$, and there is a strong agreement between them. At $k_x = 0$, the peak of the simulated field is 8% higher than the theoretical one. Additionally, we observe that the intensity of the ripples in the region $|k_x/k_0| < 0.5$ is higher in the simulated results compared to the theoretical results (maximum difference of 5%).

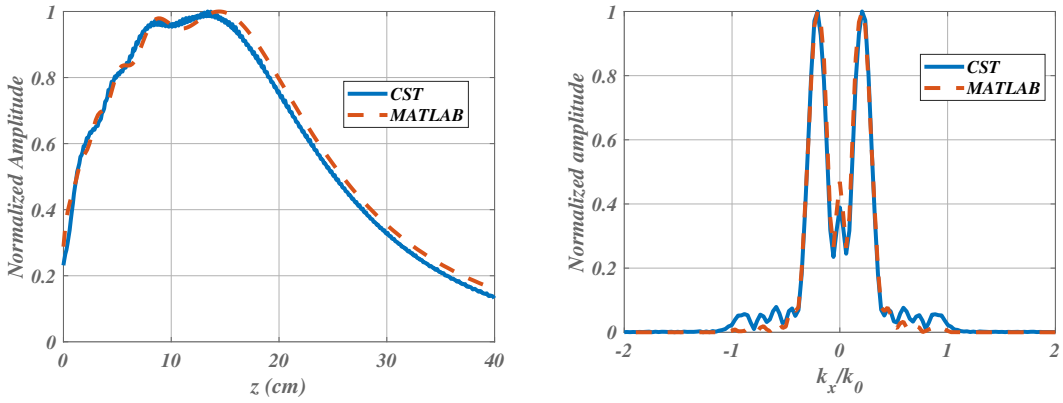

(a) (b)

Figure 4.14 – Comparison of the tangential electric field from CST and from the theoretical model. In (a) the normalized amplitude along the z-axis is presented, and in (b) the normalized spectral content over the radiating aperture is compared.

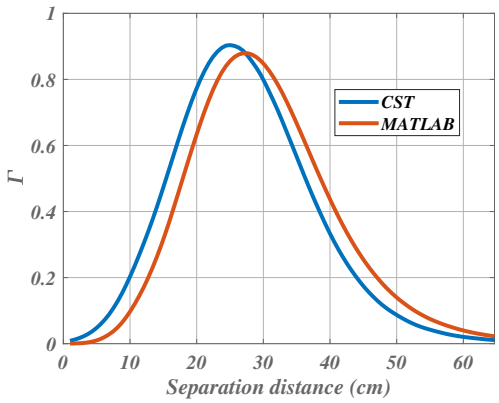

Figure 4.15 – Comparison of the WPTE as a function of the separation distance, from CST and theoretical model

In figure 4.15, the WPTE which would characterize a link between two meta-axicons facing each other is depicted. This efficiency is computed under the assumption of two identical and axially aligned apertures, referred to as emitter and receiver. To obtain the WPTE of the meta-axicon simulated using full-wave software, the tangential electric fields over the apertures were extracted from the commercial full-wave software, and a MATLAB routine was developed. This procedure is presented schematically in figure 4.16. Again, the theoretical and simulated results demonstrate a strong concordance, and the offset observed between them is due to the slight aperture field differences between the two. We notice a focusing behavior on the WPTE, with a maximum of 90% at $z = 25\,\text{cm}$ for the simulated results, and 88% at $z = 27\,\text{cm}$ for the theoretical results. Furthermore, we observe that the efficiency remains higher

than 50% in the region 15 cm $\leq z \leq$ 36 cm, which represents 30% of the maximum separation distance considered.

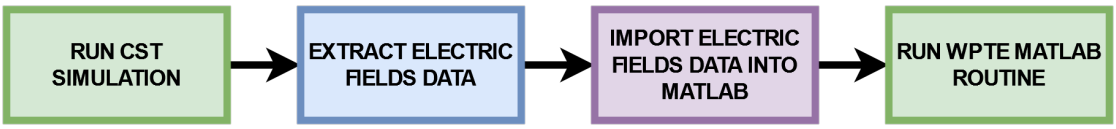

Figure 4.16 – Flowchart illustrating the process used to calculate the WPTE from the CST simulation.

4.4.1 Phase Quantization

Studying phase quantization in our theoretical model is essential because practical metasurfaces are fabricated with quantized or staircased phase variations, unlike the continuous linear variation assumed in our model. This discretization can affect performance parameters such as efficiency and beam shape. Therefore, understanding phase quantization is crucial for accurately predicting real-world behavior and optimizing metasurface design.

For the study of the effect of discretization into the phase variation of the transmitted field we consider a squared metasurface cell of 2.6 mm, frequency $f = 30$ Ghz, aperture radius $r_a = 7.5\lambda$ and axicon angle $\theta_a = 13°$. The maximum phase value occurs at the rim of the aperture and can be expressed as follows: $\phi_{max} = r_a k_0 \sin\alpha$. In our case, $\phi_{max} = 10.6$ rad.

Our objective is to determine the minimum required number of levels that render acceptable results in terms of radiated fields. Figure 4.17 depicts the comparison between the continuous phase variation and a phase quantization scheme considering 5 levels that presents abrupt phase changes due to quantization.

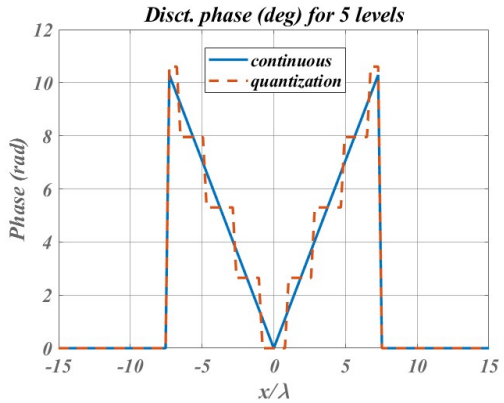

Figure 4.17 – Comparison between the continuous and the staircased phase variations for 5 levels.

Figures 4.18 and 4.19 present, respectively, the radiated tangential electric field along the z-axis ($x = y = 0$) and the phase distribution over the aperture for various

quantization levels ($n = 5, 10, 15$, and 20). In figure 4.18, the calculated fields are compared with CST data. For $n = 5$, the results are not satisfactory, exhibiting strong oscillations in the region $0 \leq z \leq 10$ and unexpected field amplitudes. At $n = 10$, oscillations are still present near the aperture, but the field amplitude presents the expected behavior after $z = 18\lambda$, showing good agreement with CST results. For $n = 15$, minor oscillations are observed near the aperture, but the overall amplitude profile aligns well with CST results. Starting from $n = 20$, the model and CST results show good agreement, with minimal differences in amplitude.

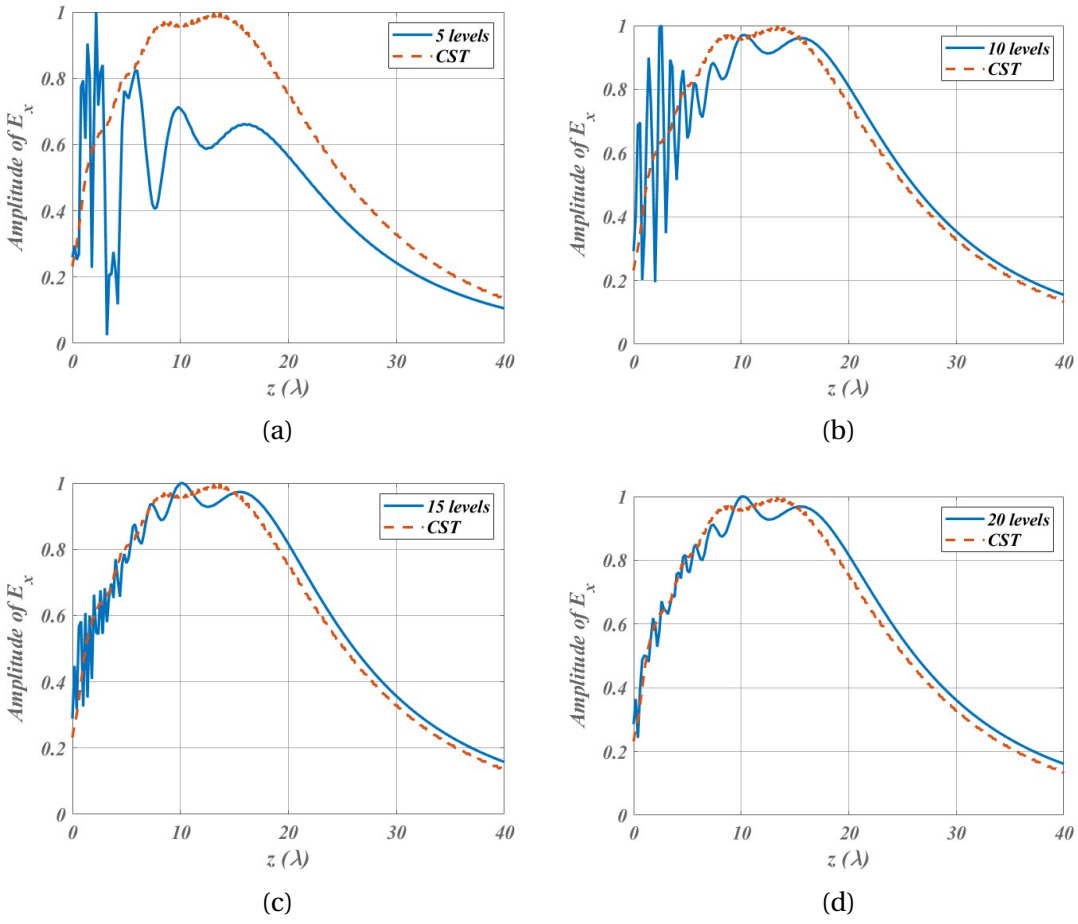

Figure 4.18 – Normalized tangential electric field amplitude along z-axis for different quantization level n: (a) $n = 5$, (a) $n = 10$, (a) $n = 15$, and (d) $n = 20$.

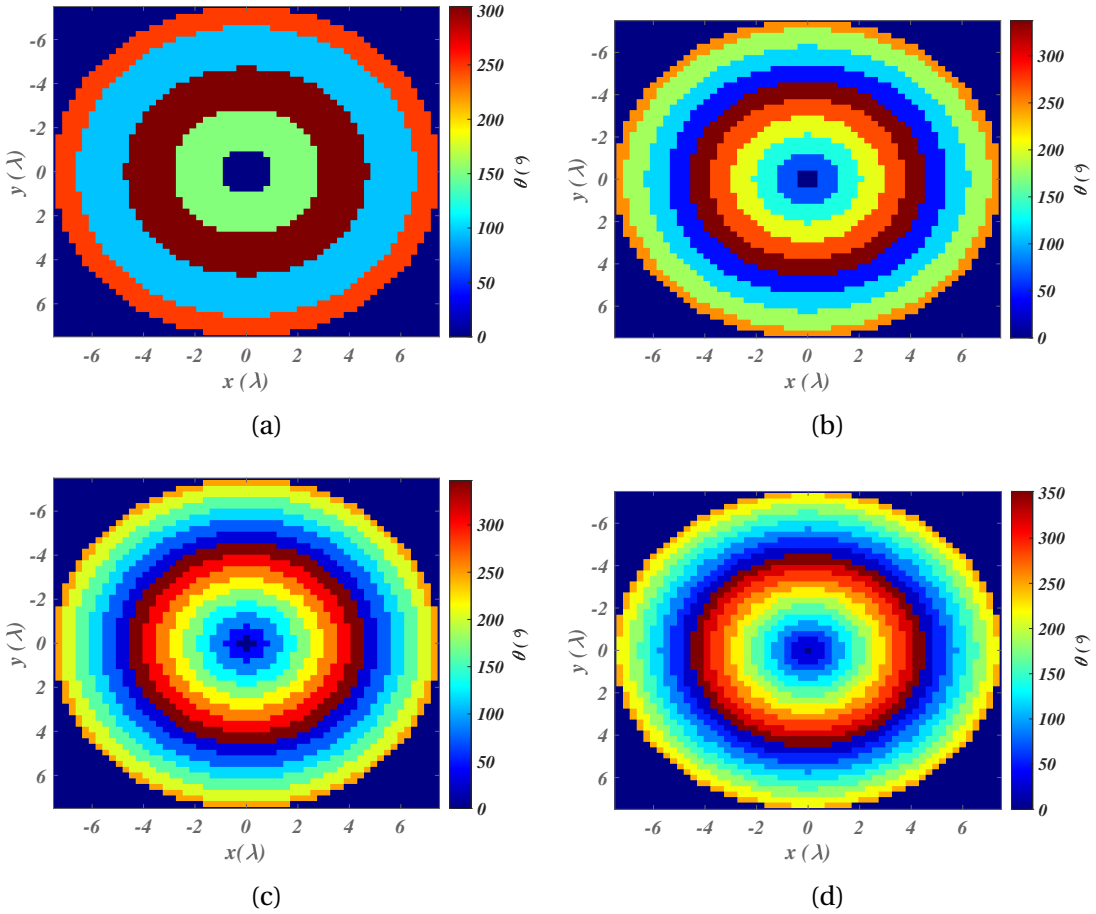

Figure 4.19 – Phase distribution over the radiating aperture for different quantization level n: (a) $n = 5$, (a) $n = 10$, (a) $n = 15$, and (d) $n = 20$.

4.5 Characteristics of Operation

4.5.1 Design Limitations and Operation Zones

According to [109], for a finite aperture, the minimum axicon angle that produces a truncated Bessel beam, is given by

$$\theta_{min} = \arcsin \frac{\lambda j_{01}}{2\pi r_a} \tag{4.15}$$

where $j_{01} \simeq 2.405$ is the first zero of the Bessel function of the first kind and zeroth order. This criterion is based on the principle that the null-to-null transverse spot size must be small enough to fit within the physical dimensions of the aperture responsible for its radiation. Considering $r_a = 7.5\,\text{cm}$ and $f = 30\,\text{GHz}$, the calculated minimum angle is $\theta_{min} = 2.93°$. This approach is very interesting but does not take into account the spectral content of the generated beam. Therefore, we decided to derive a numerical

metric that could also include the spectral behavior expected for a Bessel beam.

The most distinguishable feature of the spectral content of a Bessel beam is its ring-like shape, characterized by two amplitude peaks when $k_y = 0$ or $k_x = 0$. According to equation 4.9, if $\theta_a = 0$, the distribution over the aperture is simply Gaussian. The spectral content profile of a Gaussian distribution is shown in figure 4.20, where we can see that its amplitude profile presents a single peak.

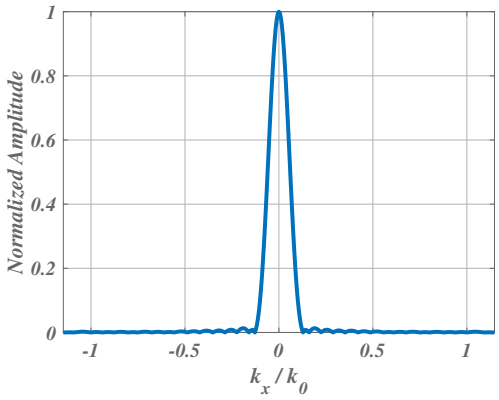

Figure 4.20 – Normalized spectral content profile of Gaussian distribution, $k_y = 0$.

As we increase θ_a, the Gaussian spectrum gradually transitions to that of a truncated Bessel beam, as shown in figure 4.21, where the normalized amplitude of the spectral content of the tangential electric field over the radiating aperture, $z = 0$, for different axicon angles, is presented. The amplitude is normalized by the maximum amplitude when $\theta_a = 0°$.

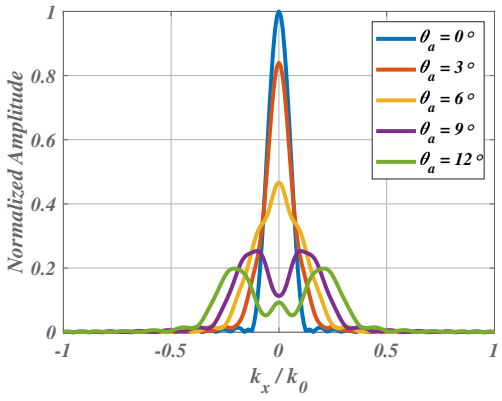

Figure 4.21 – Normalized spectral content of the tangential electric field over the axicon aperture with $k_y = 0$, for different axicon angles θ_a.

Consequently, there is a limiting θ_c that separates these two spectral behaviors, Gaussian and Bessel. We determined this angle numerically, identifying it as minimum θ_a where the maximum amplitude is no longer located at $k_x = k_y = 0$. Figure 4.22

depicts θ_c as a function of the diameter of radiating aperture. We notice that according to this metric, $\theta_c = 7.33°$ for $r_a = 7.5\,\text{cm}$, which is greater than the limit proposed in [109].

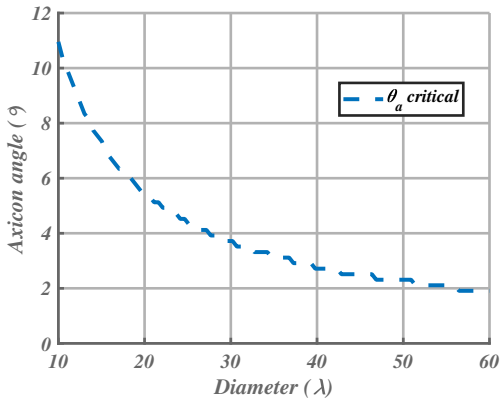

Figure 4.22 – Critical θ_a as a function of the diameter of the aperture and axicon angle.

Figure 4.23 shows the distance d_w for which the WPTE between two identical axially aligned meta-axicons drops to 50% after its maximum as a function of the axicon angle and the diameter of the aperture. The colorbar represents d_w in terms of the wavelength. Also, the dashed purple curves are contour lines which also represent d_w in terms of λ. The chart is divided in 4 regions. Zone 1 represents the region where the combination of the angle-diameter pair produces a beam with the spectrum of a Bessel beam and it is limited by the θ_c curve on white and by the technological constraint (red) on the right.

Its is important to mention that the technological limit is fluid, so we can perhaps build a prototype that works on zone 2, where we also have a Bessel beam spectrum. In zones 3 and 4 we observe that the beam generated does not present the spectral content of a Bessel beam. The difference between zones 3 and 4 is that the latter is beyond our technological limit.

Figure 4.24 shows the WPTE as a function of the aperture diameter and axicon angle, for different plans z. Each plot contains also the θ_c curve. We can notice that the θ_c curve clearly separated two WPTE regimes with its two own maximum efficiency levels. Finally, figures 4.25-4.28 shows the WPTE, the tangential field radiated along z and the spectrum of a beam generated in zone 1, 2, 3 and 4.

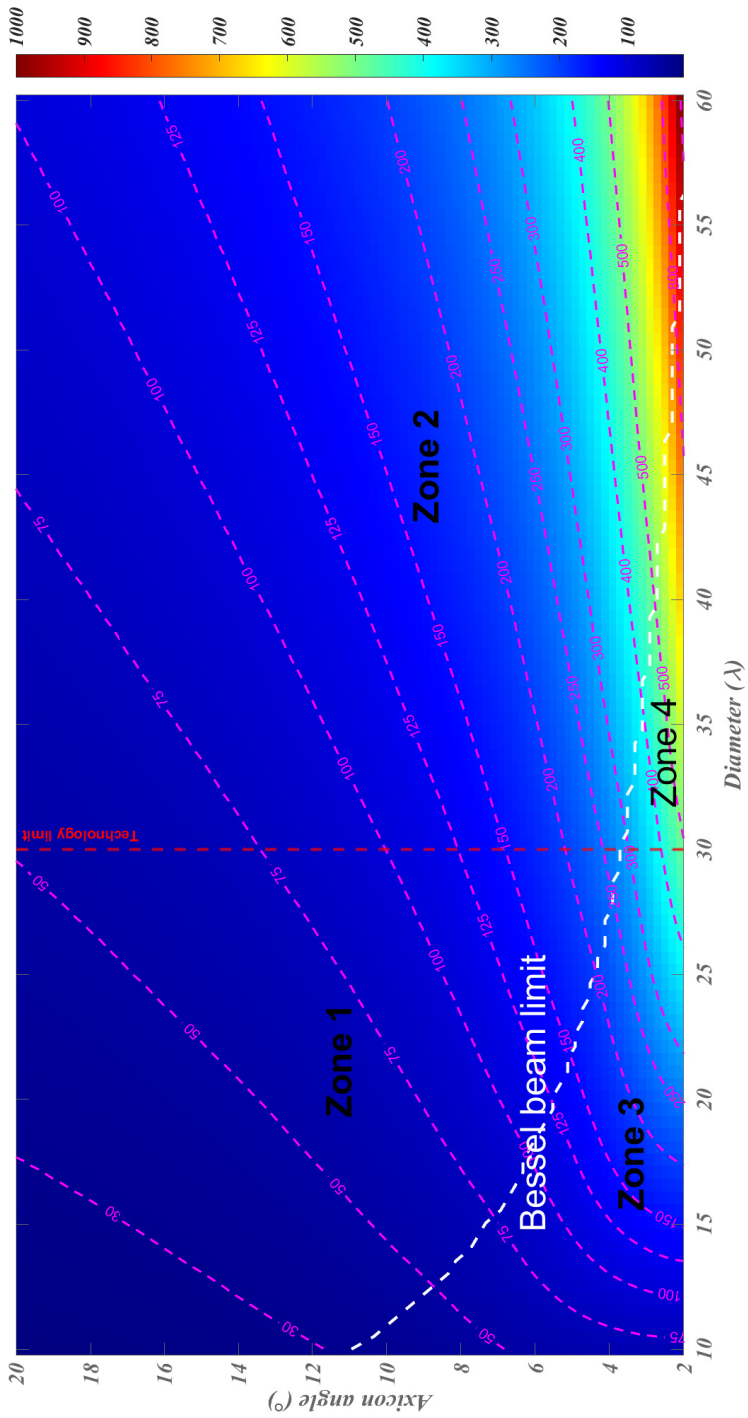

Figure 4.23 – Distance where the WPTE drops to 50% after its maximum value as a function of the axicon angle and aperture diameter. Four zones are depicted relating the technological limit and θ_c.

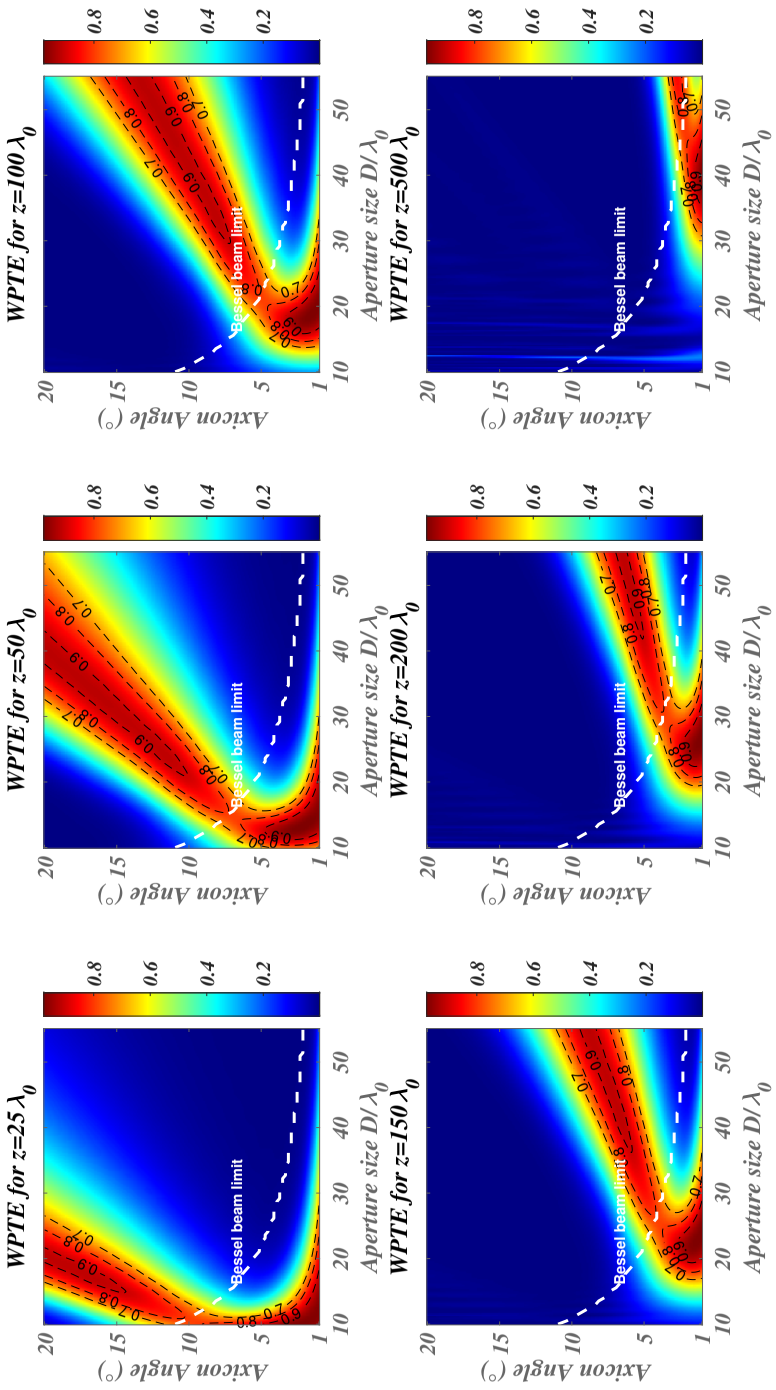

Figure 4.24 – WPTE as a function of the axicon angle and aperture diameter for different z planes. The θ_c line presented separating the two regimes of operation.

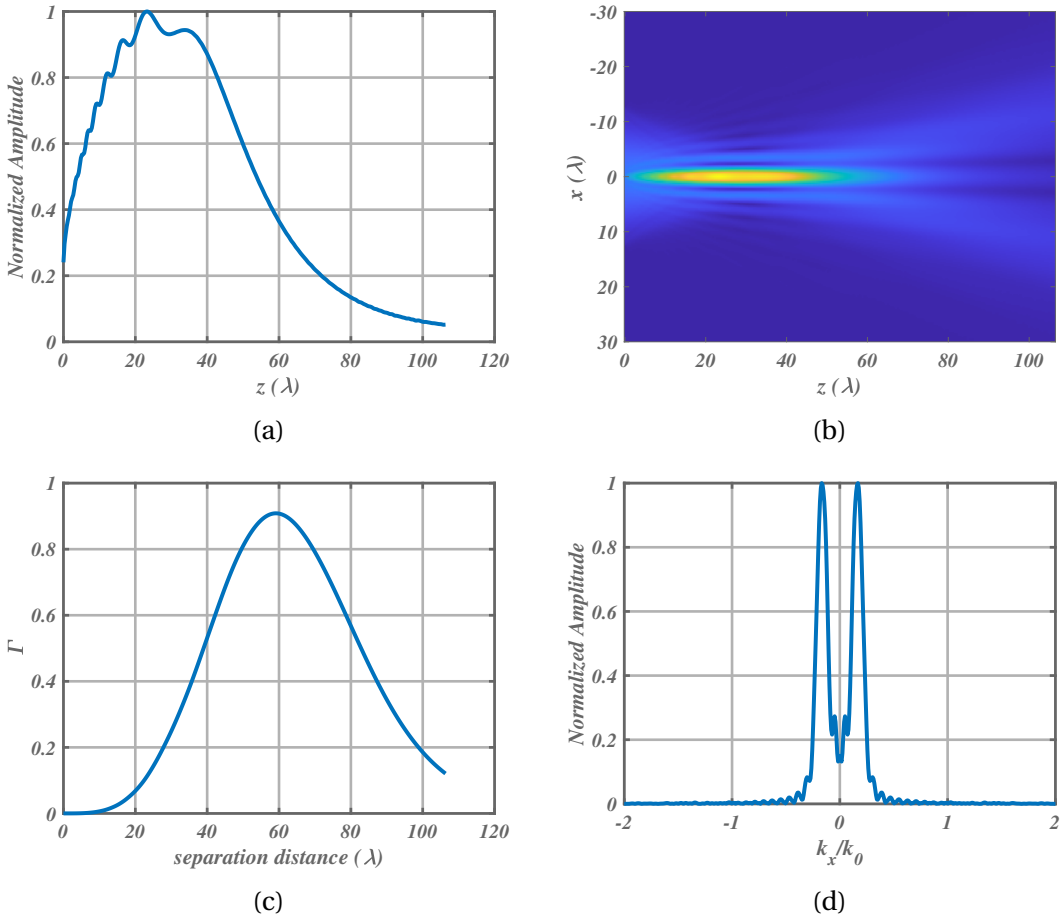

Figure 4.25 – Meta-axicon operating in zone 1, $D = 25\lambda, \theta_a = 10°$. In (a), normalized $|E_x|$ along z-axis, in (b) normalized $|E_x|$ in the plane xz, in (c), the WPTE as a function of the separation distance, and in (d), the normalized amplitude of the spectrum of $|E_x|$ with $k_y = 0$.

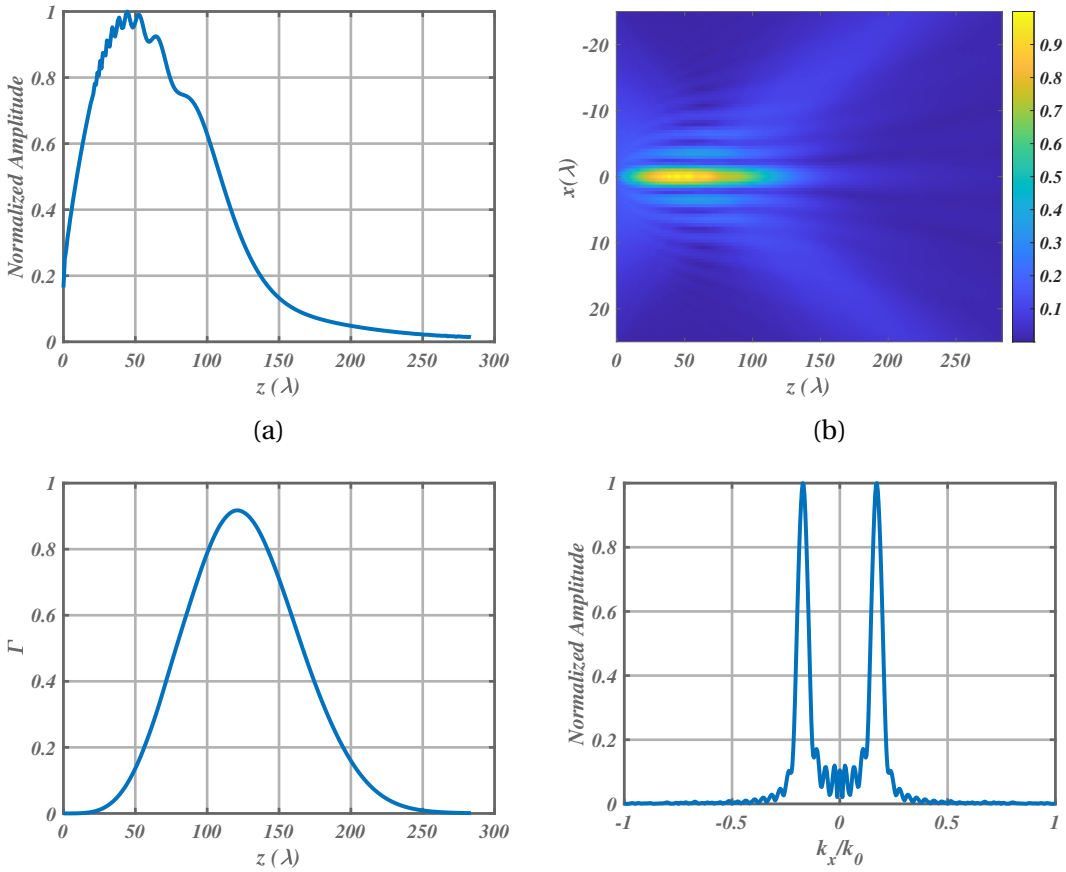

Figure 4.26 – Meta-axicon operating in zone 2, $D = 50\lambda, \theta_a = 10°$. In (a), normalized $|E_x|$ along z-axis, in (b) normalized $|E_x|$ in the plane xz, in (c), the WPTE as a function of the separation distance, and in (d), the normalized amplitude of the spectrum of $|E_x|$ with $k_y = 0$.

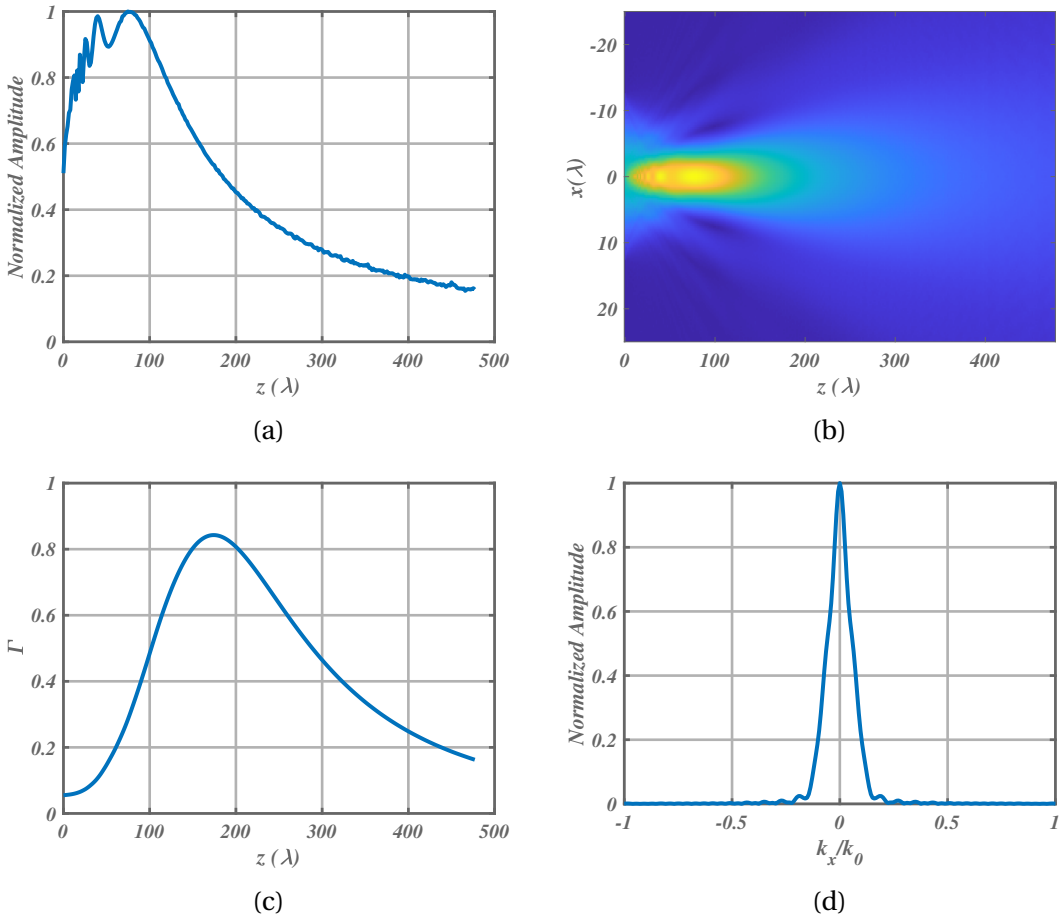

Figure 4.27 – Meta-axicon operating in zone 3, $D = 25\lambda, \theta_a = 3°$. In (a), normalized $|E_x|$ along z-axis, in (b) normalized $|E_x|$ in the plane xz, in (c), the WPTE as a function of the separation distance, and in (d), the normalized amplitude of the spectrum of $|E_x|$ with $k_y = 0$.

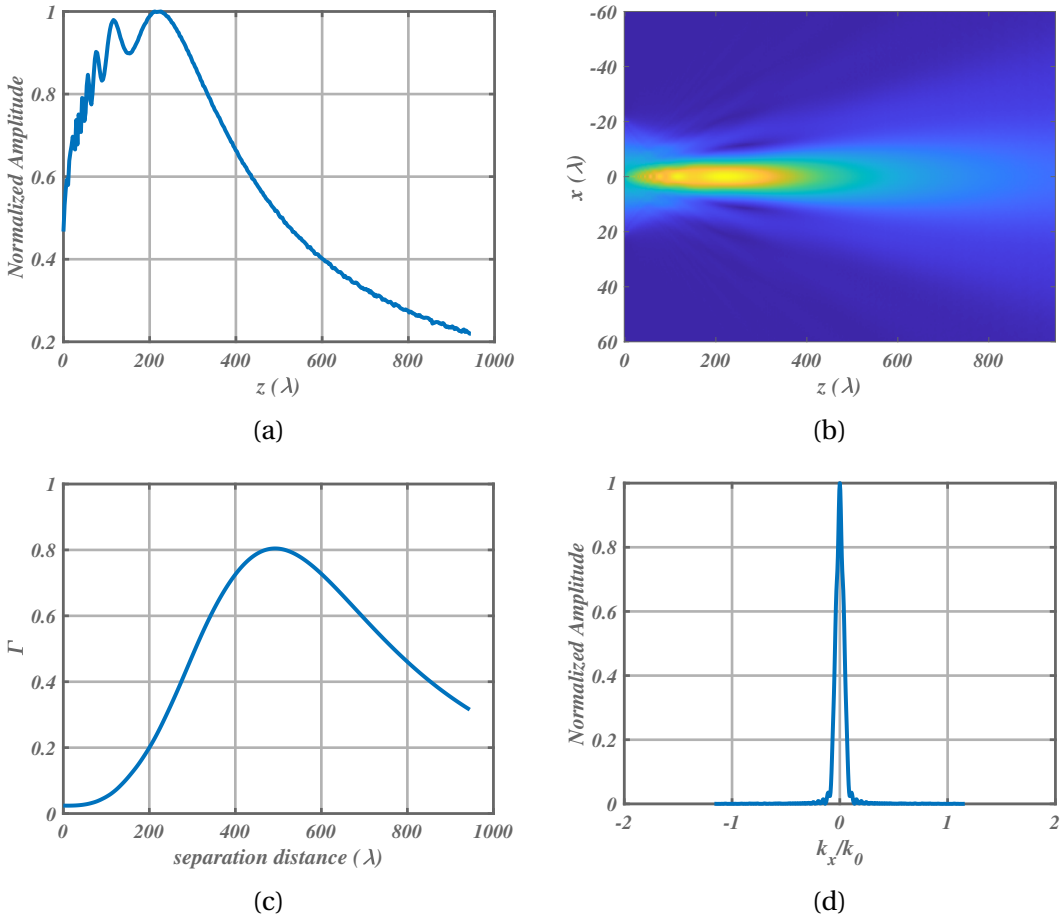

Figure 4.28 – Meta-axicon operating in zone 4, $D = 44\lambda, \theta_a = 2°$. In (a), normalized $|E_x|$ along z-axis, in (b) normalized $|E_x|$ in the plane xz, in (c), the WPTE as a function of the separation distance, and in (d), the normalized amplitude of the spectrum of $|E_x|$ with $k_y = 0$.

4.5.2 Analysis of Beam Waist Characteristics

When comparing Bessel and Gaussian beams, it is important to establish parameters for proceeding with a fair comparison. Initially, our analysis is based on the waist of both beams. The waist of the Gaussian beam is a classical quantity while the Bessel beam waist can be defined in terms of its intensity distribution and it is given as [124]

$$w_B = \frac{\lambda j_{0e}}{2\pi \sin\theta_a} \tag{4.16}$$

where $j_{0e} = 1.752$ is the value for which the zeroth-order Bessel function of the first kind $J_0(j_{0e}) = 1/e$. According to this criteria, the minimal Bessel beam waist value is

given by

$$w_{B_{min}} = \frac{\lambda j_{0e}}{2\pi} \tag{4.17}$$

obtained when $\theta_a = 90°$.

In our launcher, we use a Gaussian tangential amplitude field distribution over the meta-axicon's radiating aperture to efficiently cover the surface and minimize edge diffraction. Notably, in zone 1 of figure 4.23, where the spectrum of the generated beam resembles that of a Bessel beam, the Gaussian distribution over the aperture will always have a waist much larger than that of the generated beam.

We take as an example two radiating apertures, a and b operating at 30 GHz. Aperture a is a meta-axicon with parameters $r_a = 15\lambda$, $w_0 = 0.0989$ m and $\theta_a = 3.71°$, which is the minimum angle and maximum radius to remain on zone 1. Aperture b is also a meta-axicon with $r_a = 15\lambda$, $w_0 = 0.0989$ m but $\theta_a = 0$. Consequently, aperture b will radiate a truncated Gaussian beam.

The radiated Bessel beam has a waist of $w_B = 0.0431$ m and an NDR of 2.3 m, while the truncated Gaussian beam has a waist of $w_0 = 0.0989$ m and a respective Rayleigh range [38] of $z_R = 3.0729$ m. The Gaussian waist is more than two times larger than that of the radiated Bessel beam, and the Rayleigh range is over one meter greater. Thus, considering these parameters, the Gaussian beam would outperform the radiated Bessel beam in terms of focusing efficiency [124] and, consequently, in terms of WPTE. The comparison of their WTPE is depicted in figure 4.29, where we see a clear advantage for the Gaussian beam. In other words, the Gaussian beam used to generate the Bessel beam is more efficient than the Bessel beam itself for our purposes, which is a peculiar situation. Therefore, we decided to investigate meta-axicon configurations operating in zone 3 going below the minimum angle limitation to seek more interesting implementations.

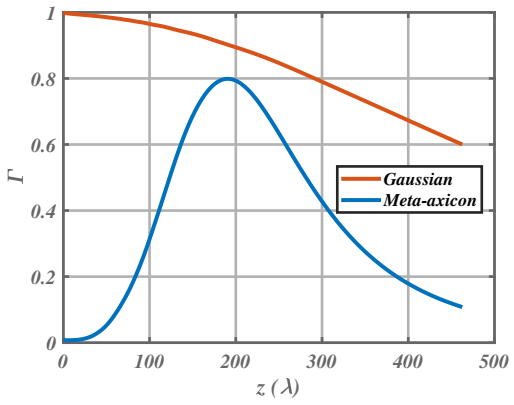

Figure 4.29 – Comparison of the WPTE, as a function of the separation distance, of a truncated Gaussian beam and the radiated Bessel beam.

4.5.3 Exploring Smaller Axicon Angles

In zone 3, the spectrum of the radiated beam lacks the two peaks typical of a Bessel beam. When considering a system with identical apertures acting as emitter and receiver, increasing the axicon angle gradually causes the WPTE level at the minimum separation distances to decrease, shifting the WPTE maximum away from this point. In figure 4.30a, we note that as the axicon angle increases, the maximum amplitude of the tangential electric field also increases, suggesting a reduction on the width of the radiated beam. Furthermore, as the axicon angle is reduced, the WPTE behavior of the radiated beam more closely approximates that of a truncated Gaussian beam. This effect can be observed in figure 4.30b.

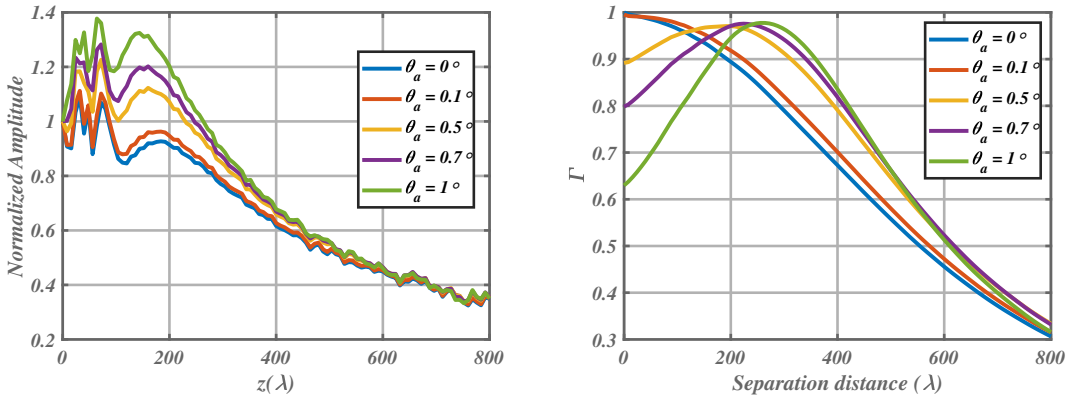

(a) (b)

Figure 4.30 – Axicon angle effect on the WPTE and radiated field intensity. In (a) the tangential electric field radiated by an aperture along z-axis is presented. In (b) the WPTE as a function of the separation distance is shown.

Using an axicon angle of 0.7°, we have observed a very interesting behavior. Figure 4.31a illustrates the radiated beam for this axicon angle, while figure 4.31b compares its spectrum to that of the truncated Gaussian beam. Notably, we can observe that the beam's waist is narrower than that of the Gaussian beam, although their spectra exhibit great similarity.

To evaluate the performance of the phased beam ($\theta_a = 0.7°$), we provide the intensity at the center of the beam along the propagation axis, and the WPTE considering two identical apertures, in figures 4.32a and 4.32b, respectively. Both figures include the Gaussian beam for comparison. In figure 4.32a, we observe that the maximum intensity of the phased beam is 20% higher than that of the Gaussian beam. Moreover, the intensity decay of the phased beam after $z = 800\,\text{cm}$ closely resembles that of the Gaussian beam. In figure 4.32b, we notice a significant expansion in the operating range by 65 cm compared to the Gaussian beam. Additionally, the point of maximum efficiency (98%) for the phased beam shifts from $z = 0$ (Gaussian beam) to $z = 224\,\text{cm}$.

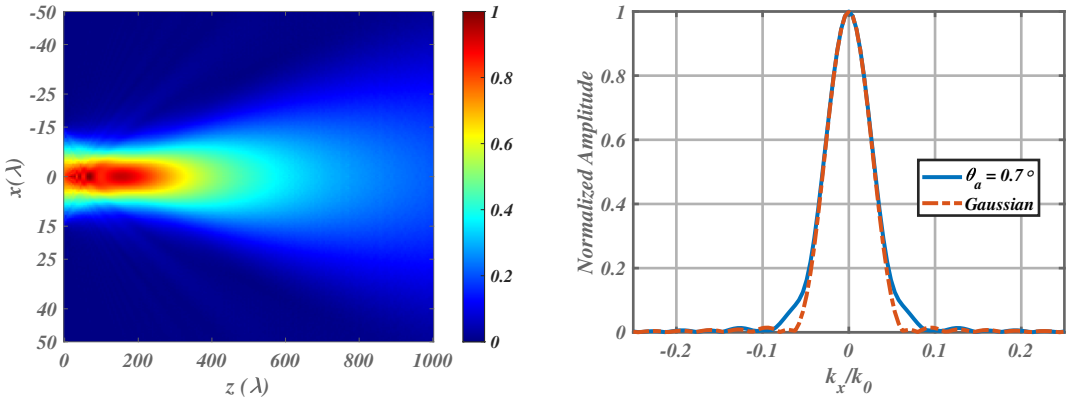

(a) (b)

Figure 4.31 – Comparison of a truncated Gaussian beam and the radiated phased beam. In (a), normalized amplitude of $|E_x|$ in the plane xz for the phased beam ($\theta_a = 0.7°$) is shown. In (b), the normalized amplitude spectrum of the tangential component of the truncated Gaussian beam is compared with that of the radiated beam with $\theta_a = 0.7°$.

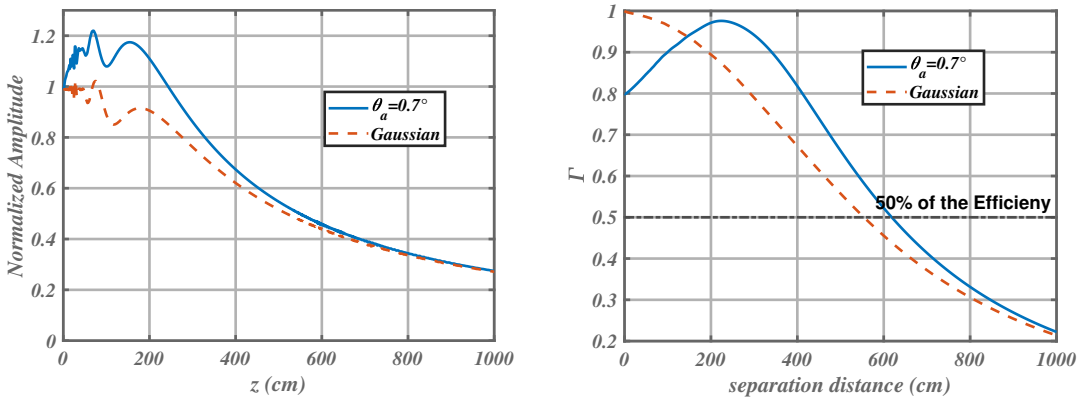

(a) (b)

Figure 4.32 – Comparison of the truncated Gaussian beam and the radiated phased beam ($\theta_a = 0.7°$). In (a) the amplitude of $|E_x|$ along z-axis is depicted, while in (b), the WPTE as a function of the separation distance is shown.

Compared to configurations with a larger axicon angle and the truncated Gaussian beam, using an axicon angle of 0.7° yields notable benefits. Specifically, the radiated beam achieves a narrower waist, leading to a remarkable 20% increase in maximum intensity compared to the Gaussian beam. Furthermore, the phased beam presents expanded operating range, a shift in maximum efficiency position and an WPTE of 80% for small separation distances.

4.5.4 Feeding considerations

In a practical implementation, the field distribution over the meta-axicon is not an ideal Gaussian amplitude distribution, but rather an approximation to it. Usually a horn antenna is used as the feeding device to the axicon [2, 125]. Therefore, the meta-axicon is responsible to compensate the phase due to its distance to the feeding horn and to provide the linear phase required to radiate the desired beam. Here, we present an analysis of considering a real horn instead of the ideal Gaussian distribution used before. We proceed by utilizing MATLAB to simulate a horn antenna, where the field generated by the horn will act as the incident field on the meta-axicon plane.

The selected commercial horn antenna is the WR-28 Waveguide Antenna, 26.5 GHz to 40 GHz Frequency Range, 10 dBi Gain, UG-599/U Flange, Integrated Cage-Style Mount, from Pasternack (see Pasternack's product page: WR-28 Waveguide Antenna). This antenna is show in figure 4.33. This antenna was chosen due to its large operating range and also for its ease to integrate with the meta-axicon.

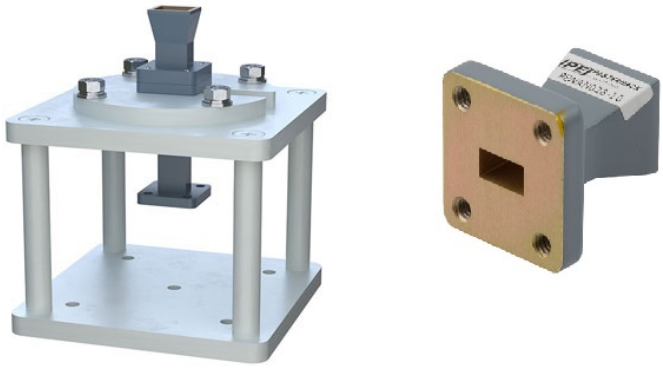

Figure 4.33 – WR-28 Waveguide Antenna used in the project

Our initial objective is to determine the optimal distance d between the horn and the meta-axicon, defined as the distance at which the incident field over the meta-axicon most closely approximates the ideal Gaussian distribution with a 10 dB drop at the edge of the aperture for $r_a = 15\,\text{cm}$. The system operates at 30 GHz. The dimensions of the simulated horn are as follows: aperture width 12.3 mm, aperture length 9 mm, and horn length 26.7 mm.

To obtain d, we calculated the squared error between the field radiated by the horn and the expected Gaussian distribution for different z positions. The optimal calculated distance is $d = 124\,\text{mm}$, and the results are shown in figure 4.34, where the incident filed is compared to the ideal Gaussian beam amplitude at the optimal distance.

Analyzing figure 4.34, we can see that there is a portion of the field radiated by the horn that is not used by the meta-axicon. This spill-over [63], representing the part not intercepted by the aperture, is considered wasted energy. To quantify the spill-over [5], we compare the energy intercepted by the aperture with the total energy radiated by

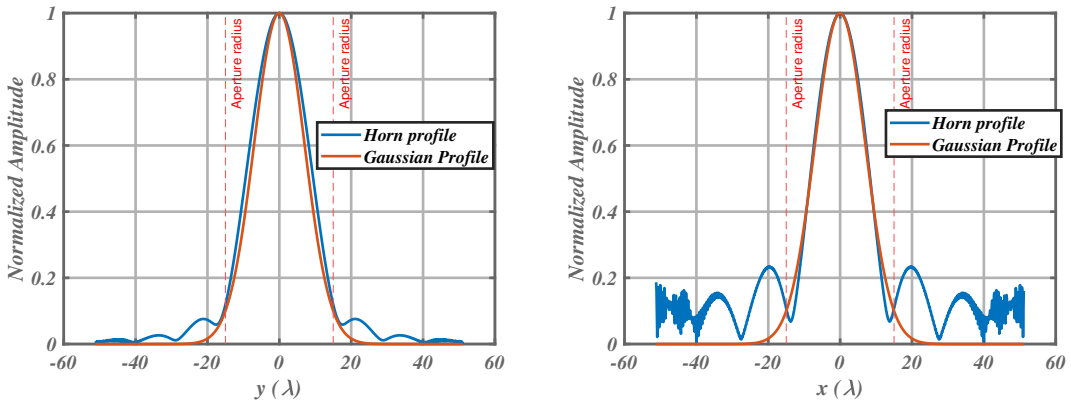

(a) (b)

Figure 4.34 – Comparison between horn's tangential electric field and ideal Gaussian distribution at optimal distance, $z = 124\,\text{mm}$.

the horn. We write the spill-over efficiency η_s as

$$\eta_s = \frac{P_i}{P_h} \tag{4.18}$$

where P_i represents the power collected by the aperture and P_h represents the power radiated by the horn. For our system, we obtained a spill-over efficiency of 91%. This means that only 9% of initial energy is not intercepted by the aperture.

4.6 Transmitter Realization

We are designing a linearly polarized transmitter operating at 30GHz which comprises a horn and a meta-axicon. Figure 4.35 depicts the transmitter system. Our objective is to design a launcher which is capable of operating at large distances with reasonable WPTE.

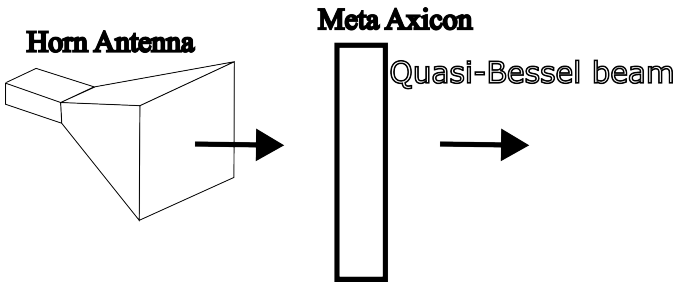

Figure 4.35 – Designed Transmitter System

The maximum meta-axicon radius achievable with the available technology is 15 cm. Therefore, we set $r_a = 15\,\text{cm}$ as the aperture size, since it directly impacts the operating

range of our system. The chosen unit cell characteristics are: pitch 2.6 mm, pillar height $h = 15.5$ mm and permittivity $\varepsilon_r = 8.8$. The local incidence was taken into account for designing the radius of the pillar and the transmitted phase, as the angle of incidence in the cell has a strong influence on the transmitted amplitude and phase. Figure 4.36 depicts the amplitude and phase of the unit cell's transmitted coefficient.

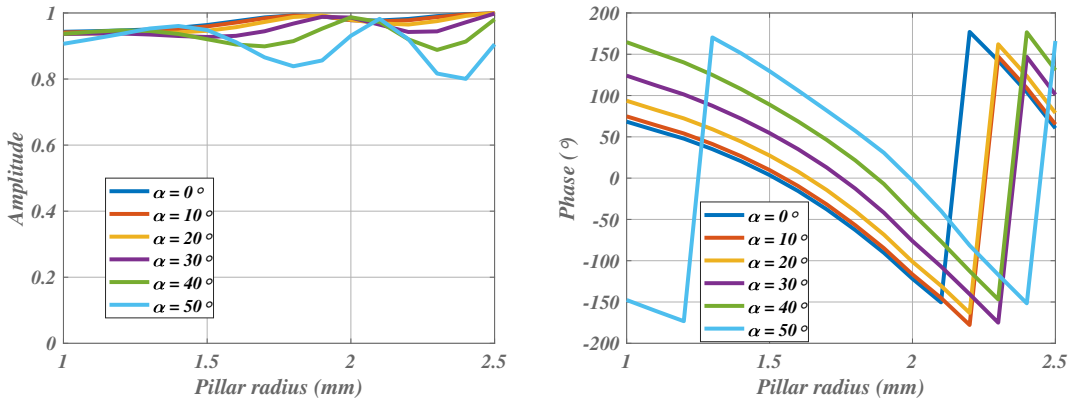

(a) (b)

Figure 4.36 – Amplitude (a) and phase (b) of the unit cell's transmission coefficient as a function of the pillar radius for fixed height $h = 15.5$ and frequency $f = 30$ GHz. The variable α represents incidence angle.

Figures 4.36a and 4.36b show that the incidence angle α influences both the phase and amplitude of the transmitted fields. In figure 4.36a it is evident that for $\alpha \leq 20°$ the amplitude is minimally affected. The impact of α on amplitude becomes more pronounced for radii greater than 1.5 mm. For instance, for a radius of 1 mm, the amplitude difference between $\alpha = 50°$ and $\alpha = 0°$ is approximately 5%. In contrast, for a radius of 2.4 mm, this difference increases to 19%. In figure 4.36b, we observe that for all different α we have an excursion exceeding 300° within the specified radius range. Also, the effect of α in the phase can be understood as an offset from the normal incidence. As α increases the phase variation between the the incident and the output fields increase.

Based on previous discussions, the launcher is designed to operate in zone 3, rather than zone 1. Consequently, the spectrum of the radiated beam will not resemble that of a truncated Bessel beam, and we will refer to our launcher as a Quasi-Bessel beam launcher. The chosen axicon angle is $\theta_a = 1°$. With this angle the WPTE at small $z = 0$ is not drastically reduced. The chosen parameters are summarized in table 4.1. The results for the theoretical model of the meta-axicon are presented in figures 4.37-4.38, while the results obtained from fullwave software are shown in figures 4.40-4.41. Also, a comparison between them is presented in figures 4.42, 4.43 and 4.44, while the results related to bandwidth are presented in figure 4.45. The analysis of diffraction is presented in figures 4.46, 4.47, 4.48 and 4.49.

Table 4.1 – Design Parameters

Operating Frequency	Aperture radius	Axicon angle
30 GHz	15 cm	$\theta_a = 1°$

4.6.1 Theoretical Model Results

Figure 4.37a shows the normalized amplitude of the tangential field E_y in the plane xz, with the center of the aperture positioned at $x = y = z = 0$. We observe a pencil-beam-like pattern displaying clear symmetry around the x-axis. Additionally, slight diffraction is noticeable at the aperture edges, attributed to the reduced amplitude of the tangential field in this region. The normalized amplitude of E_y at the center of the beam (z-axis) is depicted in figure 4.37b. We notice that close to the aperture ($0 \leq z \leq 75\lambda$) a strong oscillating behavior exists. In this region, the field is still in the process of forming the desired interference pattern, with different parts of the wavefront interacting and interfering with each other. Additionally, diffraction at the aperture edges contributes to this strong oscillatory behavior.

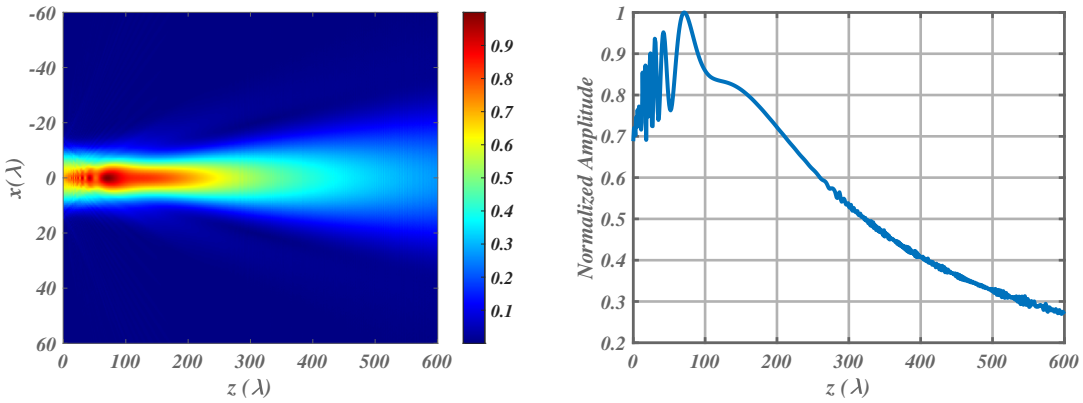

(a) (b)

Figure 4.37 – Meta-axicon results from the theoretical model. In (a), the normalized amplitude of $|E_y|$ in the plane xz for is shown, while in (b), the normalized amplitude of $|E_y|$ along z-axis is depicted.

The normalized amplitude of the spectrum of E_y is presented in figure 4.38a, where the spectral variable $k_y = 0$. We can see that most of the spectral content is located in the region $-0.12 \leq k_x/k_0 \leq 0.12$, which again justifies our choice for using the paraxial approximation to calculate the radiated beams. Also, only one central peak is observed. Figure 4.38b shows the results for the WPTE considering two identical and perfectly aligned Quasi-Bessel launchers. We observe that the operating range of the system is 520λ while its maximum efficiency of 94% is located at a separation distance of 205λ. The WPTE value at the smallest separation distance is 67%. The calculated NDR is 566λ.

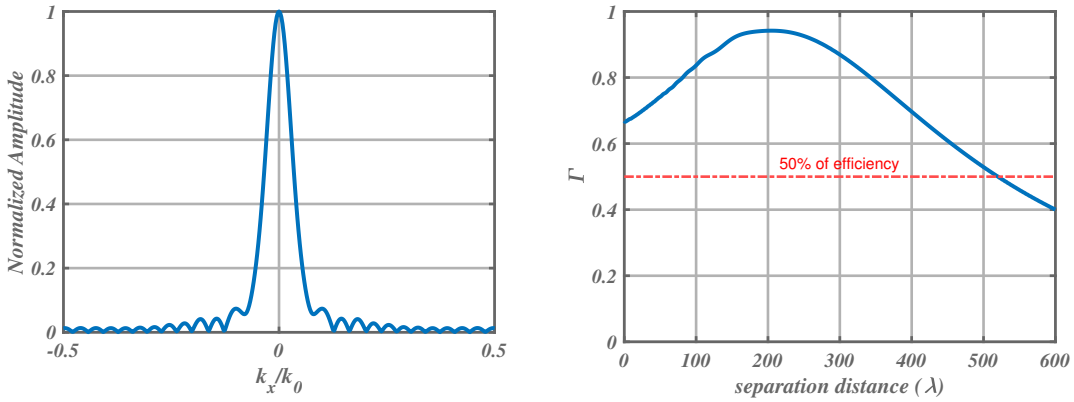

(a) (b)

Figure 4.38 – Meta-axicon results from the theoretical model. In (a), the normalized amplitude of the spectrum of E_y over the aperture considering $k_y = 0$ is shown, while in (b), the WPTE as a function of the separation distance is shown.

4.6.2 CST simulations

The electric and magnetic fields were extracted from the CST simulation, which included models of both the commercial horn and the meta-axicon. Due to computational resource constraints, the simulation space was limited, and the fields were only propagated to a short distance beyond the meta-axicon. Figure 4.39 shows the structure simulated in CST, where we can see the horn antenna and the metasurface.

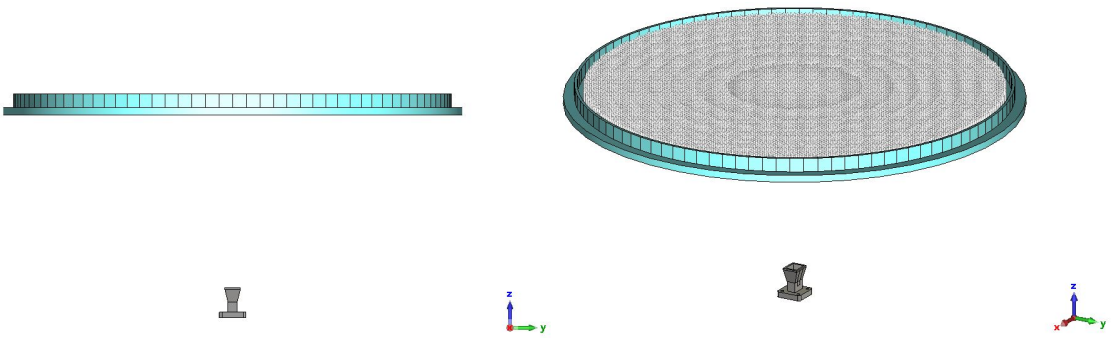

(a) (b)

Figure 4.39 – Simulated structure. In (a), we can see a lateral view, while (b) provides an isometric view.

Specifically, the fields were extracted 10 mm away from the meta-axicon's radiating aperture. These extracted fields were then propagated using a spectral domain approach implemented in a MATLAB routine developed for this purpose. Consequently,

while the results presented here are referred to as CST results, they are actually the outcome of combined processing using both CST and MATLAB.

Figure 4.40a presents the amplitude of E_y in the plane xz. Again, the radiating aperture of the meta-axicon is positioned at $x = y = z = 0$. The pencil beam-like profile and the symmetry around x-axis are observed, as well as the diffraction at the edges. Figure 4.40b shows the amplitude of E_y along axis z, where an oscillatory behavior is observed near the aperture, with a pronounced amplitude peak at $z = 12\lambda$.

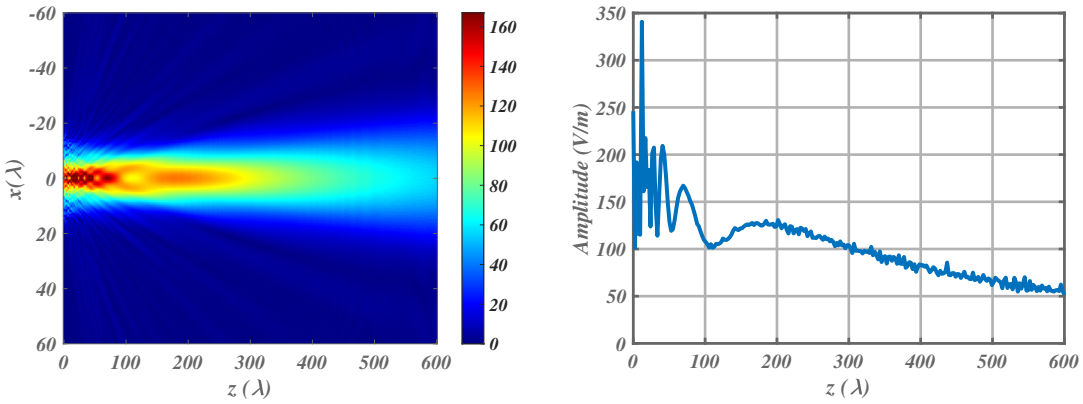

(a) (b)

Figure 4.40 – Meta-axicon results from CST. In (a), the normalized amplitude of $|E_y|$ in the plane xz for is shown, while in (b), the normalized amplitude of $|E_y|$ along z-axis is depicted.

The spectral content is presented in figure 4.41a, where we observe a central peak with most of the content confined within the region $-0.14 \leq k_x/k_0 \leq 0.14$. Once more, the WPTE result was obtained following the sequence shown in figure 4.16, assuming identical and axally-aligned apertures. It is depicted in figure 4.41b, where we observe an operating range of 505 cm and a maximum power transfer efficiency of 77% located in the region 88 cm $\leq z \leq$ 226 cm. An efficiency value of 69% is observed at the smallest separation distance.

We define P_{in} as the input power at the horn and P_a as the total power radiated by the aperture in the CST simulation. Using the Poynting vector, we calculate P_a, and we observe that it represents 68% of the input power. This loss of 32% accounts for the spill-over, non-uniformity of the amplitude and phase distributions over the meta-axicon, reflections, and possible random effects over the meta-surface [5]. We can separate the spillover efficiency from the others (η_c), as it was previously calculated using the theoretical model ($\eta_s = 0.91$). We can then write the antenna radiation efficiency as

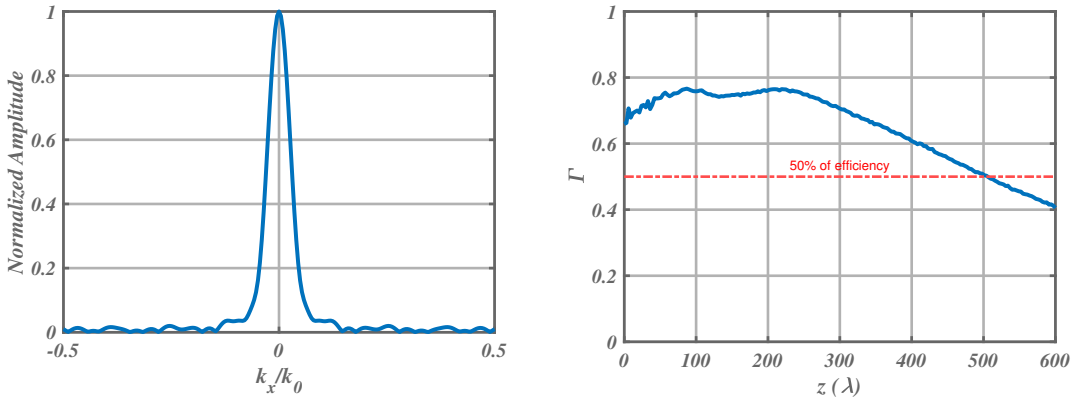

(a) (b)

Figure 4.41 – Meta-axicon results from CST. In (a), the normalized amplitude of the spectrum of $|E_y|$ over the aperture considering $k_y = 0$ is shown, while in (b), the WPTE as a function of the separation distance, assuming identical and axially aligned apertures, is shown.

$$A_e = \frac{P_a}{P_{\text{in}}} = \eta_s \eta_c = 0.68 \tag{4.19}$$

$$\eta_c = 0.75 \tag{4.20}$$

where the antenna efficiency is denoted as A_e.

4.6.3 Comparison of Theoretical and CST results

Overall we observe a good agreement between the theoretical model and the CST results. However we can observe some interesting differences between the results. We start analyzing the tangential field distribution over the radiating aperture of the meta-axicon in terms of amplitude and phase.

Figure 4.42 shows the phase profile of the tangential field distribution across the meta-axicon aperture, as obtained from both the theoretical model and CST simulations. In figure 4.42a, $y = 0$, while in figure 4.42b $x = 0$. In both figures, the CST results reveal an oscillating phase profile, contrasting with the steady behavior predicted by the theoretical model.

In figure 4.42a, the CST phase profile shows a noticeable inclination within the range $-7.5 \leq y \leq 7.5$, consistent with the theoretical model. However, for $|y| > 7.5$ the oscillations make it difficult to confirm whether the inclination persists. In figure 4.42b the oscillations in the CST phase profile obscure any clear indication of its inclination across the entire aperture.

The normalized amplitude profile of the tangential field over the meta-axicon is presented in figure 4.43. The field profile considering $x = 0$ is shown in figure 4.43a

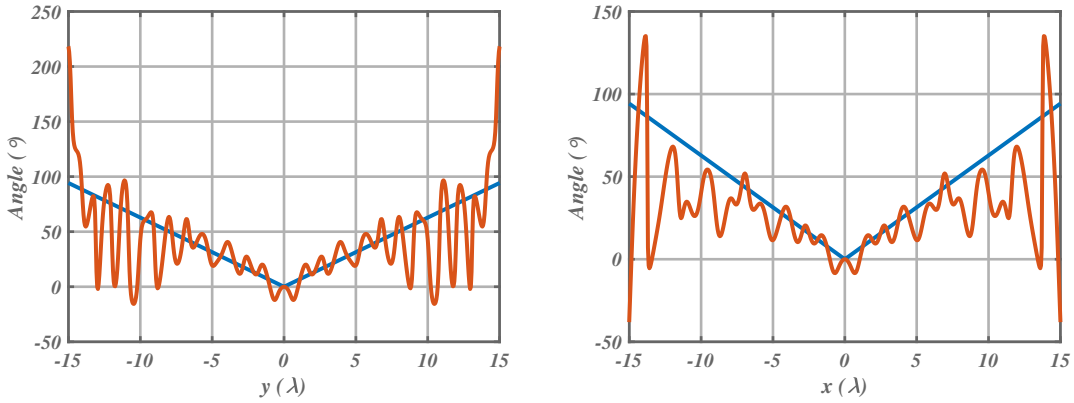

(a) (b)

Figure 4.42 – Comparison theoretical model and CST simulation. In (a), the phase profile of the tangential electric field, considering $x = 0$, is shown, while in (b), the phase profile is presented for $y = 0$.

while the results considering $y = 0$ is depicted in 4.43b. While the theoretical model shows a Gaussian-like profile, the CST results show a narrow peak at the center of the aperture along with an oscillating behavior. Notably, the field levels at the edges of the aperture are low in both cases, though the CST results display slightly higher levels at the edges compared to the theoretical model.

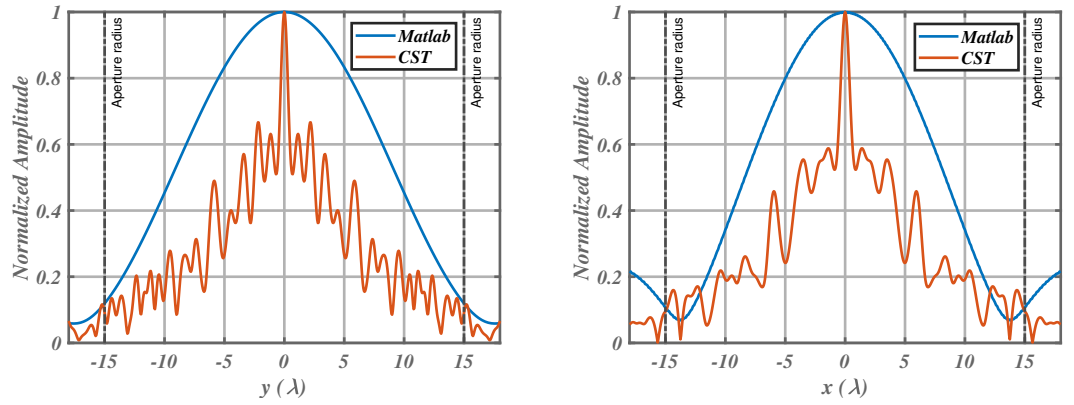

(a) (b)

Figure 4.43 – Comparison theoretical model and CST simulation. In (a), the amplitude profile of the tangential electric field, considering $x = 0$, is shown, while in (b), the amplitude profile is presented for $y = 0$.

The comparison of the spectral content of E_y is presented in figure 4.44a and the comparison of WPTE is shown in figure 4.44b. The spectral content of both cases is very similar, with a slight difference after $|k_x/k_0| > 0.1$, where the oscillations of the theoretical model appear to have higher amplitude. Analyzing the WPTE in figure

4.44b, we observe that the operating ranges of the two curves are very similar: 505λ for the CST results and 520λ for the theoretical model. The two curves show good agreement between $0 \leq z \leq 80\lambda$ and $z \geq 555\lambda$. However, between 100λ and 450λ, the efficiency of the theoretical model increases to a maximum before decreasing, while the CST curve does not exhibit a similar rise. Instead, the CST efficiency remains close to 77% before decreasing. These discrepancies can be attributed to variations in the amplitude and phase of the tangential fields across the apertures in the theoretical model and CST simulations, as well as the approximations made in the theoretical model.

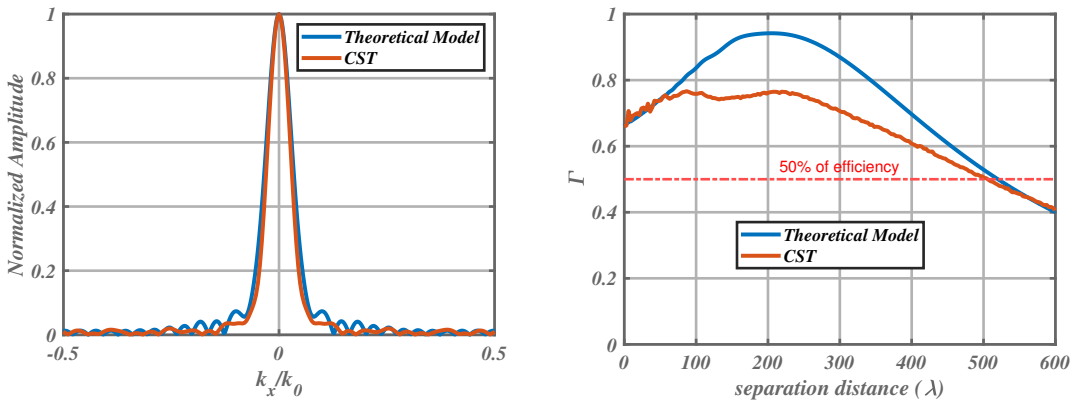

Figure 4.44 – Comparison theoretical model and CST simulation. In (a), the normalized amplitude of the spectral content of E_y for $k_y = 0$ is shown, while in (b), the WPTE as a function of the separation distance, assuming identical and axially aligned apertures, is compared.

4.6.4 Bandwidth Analysis

The bandwidth analysis was conducted using CST results, as they allow for an easy assessment of the frequency variation effects on the metasurface cells. To define the bandwidth we focus our attention on the WPTE. The launcher was examined across the frequency range of 27-33 GHz. We observed that lowering the frequency has a similar impact on the WPTE as increasing the axicon angle. The results of the WPTE for 28.5-30.5 GHz are presented in figure 4.45.

We observed that below 29.5 GHz, the WPTE level at $z = 0$ drops below 40%, establishing 29.5 GHz as the lower frequency limit. Conversely, for frequencies above 30.5 GHz, the WPTE pattern resembles that of a collimated beam ($\theta_a = 0$), defining 30.5 GHz as the upper limit. As a result, the bandwidth is determined to be 1 GHz, spanning from 29.5 GHz to 30.5 GHz.

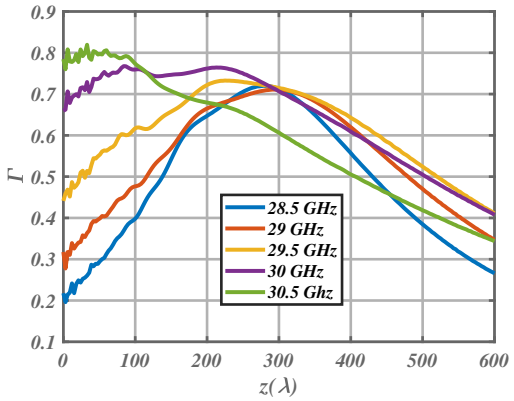

Figure 4.45 – WPTE as a function of the separation distance considering different operating frequencies.

4.6.5 Diffraction Analysis

To examine the launcher response in a case of obstruction, we evaluate its radiated fields and WPTE considering a metallic disk as obstacle. Also, we calculate its self-healing degree at specific positions as a function of the radius of the obstruction. The obstacle is initially positioned at $z = 120\lambda$, axially aligned with the launcher. This location is selected because it lies beyond the region of significant oscillations, where the beam is expected to be fully formed and stable. Figure 4.46 shows the normalized electric field magnitude $|E_y|$ of the obstructed field in the xz plane. The obstacle's radius is 20% of the aperture radius, and the field is calculated using the scattered field approach discussed in Section 1.2.4. The shadow distance is 171λ, and after this distance, the beam appears to be reformed.

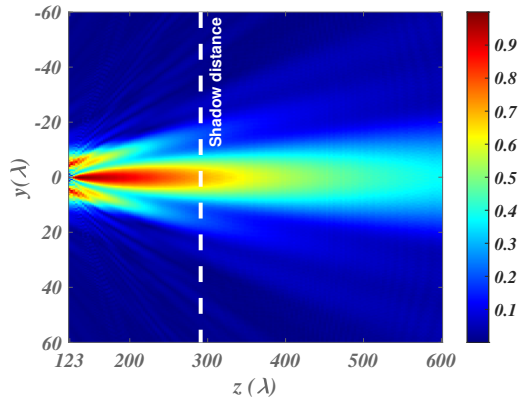

Figure 4.46 – Radiated obstructed tangential electric component in the plane xz. The obstacle is axially aligned and placed at $z = 120\lambda$.

A comparison of the transmitter's beam, with and without the obstruction, is illustrated in figure 4.47. The obstacle is a circular disk composed of perfectly electrically

conducting (PEC) material, axially aligned to the aperture and placed at $z = 120\lambda$. While figure 4.47a shows the amplitude profile at $z = 180\lambda$ with $y = 0$, in figure 4.47b the amplitude is evaluated at $z = 505\lambda$. The impact of the obstruction can be seen, but the maximum intensity of the obstructed beam is only 10% lower than the unobstructed beam at 505λ. Furthermore, we can see that both beams are quite similar in the range $-25 \leq x \leq 25$. At $z = 180\lambda$, which lies inside the predicted shadow region, the total field presents high intensity, close to that of the incident field. However, their profile is distinct, and the obstructed field presents three peaks rather than one as exhibited by the incident beam.

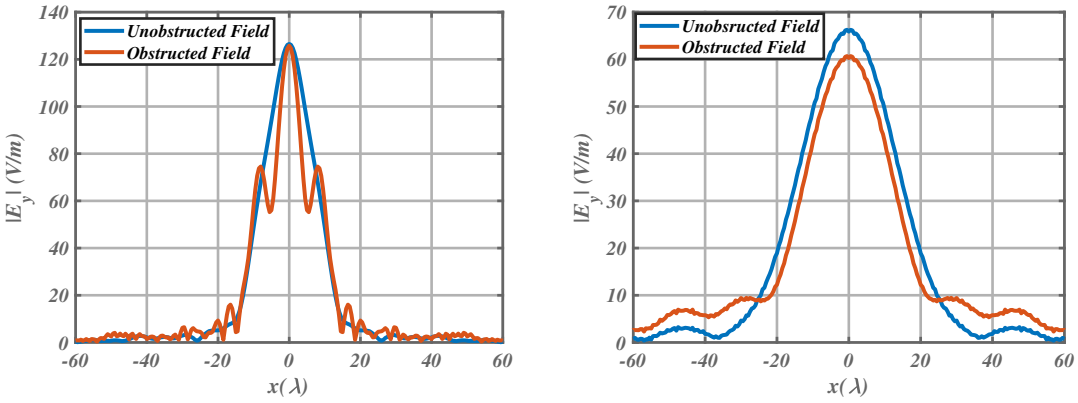

(a) (b)

Figure 4.47 – Comparison of unobstructed and obstructed amplitude profile of $|E_y|$ with $y = 0$ at different z. The obstacle is placed at $z = 120\lambda$. In (a), $z = 180\lambda$ and in (b) at $z = 505\lambda$

The self-healing degree of the launcher as a function of the obstacle radius is presented in figure 4.48. Again, the obstacle is positioned at $z = 120\lambda$ and the self-healing degree is evaluated at $z = 505\lambda$. The radius of the obstruction varies from 5% to 100% of the aperture radius. Notably, the region where $0.2 \leq r_o/r_a \leq 0.8$ exhibits a steeper decline compared to other sections of the curve.

The WPTE was evaluated for a scenario with axially aligned identical launchers, with an obstacle positioned in their line of sight. The obstacle's position remains fixed, while the distance between the two launchers is varied. We present the results for the obstacle positioned at $z = 120\lambda$ and $z = 240\lambda$, examining the effects of obstacles with radii of $0.1r_a$, $0.2r_a$, $0.3r_a$, $0.4r_a$ and $0.5r_a$. The results are presented in figure 4.49.

We observe that while the obstruction impacts the WPTE, the distance of the obstacle's placement appears to have a relatively minor effect. For instance, when the obstacle is positioned at $z = 120\lambda$, the WPTE evaluated at $z = 505\lambda$ are 47% for $r_o/r_a = 0.1$, 38% for $r_o/r_a = 0.2$, 25% for $r_o/r_a = 0.3$ and less than 20% for $r_o/r_a = 0.4$ and $r_o/r_a = 0.5$.

Similarly, for an obstacle at $z = 240\lambda$, the WPTE evaluated at $z = 505\lambda$ are 46% for $r_o/r_a = 0.1$, 35% for $r_o/r_a = 0.2$, 23% for $r_o/r_a = 0.3$ and less than 20% for $r_o/r_a = 0.4$

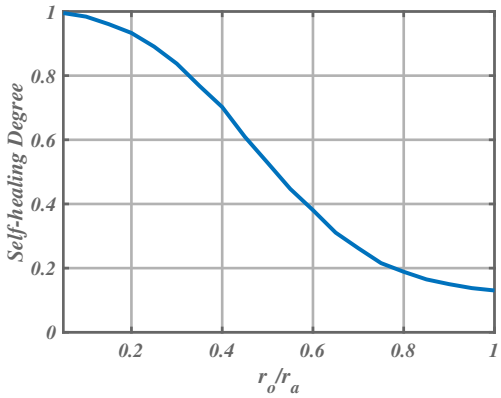

Figure 4.48 – Self-healing degree as a function of the radius of the obstacle, normalized by the radius of the aperture, calculated at $z = 536\lambda$.

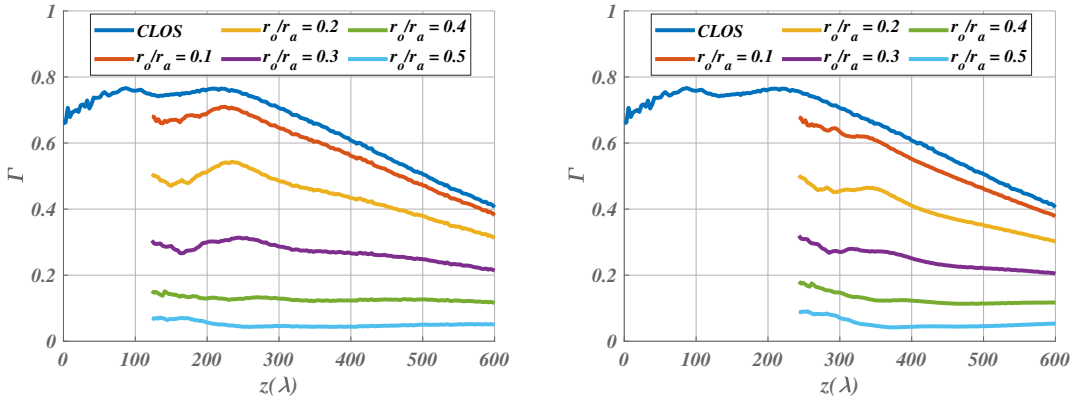

(a) (b)

Figure 4.49 – WPTE, as a function of the separation distance, of obstructed link for obstacles with different radii. In blue, the WPTE assuming no obstructions.

and $r_o/r_a = 0.5$. This indicates that the obstacle position does not significantly alter the WPTE values.

Figure 4.50 shows normalized amplitude of E_y of the beam obstructed by an obstacle that is not axially aligned with the aperture, in the plane yz. The off-centered obstacle is placed at two different positions $x = y = 3\lambda, z = 120\lambda$ and $x = y = 5\lambda, z = 120\lambda$. The obstacle's radius is $r_o = 0.2r_a$. We can see the disturbance caused by the obstruction in the lower part of the figure. Due to the off-centered placement, an asymmetry in the radiated fields is observed. Additionally, as the obstacle moves farther from the center of the coordinate system, the beam becomes less affected by the obstruction.

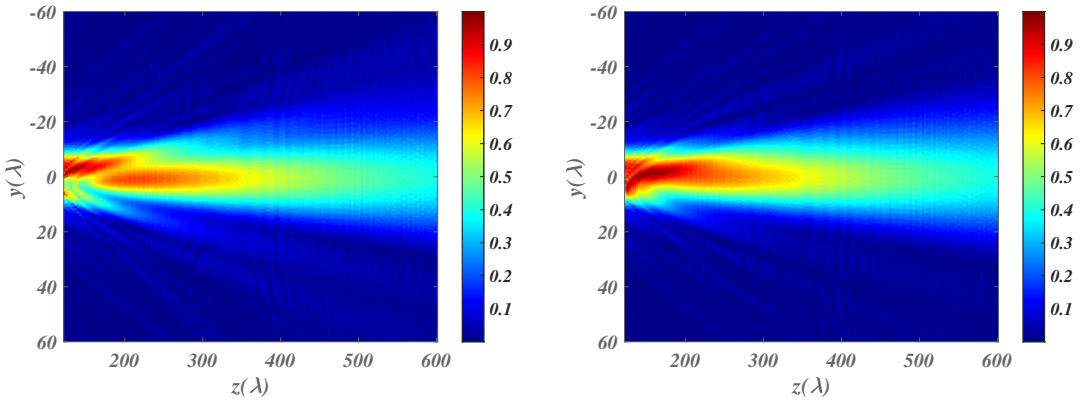

(a) . (b)

Figure 4.50 – Radiated obstructed tangential electric component in the plane yz. The obstacle off-centered, placed at $x = 3\lambda, y = 3\lambda, z = 120\lambda$ in (a), and at $x = 5\lambda, y = 5\lambda, z = 120\lambda$ in (b).

Still analyzing the off-centered obstruction, figure 4.51 presents the WPTE as a function of the separation distance, for an obstacle placed at three different positions: $x = y = 3\lambda, z = 120\lambda$, $x = 5y = 5\lambda, z = 120\lambda$ and $x = 7.5 = 7.5\lambda, z = 120\lambda$. We also plot the curves for the unobstructed system for comparison. As the distance from the coordinate system's center increases, the impact on WPTE diminishes. This is expected, as a smaller portion of the beam is intercepted when the obstacle is positioned further from the beam's center.

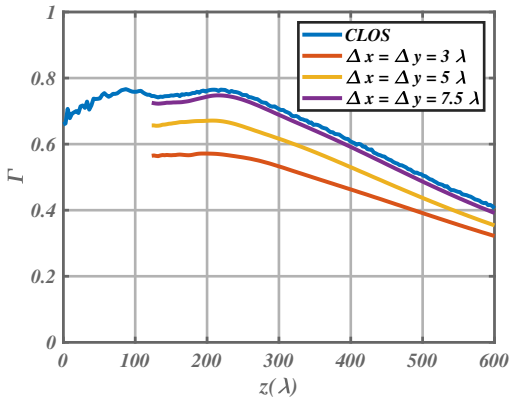

Figure 4.51 – WPTE, as a function of the separation distance, of the obstructed link for the off-centered obstacle with radius $r_o = 0.2r_a$ placed at $z = 120\lambda$. The distance from the obstacle's center to the coordinate system's center is denoted by Δx and Δy. In blue, the WPTE assuming no obstructions.

4.7 Conclusion

This chapter has provided a comprehensive exploration of the meta-axicon, which is a metasurface engineered to replicate the effects of a axicon. The meta-axicon was modeled using a theoretical approach, and the comparison of this model with full-wave simulations confirmed the meta-axicon's ability to closely mimic the idealized behavior of a linear axicon. Also, we highlighted the impact of phase quantization and aperture illumination on its performance.

Then, the chapter delved into the operational characteristics of the meta-axicon, focusing on the implications of the axicon angle and aperture diameter on beam generation. By introducing a numerical metric that accounts for the spectral content of the generated beam, we were able to define a critical angle that distinguishes between Gaussian and Bessel spectral regimes. We have defined four operation zones relating the axicon angle and aperture size. This analysis proved itself very valuable, guiding the optimization of the meta-axicon design for different applications.

Finally, the chapter presented the final design of a linearly polarized transmitter operating at 30 GHz, composed of a rectangular horn antenna coupled with the meta-axicon. The transmitter is referred to as the Quasi-Bessel launcher because the spectrum of its radiated tangential electric field differs from that of a truncated Bessel beam.

This transmitter system, optimized for high WPTE over long distances, exemplifies the practical application of the meta-axicon design and operation zones. The theoretical and simulation results validated the system's performance, while additional analysis of bandwidth, diffraction effects, and practical considerations underscored the robustness and versatility of the meta-axicon in real-world scenarios. Table 4.2, compares two state of the art launchers using axicons to the proposed one. We observe that we achieved a lower axicon angle, resulting in a larger operating range.

Table 4.2 – Comparison with other launchers composed of axicons

Technology	θ_a	Range	Radius	f (GHz)
Meta-axicon (Proposed)	1°	505λ	15λ	30
Meta-axicon [1]	3°	80λ	6.25λ	15
Meta-axicon [2]	20°	15λ	7.5λ	300

Conclusion and Future Perspectives

Concluding Remarks

This thesis presented the analysis of wireless links radiating non-diffractive Bessel beams operating in the near field. We started by defining the theoretical bases and assumptions used to study wireless links operating in the near-field. We assume radiating circular apertures cut in perfectly conducting planes, and the fields are computed resorting to a spectral Green's function approach, calculated using the Fourier Transform. We also assume a paraxial approximation, which is justified by the geometry of the problem.

We derive the wireless power transfer efficiency (WPTE) formula between two antennas that can be used both in near field and far field regions. We neglect possible reflections between the antennas, and the electromagnetic reaction is used to evaluate the coupling between them. To perform this derivation, we resort to the connection between circuital and electromagnetic field quantities and to the reciprocity theorem. We compared the obtained formula to the Friis transmission equation showing that they render identical results in the far-field, while producing distinct results in the near field. The differences observed in the near-field highlight the electromagnetic coupling, even in the context of the adopted reflection-less approximation.

The WPTE formula is initially derived for free-space radiation and then extended to account for possible obstructions in the wireless link. This formulation accounted for metallic obstacles that obstruct the line-of-sight between transmitter and receiver, using both Physical Optics (PO) and Variational approaches. The PO technique provided a baseline solution, while the variational approach refined the results by minimizing errors due to approximation due to PO.

Then, Bessel beams radiated by finite apertures (truncated Bessel beams) were characterized in terms of propagation, WPTE and self-healing. Concerning the radiated beams, we compared Bessel beams with transverse electromagnetic (TEM) and Gauss-Bessel beams, concluding that the Bessel beam demonstrates greater robustness. As for the WPTE, we showed that the smallest transverse wave number provides the most efficient beam, despite diffraction at the edges due to truncation. We showed that for obstacle up to 30% of the aperture radius, the WPTE can by fully restored. We also showed that not only the radius of the obstruction but also its position is a determinant factor in the impact of the obstacle on the WPTE of the link. The link appears to be more affected when the obstacle is located halfway between the receiver

and transmitter, and its size is comparable to the radius of the radiating apertures.

We proposed a new design parameter, the operating range, defined as the separation distance over which the WPTE remains greater than 50%. We observed that it is possible to increase the operating range of truncated Bessel beams by applying a linear phase modulation on the tangential field distribution over the radiating aperture. We demonstrated that using a linear or quadratic phase profile delivers similar results for the examined range of angles and aperture sizes. The relative increase in the operating range can be predicted by the angle difference between the center of the aperture and its edge. We observed an increase of 15% in the operating range when using the first root of the Bessel function of first kind and first order to truncate the amplitude of the tangential field distribution over the radiating aperture. An increase of 20% and 16% was verified when using the second and the third roots, of the same Bessel function, respectively. Moreover, our analysis indicates that the spectral content experiences small variations due to phase modulation, for the studied range of angles. The improvement in operational range allows for a reduced aperture size to achieve the desired performance. We also demonstrated that, for our specific objectives, our approach outperforms of Bessel-Gauss beams.

Next, we ventured in investigating Bessel beam generation using axicons. More specifically, we used a theoretical model to design a Quasi-Bessel transmitter based on a metasurface capable of replicating the properties of an axicon (meta-axicon). The transmitter is linearly polarized and is composed of this metasurface coupled with a horn antenna. The model was compared to full-wave simulations to verify its applicability. We studied the effect of phase quantization and non-uniform illumination.

We focused our attention on the implications of the axicon angle and aperture diameter on beam generation. We introduced a numerical metric that evaluates the spectral content of the generated beam, enabling us to define a critical angle that differentiates between Gaussian and Bessel spectral regimes. Based on this, we identified four operational zones by relating the axicon angle to the aperture size, deciding to use an axicon angle of 1°.

To compute the WPTE of the designed transmitter using full-wave software, we first extracted the electric fields over the meta-axicon aperture and subsequently used them as inputs in the MATLAB code developed for WPTE calculation. This analysis yielded an operating range of 505λ and a maximum WPTE of 77%, compared to 520λ and 94% predicted by the theoretical model. These discrepancies are attributed to the metasurface cell size, which is nearly a quarter of the operating wavelength, as well as the quasi-periodicity and non-uniform illumination of the metasurface, resulting in significant variations in the tangential field distribution over the meta-axicon aperture between the theoretical and full-wave models.

The designed transmitter and its detailed analysis serve as a testament to the practical application of the methodologies and tools developed in this thesis, demonstrating their effectiveness in advancing the design of wireless systems. Specifically created for use during the conception phase of wireless system development, these tools enable designers to explore various configurations. Their low computational resource requirements make them particularly advantageous, allowing for preliminary evaluations

before transitioning to more demanding full-wave simulations.

Future Works

The Quasi-Bessel beam transmitter has already been fabricated by Thales Research and Technology (TRT); therefore, the next logical step in this work is to conduct measurements, which will be divided into two distinct campaigns. The first campaign will focus on characterizing the radiated beams. The collected data will be used in conjunction with the WPTE MATLAB routine to validate the accuracy of our model. In the second campaign, the objective will be to measure the WPTE using two identical transmitters. The results from these measurements will help assess the impact of neglecting reflections in the computation of the WPTE.

Concerning the WPTE formula, the idea is to derive a formulation capable of quantifying the efficiency drop when emitter and receiver are misaligned with respect to the direction of maximum efficiency, which may necessitate moving beyond the paraxial approximation. More than quantifying the impact on the WPTE, efforts will focus on proposing solutions to mitigate this issue.

Additionally, future research will investigate obstacles composed of dielectric materials featuring more complex geometries, aiming to evaluate their impact on the self-healing properties of truncated Bessel beams. The aim is also to extend the WPTE variational formula to better predict the effects of such obstructions on WPTE.

We also plan to fabricate an under-focused Bessel beam launcher and validate its performance through experimental measurements. This will provide crucial insights into the coupling between metasurfaces, such as those responsible for Bessel beam radiation and phase profile manipulation. Moreover, this research will open new paths for exploring systems that combine Bessel beam launchers with metalenses.

Bibliography

[1] M. Q. Qi, W. X. Tang, and T. J. Cui. “A broadband Bessel beam launcher using metamaterial lens”. In: *Scientific Reports* 5.1 (2015) (cit. on pp. 15, 38, 80, 81, 154).

[2] G. Wu, K. F. Chan, S. Qu, and C. H. Chan. “A 2-d beam-scanning Bessel launcher for terahertz applications”. In: *IEEE Transactions on Antennas and Propagation* 68.8 (2020), pp. 5893–5903 (cit. on pp. 15, 38, 80, 81, 141, 154).

[3] S. R. Saunders and A. Aragón-Zavala. *Antennas and Propagation for Wireless Communication Systems*. Wiley, 2007 (cit. on p. 33).

[4] T. Shaw, B. Mandal, D. Mitra, and R. Augustine. “Wireless power transfer system design in reactive near-field for implantable devices”. In: *2020 14th European Conference on Antennas and Propagation (EuCAP)*. 2020, pp. 1–5 (cit. on p. 33).

[5] C. A. Balanis. *Antenna Theory: Analysis and Design*. Wiley-Interscience, 2005 (cit. on pp. 33, 34, 36, 37, 41–43, 49, 51, 55, 66, 80, 141, 146).

[6] J. C. Maxwell. *A Dynamical Theory of the Electromagnetic Field*. Torrance collection. Wipf & Stock Publishers, 1996 (cit. on p. 36).

[7] C. Shu, S. Hu, Y. Yao, and X. Chen. “High-gain reflector antenna with beam steering for terahertz wireless communications”. In: *2017 10th UK-Europe-China Workshop on Millimetre Waves and Terahertz Technologies (UCMMT)*. 2017, pp. 1–4 (cit. on p. 36).

[8] V. H. Rumsey. “Reaction concept in electromagnetic theory”. In: *Phys. Rev.* 95 (6 Sept. 1954), pp. 1705–1705 (cit. on pp. 37, 42, 49, 51, 59, 63, 64).

[9] M. Hu. “Near-zone power transmission formulas”. In: *1958 IRE Nat’l Conv. Rec.* 6.8 (1958), pp. 128–135 (cit. on pp. 37, 39, 42, 49, 50, 56–58).

[10] J. Robieux. “Lois Générales de la Liaison entre Radiateurs d’Ondes : Application aux Ondes de Surface et à la Propagation”. PhD thesis. Faculté des sciences, Université de Paris, 1959 (cit. on pp. 37, 39).

[11] M. Hu. “On the generality of "near-zone power transmission formulas"”. In: *Proceedings of the IRE* 48.3 (1960), pp. 357–369 (cit. on p. 37).

[12] G. V. Borgiotti. “Maximum power transfer between two planar apertures in the Fresnel zone”. In: *IEEE Transactions on Antennas and Propagation* 14.2 (1966), pp. 158–163 (cit. on pp. 37, 38, 57, 58).

[13] S. Paković, S. Zhou, D. González-Ovejero, S. C. Pavone, A. Grbic, and M. Ettorre. "Bessel–gauss beam launchers for wireless power transfer". In: *IEEE Open Journal of Antennas and Propagation* 2 (2021), pp. 654–663 (cit. on pp. 37, 38, 55, 58, 95, 108, 109).

[14] K. A. Milton and J. Schwinger. *Electromagnetic Radiation: Variational Methods, Waveguides and Accelerators*. Springer Berlin Heidelberg, 2006 (cit. on pp. 37, 63).

[15] R. F. Harrington. *Time-Harmonic Electromagnetic Fields*. IEEE-Press, 2001 (cit. on pp. 37, 42–44, 48–50, 52, 59, 61–64, 68, 74, 75).

[16] J. Durnin. "Exact solutions for nondiffracting beams. I. The scalar theory". In: *Journal of the Optical Society of America A* 4.4 (Apr. 1987), pp. 651–654 (cit. on pp. 37, 73–76).

[17] J. Durnin, J. J. Miceli, and J. H. Eberly. "Diffraction-free beams". In: *Phys. Rev. Lett.* 58 (15 Apr. 1987), pp. 1499–1501 (cit. on pp. 37, 74, 80).

[18] W. Fuscaldo. "Advanced Radiating Systems based on Leaky Waves and Non-diffracting Waves". PhD thesis. Université Rennes 1; Université de Rome Sapienza; Università degli studi La Sapienza (Rome), 2017 (cit. on pp. 38, 75, 76).

[19] M. Ettorre and A. Grbic. "Generation of propagating Bessel beams using leaky-wave modes". In: *IEEE Transactions on Antennas and Propagation* 60.8 (2012), pp. 3605–3613 (cit. on pp. 38, 76, 77, 80, 104).

[20] M. Ettorre, S. M. Rudolph, and A. Grbic. "Generation of propagating Bessel beams using leaky-wave modes: experimental validation". In: *IEEE Transactions on Antennas and Propagation* 60.6 (2012), pp. 2645–2653 (cit. on pp. 38, 80, 104).

[21] P. Lemaitre-Auger, S. Abielmona, and C. Caloz. "Generation of Bessel beams by two-dimensional antenna arrays using sub-sampled distributions". In: *IEEE Transactions on Antennas and Propagation* 61.4 (2013), pp. 1838–1849 (cit. on pp. 38, 80).

[22] M. Ettorre, M. Casaletti, G. Valerio, R. Sauleau, L. Le Coq, S. C. Pavone, and M. Albani. "On the near-field shaping and focusing capability of a radial line slot array". In: *IEEE Transactions on Antennas and Propagation* 62.4 (2014), pp. 1991–1999 (cit. on pp. 38, 80).

[23] S. Busch, G. E. Town, and M. Koch. "Broadband "focus-free" terahertz imaging using axicons". In: *2014 39th International Conference on Infrared, Millimeter, and Terahertz waves (IRMMW-THz)*. 2014, pp. 1–2 (cit. on pp. 38, 115).

[24] A. Mazzinghi, M. Balma, D. Devona, G. Guarnieri, G. Mauriello, M. Albani, and A. Freni. "Large depth of field pseudo-Bessel beam generation with a rlsa antenna". In: *IEEE Transactions on Antennas and Propagation* 62.8 (2014), pp. 3911–3919 (cit. on pp. 38, 80).

[25] S. C. Pavone, M. Ettorre, and M. Albani. "Analysis and design of Bessel beam launchers: longitudinal polarization". In: *IEEE Transactions on Antennas and Propagation* 64.6 (2016), pp. 2311–2318 (cit. on pp. 38, 80).

[26] J. D. Heebl, M. Ettorre, and A. Grbic. "Wireless power transfer with Bessel beams". In: (2016), pp. 1–2 (cit. on p. 38).

[27] W. Fuscaldo, G. Valerio, A. Galli, R. Sauleau, A. Grbic, and M. Ettorre. "Higher-order leaky-mode Bessel-beam launcher". In: *IEEE Transactions on Antennas and Propagation* 64.3 (2016), pp. 904–913 (cit. on pp. 38, 80).

[28] S. C. Pavone, M. Ettorre, M. Casaletti, and M. Albani. "Transverse circular-polarized Bessel beam generation by inward cylindrical aperture distribution". In: *Optics Express* 24.10 (May 2016), pp. 11103–11111 (cit. on pp. 38, 80).

[29] N. Chiotellis, V. Mendez, S. M. Rudolph, and A. Grbic. "Experimental demonstration of highly localized pulses (X waves) at microwave frequencies". In: *Phys. Rev. B* 97 (8 Feb. 2018), p. 085136 (cit. on pp. 38, 80, 81).

[30] D. Comite, W. Fuscaldo, S. K. Podilchak, P. D. H. Re, V. G. Buendía, P. Burghignoli, P. Baccarelli, and A. Galli. "Radially periodic leaky-wave antenna for Bessel beam generation over a wide-frequency range". In: *IEEE Transactions on Antennas and Propagation* 66.6 (2018), pp. 2828–2843 (cit. on pp. 38, 80).

[31] G. Wu, K. F. Chan, W. C. Mok, and C. H. Chan. "3-d printed terahertz lens for Bessel beam generation". In: *2019 IEEE Asia-Pacific Microwave Conference (APMC)*. 2019, pp. 637–639 (cit. on pp. 38, 80, 81).

[32] N. Chiotellis, S. Zhang, Y. C. Vardaxoglou, and A. Grbic. "X wave radiator implemented with 3-d printed metamaterials". In: *IEEE Transactions on Antennas and Propagation* 68.7 (2020), pp. 5478–5486 (cit. on pp. 38, 80, 81).

[33] Q. Liu, P. Lu, K. Huang, and D. Qian. "A planar Bessel lens with non-diffraction beam deflection based on metasurfaces". In: *2020 IEEE MTT-S International Wireless Symposium (IWS)*. 2020, pp. 1–3 (cit. on pp. 38, 80, 81).

[34] W. Fuscaldo, A. Benedetti, D. Comite, P. Baccarelli, P. Burghignoli, and A. Galli. "Bessel-gauss beams through leaky waves: focusing and diffractive properties". In: *Physical Review Applied* 13 (6 June 2020), p. 064040 (cit. on pp. 38, 109).

[35] D. Comite, W. Fuscaldo, P. Burghignoli, A. Galli, and P. Baccarelli. "Bessel-Beam Antennas". In: *Wiley Encyclopedia of Electrical and Electronics Engineering*. John Wiley & Sons, Ltd, 2021, pp. 1–12 (cit. on pp. 38, 80, 81).

[36] F. Benassi, W. Fuscaldo, D. Masotti, A. Galli, and A. Costanzo. "Wireless power transfer in the radiative near-field through resonant Bessel-beam launchers at millimeter Waves". In: *2021 IEEE Wireless Power Transfer Conference (WPTC)*. 2021, pp. 1–4 (cit. on p. 38).

[37] S. Paković, N. Bartolomei, M. J. Mencagli, M. Ettorre, R. Sauleau, and D. González-Ovejero. "A fast and accurate method of synthesizing x-wave launchers by metallic horns". In: *IEEE Access* 9 (2021), pp. 1996–2006 (cit. on pp. 38, 80, 81).

[38] M. Born, E. Wolf, and A. B. Bhatia. *Principles of Optics*. Cambridge University Press, 2019 (cit. on pp. 38, 74, 115, 117, 138).

[39] A. Aiello, G. S. Agarwal, M. Paúr, B. Stoklasa, Z. Hradil, J. Řeháček, P. de la Hoz, G. Leuchs, and L. L. Sánchez-Soto. "Unraveling beam self-healing". In: *Optics Express* 25.16 (Aug. 2017), pp. 19147–19157 (cit. on pp. 38, 76, 98).

[40] S. Takeshita. "Power transfer efficiency between focused circular antennas with Gaussian illumination in Fresnel region". In: *IEEE Transactions on Antennas and Propagation* 16.3 (1968), pp. 305–309 (cit. on pp. 38, 106).

[41] F. Alsolamy, W. A. Alomar, and A. Grbic. "Cylindrical vector beams for wireless power transfer". In: *IEEE Transactions on Antennas and Propagation* 69.3 (2021), pp. 1716–1727 (cit. on pp. 38, 58, 92, 106, 108).

[42] J. H. McLeod. "The axicon: a new type of optical element". In: *Journal of the Optical Society of America* 44.8 (Aug. 1954), pp. 592–597 (cit. on pp. 39, 80, 104, 114, 115).

[43] T. Q. van Hoang, M. Bertrand, E. Vandelle, and B. Loiseaux. "Low-profile highly directive 2d-beam-steering antenna in ka-band with 3d-printed all-dielectric sub-wavelength deflectors". In: *2022 52nd European Microwave Conference (EuMC)*. 2022, pp. 852–855 (cit. on p. 39).

[44] T. Q. Van Hoang, J. Sourice, E. Vandelle, R. Faye, M. Bertrand, and B. Loiseaux. "Additive manufacturing of a 460mm-diameter flat off-axis lens for ka-band communications". In: *2023 17th European Conference on Antennas and Propagation (EuCAP)*. 2023, pp. 1–4 (cit. on pp. 39, 122, 123).

[45] T. S. Bird. *Fundamentals of Aperture Antennas and Arrays: From Theory to Design, Fabrication and Testing*. Wiley, 2016 (cit. on pp. 39, 41, 42, 69).

[46] R. C. M. Pimenta, G. Soriano, K. D. Paschaloudis, M. Ettorre, M. Zerrad, and C. Amra. "Power transfer efficiency for obstructed wireless links using Bessel beams". In: *Optic Express* 31.22 (Oct. 2023), pp. 35493–35506 (cit. on pp. 40, 79).

[47] C. Pfeiffer and A. Grbic. "Planar lens antennas of subwavelength thickness: collimating leaky-waves with metasurfaces". In: *IEEE Transactions on Antennas and Propagation* 63.7 (2015), pp. 3248–3253 (cit. on p. 40).

[48] E. V. Jull. *Aperture Antennas and Diffraction Theory*. IEE electromagnetic waves series. P. Peregrinus, 1981 (cit. on p. 41).

[49] P. C. Clemmow. *The Plane Wave Spectrum Representation of Electromagnetic Fields*. Pergamon Press, 1996 (cit. on p. 42).

[50] R. F. Harrington. "On scattering by large conducting bodies". In: *IRE Transactions on Antennas and Propagation* 7.2 (1959), pp. 150–153 (cit. on pp. 42, 43, 49, 60, 63, 110).

[51] C. A. Balanis. *Advanced Engineering Electromagnetics*. Wiley, 2012 (cit. on pp. 42–44, 47–51, 62).

[52] A. J. Booysen. “Aperture theory and the equivalence principle”. In: *IEEE Antennas and Propagation Magazine* 45.3 (2003), pp. 29–40 (cit. on p. 44).

[53] D. Cavallo. “Connected Array Antennas : Analysis and Design”. English. PhD Thesis 1 (Research TU/e / Graduation TU/e). Electrical Engineering, 2011 (cit. on pp. 45, 46).

[54] J. W. Goodman. *Introduction to Fourier Optics*. McGraw-Hill Physical and Quantum Electronics Series. W. H. Freeman, 2005 (cit. on pp. 45, 47, 49, 117, 122).

[55] L. B. Felsen and N. Marcuvitz. *Radiation and Scattering of Waves*. IEEE Press Series on Electromagnetic Wave Theory. Wiley, 1994 (cit. on p. 45).

[56] N. Marcuvitz. *Waveguide Handbook*. GBR: Institution of Electrical Engineers, 1986 (cit. on p. 45).

[57] A. T. de Hoop. *Handbook of Radiation and Scattering of Waves: Acoustic Waves in Fluids, Elastic Waves in Solids, Electromagnetic Waves*. Academic Press, 1995 (cit. on p. 47).

[58] K. Heidary. “Scattering from an infinite conducting cylinder covered with a finite two-layer dielectric coating (modal approach)”. In: *IEEE Transactions on Electromagnetic Compatibility* 38.1 (1996), pp. 70–77 (cit. on p. 49).

[59] R. F. Harrington. *Field Computation by Moment Methods*. Macmillan Series in Electrical Science. R.E. Krieger Publishing Company, 1982 (cit. on pp. 49, 57).

[60] R. G. Kouyoumjian. “The Calculation of the Echo Areas of Perfectly Conducting Objects by the Variational Method”. PhD thesis. 1953 (cit. on p. 49).

[61] D. M. Pozar. *Microwave Engineering*. Wiley, 2011 (cit. on pp. 49, 54, 55).

[62] S. Ramo, J. R. Whinnery, and T. Van Duzer. *Fields and Waves in Communication Electronics*. Wiley, 1994 (cit. on p. 49).

[63] S. Silver. *Microwave Antenna Theory and Design*. IEE electromagnetic waves series vol. 19. P. Peregrinus, 1984 (cit. on pp. 50, 141).

[64] J. Richmond. “A reaction theorem and its application to antenna impedance calculations”. In: *IRE Transactions on Antennas and Propagation* 9.6 (1961), pp. 515–520 (cit. on pp. 53, 58).

[65] M. Ettorre and A. Grbic. “A transponder-based, nonradiative wireless power transfer”. In: *IEEE Antennas and Wireless Propagation Letters* 11 (2012), pp. 1150–1153 (cit. on p. 55).

[66] W. C. Gibson. *The Method of Moments in Electromagnetics*. C&H/CRC Press, 2021 (cit. on p. 57).

[67] A. Taflove and S. C. Hagness. *Computational Electrodynamics: The Finite-difference Time-domain Method*. Artech House Antennas and Propagation Library. Artech House, 2005 (cit. on p. 57).

[68] A. Z. Elsherbeni and V. Demir. *The Finite-difference Time-Domain Method for Electromagnetics with MATLAB Simulations*. SciTech Pub., 2009 (cit. on p. 57).

[69] J. L. Volakis, A. Chatterjee, and L. C. Kempel. *Finite Element Method Electromagnetics: Antennas, Microwave Circuits, and Scattering Applications*. IEEE Press Series on Electromagnetic Wave Theory. Wiley, 1998 (cit. on p. 57).

[70] A. C. Polycarpou. *Introduction to the Finite Element Method in Electromagnetics*. Synthesis Lectures on Computational Electromagnetics. Morgan & Claypool Publishers, 2006 (cit. on p. 57).

[71] W. C. Chew. *Waves and Fields in Inhomogeneous Media*. Electromagnetic waves. IEEE Press, 1995 (cit. on p. 59).

[72] J. B. Breckinridge and D. G. Voelz. *Computational Fourier Optics: A MATLAB Tutorial*. SPIE Press monograph. SPIE Press, 2011 (cit. on p. 64).

[73] A. Kay. "Near-field gain of aperture antennas". In: *IRE Transactions on Antennas and Propagation* 8.6 (1960), pp. 586–593 (cit. on p. 70).

[74] William H. C. "Electromagnetic beam fields". In: *Optica Acta: International Journal of Optics* 21.11 (1974), pp. 871–892 (cit. on p. 74).

[75] D. Marcuse. *Light Transmission Optics*. Bell Laboratories series. Van Nostrand Reinhold, 1982 (cit. on p. 74).

[76] J. A. Stratton. *Electromagnetic Theory*. International Series in Physics. McGraw-Hill book Company, Incorporated, 1941 (cit. on p. 74).

[77] H. Jeffreys and B. S. Jeffreys. *Methods of Mathematical Physics*. University Press, 1966 (cit. on p. 74).

[78] Z. Bouchal and M. Olivík. "Non-diffractive vector Bessel beams". In: *Journal of Modern Optics* 42.8 (1995), pp. 1555–1566 (cit. on pp. 75, 98).

[79] Y. Z. Yu and W. B. Dou. "Scalar and vectorial properties of diffraction-free bessel beams". In: *2008 Asia-Pacific Microwave Conference*. 2008, pp. 1–5 (cit. on p. 75).

[80] J. J. Wang, T. Wriedt, J. A. Lock, and Y. C. Jiao. "General description of transverse mode Bessel beams and construction of basis Bessel fields". In: *Journal of Quantitative Spectroscopy and Radiative Transfer* 195 (2017). Laser-light and Interactions with Particles 2016, pp. 8–17. ISSN: 0022-4073 (cit. on p. 76).

[81] D. McGloin and K. Dholakia. "Bessel beams: diffraction in a new light". In: *Contemporary Physics* 46.1 (2005), pp. 15–28 (cit. on pp. 76, 92).

[82] A. Aiello and G. S. Agarwal. "Wave-optics description of self-healing mechanism in Bessel beams". In: *Optics Letters* 39.24 (Dec. 2014), pp. 6819–6822 (cit. on p. 76).

[83] Z. Bouchal, J. Wagner, and M. Chlup. "Self-reconstruction of a distorted non-diffracting beam". In: *Optics Communications* 151.4 (1998), pp. 207–211. ISSN: 0030-4018 (cit. on p. 76).

[84] R. C. M. Pimenta, G. Soriano, K. D. Paschaloudis, M. Ettorre, M. Zerrad, and C. Amra. "Self-healing analysis of distorted weakly-diffracting vector beams". In: *2023 17th European Conference on Antennas and Propagation (EuCAP)*. 2023, pp. 1–3 (cit. on p. 76).

[85] X. Chu and W. Wen. "Quantitative description of the self-healing ability of a beam". In: *Optics Express* 22.6 (Mar. 2014), pp. 6899–6904 (cit. on p. 76).

[86] N. Mphuthi, R. Botha, and A. Forbes. "Are Bessel beams resilient to aberrations and turbulence?" In: *Journal of the Optical Society of America A* 35.6 (June 2018), pp. 1021–1027 (cit. on p. 76).

[87] M. Anguiano-Morales, A. Martínez, M. D. Iturbe-Castillo, S. Chávez-Cerda, and N. Alcalá-Ochoa. "Self-healing property of a caustic optical beam". In: *Applied Optics* 46.34 (Dec. 2007), pp. 8284–8290 (cit. on p. 76).

[88] J. Arlt and K. Dholakia. "Generation of high-order Bessel beams by use of an axicon". In: *Optics Communications* 177.1 (2000), pp. 297–301. ISSN: 0030-4018 (cit. on p. 76).

[89] S. N. Khonina, N. L. Kazanskiy, S. V. Karpeev, and M. A. Butt. "Bessel beam: significance and applications — a progressive review". In: *Micromachines* 11.11 (2020). ISSN: 2072-666X (cit. on pp. 79, 80).

[90] Cisco Systems. *Cisco Annual Internet Report*. [Online; https://www.cisco.com, accessed 27-February-2023]. 2018-2023 (cit. on p. 80).

[91] R. M. Herman and T. A. Wiggins. "Production and uses of diffractionless beams". In: *Journal of the Optical Society of America A* 8.6 (June 1991), pp. 932–942 (cit. on p. 80).

[92] J. Turunen, A. Vasara, and A. T. Friberg. "Holographic generation of diffraction-free beams". In: *Applied Optics* 27.19 (Oct. 1988), pp. 3959–3962 (cit. on p. 80).

[93] E. Negri, W. Fuscaldo, P. Burghignoli, and A. Galli. "Leaky-wave analysis of tm-, te-, and hybrid-polarized aperture-fed Bessel-beam launchers for wireless-power-transfer Links". In: *IEEE Transactions on Antennas and Propagation* 71.2 (2023), pp. 1424–1436 (cit. on p. 80).

[94] F. Benassi, E. Negri, W. Fuscaldo, G. Paolini, F. Maita, P. Burghignoli, D. Masotti, A. Galli, and A. Costanzo. "TE-polarized Bessel-beam launchers for wireless power transfer at millimeter waves: theory, design, and experimental validation". In: *IEEE Transactions on Microwave Theory and Techniques* (2024), pp. 1–12 (cit. on p. 80).

[95] COMSOL AB. *COMSOL Multiphysics*. https://www.comsol.com. Jan. 2023 (cit. on p. 90).

[96] K. D. Paschaloudis, R. C. M. Pimenta, G. Soriano, and M. Ettorre. "Near-field links with obstructed line of sight via Bessel beams". In: *2023 17th European Conference on Antennas and Propagation (EuCAP)*. 2023, pp. 1–3 (cit. on p. 101).

[97] K. D. Paschaloudis, R. C. M. Pimenta, D. González-Oveiero, G. Soriano, and M. Ettorre. "Metasurface-based Bessel-beam launcher with 100λ non-diffractive range". In: *2024 18th European Conference on Antennas and Propagation (EuCAP)*. 2024, pp. 1–3 (cit. on p. 101).

[98] C. Lyu, Y. Zhang, M. R. Belić, Y. Li, and Y. Kang. "Diffraction-free distance enhancement of Bessel beams based on spatial domain phase modulation". In: *Journal of the Optical Society of America B* 40.11 (Nov. 2023), pp. 2906–2912 (cit. on pp. 104, 105).

[99] Dassault Systèmes. *CST Studio Suite 2024*. Electromagnetic field simulation software. Available: https://www.3ds.com/products-services/simulia/products/cst-studio-suite/. CST AG, part of Dassault Systèmes. 2024 (cit. on p. 114).

[100] Z. Jaroszewicz. *Axicons: Design and Propagation Properties*. Research & Development Treatises vol. 5. Polish Chapter of SPIE, 1997 (cit. on pp. 115, 117, 118).

[101] A. Thaning, Z. Jaroszewicz, and A. T. Friberg. "Diffractive axicons in oblique illumination: analysis and experiments and comparison with elliptical axicons". In: *Applied Optics* 42.1 (Jan. 2003), pp. 9–17 (cit. on pp. 115, 117, 118).

[102] A. Thaning. "Asymptotic Methods in Design and Characterization of Diffractive Axicons". NR 20140805. PhD thesis. Mikroelektronik och informationsteknik, 2002 (cit. on pp. 115, 117, 118).

[103] S. N. Khonina, N. L. Kazanskiy, P. A. Khorin, and M. A. Butt. "Modern types of axicons: new functions and applications". In: *Sensors* 21.19 (2021) (cit. on p. 115).

[104] J. Dyson. "Circular and spiral diffraction gratings". In: *Proceedings of the Royal Society of London. Series A, Mathematical and Physical Sciences* 248.1252 (1958), pp. 93–106 (cit. on p. 115).

[105] S. Monk, J. Arlt, D. A. Robertson, J. Courtial, and M. J. Padgett. "The generation of Bessel beams at millimetre-wave frequencies by use of an axicon". In: *Optics Communications* 170.4 (1999), pp. 213–215. ISSN: 0030-4018 (cit. on p. 115).

[106] L. M. Soroko. *Meso-optics: Foundations and Applications*. World Scientific, 1996. ISBN: 9789810227005 (cit. on p. 116).

[107] X. Yu, M. Zhang, and S. Lei. "Multiphoton polymerization using femtosecond Bessel beam for layerless three-dimensional printing". In: *Journal of Micro and Nano-Manufacturing* 6.1 (Dec. 2017), p. 010901. ISSN: 2166-0468 (cit. on p. 118).

[108] D. C. Palangyos and R. A. Guerrero. "Variable Bessel beam profiles generated through refraction by liquid media". In: *Micromachines* 14.8 (2023). ISSN: 2072-666X (cit. on p. 119).

[109] W. Fuscaldo and S. C. Pavone. "Metrics for localized beams and pulses". In: *IEEE Transactions on Antennas and Propagation* 68.2 (2020), pp. 1176–1180 (cit. on pp. 119, 129, 131).

[110] I. Neshev D. and Aharonovich. "Optical metasurfaces: new generation building blocks for multi-functional optics". In: *Light: Science & Applications* 7.1 (Aug. 2018), p. 58 (cit. on p. 121).

[111] J. Billuart. "Conception d'Optiques Planes Multifonctionelles par Stucturation Sub-longueur d'Onde". PhD thesis. Aix-Marseille Université, 2021 (cit. on p. 121).

[112] F. Alsolamy. " Cylindrical vector beam generation using spatially-dispersive, mode-converting metasurfaces". PhD thesis. University of Michigan, Horace H. Rackham School of Graduate Studies, 2022 (cit. on p. 122).

[113] G. Minatti, M. Faenzi, E. Martini, F. Caminita, P. De Vita, D. González-Ovejero, M. Sabbadini, and S. Maci. "Modulated metasurface antennas for space: synthesis, analysis and realizations". In: *IEEE Transactions on Antennas and Propagation* 63.4 (2015), pp. 1288–1300 (cit. on p. 122).

[114] M. Faenzi, G. Minatti, D. Gonzalez-Ovejero, F. Caminita, E. Martini, C. Della Giovampaola, and S. Maci. "Metasurface antennas: new models, applications and realizations". In: *Scientific Reports* 9.1 (Dec. 2019) (cit. on p. 122).

[115] J. Lee and H. Lee. "Metasurface-enhanced antenna system for terahertz band wireless communications". In: *2020 IEEE Wireless Communications and Networking Conference Workshops (WCNCW)*. 2020, pp. 1–6 (cit. on p. 122).

[116] B. O. Raeker and A. Grbic. "Compound metaoptics for amplitude and phase control of wave fronts". In: *Phys. Rev. Lett.* 122 (11 Mar. 2019), p. 113901 (cit. on p. 122).

[117] S. Zahra, L. Ma, W. Wang, J. Li, D. Chen, Y. Liu, Y. Zhou, N. Li, Y. Huang, and G. Wen. "Electromagnetic metasurfaces and reconfigurable metasurfaces: a review". In: *Frontiers in Physics* 8 (Jan. 2021) (cit. on p. 122).

[118] N. Yu and F. Capasso. "Flat optics with designer metasurfaces". In: *Nature Materials* 13.2 (Feb. 2014), pp. 139–150 (cit. on p. 122).

[119] S. Kar. *Metasurfaces—fundamentals, physics, modelling, and applications*. 2053-2563. IOP Publishing, 2023, 6-1 to 6–51 (cit. on p. 122).

[120] A. Cano-Vicent, M. M. Tambuwala, S. S. Hassan, D. Barh, A. A. A. Aljabali, M. Birkett, A. Arjunan, and A. Serrano-Aroca. "Fused deposition modelling: Current status, methodology, applications and future prospects". In: *Additive Manufacturing* 47 (2021), p. 102378 (cit. on p. 122).

[121] M. S. Islam. "Metalens-based Receiver Design for Free Space Optical Communication". PhD thesis. UC Irvine, 2024 (cit. on p. 123).

[122] R. Czarny, T. Q. Van Hoang, B. Loiseaux, G. Bellomonte, R. Lebourgeois, A. Leuliet, L. Qassym, C. Galindo, J. Heintz, N. Penin, L. Fourier, C. Elissalde, J. Silvain, T. Fournier, C. Jegou, and P. Pouliguen. "High permittivity, low loss, and printable thermoplastic composite material for rf and microwave applications". In: *2018 IEEE Conference on Antenna Measurements & Applications (CAMA)*. 2018, pp. 1–4 (cit. on p. 123).

[123] D. T. McGrath and V. P. Pyati. "Periodic boundary conditions for finite element analysis of infinite phased array antennas". In: *Proceedings of IEEE Antennas and Propagation Society International Symposium and URSI National Radio Science Meeting*. Vol. 3. 1994, 1502–1505 vol.3 (cit. on p. 124).

[124] W. Fuscaldo, P. Burghignoli, and A. Galli. "A comparative analysis of Bessel and Gaussian beams beyond the paraxial approximation". In: *Optik* 240 (2021), p. 166834. ISSN: 0030-4026 (cit. on pp. 137, 138).

[125] Y. C. Zhong and Y. J. Cheng. "Wideband quasi-nondiffraction beam with accurately controllable propagating angle and depth-of-field". In: *IEEE Transactions on Antennas and Propagation* 65.10 (2017), pp. 5035–5042 (cit. on p. 141).